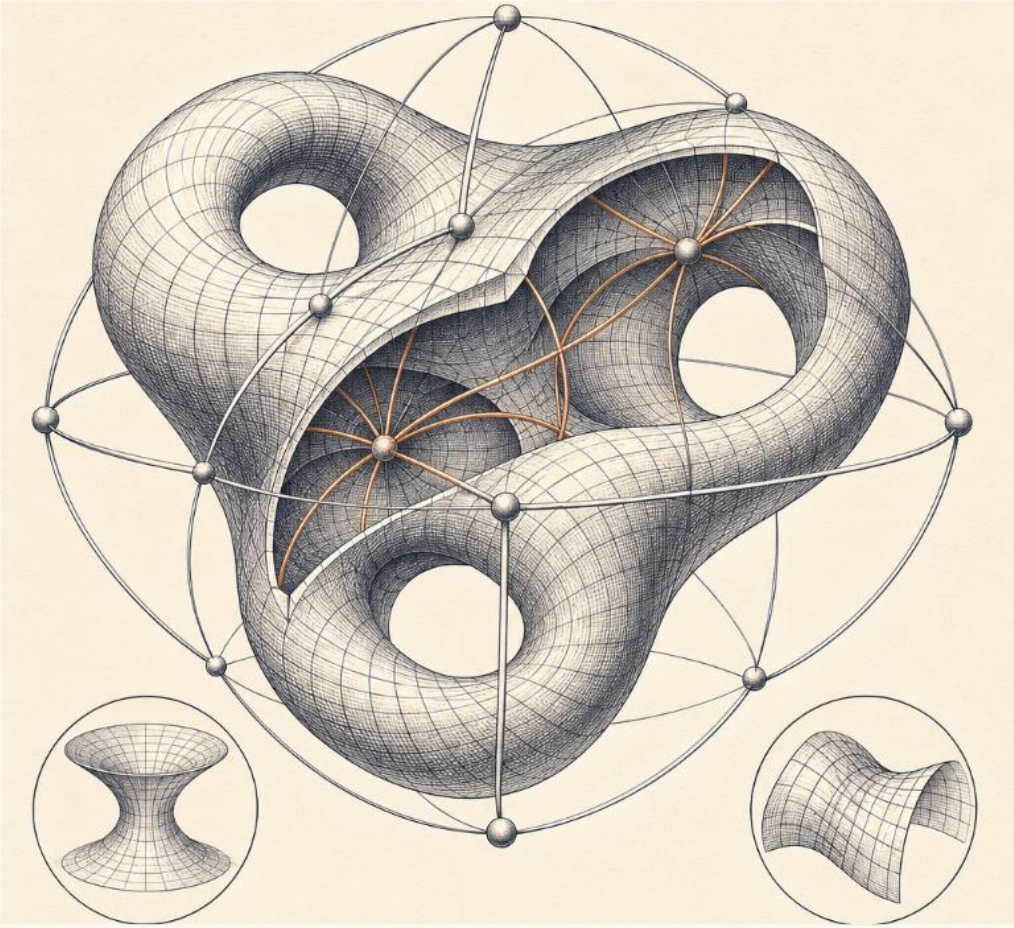
Space from Within



Eudgene Brenev
Mira Veyran

2026

Eudgene Brenev
Mira Veyran

Space from Within

Hypotheses about Space and Instruments for Testing Them

2026

Contents

Preface 4
How to Read This Book 5
Chapter 1 Space without an external observer 7
Chapter 2 How is dimension measured? 16
Chapter 3 When dimension depends on scale 28
Chapter 4 Hidden and synthetic directions 34
Chapter 5 Geometry from quantum relations 42
Chapter 6 Can space be reconstructed from its response? 50
Chapter 7 The hypothesis of shared sparse connectivity 59
Chapter 8 A computational experiment and its robustness 67
Chapter 9 From a network analogue to a causal physical model 85
Chapter 10 Hidden Geometry Spectroscopy 92
Chapter 11 Clocks and gravimeters as a joint probe of space 103
Chapter 12 What can an interferometer hear? 117
Chapter 13 Three instruments and the path from signal to inference 128
Chapter 14 How to distinguish a discovery from a convincing mistake 138
Chapter 15 What has been established and how to continue testing 145
Appendix A Mathematical Conventions 150
Appendix B Repetition of computational experiments 153
Appendix C A map of testable claims 155
Appendix D Dictionary of basic concepts 156
Appendix E Practical work: from voltages to link reconstruction 159
References 169
Index of illustrations 173

Preface

From Distance to the Structure of Space

We know space through action: an object can be moved, a distance measured, a signal sent and received. Yet the same result in a single experiment does not determine how the world is structured. Two systems may have the same oscillation frequencies but different paths for transmitting a disturbance. A change in readings may result from a new connection, instrument drift, or a poorly chosen model. This book begins by asking what observations can distinguish these possibilities.

The main line of inquiry concerns reconstructing connectivity from response. A hidden connection is introduced into a known network, and its location is then recovered using a few accessible ports. The next step makes the problem more realistic: ordinary connections are also known only with finite precision. We must then determine how much of the unusual signal can still be explained by calibration and what additional measurement could change the conclusion.

The book pursues this question through complete examples. Small networks provide explicit matrices and reveal the source of ambiguity. A larger numerical experiment tests the reconstruction. A constrained drift model defines the limits of an admissible explanation. Multiple probes and selected measurement contrasts test what new information has actually been obtained. A practical exercise with a resistive-capacitive (RC) network connects this mathematics to voltages, recording time, and readout errors.

Other chapters examine a compact direction, joint clock and gravimetric signals, and interferometric response. Each line of inquiry selects a particular operator or field, derives an observable quantity, and identifies a competing mechanism. These models share a method of investigation. They are not derived from a single fundamental action and have different physical assumptions.

The book addresses readers interested in the structure of space who are willing to test their own assumptions. Formulas accompany the argument, while numerical examples let us move back from notation to observation. The computational route requires linear algebra, basic probability, and familiarity with differential equations. Spectral density, the response matrix, and common causes are introduced through specific problems.

The principal results of our own experiments were obtained using specified mathematical systems and synthetic data. Experimental information about nature is drawn from primary publications. Keeping these levels separate allows us to assess each conclusion: where a proved identity applies, where an algorithm has been tested, and where a physical prediction awaits measurement.

How to Read This Book

Two Routes

On a first reading, it helps to follow one question: what exactly does the next measurement add? In Chapter 1, this concerns comparing geometric operations; in Chapter 2, moving from an average spectrum to local response; in Chapters 6–8, distinguishing structure from drift; and in Chapter 11, a joint test using two kinds of instrument. After this first pass, the technical derivations have a clear purpose.

Route	Main Sequence	Prerequisites
Conceptual	Chapters 1–2; opening and concluding sections of 3–5; examples in 6–8; physical problem formulations in 10–13; conclusions in 15	Functions, proportions, units, and a willingness to follow a small matrix example
Computational	All derivations in 2–12; the statistical protocol in 14; the RC practical exercise and computational appendix	Matrices, eigenvalues, derivatives, probabilities, and the spectral representation of signals

Chapter 3 can initially be read as an overview of different mechanisms. The holographic formulas in Chapter 5 require their own theoretical context and are not prerequisites for the network experiment. If matrices become difficult, return to the three-node example in Chapter 2: each row of the operator and each column of the response is tied to an action on the system.

Detailed conditions of applicability are retained wherever a conclusion depends on them. A glossary, notation table, and map of claims support later readings. The computational appendix specifies the parameters and limitations of the calculations; running commands are collected in the accompanying instructions. The technical procedure for the RC experiment is presented separately so that the main account does not become a list of settings.

Three Lines of Inquiry

Direction	Observed Data	What Is Tested
Connectivity	The response matrix between accessible inputs and outputs	An additional connection, admissible drift, and the set of indistinguishable structures
A compact direction	The static force and dynamic response of a selected scalar probe	A single ladder of modes with specified source-detector coupling
Consistent perturbations	Spectra of clock differences, accelerations, and interferometric phase	The joint prediction of a specific field and its distinction from an instrumental or kinematic cause

The network analog lets us test an algorithm against known ground truth. The compact model specifies a concrete alternative to ordinary geometry. Stochastic and interferometric models connect

spatial assumptions with several recording channels. Success in one line of inquiry does not transfer its physical interpretation to the others. The shared procedure is to specify a model, derive an observation, compare alternatives, and define the limits of the conclusion.

Distinguishing Levels of Results

Status	What It Means in This Book
An established result	A method or physical proposition with its original publication and conditions of application identified
A model-derived result	A formula follows from an explicitly stated operator, kernel, or geometry
A numerical test	A program has carried out the specified experiment; inputs, parameters, and commands are available
A measurement design	A signal has been predicted and requirements calculated; a physical apparatus must still test it
An observation of nature	The result of a published experiment applying to a defined class of models

The rank of a response matrix, the number of spatial directions, and the number of model parameters answer different questions. In what follows, the name of each quantity comes with its operational meaning. Cases in which the data can reject one model but cannot uniquely reconstruct another are especially important.

The illustration index at the end of the book helps you find a particular diagram. A conceptual illustration does not replace an engineering drawing, calibration, or experimental data.

Chapter 1
Space without an external observer

Observer inside space

Let's imagine a researcher who has access to a clock, light sources, reflectors, and several moving bodies. He does not have a photograph of the world from the outside and does not have the opportunity to rise above space to examine its shape. Everything he knows comes from the meetings of bodies, instrument readings and the exchange of signals. This is exactly the situation physics finds itself in. Even the space observatory remains part of the world being explored. Therefore, the question of space begins with the relationships between observable events. Which movements are independent of each other? How to compare distances? How to distinguish the curvature of space from changes in the measuring device itself? The answers must be available to the observer who never leaves his universe.

To begin with, it is enough to ask what relationships are verifiable. You can compare lengths, signal travel times, free movement and closed loop results. The agreement of these procedures supports the selected geometry. Their discrepancy shows where it is necessary to check the device, the environment, or the rule itself for describing space.

In Figure 1, the observer is included in the same network of measurement operations from which the geometry is reconstructed.

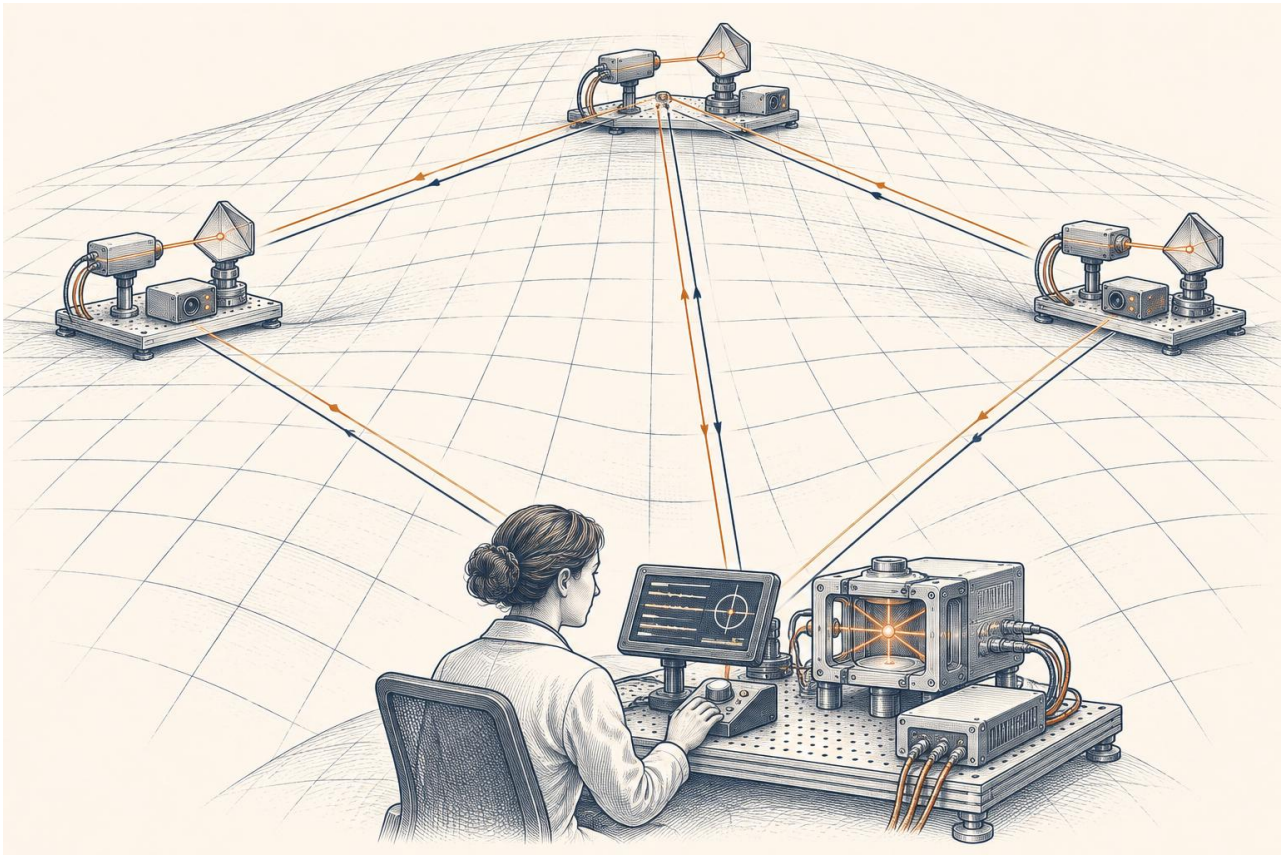


Figure 1. Observer inside the measuring network. Clocks, emitters and reflectors form a system of accessible comparisons: signal transmission, distance measurement and closed circuits. A perspective surface serves as a symbolic way to show the relationships between nodes; it does not presuppose an external observer of the Universe. This is a conceptual illustration of measurement operations and not a depiction of a specific experiment performed.

Terminology can also complicate the discussion. Here, measurement means an operation performed by an instrument, a dimension means an independent direction, and dimensionality means the number of such directions. A third concept is a variable in a mathematical model. Temperature, concentration, and electric potential can be independent variables without becoming new spatial directions. A researcher can plot data in a space of hundreds of features while remaining in an ordinary laboratory. Before discussing a fifth or tenth dimension, we must therefore identify what the number describes: a body’s position, a system’s state, observational data, or fundamental geometry.

Coordinates and independent directions

The number of recorded coordinates in itself does not prove anything. The position of a point on the surface of a sphere can be specified by three Cartesian coordinates, but they are related by the condition of constant radius. If two coordinates are slightly changed in the feasible region, the third is determined by the surface equation with the selection of the appropriate area. Locally, two

independent degrees of freedom remain. And vice versa, two angular coordinates do not cover the sphere with one completely regular map: at the poles the usual notation loses its convenience. A grid malfunction does not mean a physical malfunction of the surface. This simple example allows you to immediately separate the geometry from the way it is written.

$$x^2 + y^2 + z^2 = R^2, \qquad d_{\text{local}} = 3 - 1 = 2 \qquad (1.1)$$

The equality on the right side is true for this example because one smooth independent constraint reduces the local number of free coordinates by one. It cannot be applied mechanically to any set of equations: the constraints can depend on each other, and at singular points their rank can change. The practical meaning of independence is easier to see by the movements. If all small permissible movements are expressed in terms of two independent directions, the third coordinate record remains redundant. For physical additional dimension, it is necessary to show a new class of independent displacements or a corresponding additional set of propagating modes. Adding a letter to the equation is not enough.

Another common confusion arises in many-body mechanics. Three free particles in three-dimensional space require nine position coordinates. When including momenta, the description of the phase-space state already contains eighteen numbers. This does not mean that the particles have moved into physical space with eighteen directions. High dimensionality belongs to the space of possible states of the entire system. A similar distinction persists in quantum theory, where state space has an even richer structure. In the future, any statement about high dimensionality will be accompanied by an indication of which objects are its points and what changes correspond to movement between these points.

How distance gets physical meaning

Coordinates become geometry only after the appearance of a rule for comparing close positions. On a smooth space, such a rule is given by a metric. It turns small changes in coordinates into physical length and allows us to take into account that the same numerical change in different coordinates does not necessarily mean the same movement. In the Cartesian system, the units along the axes are usually chosen to be identical, so the structure of the metric is almost invisible. In other coordinates it comes to the fore. The general notation below refers to a positive definite spatial metric; repeating indices mean summation over independent coordinates. The length is obtained after integration along the selected curve.

$$d\ell^2 = g_{ij}(x)\, dx^i dx^j, \qquad L[\gamma] = \int_\gamma \sqrt{g_{ij}\, dx^i dx^j} \qquad (1.2)$$

For a plane, let's move from Cartesian coordinates to radius and angle. A small radial movement has a length equal to the change in radius. A small angular displacement at a constant radius follows an arc, so its length is proportional to both the angle and the distance to the center. Substituting coordinate transformations into the usual Pythagorean theorem gives the following formula. The coefficient before the square of the angle change depends on the position, although the plane remains flat. Consequently, the dependence of the metric components on the coordinates does not in

itself indicate curvature. We need quantities whose meaning is preserved when moving to another coordinate grid.

$$x = r\cos\varphi, \quad y = r\sin\varphi, \qquad d\ell^2 = dr^2 + r^2 d\varphi^2 \qquad (1.3)$$

A physical metric requires a more meaningful justification than a neat recording of distances. The ruler can expand when heated, and the light transit time depends on the medium. Therefore, the geometric description is checked by matching different devices and taking into account their structure. In the general theory of relativity, the metric field simultaneously participates in the description of intervals and gravitational interaction; free movement and ideal clock readings are connected by one structure. It is this connection that turns geometry into a physical theory, and not just into a drawing language. A new description of space should offer a comparable clear rule for the connection between mathematical objects and real observations. [1]

The difference between coordinates, directions and lengths can be conveniently seen in two geometric examples (Fig. 2).

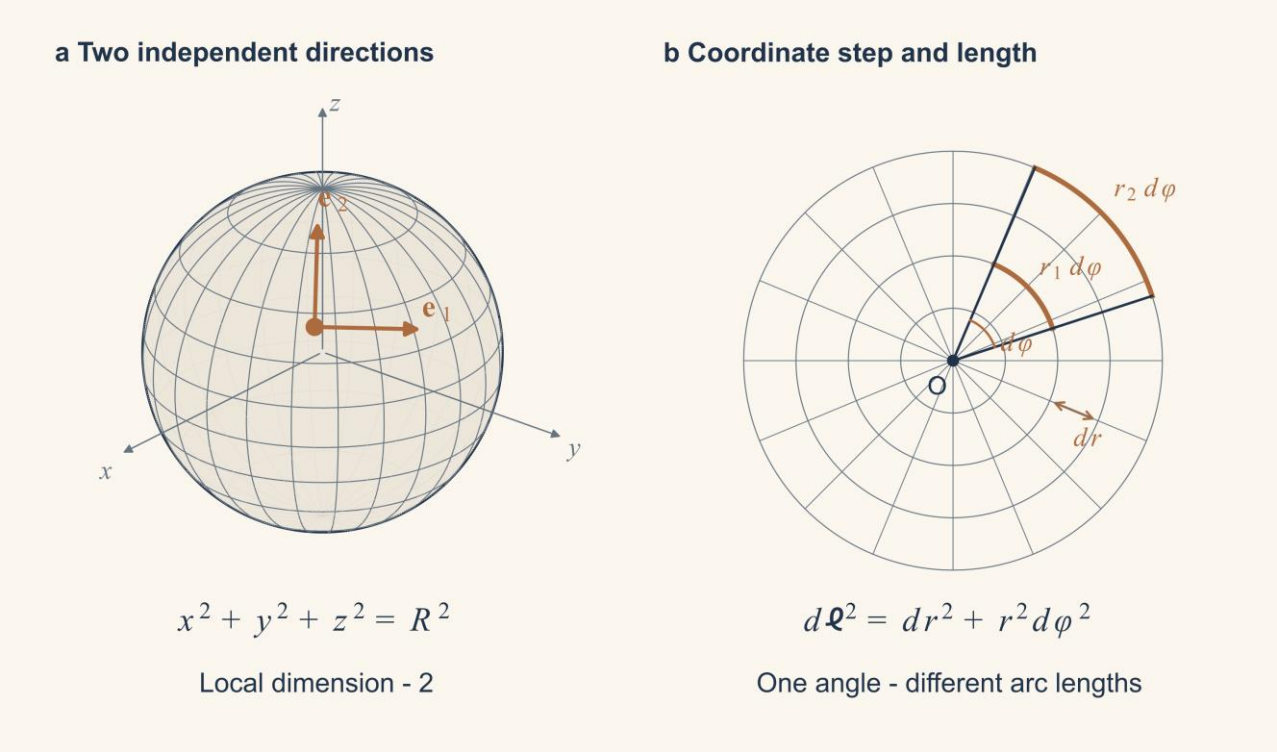


Figure 2. The number of coordinates in a record does not define the internal dimension. The position on the sphere is described by three numbers, but the condition of belonging to the surface leaves two independent tangent directions. On the right, the same change in angle corresponds to different arc lengths at different radii. The polar metric converts coordinate increments into physical length; the peculiarity of the coordinates at the beginning does not mean a defect in the plane.

Curvature is revealed from within

An inhabitant of the surface does not need to see its bend in the surrounding space. He can construct a circle by measuring the same shortest distance from a chosen center, and then measure its length. On a plane, the ratio of length to radius is constant. On a sphere of radius R, the circle of

geodesic radius r has a different length. Here r is measured along the surface from the center of the circle, and not along a straight line through the volume of the ball. For a sufficiently small r, the difference is small, so the local area looks almost flat. As the area covered increases, the deviation accumulates and becomes visible to the internal observer without any external point of view.

$$C(r) = 2\pi R\sin(r/R) = 2\pi r\left[1 - \frac{r^2}{6R^2} + O\left(\frac{r^4}{R^4}\right)\right] \qquad (1.4)$$

The expansion shows that the first relative difference from the flat result is proportional to the square of the size of the experiment. This is a useful hint for the future device: changing the scale of the measuring figure may be more important than endlessly increasing the accuracy of one distance. In this case, it is necessary to control systematic changes in the method itself as the size increases. If the experiment uses signals, increasing the path can increase the influence of the environment and imitate the geometric effect. A mathematical formula specifies the expected scaling, but a physical interpretation emerges only after comparing alternative causes. The two-dimensionality of the sphere is preserved throughout this argument: its geometry changes, and not the number of independent small displacements.

Another internal comparison method uses direction transfer along a closed path. On a plane, an ideal parallel translation returns the arrow with its previous orientation. On a curved surface the result may vary; for a small contour, the deviation is related to the curvature of the area covered. In real space, a similar concept requires specifying what sets the direction and what external influences act on the device. The gyroscope rotation, support deformation, and geometric translation must be different in the observation model. The meaning of the example is different: curvature manifests itself in the comparison of paths and closure of operations. A single segment measurement typically reports significantly less than a consistent network of measurements.

For a numerical reference, we take a sphere of radius 10 m and a geodesic circle of radius 1 m. The flat formula gives the length 6.283185 m, the spherical one - 6.272719 m. The difference is 10.47 mm. It is small in relation to the circumference, but quite definite. When the contour size is halved, the relative effect, to a first approximation, will decrease by a factor of four.

$$K_{\text{est}} = \frac{6}{r^2}\left(1 - \frac{C(r)}{2\pi r}\right), \qquad r/R \ll 1 \qquad (1.5)$$

This estimate of the Gaussian curvature is obtained directly from the previous expansion. In the selected example, it is equal to 0.009995 m^{-2} with the exact value $1/R^2 = 0.01$ m^{-2}. The difference between them is the series truncation error. The measurement error in length would be another contribution and must be taken into account separately. This is how the formula turns into an experiment: the figure, magnitude, scale of the expected deviation and the accuracy of the approximation are given.

The circle and the closed translation provide two independent images of the internal curvature check (Fig. 3).

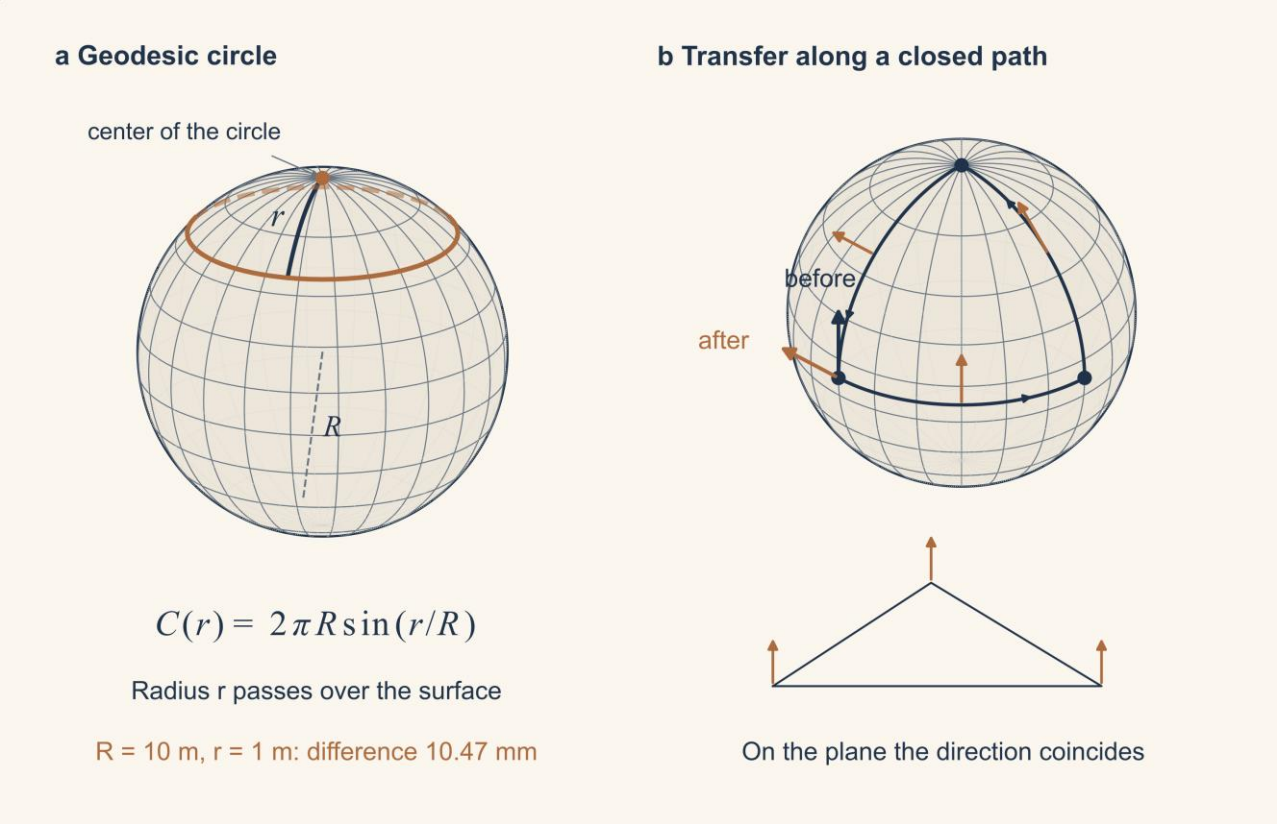


Figure 3. Two ways to detect curvature while remaining on the surface. On the left, the radius r is measured by the geodesic, while R refers to the entire sphere; The circle image is enlarged for clarity and does not maintain the ratio of the radii of the numerical example. On the right, the arrow is moved in parallel along three arcs of great circles. On a sphere, its final direction differs from the initial one; on a plane, the closure of the contour preserves the direction.

Another subtlety will appear in space-time. Accelerated observers can detect differences in clock rates even in flat geometry. Therefore, clock gradient and curvature will require different checks. A complete example of the accelerated system and tidal control will be discussed in chapter 11.

Topology and the limits of a local experiment

Spaces can have the same local geometry and differ in global structure. The sheet can be rolled into a cylinder without stretching it; small shapes on its surface will maintain a flat geometry. However, the path around the cylinder cannot be contracted to a point while remaining on the surface. This is how the difference in topology manifests itself. For this purpose, bending is not required as an independent physical cause: flat space with a periodic coordinate can be defined directly through the rule for identifying points. The drawing of a cylinder only helps the imagination. Therefore, the absence of noticeable curvature does not exclude unusual global connectivity and does not determine whether space is finite or infinite.

Different topologies require observations spanning the appropriate scale. If the length of a closed direction significantly exceeds the accessible area, a local experiment may not distinguish it from an open direction. This is not a shortcoming of the researcher, which is necessarily corrected by a bolder hypothesis, but a limitation of information. Two mathematical models are able to describe all available data in the same way. Then the result should be formulated through the region of discernibility: what sizes or types of closure are excluded and under what conditions. The statement “no boundaries are found” is not the same as the statement “space is infinite.” Likewise, failure to see an edge does not prove the existence of an external space beyond the supposed edge.

Topology, metric and dimension must therefore be discussed separately. Topology describes the neighborhood and methods of global connection, the metric specifies lengths, angles and intervals, dimension characterizes the number of independent local directions or a certain scaling law. These structures interact, but do not replace each other. In a research project, it is useful to explicitly record which of these changes in the hypothesis. A closed coordinate, a new short connection between distant areas and a different law of wave propagation lead to various mathematical problems. If you combine them with one word “space”, you can get a beautiful description that does not allow you to choose either a calculation or a device for testing.

The stripe-cylinder juxtaposition separates global closure from intrinsic curvature (Figure 4).

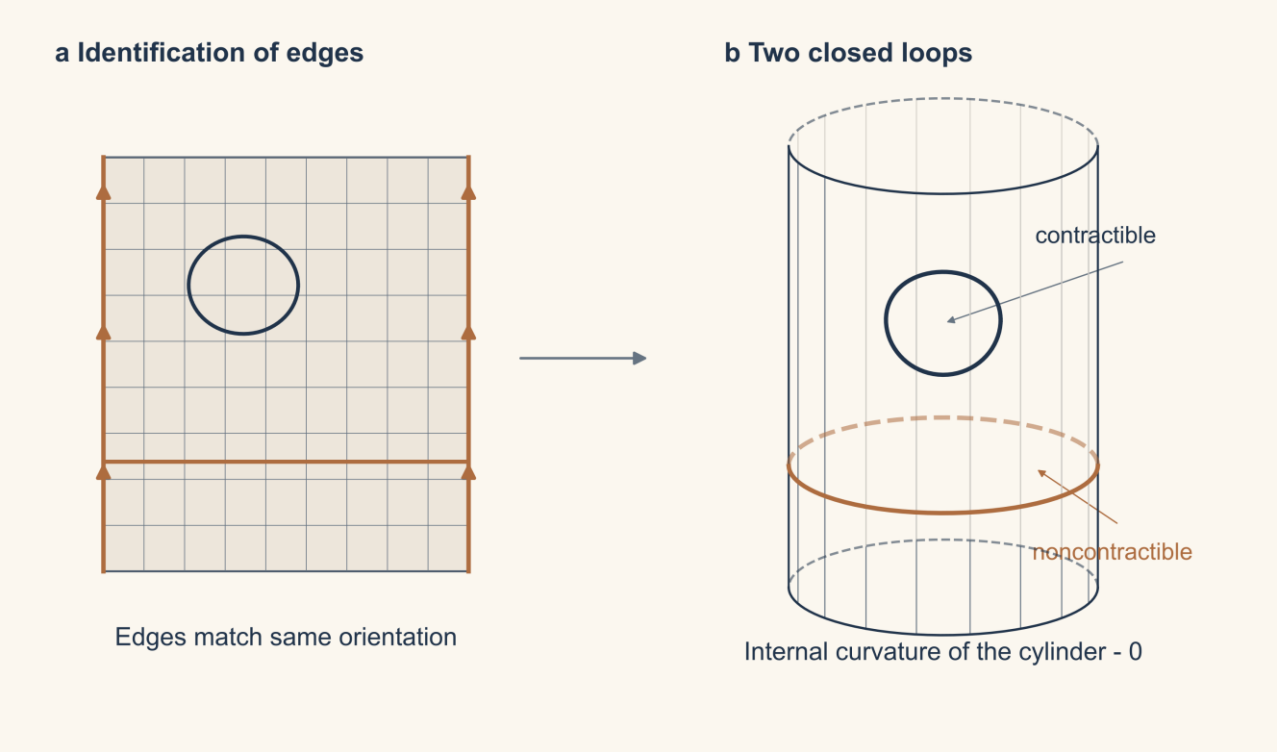


Figure 4. The opposite edges of the flat strip are identified with the same orientation and form a cylinder. A small closed contour on its surface can be continuously contracted to a point; a contour enclosing a closed direction cannot be contracted. In this case, the internal Gaussian curvature of the cylinder is zero. Visible curvature serves as a way to depict a surface and does not replace the measurement of its internal geometry.

Why time is not another spatial axis

In the relativistic description, time and space are included in a single structure of events, but retain differences in the signs of the interval. Let us choose an agreement in which the time part has a negative sign. For a local inertial description in flat space-time, the interval is written in terms of the speed of light and coordinate increments. The proper time of a clock is determined along its time-like trajectory. The numerical combination of four coordinates does not turn the temporal direction into an ordinary road along which you can arbitrarily turn and return. The metric signature organizes light cones and valid causal relationships between events; it forms the physical part of the model, and not the graphic design of the formula.

$$ds^2 = -c^2 dt^2 + dx^2 + dy^2 + dz^2, \qquad d\tau^2 = -\frac{ds^2}{c^2} \quad \text{for a timelike trajectory} \qquad (1.6)$$

The proposal to introduce additional time therefore requires independent verification. It is necessary to specify the initial data, the evolution rule and the conditions under which the solution is determined uniquely and stable. Simply adding another negative term to an interval does not guarantee these properties. Such models can be studied mathematically, but their physical validity does not follow from the ability to write down the metric. The same principle applies to variable-dimensional spaces: first we need to figure out what exactly is changing, how the transition affects field states, and how observations on both sides of the transition compare. Without these clarifications, the formula remains a designation of a problem that has yet to be solved.

The light cone visually connects the sign of the interval with the permissible trajectory of the clock (Fig. 5).

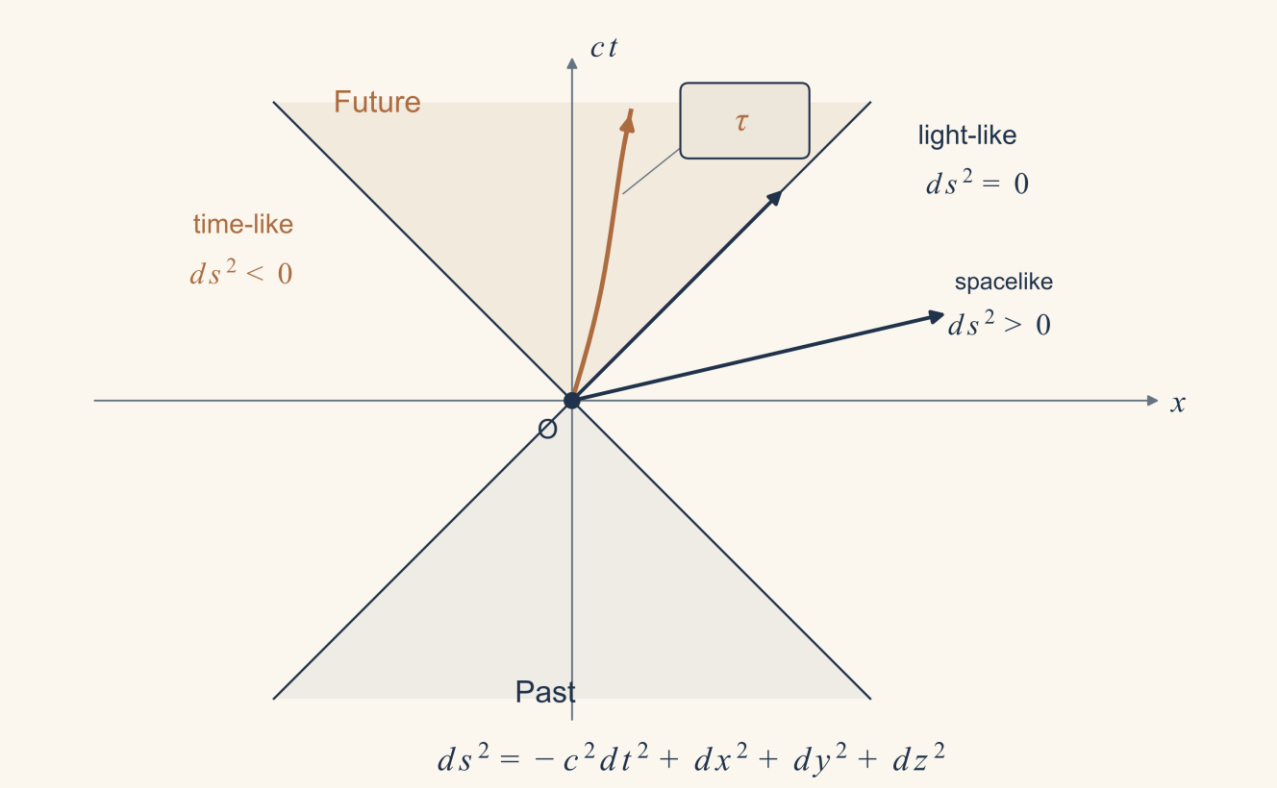


Figure 5. Projection of space-time onto one spatial coordinate and ct. Light directions form the boundary between the future and the past; the timelike world line passes inside the cone and allows readings of its own clock. The spacelike direction lies outside the cone. The interval signs correspond to the signature accepted in the text (−,+,+,+). The diagram shows the classification of intervals, not the measured trajectory of the instrument.

The spatial description is now associated with verifiable relationships: distances, spectra, transmission times and closure of operations. An unusual result should indicate which of these relationships has changed. The next chapter introduces different ways of assessing dimensionality and shows why a single object can receive different numerical scores depending on the dimension chosen.

Chapter 2
How is dimension measured?

Volume as a response to increasing scale

The most visual way to estimate dimensionality starts with a growing region. Along a straight line, the length of a segment increases in proportion to its radius; on a plane, the area of a disk grows as the square of the radius, and in ordinary three-dimensional space, the volume of a ball grows as a cube. The general meaning is the same: how quickly available positions arrive as the allowed distance increases. The experiment requires determining the distance, center of the area, and how to measure its volume. If particles or sensors are counted instead of volume, a model of their distribution density will be additionally needed. Otherwise, the heterogeneous population of space can easily be mistaken for the unusual dimension of space itself.

$$d_V(\ell) = \frac{d\ln[V(\ell)/V_0]}{d\ln(\ell/\ell_0)}, \qquad V(\ell) = A\ell^D \;\Rightarrow\; d_V = D \qquad (2.1)$$

Reference quantities in logarithms are needed so that their arguments are dimensionless; after differentiation, the constants disappear. The designation dV here means the operational volumetric dimension on the selected scale. It is not an automatic synonym for the strict Hausdorff dimension. The latter is determined through the coverage of the set by arbitrarily small areas and the corresponding limit. On a sufficiently regular space with a suitable measure, both approaches can be consistent. However, a real device operates on a finite range, and the derivative characterizes precisely this range. Therefore, the number 2.7, obtained from several scales, should first be read as a measured growth rate and only then its geometric status should be ascertained.

Determining the volumetric dimension begins with simple laws of growth of the measure (Fig. 6).

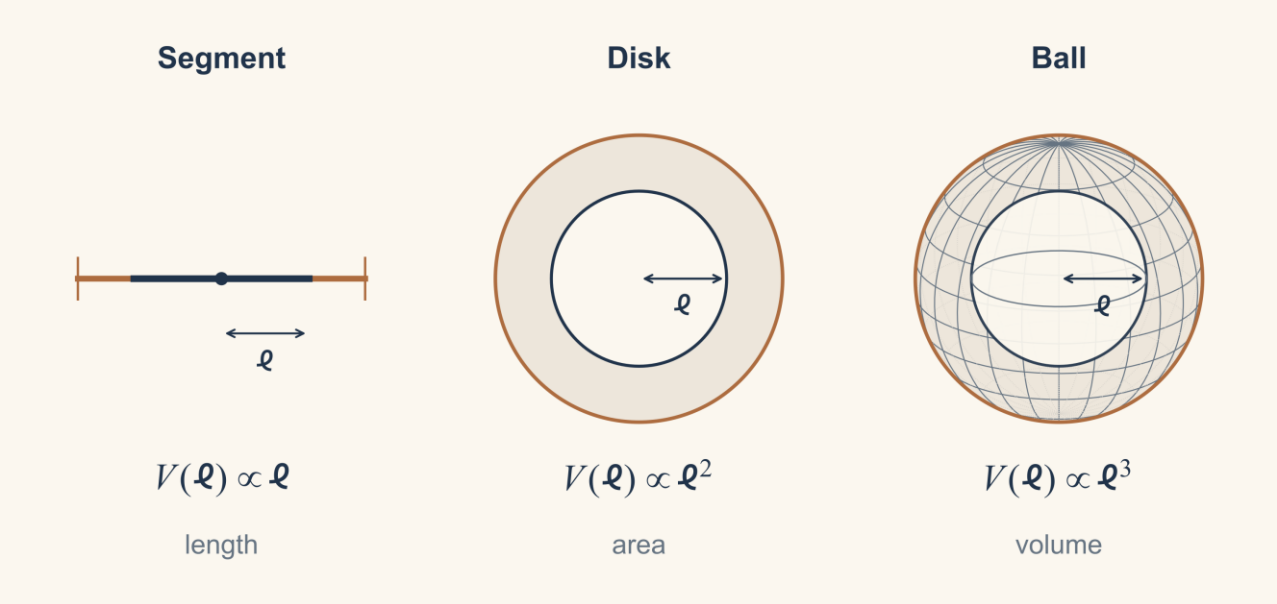


Figure 6. Reference Euclidean regions with increasing characteristic radius: segment, disk and ball. Their measures grow accordingly as the first, second and third degrees of scale. The smaller area is highlighted with a dark outline, the larger one with a copper outline. These mathematical examples explain the definition of volumetric exponent; they are not an observation of the dimension of real space or the result of a specific experiment.

Even a smooth sphere allows you to get an indicator that depends on the radius of the area. The area of the geodesic disk is calculated using the formula below. At a small radius it is almost equal to the area of a flat circle, and when it covers the entire sphere it stops growing. If you apply the logarithmic derivative without checking the range, the indicator will begin to decrease. In this case, the surface does not turn into a line: the ability to expand the disk on the final object is reduced. The example shows why deviation from a whole number is not enough to discover fractional geometry. The contributions of curvature, finite size, and region selection rules must be separately assessed.

$$A(r) = 2\pi R^2[1 - \cos(r/R)], \qquad 0 < r < \pi R \qquad (2.2)$$

$$d_V(r) = \frac{r}{R}\cot\left(\frac{r}{2R}\right) \qquad (2.3)$$

Differentiating the area gives the last equality. When r/R → 0 the indicator tends to two, and when covering the entire sphere - to zero. Figure 7 shows both relationships together: the area saturates, so its logarithmic slope decreases. The number of local surface directions remains equal to two throughout the example.

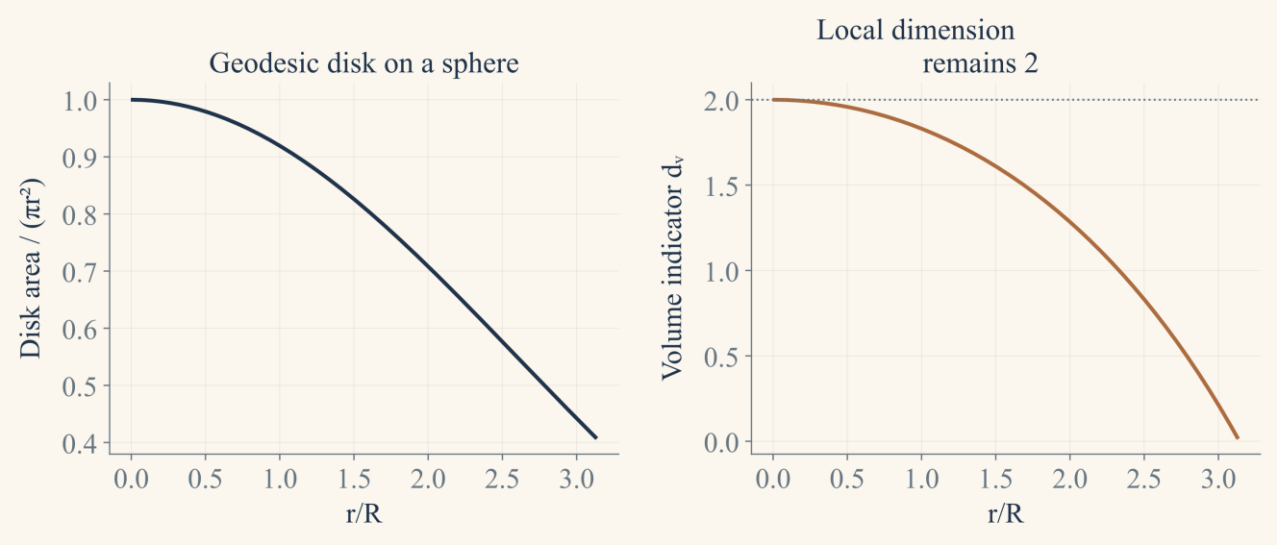


Figure 7. Geodesic disks on a smooth sphere. On the left, the area is related to the area of a flat circle of the same geodesic radius; on the right, its logarithmic slope is calculated. The change in indicator is caused by curvature and finite size. This is an exact geometric example, and not a registration of changes in the dimension of physical space.

Return probability as a probe of accessible space

The second method probes the propagation of an initial disturbance. Consider ordinary diffusion in infinite flat space, initially absorbing the diffusion coefficient into the parameter σ. Then σ has dimensions of area, and the equation involves the Laplacian over spatial coordinates. The initial distribution is concentrated at one point. The Gaussian solution has a width that grows as the square root of σ. At this stage, σ is a parameter of a mathematical process. To identify it with laboratory time, a specific propagation mechanism must be supplied and the corresponding diffusion coefficient reinstated. In quantum geometry, such a physical interpretation is often absent altogether.

$$\partial_\sigma K = \nabla^2 K, \qquad K(x, x_0; \sigma) = \frac{\exp\left[-|x - x_0|^2/(4\sigma)\right]}{(4\pi\sigma)^{D/2}} \qquad (2.4)$$

At the starting point, the exponent is equal to unity, so a simple power of the diffusion parameter remains. In continuous space we are talking about the probability density of return, since the probability of hitting exactly a single mathematical point is usually zero. The device uses a small receiving volume instead of a point, and the calculation must take its size into account. The spectral dimension is derived from the rate of decrease of this density. Substituting a Gaussian solution immediately returns the usual dimension D. It is this check that makes the definition meaningful: it reproduces a familiar result where the geometry and propagation law are known in advance, and can then be transferred to more complex operators.

$$P(\sigma) = K(x_0, x_0; \sigma), \qquad d_s(\sigma) = -2\frac{d\ln[P(\sigma)/P_0]}{d\ln(\sigma/\sigma_0)} \qquad (2.5)$$

In an inhomogeneous space, the return may depend on the starting point. Then you need to explicitly choose local measurement or volume averaging. For a compact region, the average heat

trace is determined by the sum of the contributions of all eigenmodes of the propagation operator. If the operator is not the generator of a probabilistic process, the name "return probability" becomes just an analogy: the spectral dimension can still be determined from the positive trace, but the individual kernel may not have a probabilistic meaning. The difference is especially significant for higher spatial derivatives. Reliable interpretation begins with specifying the operator and its properties, and not with a single numerical value of the indicator.

The rate of random-walk spreading and the relation between definitions

The return probability tells you how quickly the disturbance leaves the original region, but does not itself indicate how far it spreads. To do this, measure the average square of the distance from the beginning. With independent symmetric steps, the mixed products disappear after averaging, and the mean squares of the individual steps are added. Therefore, the result is proportional to the number of steps. In the continuous Gaussian example, integration gives the mean square of the distance equal to the product of 2D and the parameter σ. This is normal diffusion. If the average square is growing differently, you need to determine the walk exponent separately and then compare it with the return exponent.

$$\langle r^2(\sigma)\rangle = 2D\sigma, \qquad d_w = 2\left[\frac{d\ln\langle r^2\rangle}{d\ln\sigma}\right]^{-1} \qquad (2.6)$$

The exponent dw is called the dimension of the walk. With ordinary diffusion it is equal to two. If a spreading cloud is trapped in traps, its characteristic radius may increase more slowly and the exponent increases. But this behavior does not require changing the number of geometric directions: it is enough to change the dynamics. Ballistic motion, on the contrary, has a different growth law, and the diffusion interpretation should be applied to it with caution. In addition, the mean square may be poorly defined with heavy tails of the distribution. In this case, you have to choose another stable measure of width and re-establish the connection between this measure and the geometric derivation.

Figure 8 compares return to source and propagation distance.

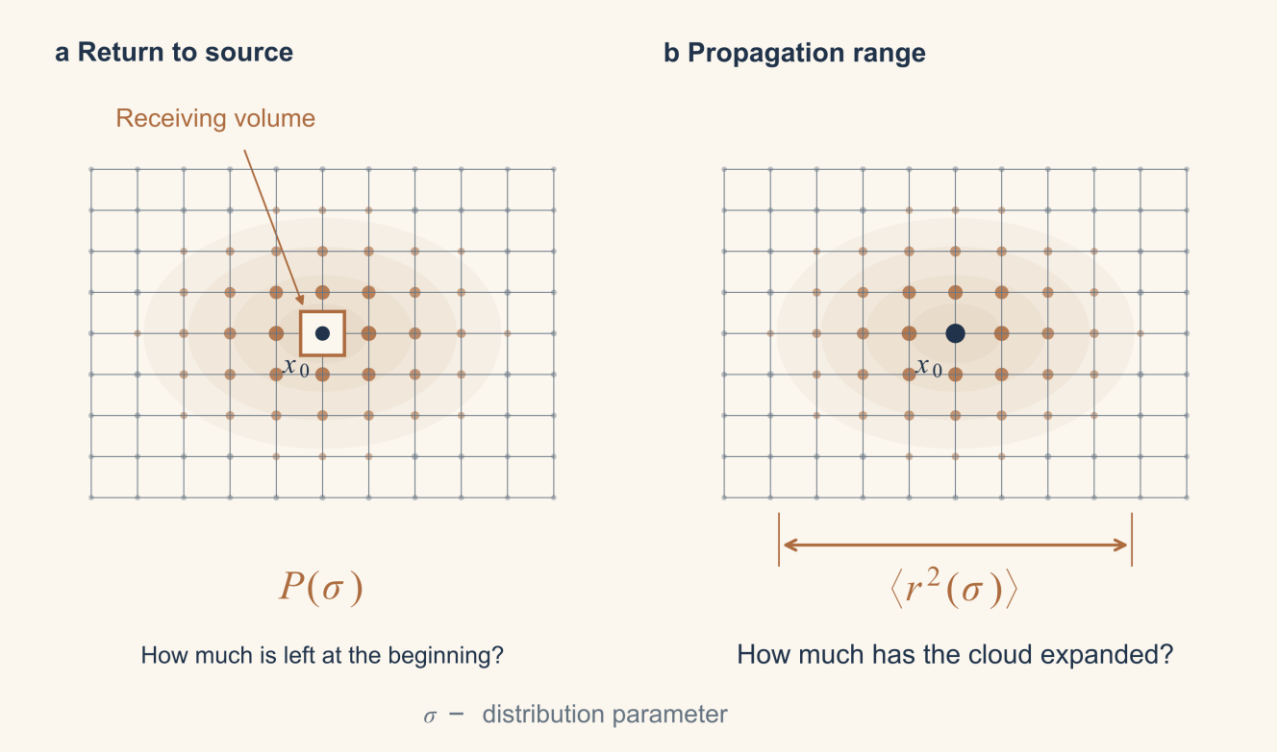


Figure 8. A single propagating disturbance allows for different read protocols. On the left, a small receiving volume near the source highlights the return; on the right, the spatial distribution characterizes the cloud width. The grid and intensity are depicted qualitatively, without experimental readings and a numerical scale. The parameter σ refers to the propagation model; its translation into laboratory time requires a given transfer coefficient and calibration.

The connection between the three indicators can be deduced under additional prerequisites. Let the characteristic radius grow as a power of σ, the volume of the accessible region as a power of the radius, and the distribution be uniform enough that the return is inversely proportional to this volume. Successive substitution gives the given relation. It is useful as a consistency check, but is not identical for every environment. Heterogeneity, multiple scales, pitfalls and different choice of measure violate the initial assumptions. Therefore, a non-zero remainder in the right-hand formula first means the failure of the chosen joint description. The transition to a statement of new physics requires eliminating more ordinary reasons for the discrepancy.

$$r \sim \sigma^{1/d_w}, \quad V(r) \sim r^{d_V}, \quad P \sim V^{-1} \Rightarrow d_s = \frac{2d_V}{d_w}, \qquad \Delta = d_s d_w - 2d_V \qquad (2.7)$$

Vibration spectrum as another record of the same information

Measuring returns does not need to be done using a real random walk. If the eigenvalues of the positive operator L are known, the heat trace can be constructed directly. Each mode makes an exponential contribution, and the parameter σ determines which spectral scales are noticeable. Large eigenvalues are quickly suppressed as σ increases. For the Laplacian, their dimension corresponds to

the inverse square of the length. Normalization to volume makes the result comparable for areas of different sizes. In the laboratory, eigenvalues can be reconstructed from resonant frequencies, but only after establishing the dispersion law: the frequency and the eigenvalue of the spatial operator are not the same object.

$$L\psi_n = \lambda_n \psi_n, \qquad P(\sigma) = \frac{1}{V}\sum_n e^{-\sigma \lambda_n} \qquad (2.8)$$

For a smooth region and an ordinary Laplacian, the number of modes below a large threshold is related to the volume and dimension. This is the content of Weyl's law; the shape of the boundary influences subsequent corrections, and the leading term specifies the power-law growth. In the above notation, ωD means the volume of a unit D-dimensional ball, and Λ is the threshold of eigenvalues. The formula makes an important transition from geometry to spectroscopy: dimensionality is reflected in how quickly new modes are added as the frequency range expands. But the applicability of the leading term requires a sufficient range, suitable boundary conditions and separation of additional internal degrees of freedom of the measured field. [2]

$$N(\Lambda) \sim \frac{V\,\omega_D}{(2\pi)^D}\,\Lambda^{D/2} \qquad (2.9)$$

Here a subtlety arises that is important for the future experimental project. Spectral density and heat trace calculated from the same set of modes are not two completely independent confirmations. These are two representations of the same information. Their agreement is useful for checking calculations, but does not eliminate the shared error in operator definition. The independence is enhanced when spectroscopy is coupled with direct pulse propagation or with geometric volume measurement. If both procedures use the same frequency calibration and the same assumed dispersion relation, their errors may coincide. A convincing result depends on the structure of dependencies between the data, and not on the number of graphs constructed.

Three nodes from circuit to measurement

Before moving on to the large network, it is useful to work through a small one in full. Let three identical reservoirs be designated by the numbers 0, 1 and 2. The first is connected to the second, the second to the third. The transfer intensity along each edge is equal to $r_0 = 1\ s^{-1}$. If the values in adjacent nodes are the same, there is no transfer between them; if different, the flow is proportional to the difference.

$$\dot{x}_0 = -r_0(x_0 - x_1), \quad \dot{x}_1 = -r_0(2x_1 - x_0 - x_2), \quad \dot{x}_2 = -r_0(x_2 - x_1) \qquad (2.10)$$

It is convenient to write these three equations in one line: $\dot{x} = -Lx$. Matrix L contains on the diagonal the sum of the connection intensities of a given node, and outside the diagonal - the connection intensity with a minus sign. Each row has a sum equal to zero: the uniform state does not change. The matrix here simply stores the already written transfer rules.

$$L_A = r_0 \begin{pmatrix} 1 & -1 & 0 \\ -1 & 2 & -1 \\ 0 & -1 & 1 \end{pmatrix} \qquad (2.11)$$

If at the initial moment a unit is inserted only into node j, the state after time t gives column j of the matrix K(t) = exp(−Lt). The element K_{ij} answers a specific question: what fraction of the initial disturbance reached node i? Averaging the three diagonal elements gives the average return P(t). This is a different protocol that requires access to all three initial states and the corresponding outputs.

A second convenient form of data is the exponentially weighted sum of the time response. The positive parameter s has reciprocal time units. By more strongly suppressing late readings, one can change the sensitivity to fast and slow processes.

$$G(s) = \int_0^\infty e^{-st}\, K(t)\, dt = (sI + L)^{-1}, \qquad s > 0 \qquad (2.12)$$

$$G_A(r_0) = \frac{1}{8r_0}\begin{pmatrix} 5 & 2 & 1 \\ 2 & 4 & 2 \\ 1 & 2 & 5 \end{pmatrix} \qquad (2.13)$$

The result is checked by ordinary multiplication: $(r_0 I + L_a)G_a(r_0) = I$. The middle column corresponds to the excitation of the 1 node. The weighted response in the node itself is equal to 0.5 s, in each extreme one - 0.25 s. The inverse matrix now has a measurement meaning, and each of its elements is associated with a specific pair of input and output.

It is useful to stop at this point and reconstruct one row L from the diagram, and then read one column G as the result of the experiment. For later chapters, this correspondence is more important than the skill of inverting large matrices manually.

One preparation of the central node allows one to literally read the middle column of the response matrix (Figure 9).

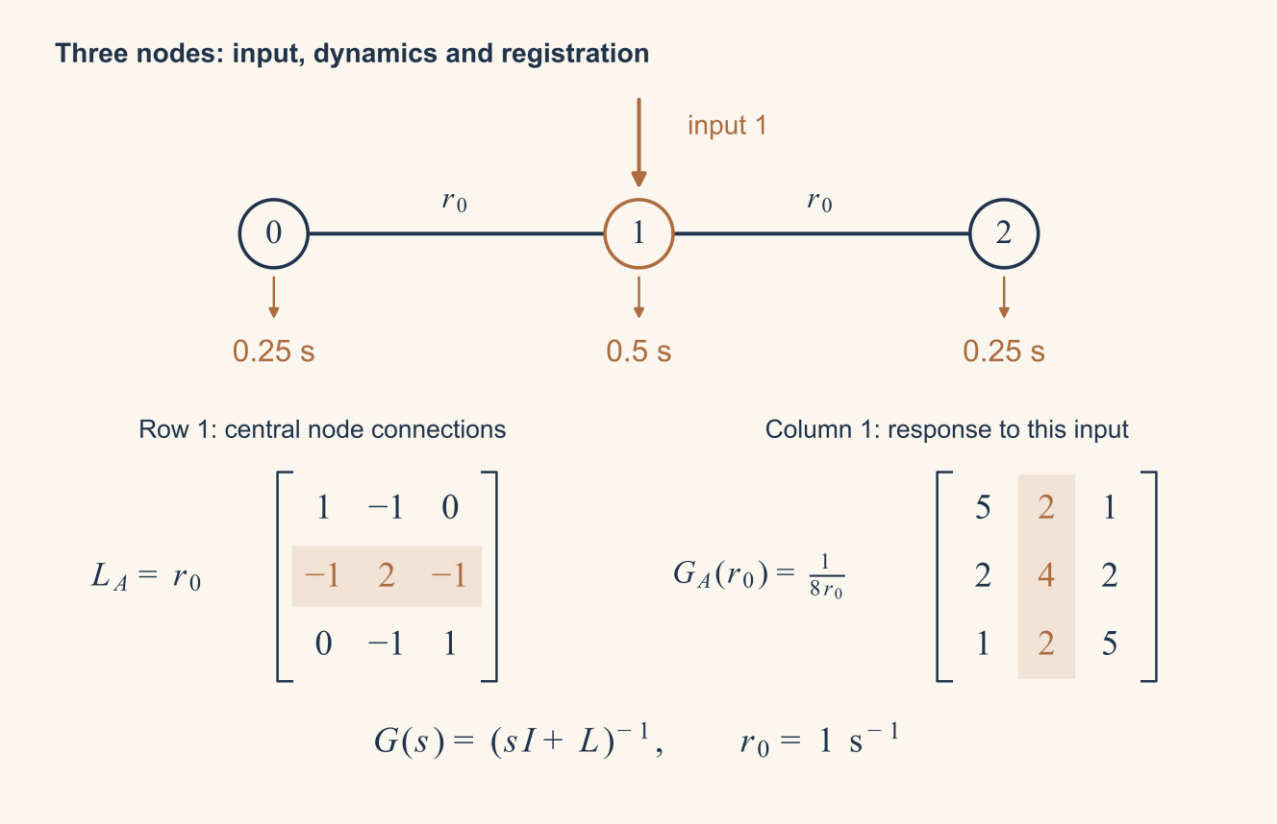


Figure 9. A chain with equal intensities $r_0 = 1\ s^{-1}$ connects physical preparation with the model matrices. The middle row L_a encodes both links of node 1; the middle column $G_a(r_0)$ specifies the exponentially weighted responses when this node is excited. The results are 0.25 s, 0.5 s and 0.25 s. The copper color highlights the selected channel and its entry in the matrix, rather than the additional network connection.

Same dimensions for different networks

Let's change the structure of the same triplet. We will weaken the connections 0-1 and 1-2 to $r_0/3$, and add a connection between nodes 0 and 2 $4r_0/3$. The result is triangle B. In circuit A there was no direct transition 0-2. The number of edges and their weights are different, so these are two different devices with pre-fixed node numbers.

$$L_B = \frac{r_0}{3}\begin{pmatrix} 5 & -1 & -4 \\ -1 & 2 & -1 \\ -4 & -1 & 5 \end{pmatrix}, \qquad \operatorname{spec} L_A = \operatorname{spec} L_B = \{0, r_0, 3r_0\} \qquad (2.14)$$

The eigenvalues of both matrices are the same. Consequently, the heat trace and any dimension calculated only from it coincide. This equality is valid for all positive t, so expanding the band or increasing the accuracy of measuring just one trace does not eliminate the ambiguity.

$$P_A(t) = P_B(t) = \frac{1 + e^{-r_0 t} + e^{-3r_0 t}}{3} \qquad (2.15)$$

$$d_s(t) = \frac{2r_0 t\left[e^{-r_0 t} + 3e^{-3r_0 t}\right]}{1 + e^{-r_0 t} + e^{-3r_0 t}} \qquad (2.16)$$

A shared spectrum says nothing about how the corresponding eigenvectors are distributed over the labeled nodes. The information that distinguishes the networks remains here. If the central node 1 is excited and its response measured, the two networks yield different functions:

$$K_{11}^{A}(t) = \frac{1}{3} + \frac{2}{3}e^{-3r_0 t}, \qquad K_{11}^{B}(t) = \frac{1}{3} + \frac{2}{3}e^{-r_0 t} \qquad (2.17)$$

Observed value	Circuit A	Triangle B
Average return P at t = 1 s	0.472556	0.472556
Spectral index d_s at t = 1 s	0.729707	0.729707
Local return K_{11} at t = 1 s	0.366525	0.578586
Laplace response G_{11} at s = 1 s^{-1}	0.500000 s	0.666667 s

Figure 10 shows the same spectral index and discriminative local experiment. Let the independently established absolute measurement error $K_{11}(1\ s)$ not exceed 0.02. For A, an interval of approximately 0.347-0.387 is acceptable, for B - 0.559-0.599. They don't intersect. In a given class of two given models, one such additional observation is sufficient. With an error of the order of half the difference, around 0.106, the intervals begin to touch.

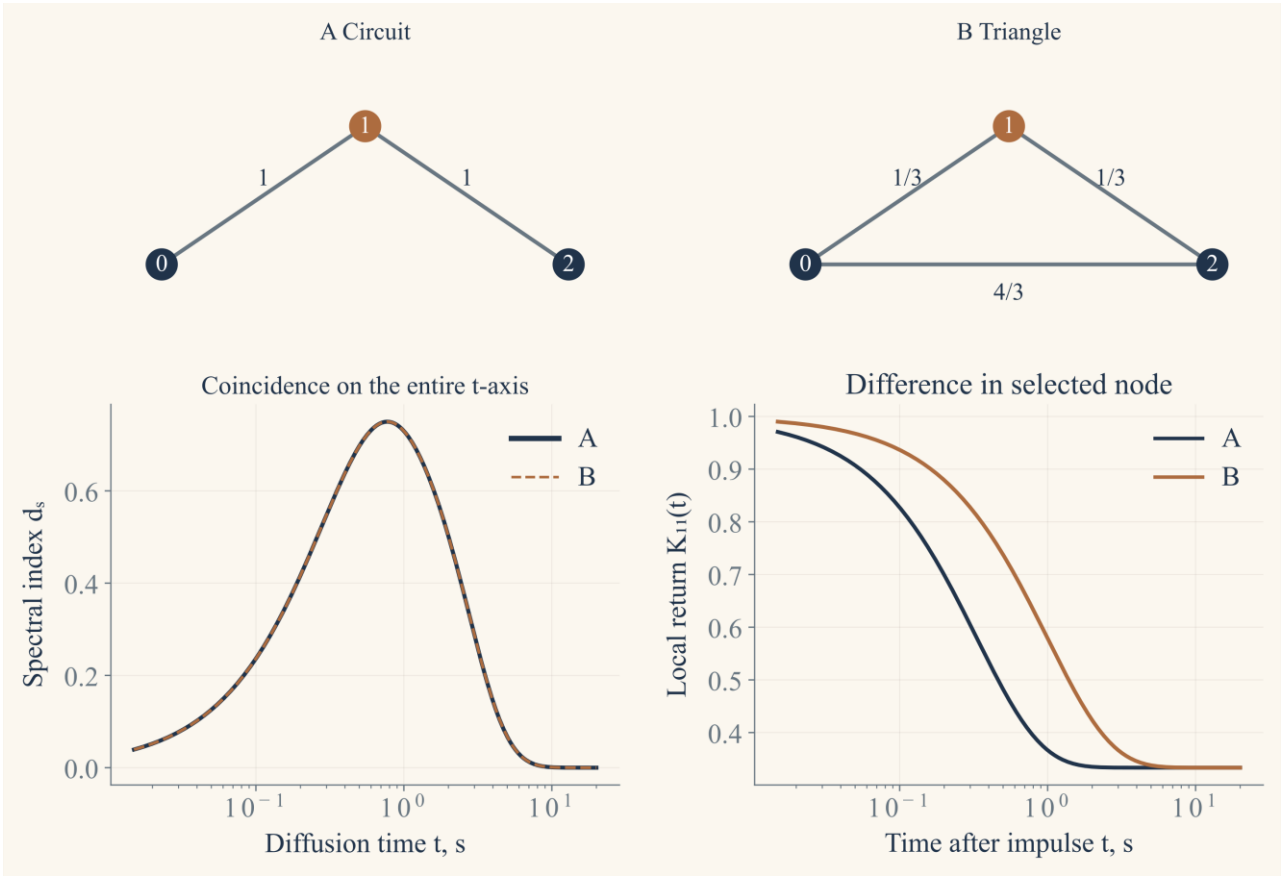


Figure 10. Two different networks with the same eigenvalues 0, 1 and 3 s^{-1}. The d_s indicator coincides along the entire time axis; The lower left panel shows the coincidence of the curves over the finite range 0.015-20 s. The local impulse response at node 1 is different. The weights in the diagrams are expressed in units of $r_0 = 1\ s^{-1}$. All lines are calculated using given matrices.

This result has a precise limit. It distinguishes between the two named devices at known nodes, intensities and error limits. An arbitrary unknown network remains a much more difficult inverse problem. However, it is already clear here what information is lost by averaging and why an additional check should refer to data that is actually not present in the first indicator. The foundations.py script reproduces the matrices, table and figure.

How a finite apparatus creates a spurious change in dimension

Consider a finite connected network of N nodes with a symmetric combinatorial graph Laplacian. For a very small parameter σ, the exponents are almost equal to unity, and the normalized trace approaches unity. Its logarithmic slope approaches zero. For very large σ, only the zero mode remains, corresponding to a uniform distribution; the trace approaches the inverse number of nodes, and the slope approaches zero again. Between these limits there may be a region where the geometry of the network appears. Therefore, two regions of low spectral dimension arise even in a completely ordinary finite discretization of space. They are not evidence of a fundamental disappearance of dimensions.

$$P_N(\sigma) = \frac{1}{N} \sum_{n=0}^{N-1} e^{-\sigma \lambda_n}, \quad \lambda_0 = 0; \qquad P_N(0) = 1, \quad P_N(\infty) = \frac{1}{N} \tag{2.18}$$

The lower limit of the useful range is set by the discreteness or resolution of the device, the upper limit by the size of the system, boundaries and time to achieve equilibrium. These boundaries must be modified regardless of the intended physical scale. For example, increasing the number of nodes while maintaining the step size should push back the overall size effect, while decreasing the step size while maintaining the physical volume changes the effect of discretization. If the transition of interest moves along with the technical parameter, its physical interpretation is weakened. This is why a series of setups or numerical grids of different sizes are often more informative than a single setup with a smoother curve. The stability of the result should be checked by the meaning of the scale, and not just by the external similarity of the graphs.

The logarithmic derivative also increases noise. Adjacent dimension values obtained from the same smoothed curve are usually correlated and do not represent independent observations. Excessive smoothing can create a plateau, and insufficient smoothing can create many false transitions. It is more reliable to simultaneously fit the input values in several reasonable models, evaluate the robustness to the window width, and store information about the error covariances. For discrete walks, parity effects are added: some networks only allow returning after an even number of steps. A continuous propagation parameter helps remove such technical structure, but does not replace the analysis of other systematic influences.

The useful range of scale lies between the two limits of the finite apparatus (Fig. 11).

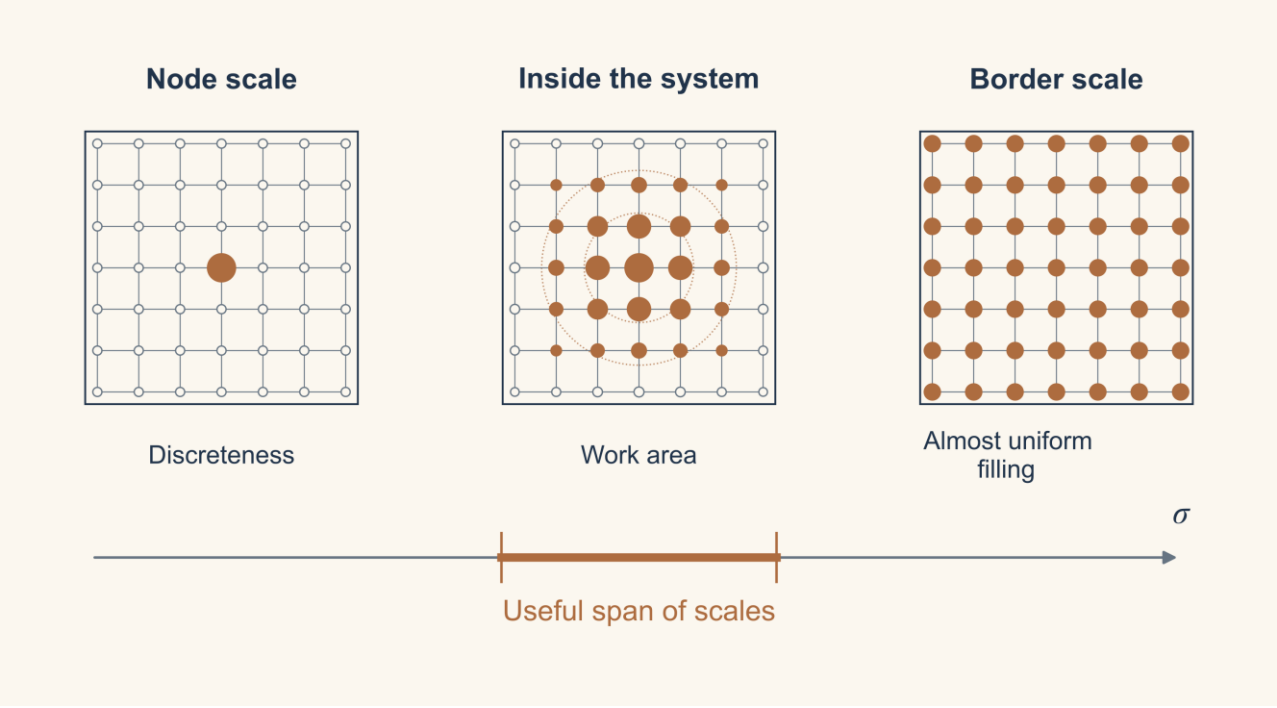


Figure 11. Three qualitative modes of one finite network: the influence of an individual node, propagation within the system, and almost uniform filling after reaching the boundaries. Neither the dimension nor the boundaries of the useful window are estimated numerically here. The highlighted area between the extreme modes reminds us that the search for scaling requires simultaneously taking into account the discreteness of the installation, its finite size and the accuracy of reconstruction of the original signal.

A measurement specification rather than one attractive number

The complete dimensionality estimation result must contain more than the central value and the error term. You must specify the object, the selected volume measure, the propagation operator, the distances used, and the scale range. Then the premises are listed that relate the directly measured quantities to the geometric derivation. For example, the spectrum of a resonator becomes information about space only if the law of propagation within it is known. In the presence of an environment, the result primarily characterizes the joint system “geometry and environment.” This does not invalidate the measurement. On the contrary, an accurate description of an object allows you to compare it with another installation and see whether the detected indicator really relates to a general property of the space.

For joint analysis of volumetric and spectral dimensions, it is especially important to coordinate the scale. The diffusion parameter is not equal to the radius of the area; their relationship is derived from the measured propagation law. If we assume in advance normal diffusion in a system with anomalous dynamics, the comparison of indicators will be biased already at the stage of constructing the horizontal axis. Anisotropy must also be checked. The same average may hide a fast transfer in one direction and a slow transfer in another. Therefore, before averaging, it is useful to examine the response in directions and find out whether the observed effect is a combination of several common, but unequal channels.

Thus, the dimension becomes the result of a certain question to the system. The volumetric method asks how much available space appears as the radius increases; spectral - how the modes of the selected operator are arranged; walk method - how quickly the disturbance propagates. In the usual mode, the answers are consistent and allow you to speak in one number. At the limit of applicability of this regime they may diverge. It is the discrepancy that is of interest for research if it persists after technical checks. But it does not yet indicate the only new theory. The next step is to study the existing mechanisms that already lead to this behavior in order to isolate the unknown effect from the known mathematical scenario.

Chapter 3
When dimension depends on scale

Transition from number to function

This chapter can be read in two ways. The main route goes through the question of the first section and the comparative conclusion of the last. The intermediate sections explain how scale dependence arises in different theories; they require more specialized preparation and serve as a prerequisite map for a computational reading.

If the dimension is determined by the scaling law, it is natural to ask whether this law remains the same when changing the resolution. The answer does not have to be positive. A long, narrow region may appear one-dimensional to a process that does not distinguish its transverse structure, but multidimensional to shorter wavelengths. Even such a simple example shows that the transition between indicators in itself does not require quantum gravity. A more radical possibility is that the characteristic scaling changes in the fundamental geometry itself or its dynamics. It is this possibility that is discussed under the name of dimensional flow. The term denotes dependence on the scale of the study, rather than necessarily changing the world with calendar time.

For initial analysis, it is convenient to write a smooth interpolation between two limit values. In the following formula, dIR denotes the indicator at long lengths, dUV - at short lengths, ℓ* specifies the characteristic transition, and the positive parameter p determines its sharpness. Such a record is a parameterization of possible data. It does not contain a mechanism that forces nature to choose this particular function. From it you can calculate the curve, estimate the parameters and compare the accuracy of the fit, but you cannot derive the quantum theory of space. The distinction between a formula for describing an observation and a law derived from physical premises must be maintained throughout the research work.

$$d(\ell) = d_{\mathrm{IR}} + \frac{d_{\mathrm{UV}} - d_{\mathrm{IR}}}{1 + (\ell/\ell_*)^p}, \qquad p > 0 \qquad (3.1)$$

The usefulness of interpolation is evident in the formulation of testable questions. Is there a transitional scale within the available range? Does it coincide among different observables? Does the data require a monotonic transition, multiple steps, or oscillations? Competing explanations should be identified in advance, since a sufficiently flexible function can describe the noise and technical features of the installation. If the parameter ℓ* constantly moves as the analysis window changes, there is little evidence of stable scale. If independent procedures produce compatible values, there is a basis for a deeper model. The following examples show that similar dimensional graphs can arise from significantly different premises, and therefore mere external similarity is not enough.

Geometries assembled from simple elements

In the approach of causal dynamical triangulations, geometry is studied through an ensemble of discrete constructions from simplices with given rules of causal organization. In the work of Ambjørn, Jurkiewicz and Loll, the spectral dimension of such a quantum ensemble was calculated using the diffusion procedure. On large scales studied, it turned out to be compatible with four, and on short scales - with approximately two. This is an important result within the specific definition of quantum gravity. Numerical “measurement” here means measuring a property of the generated geometries, rather than recording a signal from a physical detector in the surrounding space. Substituting these two meanings would create an unjustified impression of a discovery that has already taken place. [3]

The value of this calculation can be understood without promising an immediate experiment. It shows that rules for summing over geometries can produce large-scale behavior different from that of the individual building blocks. The question of the continuum limit then arises. If the blocks become smaller and more numerous, does the structure of interest survive an appropriate change of parameters? Without this check, the result may characterize the chosen discretization. A photograph provides an apt analogy: adding pixels should clarify the image rather than alter the object arbitrarily. In quantum geometry, the problem is harder because changing the resolution also changes the weights of entire configurations.

Another difficulty relates to the physical scale of the graph axis. The number of diffusion steps inside the model cannot be replaced by meters or the energy of the device without additional calculations. It is necessary to compare the internal parameters with the observed values, determine the characteristic length and check the dependence on a specific probe. Even when the mathematical limit is well controlled, communication with experiment remains a separate work. Therefore, the correct derivation from the numerical flow of dimensionality has a conditional form: if the structure under study describes the microscopic geometry of the world and if the selected probe is related to the real observable, then the corresponding scaling can be sought. Both parts of the condition require their own proof.

Causal order instead of a ready-made coordinate grid

Causal sets start from a different minimal set of elements. Discrete events and a precedence relation are specified, indicating which events may be in the causal past of others. The relation must be consistent with transitivity, and only a finite number of intermediate elements are allowed between two related events. The original work by Bombelli, Lee, Meyer and Sorkin proposed this structure as the basis of microscopic spacetime. Geometric properties then need to be restored from the order and number of elements, and not entered by ready-made coordinates. This rearrangement of the original concepts is interesting precisely because it makes the dimension the result of the analysis of connections, and not a mandatory input parameter. [4]

One estimator uses the number of events and the number of causally related pairs within a causal diamond—the area between two events. For a Poisson distribution in flat spacetime, the ratio of ensemble means is related to the dimension via the gamma function. In the formula, C1 denotes the

number of events, C2 the number of ordered causal pairs, and the brackets denote ensemble averaging. The equation can be reversed and an estimate of the dimension can be obtained. For one small sample, substituting observed numbers for means requires bias analysis. This is significant: the nonlinear transformation of the average and the average of the transformed value do not have to coincide at all. [5]

$$\frac{\langle C_2 \rangle}{\langle C_1 \rangle^2} = \frac{\Gamma(d+1)\Gamma(d/2)}{4\Gamma(3d/2)} \qquad (3.2)$$

Abajyan and Carlip studied small subsets of causal sets approximating Minkowski spaces of different dimensions. They found a decrease in the estimated dimensionality, with the limit depending on the processing of isolated events and unconnected sets. With one rule the result was behavior of about two, with the other - about zero. This result should not be hidden for the sake of a single beautiful story. It shows that the quantity under study involves both the structure of the set and the decision about what data is considered geometrically significant. For the future instrument, a practical requirement follows from this: the rules for selecting events and excluding empty observations must be specified before searching for an unusual dimension value. [5]

Figure 12 compares simplicial geometry and causal order.

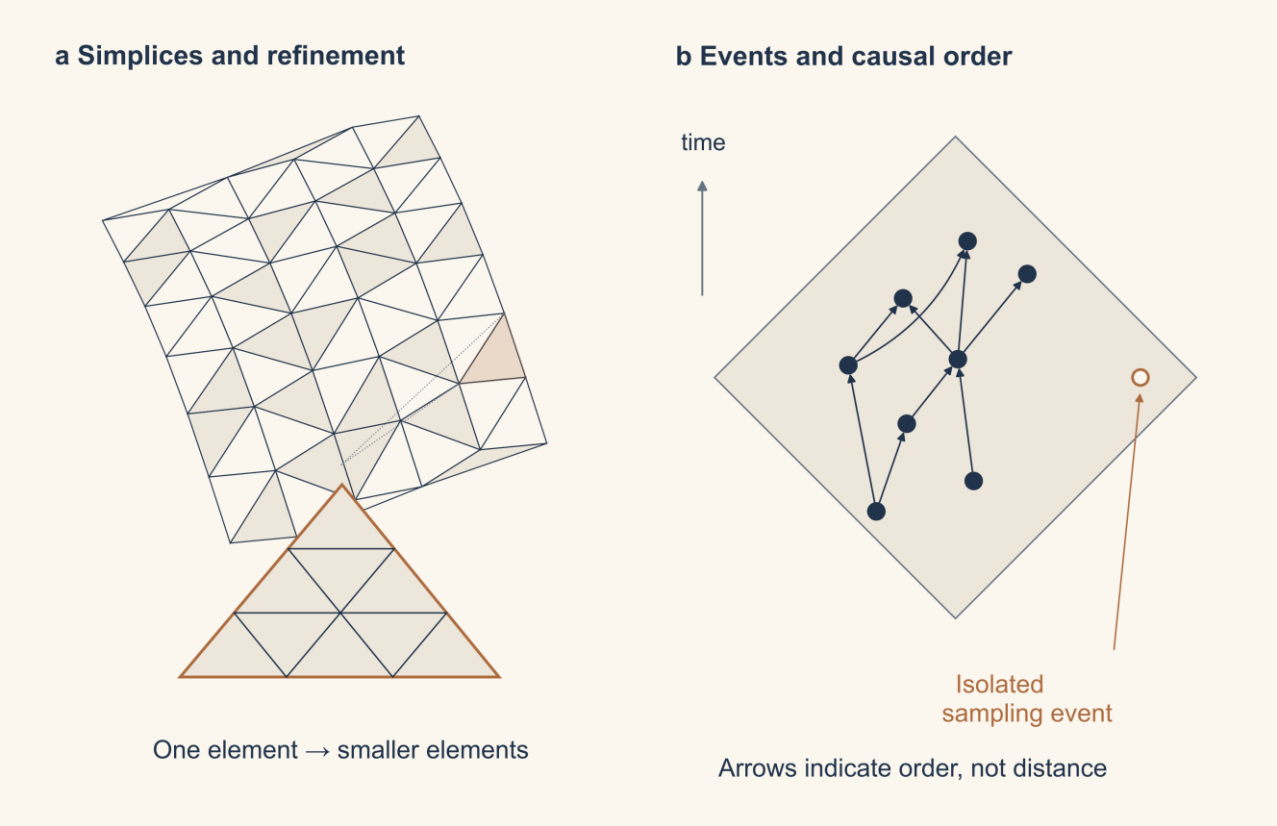


Figure 12. Two different ways to define the initial structure. On the left, the geometric surface is assembled from triangular elements, one of which is shown after refinement. On the right, events are ordered by causal relationships; arrows mark direct connections, and transitive ones follow from chains. The empty copper event is spatially similar to all other events in this sample. These are training constructs, not quantum ensemble configurations or measured data.

Reducing spectral dimension without removing coordinates

The mechanism of anisotropic scaling is especially indicative. In the work of Petr Hořava, spatial coordinates and time are scaled by different degrees. The z index characterizes this difference, and D remains the number of spatial coordinates. The resulting spatiotemporal spectral dimension is equal to one plus the ratio of D to z. With three spatial coordinates and z equal to three, the result is two. The two axes of the coordinate system do not disappear here. The behavior of the operator changes, through which the spectral indicator is determined. Therefore, the phrase “space becomes two-dimensional” requires clarification even when the mathematical calculation is performed completely correctly and its result is stable. [6]

$$\mathbf{x} \mapsto b\mathbf{x}, \quad t \mapsto b^{z} t, \qquad d_{s} = 1 + \frac{D}{z} \qquad (3.3)$$

It is convenient to check the power result by recalculating the variables in the spectral integral. In Euclidean notation, the temporal wavenumber Ω is equal to the frequency divided by c; k denotes the spatial wavenumber and k* matches the units. When Ω is replaced by a variable divided by the root of σ, the time integral gives the exponent minus one half. Spatial substitution gives the exponent minus D divided by 2z. Adding the exponents and taking the logarithmic derivative returns the formula above. The calculation establishes the dependence of the spectral trace on operator scaling and does not in itself determine the causal propagation of the real signal.

$$P(\sigma) \propto \int d\Omega \, d^{D}k \, e^{-\sigma\left[\Omega^{2} + k^{2z}/k_{*}^{2z-2}\right]} \propto \sigma^{-(1+D/z)/2} \qquad (3.4)$$

This example imposes a necessary discipline on interpretation. If an instrument detects an unusual mode density, the first question is whether the field's dispersion relation has changed. If the operator contains higher spatial derivatives, its formal heat kernel may fail to represent an ordinary positive diffusion probability, although the spectral trace remains defined. If a preferred time foliation is introduced, the observed relativistic symmetry must be recovered in the relevant regime. None of these questions prohibits research. They specify the additional calculations separating a mathematical model from a theory that can consistently explain clocks, signals, and the motion of matter.

The change in the spectral index can be shown by preserving all spatial directions (Fig. 13).

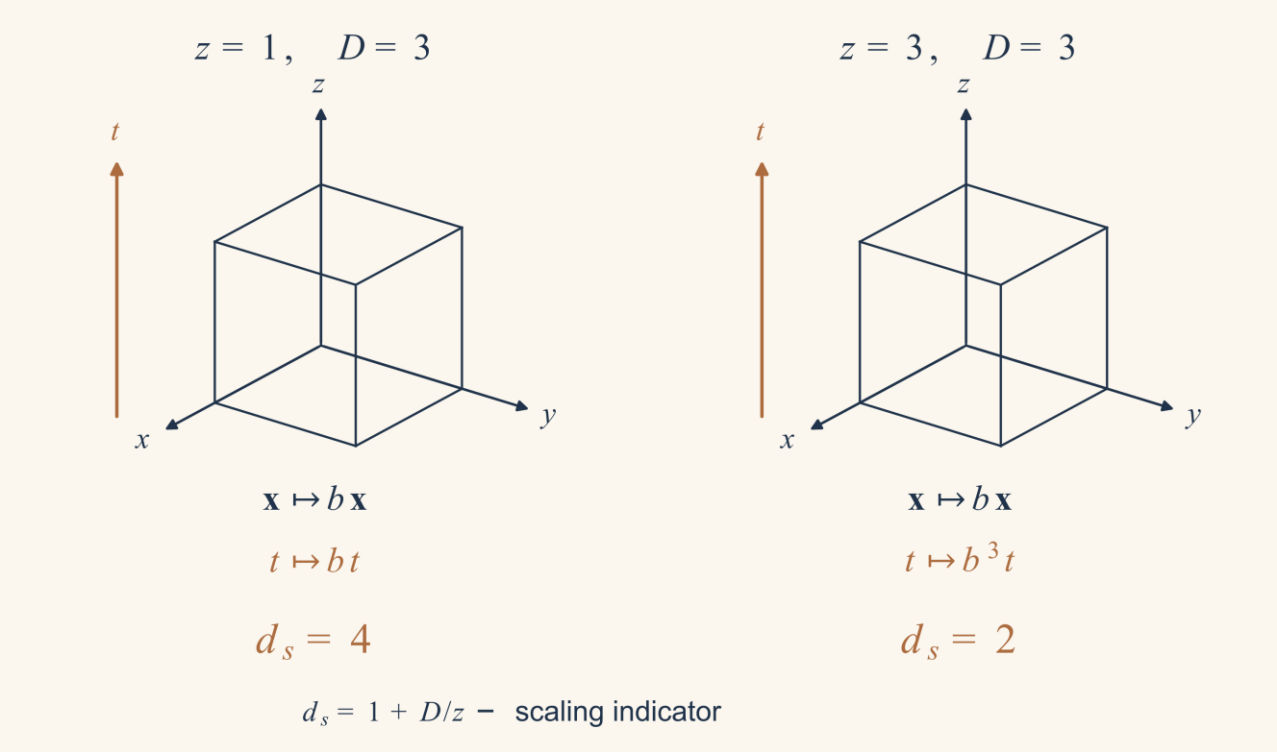


Figure 13. In both schemes, three spatial coordinates are stored. The time scaling rule is different: at z = 1 it is consistent with the spatial one, and at z = 3 it has a different degree. In the theoretical model under consideration, the formula $d_s = 1 + D/z$ gives 4 and 2, respectively. The second result does not mean the removal of spatial axes and does not depict an established property of nature.

Scale dependence of interactions

The asymptotic safety program considers the possibility that the gravitational interaction at high energies approaches a non-trivial fixed renormalization group regime. The work of Lauscher and Reuter shows how, under appropriate conditions, the spectral dimension can move from four to two. This is a different way to a similar indicator: the initial subject of research is the scale dependence of the effective dynamics. The conditional status of the output should be maintained. The presence of an agreed result within the framework of the program does not prove that nature implements this particular high-energy regime. Moreover, it does not automatically determine the way to measure its manifestations with an available laboratory device. [7]

The simplest notation shows the role of anomalous scaling. In four dimensions and units where the speed of light and reduced Planck's constant are equal to one, the dimensionless gravitational coupling can be composed of the effective Newton's constant and the square of the momentum scale. Its change contains the usual dimensional contribution and an additional contribution η. If the connection reaches a non-zero fixed point, their sum must go to zero. This algebraic condition explains why the behavior of the operator at large momenta can differ significantly from the naive classical continuation. However, the existence of the desired point and the physical feasibility of the entire trajectory are not automatically derived from this line.

$$g(k) = k^2 G(k), \qquad k\frac{dg}{dk} = [2 + \eta(k)]g(k), \qquad g_* \neq 0 \Rightarrow \eta_* = -2 \qquad (3.5)$$

Verification of such constructions requires separating the exact consequence of the premises from the accuracy of the premises themselves. In calculations, we often limit the space of possible terms of the effective action, and then check how robust the result is when expanding the description. Even the stability of several approximations does not replace a complete proof or observation, but it can justify the continuation of the program. What is important for the reader is the method of assessment: to clarify which part of the output depends on truncation, which part depends on the choice of the observable, and which follows from the general structure. This reading is more useful than arguing about whether an approach is a definitive theory or an error: between these extremes lies much of the actual research work.

What needs to be transferred from theory to observation

The considered approaches obtain scale dependence from different mechanisms: an ensemble of geometries, causal order, dispersion law, or effective interaction. The coincidence of one limiting number does not yet select the mechanism. In chapter 2, two specific networks had the same spectral dimension at all scales, although their local response differed.

For the chosen class of models, the work therefore begins with a set of observables, rather than with a single indicator. First, a value is calculated that all candidates explain in the same way. They then look for the effect where their predictions diverge: changing the excitation point, direction, probe type, or available time range. An introductory three-node experiment completes this procedure for two finite networks. It does not establish an experimental distinction between all the quantum-gravitational approaches in this chapter.

When moving to physical space, each additional dimension must be associated with the probe model. For example, a formal diffusion parameter is not converted into an optical frequency by simply changing the notation. In chapters 10-12 such transitions will be written out for specific limited models. First we need a compact direction - an example in which the change in the available set of modes can be traced analytically.

Chapter 4
Hidden and synthetic directions

Direction that closes

The additional direction does not have to go on forever. It can close like a coordinate along a circle. If the circle is small compared to the resolution of the observer, differences in position along it become difficult to discern. This does not mean that the mathematical coordinate disappears. The set of excitations available to the chosen energy and method of observation changes. The simplest example is given by the product of ordinary space and a circle of radius R. Points with coordinates y and y plus the length of the circle are considered one point. This rule defines a compact direction without necessarily depicting a tube embedded in an even higher external space.

$$\mathcal{M} = \mathbb{R}^D \times S^1_R, \qquad y \equiv y + 2\pi R \qquad (4.1)$$

The idea of combining interactions through an additional coordinate has a long history. Oskar Klein's paper 1926 explored the connection of the five-dimensional relativistic structure with the quantum description, including the periodic dependence of the field on an additional variable. A historical fact is important for assessing novelty: the very assumption of a hidden closed direction is no longer a new hypothesis. The modern research contribution must lie elsewhere - a coherent dynamic, a specific mechanism of interaction with observable fields, new discriminating implications, or a more sensitive method of testing. Repetition of a geometric pattern is helpful for learning, but does not replace these additional steps. [8]

The idea of compactness also helps distinguish the local from the global. In a sufficiently small neighborhood of a point, a circle is similar to a line, and the product has one more independent spatial direction. At scales that cover the entire circle, further enlargement of the area does not open up new positions along it. This results in a change in the volumetric indicator without singularity and without turning points into objects of a different kind. However, the specific observable depends on whether the fields under study can move along an additional coordinate. A field limited by subspace is capable of not feeling it directly at all. Therefore, the geometry and rules for the movement of fields must be specified together.

The compact direction becomes indistinguishable at coarse resolution, remaining in the model (Fig. 14).

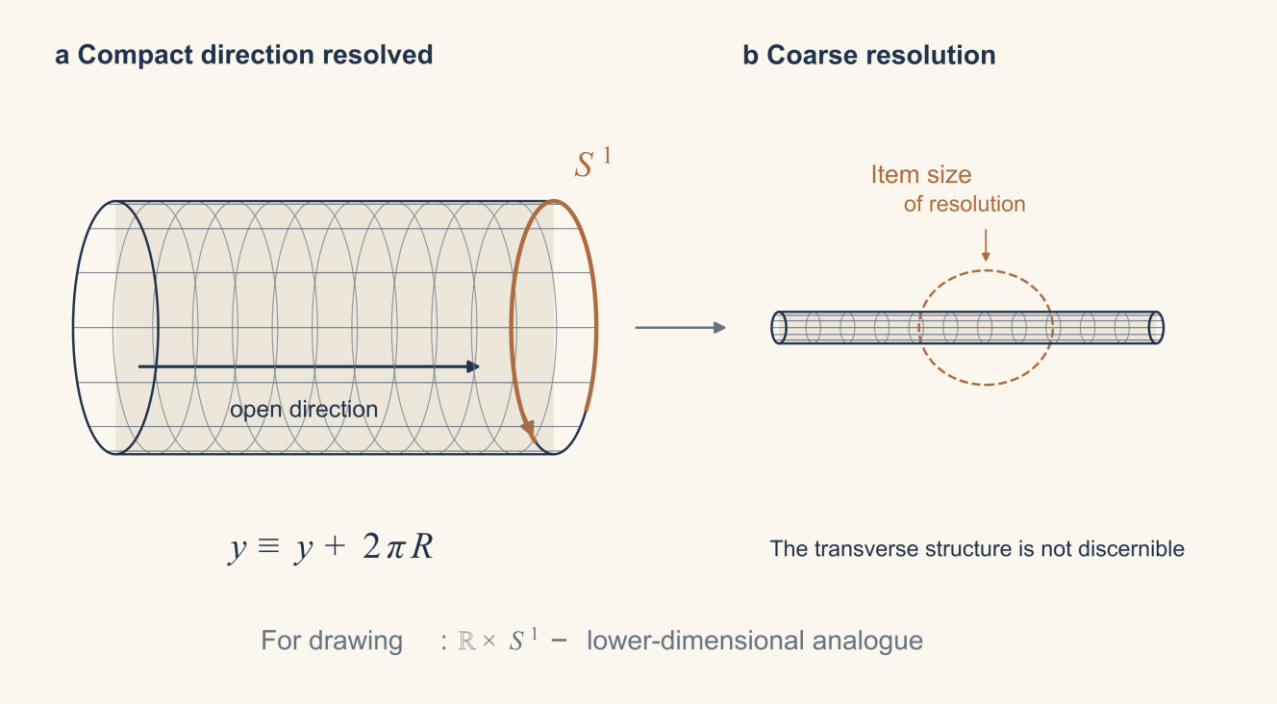


Figure 14. The product of an open direction and a circle is depicted as a cylinder as an analogue of a lower dimension. With sufficient resolution, motion along the compact direction is visible; the crude element of observation does not discern its lateral structure. The circle does not physically disappear. The external volume used for the drawing serves as a means of visualization and does not add a new hypothesis to the space $\mathbb{R}^D \times S^1$.

Periodicity becomes a ladder of modes

Let the scalar field propagate freely in a compact direction and take the same values after a complete circuit. Then the dependence on y can be expanded into a series of periodic harmonics. The integer n denotes how many periods fit along the circle, and each function φn describes the corresponding mode in the remaining coordinates. For a real field, the coefficients of positive and negative numbers are related by complex conjugation. Already at this stage, the additional geometry receives a potentially measurable consequence: instead of an arbitrary continuous momentum in a new direction, a discrete set appears. This is a consequence of the boundary condition, and not an independent new law of nature.

$$\Phi(x, y) = \sum_{n \in \mathbb{Z}} \phi_n(x) e^{iny/R}, \qquad p_y = \frac{n\hbar}{R} \qquad (4.2)$$

In the simplest flat-space case, the additional momentum enters the relativistic energy in the same way as the other spatial components. For an observer who describes only open directions, his contribution looks like an increase in the mass of the corresponding mode. In the formula below, m0 is the mass of the original field, and p is the momentum in the available open directions. The smaller the radius, the larger the energy interval before the first additional excitation. Therefore, the absence of new modes in a limited energy range can be consistent with the existence of a sufficiently small

compact direction. But a quantitative conclusion would require knowing how the source excites these modes and how the detector records them.

$$E_n^2 = c^2|\mathbf{p}|^2 + m_0^2c^4 + \frac{n^2\hbar^2c^2}{R^2}, \qquad m_n^2 = m_0^2 + \frac{n^2\hbar^2}{c^2R^2} \tag{4.3}$$

The mass ladder is obtained under specific assumptions: the direction is a circle of constant radius, the field is free, the background geometry is flat, and the boundary condition is strictly periodic. Under other conditions, the spectrum changes. Additional interactions can shift levels, break degeneracy, or reduce the availability of individual modes. Therefore, the found sequence of resonances should not automatically be called a trace of additional space. The internal states of an ordinary system also form a discrete spectrum. For a geometric interpretation, it will be necessary to agree on the levels, their connections, propagation laws and dependence on external conditions. The more independent consequences are derived from one radius and one dynamics, the more meaningful the hypothesis becomes.

It is convenient to represent the periodicity of a compact coordinate by a family of circular harmonics (Fig. 15).

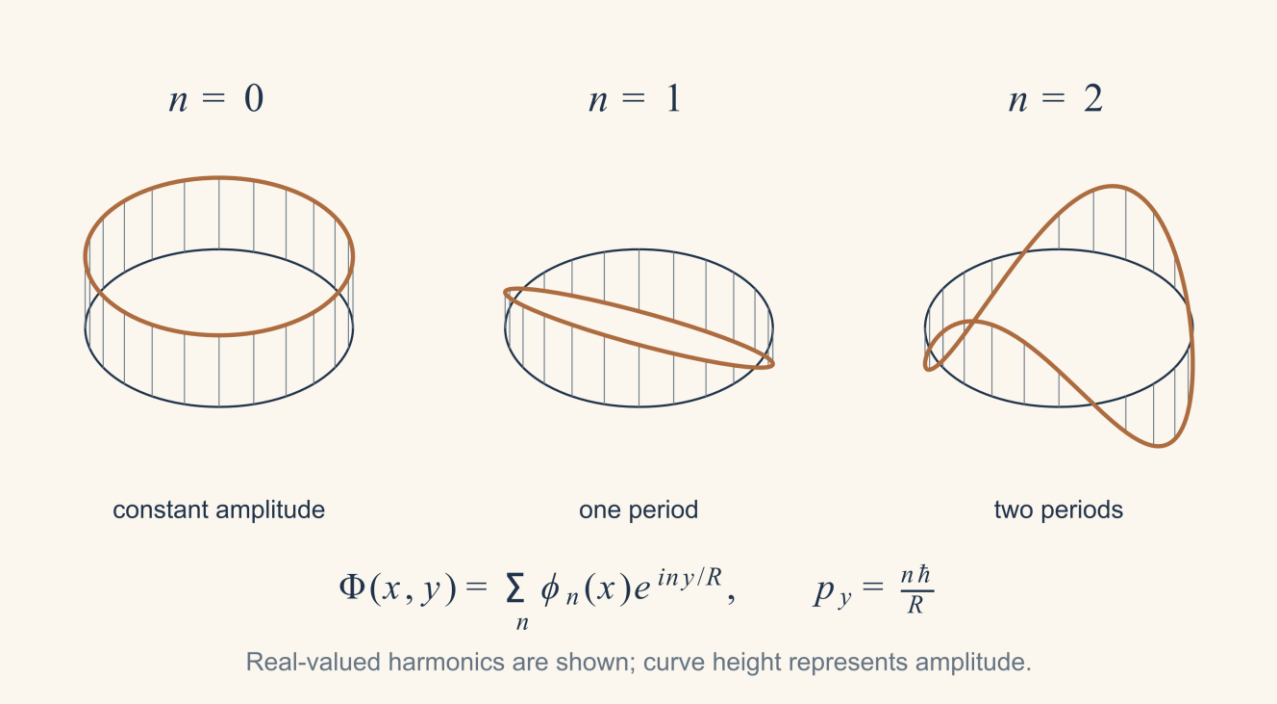


Figure 15. Real harmonics with indices n = 0, 1 and 2 are shown above the same compact circle. The height of the copper curve conveys the amplitude of the mode, rather than another spatial coordinate. The periodicity allows integer numbers and corresponding discrete values of the additional momentum. These are basic mathematical examples, not the spectrum of a manufactured detector or a set of independent new directions.

Heat trace of compact direction

Now we can calculate how compactness manifests itself in the spectral dimension. For an ordinary Laplacian, the eigenvalues along a circle are equal to the squares of its discrete wave numbers. Open directions give a Gaussian multiplier, familiar from the previous chapter. The

normalized heat trace is obtained by the product of this factor and the sum over the integer numbers of compact modes. Dividing by the circumference provides normalization to the total spatial volume. The parameter σ still has the dimension of area. It is spatial geometry that is considered here; the time direction is not included, so the resulting numbers cannot be directly compared to the space-time dimension without appropriate qualification.

$$P(\sigma) = \frac{(4\pi\sigma)^{-D/2}}{2\pi R} \sum_{n\in\mathbb{Z}} e^{-\sigma n^2/R^2} \qquad (4.4)$$

If σ is significantly greater than the square of the radius, all non-zero numbers are exponentially suppressed. The sum remains unity, and the trace decrease indicator is determined only by D open directions. If σ is significantly less than the square of the radius, many modes are involved in the sum, and it can be approximately replaced by a Gaussian integral over n. The integral gives an additional factor inversely proportional to the root of σ. Consequently, the short-scale spatial spectral dimension increases by one. This conclusion does not require the assumption of quantum gravity: it follows entirely from the ordinary Laplacian and the chosen compact geometry. The example is therefore particularly useful as a benchmark for testing methods.

$$\sum_{n\in\mathbb{Z}} e^{-\sigma n^2/R^2} \simeq \sqrt{\pi}\,\frac{R}{\sqrt{\sigma}} \quad (\sigma \ll R^2), \qquad d_s \to \begin{cases} D+1, & \sigma \ll R^2, \\ D, & \sigma \gg R^2. \end{cases} \qquad (4.5)$$

Without extreme approximation, the logarithmic derivative gives the following exact formula for this model case. In it, the ratio of the sums is the average square of the mode number with thermal weights. It shows how additional excitations are gradually connected. For three open directions, the spatial index changes between three and four; if ordinary Euclidean time is added separately, the corresponding space-time values will be one larger. The direction of change is opposite to the short-scale decrease discussed earlier. This is not a contradiction, since different mechanisms are being compared. On the contrary, the sign and shape of the transition can help distinguish models if the relationship between scale and observation is established correctly.

$$d_s(\sigma) = D + \frac{2\sigma}{R^2}\,\frac{\sum_n n^2\, e^{-\sigma n^2/R^2}}{\sum_n e^{-\sigma n^2/R^2}} \qquad (4.6)$$

Figure 16 shows the transition for three open spatial directions and one circle. If the diffusion scale is short, the ladder of compact modes is resolved; if the diffusion scale is long, the zero mode remains. In this plot, the parameter is normalized to the square of the radius; the physical time of a particular device will require a separate transfer coefficient.

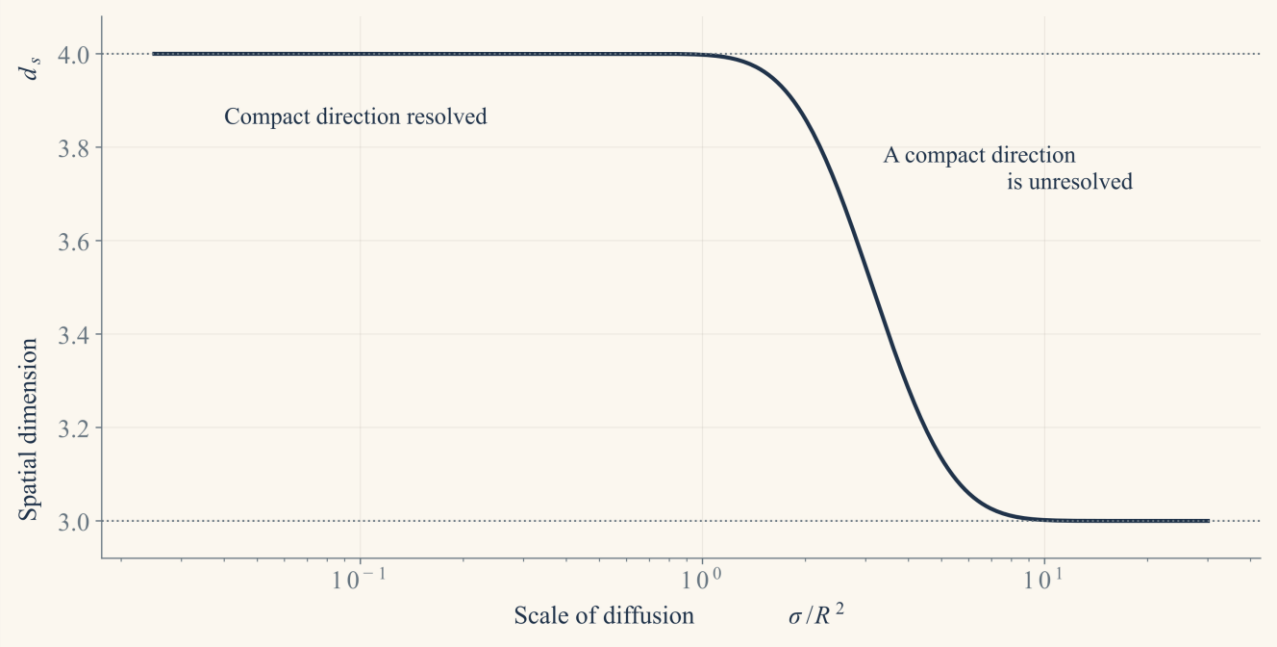


Figure 16. Spatial spectral dimension for the $R^3 \times S^1$ model. The curve is calculated from the heat trace and shows the resolution of the compact direction at small scales. This is an analytical model. The scale of the diffusion parameter is specified by the radius of the circle and is not directly the frequency scale of the optical device.

What the device could really see

The actual device does not display the number of spatial directions directly. It records intensities, frequencies, phases, pulses or arrival times. The task of the theory is to predict the distribution of these data in the presence of a compact coordinate and compare it with the distribution in the usual description. In the spectroscopic version, one can search for additional families of modes. In the propagation variant, there is a change in group velocities and excitation thresholds. But these effects must follow from one selected interaction of the field with geometry. You cannot take the spectrum from one model, the signal amplification from another, and assign the detector sensitivity independently: such a combination does not define a testable physical scenario.

Comparisons between different channels are especially useful. If a universal complementary direction is assumed, it is necessary to explain which fields sense it and why their parameters are related or different. Finding a deviation in only one material is more likely to characterize the properties of that material until a broader rationale is built. On the other hand, the hypothesis may well allow for selective interaction; then universality should not be implicitly substituted into conclusions. Comparing multiple fields is not a magical method of proof. It reduces the set of compatible models only when their various predictions are calculated in advance, including ordinary interactions that may also produce similar signals.

The compact direction radius also cannot be considered an arbitrary real-world tuning knob. If it is a dynamic quantity, a model of its stability and response to impact is needed. If fixed by an external condition of a mathematical problem, this condition must be explicitly specified. Discussion of the possibility of changing the dimension by a technical device requires much more than the existence of the parameter R in the formula. It is necessary to calculate the source of influence,

energy balance, stability of the state and the observed result. While there is no such mechanism, it is correct to talk about testing a hypothesis or modeling its consequences. This preserves the subject of the study and does not turn an accessible mathematical example into the promise of a non-existent device.

How a synthetic direction is built

Synthetic dimensionality occurs when internal states or modes are related as if they were adjacent positions on a complementary axis. The index of such an axis can be atomic levels, frequency modes of the resonator, or other controlled states. If transitions predominantly connect adjacent numbers, the dynamics resemble movement along a chain. The simplest Hamiltonian below contains the transition amplitudes Jm and natural frequency shifts δm. The create and destroy operators describe the selected modes. Complex conjugation in the pair term ensures Hermitianity, and the factor of the reduced Planck constant converts the frequency parameters into energy units. The physical design must implement precisely these connections, and not just their drawing.

$$H = \hbar \sum_{m} \left(J_m a_{m+1}^{\dagger} a_m + J_m^{*} a_m^{\dagger} a_{m+1} \right) + \hbar \sum_{m} \delta_m \, a_m^{\dagger} a_m \qquad (4.7)$$

In Lohse et al.'s experiment with ultracold atoms, two-dimensional topological pumping made it possible to study the response associated with the four-dimensional quantum Hall effect. The authors measured the topological characteristic corresponding to the second Chern number. The result shows that mathematically high-dimensional dynamics can be realized in a controlled laboratory manner. It does not mean the discovery of a fourth free spatial direction around the installation. Synthetic coordinates enter through the parameters and internal structure of the system. This is why the experiment is useful: the researcher is able to test the predictions of a high-dimensional model without having physical space of the same dimension. [9]

The practical cost of such a representation is limited implementation. The synthetic axis has a finite number of states, transitions may be unequal, and some interactions remain long-range relative to an artificially defined neighborhood. Additionally, noise and loss can affect different modes differently. Therefore, it is necessary to find out which properties of the target model are actually reproduced and which are missing. Successful spectrum simulation does not guarantee the simulation of all interactions and causal relationships. Such precision is also useful for fundamental searching: it teaches one to separate the object being measured from the mathematical structure with which it is compared, and to establish the boundaries of this comparison quantitatively.

It is useful to show the physical device and the synthetic axis separately, maintaining the connection between them (Fig. 17).

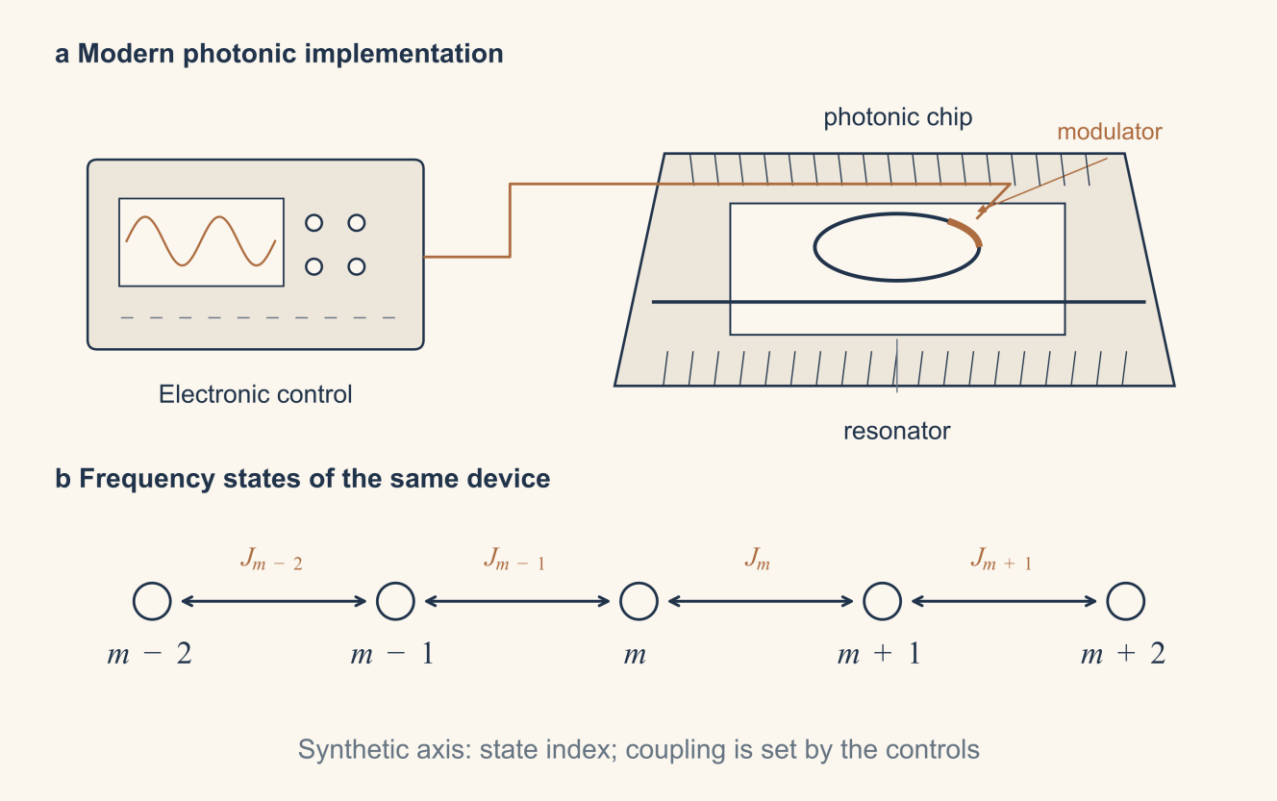


Figure 17. Illustrative state-of-the-art implementation of the synthetic direction: photonic resonator on a chip, modulator and electronic control. The bottom chain depicts the frequency states of the same device; neighboring states are connected by controlled transitions with coefficients J. Their sequential number plays the role of a synthetic coordinate. The drawing does not define a finished design and is not attributed to a specific publication; the spatial length of the chain is a graphical condition.

Laboratory for testing discrimination methods

A laboratory model allows a device with a known structure to be presented to the method. The three-node networks of the chapter 2 have already provided such control: the complete spectra coincided, and local excitation made it possible to distinguish structures. The synthetic direction expands this possibility. You can change the number of available states, close the transition chain, or introduce controlled losses and check which feature is preserved.

For a compact model, the next question is different: what physical source excites the mode ladder and what detector is sensitive to it? Chapter 10 will select one scalar probe for which the static potential and dynamic transfer are derived from the same statement. This gives a specific prediction and allows you to compare it with a regular additional field. Such a check depends on the law of connection between the source and the modes.

The synthetic test bench tests the recovery method under a controlled structure. The compact direction specifies the possible arrangement of the physical geometry. There is common mathematics between the problems, but each requires its own measurement vocabulary. The next

chapter will look at another source of geometric description - the relationships between quantum degrees of freedom.

Chapter 5
Geometry from quantum relations

What does the emergence of geometry mean?

The words “space arises” sound as if there was a void until a certain moment, and then space appeared inside it. For a physical theory this is usually too literal a picture. Emergence may mean another level of description: the original variables have no immediate geometric meaning, but their collective behavior allows for a language of distances, neighborhoods, and fields. Temperature is a familiar example of such a transition between levels, although the analogy itself does not prove anything about space. The task is to derive the rules of the new description and determine the scope of their applicability. The geometry that emerges in this way need not be an illusion; it can remain an accurate effective property of the observable world.

The simplest model helps to separate the possible mechanism from the expressive image. Let a network of interacting elements be given, and only the strengths of the connections are known in advance. You can try to determine the distance through the cost of excitation transfer or through the length of the shortest sequence of transitions. If the resulting structure is similar to a smooth manifold in some regime, an effective geometry appears. However, smoothness, dimensionality and locality do not follow from the presence of any network. A fully connected system and a regular lattice behave differently. To argue for the emergence of space, it is necessary to show why a particular dynamics selects structures with the desired properties and why these properties are resistant to small changes in the initial state.

The next question concerns universality. Different excitations of the same system can propagate at different speeds and experience different effective parameters. This is a well-defined situation, but it does not automatically yield a single geometry. For a geometric description of the shared world, it is especially important to understand why independent observers and different trial fields agree on the results. If each field is assigned its own distance without connection to the others, the theory risks losing explanatory power. Therefore, the emerging geometry must be accompanied by a rule for comparing probes, transforming coordinates and restoring the normal mode. These requirements direct the search more strongly than the statement itself about the primacy of information or connections.

Two sensors with a common cause

Before introducing quantum formulas, an experiment with two conventional recorders is useful. The source independently selects an equally likely Q bit every second and writes the same value to memory A and B. There is no transmission channel between the recorders after the write. In half of the tests the pair 00 is obtained, in half - 11.

A	B	Probability
0	0	1/2
0	1	0
1	0	0
1	1	1/2

Knowing A, the observer knows B exactly. The entropy of each bit is ln 2, the joint entropy is also ln 2: the pair contains only one random choice. The classical mutual information is therefore equal to ln 2. All of these formulas use the natural logarithm; unit of information - nat.

$$H(X) = -\sum_x p_x \ln p_x, \qquad I(A:B) = H(A) + H(B) - H(A,B) = \ln 2 \qquad (5.1)$$

Now the experimenter, after recording, forcibly sets A = 1. B still has the original Q in memory, so the probability of B = 1 is 1/2. Selecting trials where A was already equal to one would produce a different probability. The difference between observation and intervention can be expressed explicitly:

$$\Pr(B = 1 \mid A = 1) = 1, \qquad \Pr(B = 1 \mid \mathrm{do}(A = 1)) = \frac{1}{2} \qquad (5.2)$$

The high mutual information in this example clearly points to a common cause. A second experiment is required to determine the ability to transmit a new effect. Quantum theory adds special kinds of correlations and rules of measurement, but the difference between the two issues remains. The following sections use it to discuss holography and linear response.

The distinction between observation and intervention can be seen in two modern electronic recorders (Figure 18).

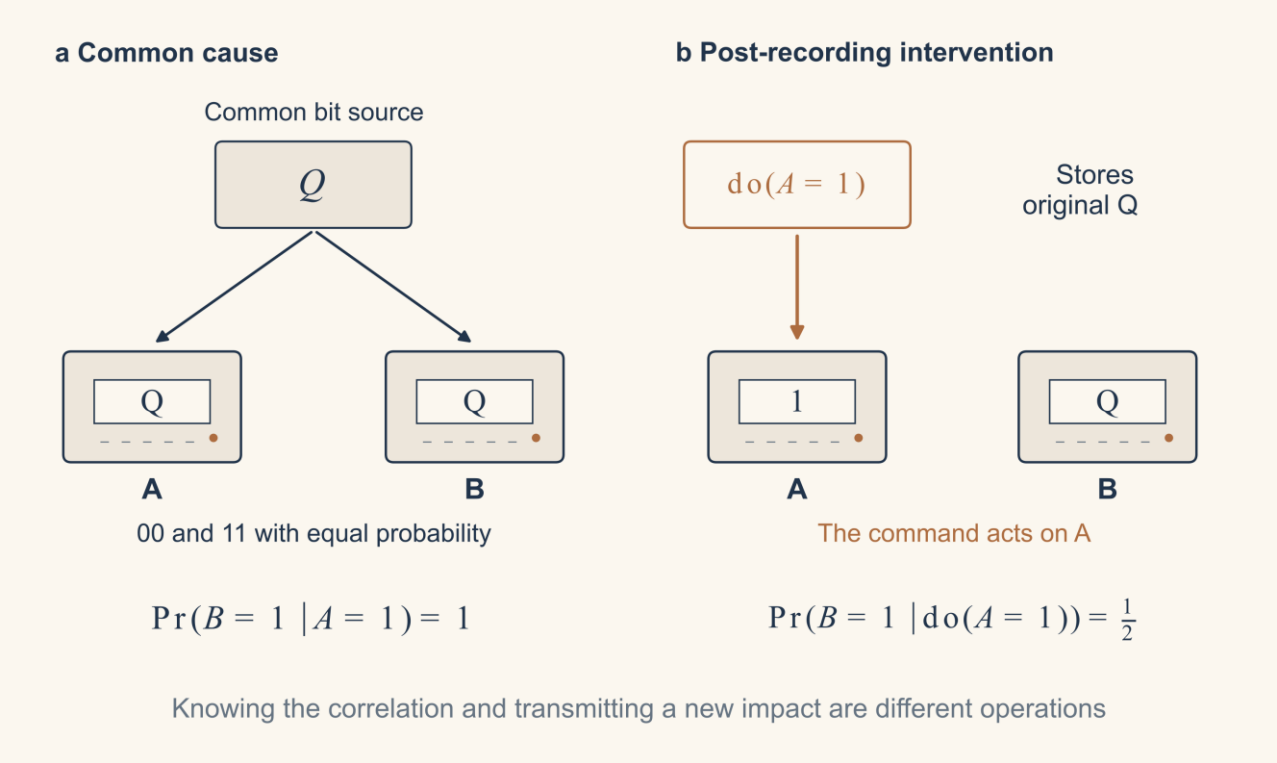


Figure 18. The classical common source writes one equally probable bit Q into two memories, so observing A completely determines B. In the second protocol, the external command after writing sets A = 1, and memory B stores the former Q. The probability of one in B remains equal to half. There is no transmission channel between recorders: the high correlation in this example indicates a common cause but not the ability to transmit a new effect.

What establishes holographic duality

One of the most concrete examples of the connection between non-gravitational and geometric descriptions was the duality proposed by Maldacena between certain conformal field theories and theories on anti-de Sitter spaces with additional compact factors. In a well-known version, four-dimensional supersymmetric gauge theory and string theory are considered on the corresponding five-dimensional anti de Sitter space multiplied by a five-dimensional sphere. A convenient classical gravitational description arises in a certain limit of parameters. This is a meaningful mathematical context where different numbers of geometric coordinates enter into equivalent descriptions. It does not establish that any quantum system or directly observable cosmology has the same holographic representation. [10]

Ryu and Takayanagi proposed in this context a connection between the entanglement entropy of a boundary theory domain and the minimal surface area in the volume. The surface must be fixed to the boundary of the selected area and satisfy the homology condition. For the classical static gravitational regime, the formula below is written in units where the speed of light, Planck's constant and Boltzmann's constant are equal to one. Gbulk means the gravitational constant of the bulk

theory. The formula gives a geometric meaning to a certain quantum information quantity and allows us to pose the inverse problem: what part of the geometry can be restored by knowing the entropies of many areas? [11]

$$S(A) = \frac{\text{Area}(\gamma_A)}{4G_{\text{bulk}}} \qquad (c = \hbar = k_B = 1) \qquad (5.3)$$

The limitations of the formula are significant for its application. The minimum surface refers to the static setting; in a more general time-dependent problem, an appropriate covariant description is required. Quantum corrections also do not disappear simply because the basic formula has a geometric form. In addition, entropy is specified for a specific region of a certain boundary theory, and not for an arbitrary set of laboratory sensors. Therefore, it is impossible to measure any correlation, substitute it for S and declare the resulting number to be the area of real space. First, it is necessary to justify the vocabulary between the physical system and the terms of the formula. Without this, beautiful equality loses precisely the precision that makes it interesting.

The conditions of fixation and homology become explicit in the geometric diagram of the static formulation (Fig. 19).

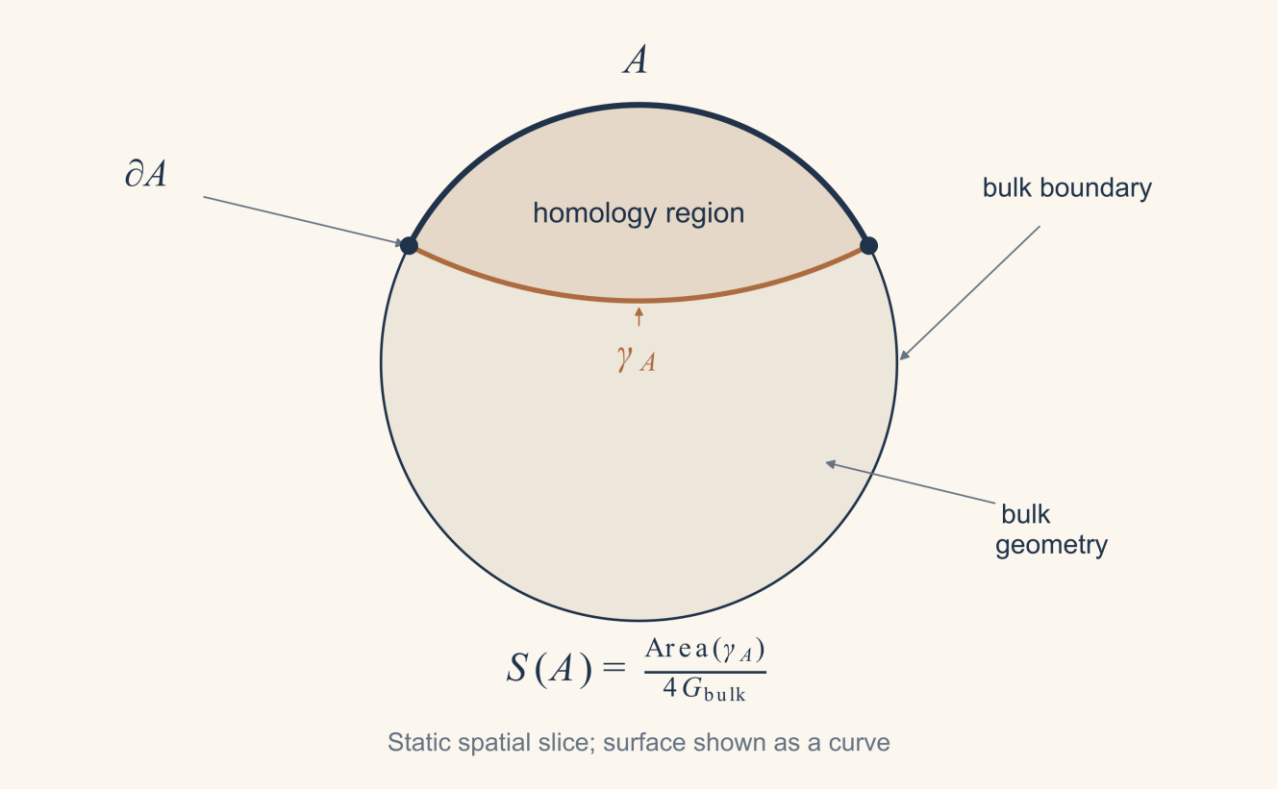


Figure 19. The static holographic formulation is shown on a lower-dimensional spatial slice. The selected boundary region A corresponds to a minimal surface γ_a fixed to ∂A, depicted here as a geodesic curve of the disk. The shaded area is bounded by A and γ_a and shows the homology condition. The geometry of the diagram is not a map of the observable Universe; the formula refers to the stipulated classical static duality regime.

Entanglement and Spatial Connectivity

Van Raamsdonk explored the idea that the classical connectivity of bulk geometry is related to the entanglement of the degrees of freedom of its quantum description. In the holographic picture under consideration, the decrease in certain entanglement connections corresponds to the geometric separation of regions. This motivates the search for space as a collective property of quantum relations. But the conclusion relates to a special theoretical context. It does not mean that any pair of entangled photons forms an accessible passage, and does not specify a technology for arbitrary distance control. To transfer an idea to another object, it is necessary to redefine degrees of freedom, dynamics and geometric vocabulary. [12]

For quantitative research of relationships, it is convenient to use mutual information. The entropy of an individual subsystem is determined by its density matrix, obtained after eliminating the remaining degrees of freedom. Mutual information of two subsystems shows how their joint state differs in information structure from the independent one. It takes into account both quantum and classical correlations, so it is not a universal measure of entanglement alone. Two detectors receiving a signal from a common source can have greater mutual information without direct interaction with each other. This observation alone shows why a strong correlation cannot automatically be equated with a small physical distance or the ability to quickly transmit an effect.

$$S(\rho) = -\mathrm{Tr}(\rho \ln \rho), \qquad I(A:B) = S(\rho_A) + S(\rho_B) - S(\rho_{AB}) \tag{5.4}$$

To turn correlations into estimated distances, sometimes you want to apply a monotonic transformation: assign a small length to a strong connection, and a large one to a weak one. But distance has additional requirements. It must be defined for the desired pairs, consistent with the choice of units, and satisfy the appropriate metric conditions, including the triangle inequality in a common spatial problem. Arbitrary transformation of mutual information does not guarantee this. Moreover, the pairwise values do not completely define the many-particle quantum state. Therefore, the reconstructed map should be considered as a testable data model and not as a geometry automatically present in any correlation table.

Shared information and causal response

To test the ability to transmit an impact, another experiment is needed: a controlled disturbance is applied to one part of the system, after which the change in the other is measured. In linear response mode, such a relationship is expressed through a commutator of observables. Let us choose a perturbation of the Hamiltonian with a minus sign, proportional to the external signal f and the operator B. Then the susceptibility χ for the observable A has the sign indicated below, and the step function θ resets it to zero before the perturbation. A stationary initial state is assumed so that the response depends on the time difference. This approach relates to the linear response theory developed by Kubo; it relates the action of the experimenter to the measured response of the system. [13]

$$H'(t) = -f(t)B, \qquad \chi_{AB}(t) = \frac{i}{\hbar}\theta(t)\langle [A(t), B(0)] \rangle \tag{5.5}$$

$$\delta\langle A(t)\rangle = \int \chi_{AB}(t-t')f(t')\,dt' \qquad (5.6)$$

For quantum spin systems with limited local interactions of finite range, Lieb and Robinson's estimates limit the speed of influence propagation. The commutator norm is suppressed outside the effective cone. The positive parameters C and μ are determined by the model and the selected observables, r denotes the distance between their regions, and v specifies the velocity boundary. This is not the universal speed of light: we are talking about propagation in a given system. Outside the cone there are usually exponentially small tails rather than strict zeroing. In other interactions, the type of restriction may change. Locality can thereby be tested through operator dynamics, separate from pre-existing state correlations. [14]

$$\| [A(t), B] \| \leq C \ \| A \| \| B \| \ e^{-\mu[r-v|t|]} \qquad (5.7)$$

The absence of superluminal communication through entanglement alone can be seen directly. If a local unitary transformation is performed on subsystem A, the reduced density matrix of B does not change: the partial trace eliminates the transformation on the excluded subsystem. Therefore, all local probabilities of observer B remain the same. A similar conclusion holds for a local trace-preserving operation when its result is not sampled conditionally. In conditional selection, state B may be described differently, but to exploit this difference it is necessary to know the selection outcome through a normal communication channel. Strong mutual information and controlled transmission of a new message remain distinct physical capabilities.

$$\rho_B{}' = \mathrm{Tr}_A\left[(U_A \otimes I_B)\rho_{AB}\left(U_A^{\dagger} \otimes I_B\right)\right] = \rho_B \qquad (5.8)$$

Geometry reconstruction is an inverse problem

Even with an accurate geometric vocabulary, reconstructing space from observations can be ambiguous. The direct problem specifies the geometry and calculates entropies, spectra or correlations. The inverse problem starts with these quantities and looks for the geometry that could generate them. Some metric changes may not affect the selected dataset or may have an impact below the resolution. In addition, coordinate transformations can change the metric record without changing the physics. It is therefore necessary to distinguish between physical ambiguity and freedom of description. An algorithm that always produces a single beautiful surface does not yet prove the uniqueness of the reconstructed space.

In Che's work 2026, formulas were obtained for the recovery of a certain class of stationary homogeneous asymptotically AdS_3-metrics from covariant holographic entropy. It is especially significant that simultaneous data preserves the ambiguity of the sign of the shift part of the metric, while the dependence on the time difference helps to eliminate it. This is a concrete example of how an additional observable resolves geometric ambiguity. The result is not a universal reconstruction of an arbitrary space from any quantum data: the chosen class of metrics and holographic formulation are essential. The principle itself is valuable for the instrument program - to look for what information the original protocol loses and what new measurement returns it. [15]

A useful standard for testing an inverse problem involves recovering some of the data and predicting the rest. If the metric is fitted using entropies alone, independent intervals, time

dependencies, or other available observables provided by the model should be examined. One must also evaluate how errors in the input data are amplified in the reconstructed quantities. Formal reversibility does not guarantee stability: a small change in the measured function can lead to a large change in the solution. Therefore, the future geometric tomograph is required to report the area of uncertainty and indistinguishable alternatives. Not being overly specific makes the instrument more useful because it shows where additional measurements are needed and where information is already sufficient.

Work program for comparing two geometric descriptions

On this basis, a limited research hypothesis can be formulated: the geometry reconstructed from state correlations and the geometry reconstructed from disturbance transfer can systematically diverge even for the same controlled system. The possible discrepancy itself is not proposed as an unknown law of quantum mechanics. The research challenge is to accurately describe the conditions of agreement, construct robust estimators, and find observables that discriminate between causes of disagreement. The starting platform is a programmable quantum system or a suitable analog stand with known dynamics. There you can change the state with a fixed connection structure and check which part of the reconstructed picture actually depends on the state.

The protocol must store separately the original mutual information, the measured time response, and the prerequisites for their geometric transformation. The signal detection threshold cannot be hidden in the distance determination: by reducing the threshold, a weak early tail can create the appearance of a shorter path. Likewise, a common cause of correlations can create false proximity between two nodes. Control changes in state, perturbation amplitude, and noise level help distinguish these effects. The meaningful result will not be any difference between two maps, but a predictable pattern of differences, reproducible under predetermined conditions and explained by a single consistent model.

The two branches of measurement should be reduced to comparing reconstructions with obvious uncertainties (Fig. 20).

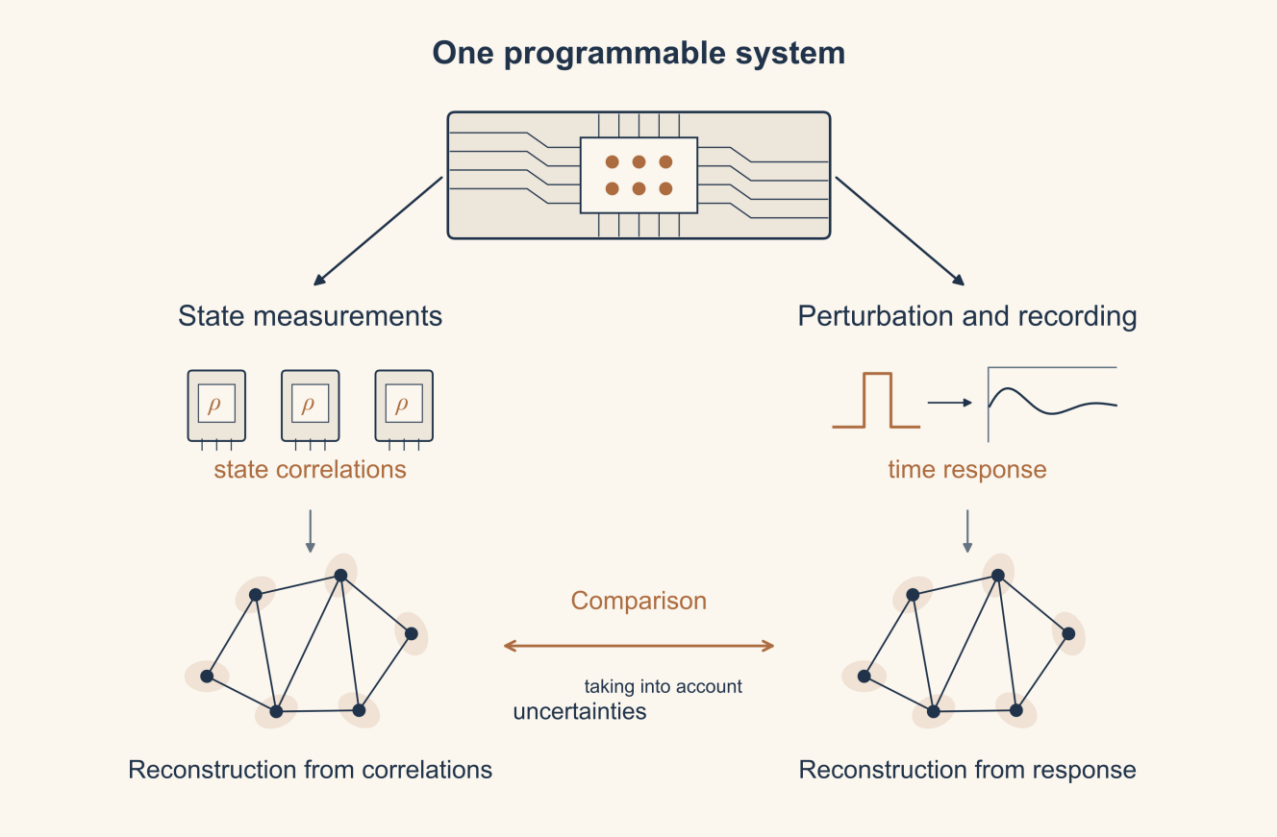


Figure 20. The proposed protocol compares two reconstructions of a single supervised system. The first branch uses state measurements and correlations, the second - local disturbance and time response. Both maps are shown conditionally, with areas of uncertainty, without numerical results. Their coincidence or divergence is not assumed in advance: comparison requires agreed upon premises, preservation of initial data and control of the registration threshold.

In the first five chapters, the language of the future device is formed. There are already two complete test cases: the scale exponent on a sphere varies with a constant local dimension, and the same spectra of finite networks allow different local responses. Next, the problem becomes inverse: the device is hidden, only selected inputs and outputs are available, and the parameters are known with finite accuracy. From this point on, what will be tested is not the expressiveness of the geometric picture, but the information that the data actually allows one to extract.

Chapter 6
Can space be reconstructed from its response?

The world inside a closed enclosure

Several connectors are routed through the wall of the closed case. An impulse is applied to one, signals are removed from the rest. There may be resistors, energy storage devices, or long lines inside. The observer needs to recognize the device by what is accessible from the outside. This is a convenient smaller version of the question about space: how do the relationships between readings make sense of the relationships within the world under study?

A direct task starts with a device and ends with a signal. The reverse starts from the signal and tries to identify the device. These directions are unequal. Several different devices may give the same answer, just as different routes may bring a passenger to a station at the same time. Even infinite precision in time measurement will not tell which route was taken if the other observables are the same. This is structural ambiguity. It differs from the usual error, which can sometimes be reduced by longer accumulation of data.

The objective meaning of the inverse problem is shown in Figure 21: the inputs and outputs of a closed system are available.

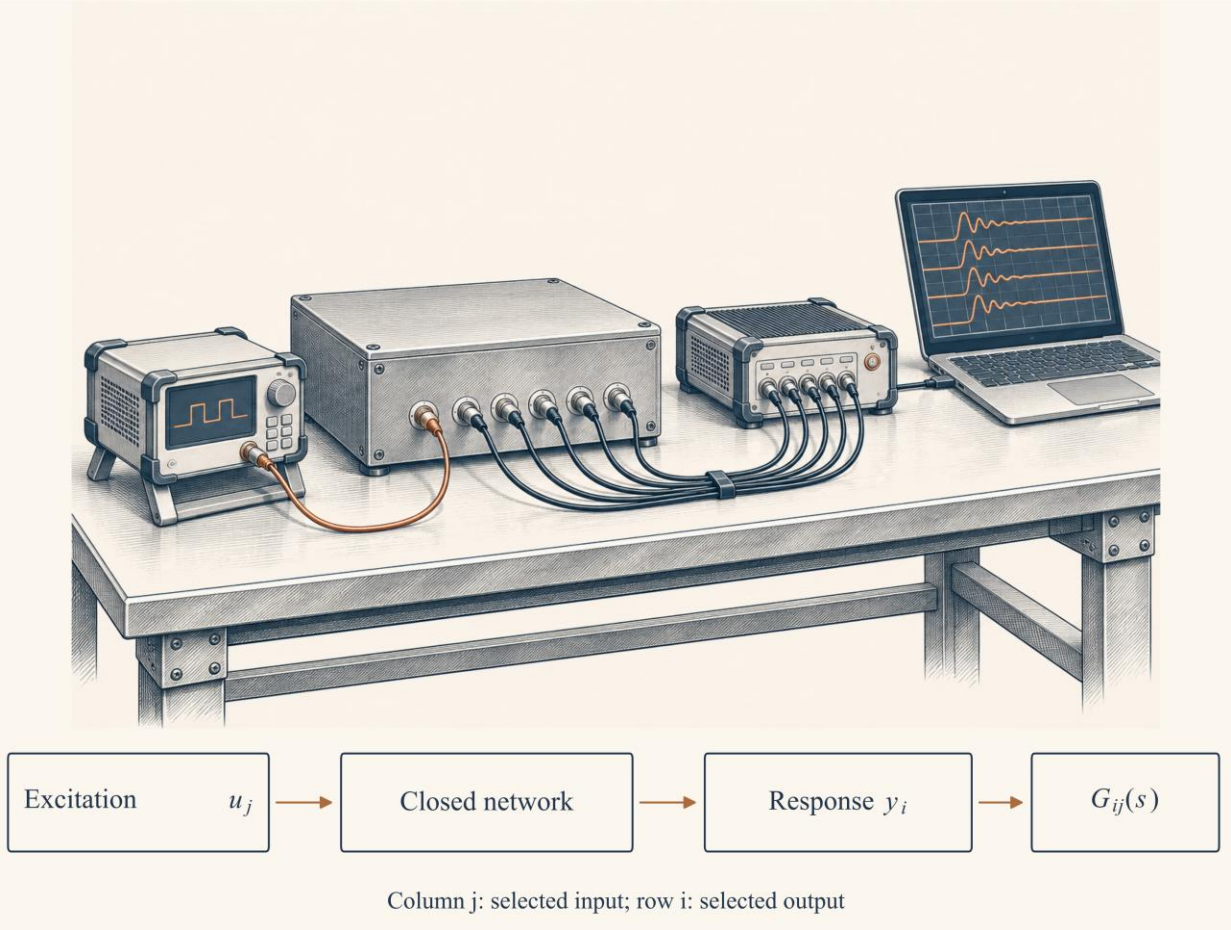


Figure 21. Closed network and interface accessible to the experimenter. The generator sets the impact on the selected port, the multichannel recorder measures the responses, and the sequential change of inputs allows you to create the matrix $G_{ij}(s)$. The row refers to the output, the column to the input. The internal structure of the case remains unknown. Devices and oscillograms are shown conditionally; The figure does not contain experimental data and does not specify a specific electronics circuit.

Therefore, the question of restoring space must be raised along with a list of acceptable explanations. If it is known in advance that a certain lattice is located inside and only one connection has changed, the problem may turn out to be solvable. By allowing arbitrary additional nodes, unknown meter connections, and internal sources, the same data allows for many more variations. The model class constraint is part of the result statement. It cannot be quietly removed from the conclusion after the calculation has found a beautiful answer.

Here a useful distinction arises between detecting a change and explaining its nature. The first question is: is the data compatible with the previous calibrated system? The second requires choosing between a changed coupling, a new internal degree of freedom, element drift, or another reason. The third, even stronger, asks whether the discovered structure is related to fundamental space. Each subsequent stage requires new prerequisites and new dimensions. A device that confidently solves the first problem does not automatically receive the right to answer the third.

Why spectrum alone is not enough

In chapter 2, two networks of three nodes had the same eigenvalues 0, 1 and 3, and therefore the same heat trace at each scale. The local response at the middle node varied. This small example remains a guideline for further reasoning: the coincidence of a compressed characteristic does not mean the coincidence of all available observations.

The spectrum of natural vibrations seems to be a natural imprint of geometry. The size of the cavity, the shape of the boundary, and the connections between its parts affect the resonances. However, natural frequencies do not always determine the shape in a unique way. Gordon, Webb and Wolpert constructed different flat regions with the same spectra. This result relates to a strictly defined mathematical problem and shows that even a complete set of ideal frequencies can lose some geometric information. To explore an unknown space, this is a reason to expand the measured data beyond the spectral list. [16]

Consider a real symmetric matrix L with orthonormal eigenvectors v_n and eigenvalues λ_n. The transfer matrix G(s) contains both the values of λ_n and the spatial profiles of v_n. Its element connects the impact at node j with the response at node i. The eigenvalues specify the positions of the characteristic scales, and the products of the eigenvector components tell which points are involved in each mode. Measuring spatial responses is therefore potentially richer than measuring resonances alone.

$$G_{ij}(s) = \sum_n \frac{v_n(i)v_n(j)}{s + \lambda_n}, \qquad s > 0 \qquad (6.1)$$

Additional information appears only when the sites of excitation and registration are actually different and known. If the instrument sums the response over the entire surface, part of the spatial structure disappears again. If nodes can be arbitrarily renamed, two matrix entries can describe the same physical network. Port labels, their coordinates, polarities and calibration coefficients must be fixed regardless of the recovery procedure. Otherwise, the algorithm is capable of producing a difference that exists only in the selected notations.

For the same reason, the spectral dimension is not a complete specification of space. It compresses a huge amount of information into a single number depending on the scale. This compression is useful for detecting transitions and comparing families of models, but is not intended for definitive identification. In a study of quantum geometry, it was separately shown that different diffusion processes can have the same spectral dimension. Therefore, changing it requires checking the propagation law itself, and not just the assumed geometry. [25]

How hidden nodes turn into long-distance connections

Now let's divide the network nodes into accessible and hidden. For brevity, we denote them by the indices o and h. In a steady-state linear problem, the latent variables can be expressed in terms of the observables and substituted back in. An external observer will receive a reduced matrix describing only the available nodes. It will include effective connections between ports, even if there

is no element directly connecting them inside. This is not an approximation arising from poor precision: under given conditions, eliminating variables is an exact algebraic transformation.

$$A_{\text{eff}}(s) = A_{oo}(s) - A_{oh}(s)A_{hh}(s)^{-1}A_{ho}(s) \qquad (6.2)$$

The expression is called Schur's complement. In electrical networks, the corresponding elimination of internal nodes is known as Kron reduction. Dörfler and Bullo examined how this procedure changes the topology and spectral properties of the graph. For the problem under consideration, the fact itself is especially significant: from the outside, a hidden chain can look like a direct connection. Therefore, the unusual connection of the reconstructed reduced model does not yet establish an unusual connection in the original physical system. [17]

The simplest example does not require matrices. Between two accessible points there are two resistors in series; their connection point is inaccessible. DC current measurements at the ends give the total resistance. Such an object is indistinguishable from a single resistor with the same resistance. No matter how many times this measurement is repeated, the internal node will not appear in the data. If there is significant capacitance at the midpoint, the transient may reveal additional time scale. But even then the conclusion concerns the class of electrical models being compared, and not any conceivable internal design.

Dynamic measurements are valuable because hidden degrees of freedom are often revealed through memory. Once internal variables are eliminated, the effective coupling begins to depend on s or frequency. Based on its delay and shape, one can distinguish several specific candidates that coincide in statics. At the same time, dynamic reduction is also an independent mathematical problem; it has been studied for classes of generalized electrical networks. The mere presence of memory does not serve as evidence of a new geometry: it can be created by an ordinary unobservable energy storage device. [20]

Figure 22 compares the original device with a hidden node and its abbreviated description. The new line in the bottom diagram represents the result of eliminating the variable. To establish whether a corresponding immediate element exists will require observation sensitive to internal dynamics; static equivalence is not enough for this.

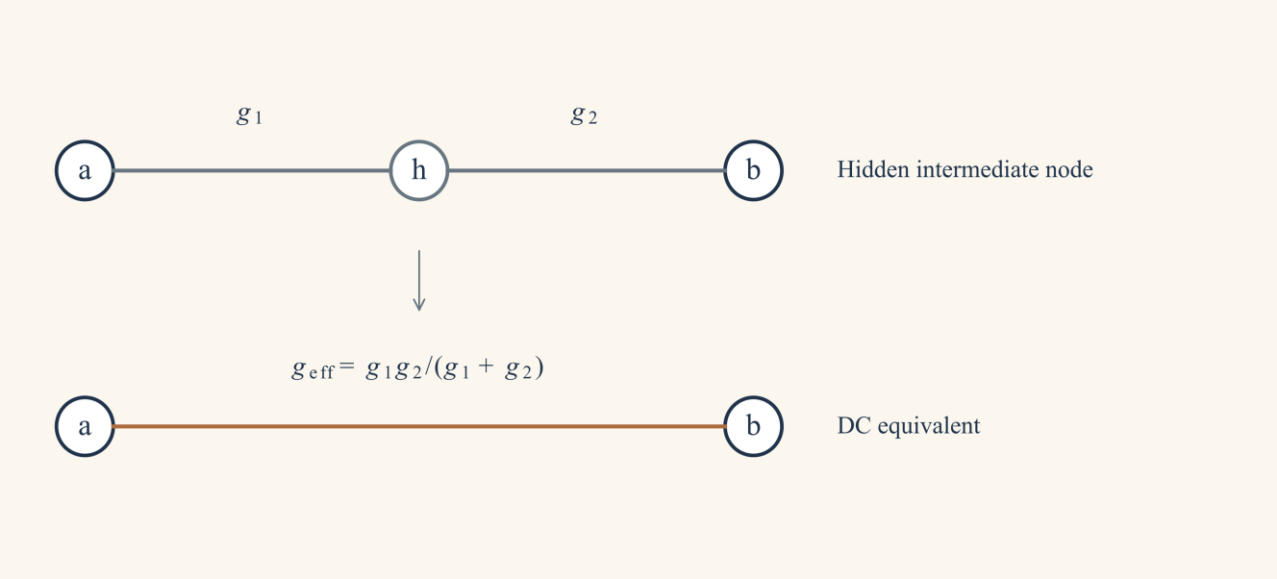


Figure 22. Hidden node and efficient communication between available ports. The shortened diagram reproduces the selected external data; its edge does not have to coincide with a separate physical conductor of the original network.

When reconstruction becomes unique

It does not follow from the above that inverse problems are hopeless. Their solvability depends on the exact conditions. If the normalization is known, all nodes are accessible, and the complete matrix G(s) for real positive s is measured, then in this finite-dimensional model the operator is restored by matrix inversion. This is a strong statement, but its strength comes at the cost of full access to the system. It does not apply to situations where a small submatrix is measured or the sensor connection coefficients are unknown.

$$L = G(s)^{-1} - sI \qquad (6.3)$$

There are also uniqueness theorems in continuous problems. Sylvester and Uhlmann showed the reconstruction of smooth isotropic conductivity from complete boundary data in a domain of dimensions not lower than three under the conditions of their theorem. This example is important precisely because of its explicit assumptions: the type of equation and domain are known, the class of coefficients is limited, and all the required boundary influences are available. Eight sensors in an unknown environment do not automatically reproduce this set of assumptions. [18]

In addition to uniqueness, there is stability. Two different models may give different answers, but the difference will be less than the instrument noise. Formally the problem is then solvable, but practically it is ill-conditioned. A reasonable research result includes not only the found configuration, but also the distance to the nearest competitors in the measured signal space. The smaller this distance is compared to the uncertainty, the more carefully one should interpret the reconstructed picture. It is useful to show such alternatives together on a chart, rather than hiding them behind a single line of best fit.

Distance between explanations

Practical discriminability begins with the choice of data space. Let all measured matrix elements be collected into a vector μ, and C describe their errors. The difference between the two predictions is compared to the noise after normalization by inverse covariance. If two families of models admit their own unknown parameters, the closest feasible predictions should be compared, not two arbitrarily chosen representative curves.

$$D^2(\mathcal{M}_0, \mathcal{M}_1) = \inf_{\mu_0 \in \mathcal{M}_0,\, \mu_1 \in \mathcal{M}_1} (\mu_1 - \mu_0)^{\mathsf{T}} C^{-1} (\mu_1 - \mu_0) \qquad (6.4)$$

Here M_0 and M_1 denote sets of expected data, rather than sets of already noisy records. Zero distance means that at least some representatives of the classes are indistinguishable by this protocol. It does not prohibit the discrimination of other representatives. In particular, the class of an additional connection with g, arbitrarily close to zero, is in contact with the class without this connection. Therefore, universal detectability of the entire such family cannot be obtained with finite noise.

When a specific g range is studied, the distance is calculated specifically for it. Another way is to set the required accuracy of independent calibration and find out at what ports the competing sets diverge. So the question “how accurate a device is needed” takes on a certain meaning: accuracy is needed to separate given predictions for given permissible changes in ordinary components.

No single minimum of the error function replaces this comparison. It tells you where the best representative of the selected class is located. If the neighboring class fits just as well, the result is left with several explanations. Such a record is useful practically: it shows exactly what new experiment should change the situation.

When the calibration is directed to the same place as the signal

It is convenient to consider the local cause of ambiguity before the full nonlinear fit. In the vicinity of the standard, the derivative with respect to the strength of the assumed edge sets the vector h. Derivatives with respect to ordinary weights make up the columns of the matrix J. If h lies almost in the space of these columns, distributed drift changes the data in almost the same direction as the desired addition.

$$\delta\mu = h\,\delta g + J\,\delta w, \qquad \rho_{\mathrm{loc}} = \frac{\| (I - J J^{+}) h \|_2}{\| h \|_2} \qquad (6.5)$$

The record uses equal independent variances of data elements. For common covariance, appropriate normalization is first applied. The matrix J^{+} is a pseudo-inverse with an explicitly specified cutoff of small singular values. The value of ρloc measures the fraction of the signal direction that remains after freely eliminating the calibration directions. It characterizes the linear approximation at a selected point.

Indicator for original corner ports	Meaning
Sensitivity matrix size	192 × 144

Indicator for original corner ports	Meaning
Relative cutoff of singular values	10^{-10}
Numerical rank	93
The remaining proportion of the norm of the signal direction	2.376 %
Norm of free coefficients per unit g	575.42

Sensitivity to numerical cutoff is tested separately. At thresholds 10^{-6}, 10^{-8}, 10^{-10} and 10^{-12} the same rank 93, residual share 0.02375875 and maximum coefficient are obtained 146.69. The reason for the stability here is visible in the spectrum: the 93rd singular value is 1.1141×10^{-6} from the largest, the next one is about 3.13×10^{-16}. The full spectrum and four results are saved by the program. This is a check of the numerical conditioning of this linearization; it does not transform free calibration directions into physically permissible finite drift.

In this network, after projection, about 2.38 percent of the original norm remains. At the same time, the necessary free coefficients are very large: the maximum absolute value is approximately 146.69 per unit g. Therefore, from a small fraction of the remainder it does not follow that a strong link of finite strength can be simulated by two percent of drift. The constrained nonlinear problem must be solved separately. This separation prevents the error of making a local conclusion without parameter limits imperceptibly turn into a statement about the real device.

The geometry of this local ambiguity in record space is shown in figure 23.

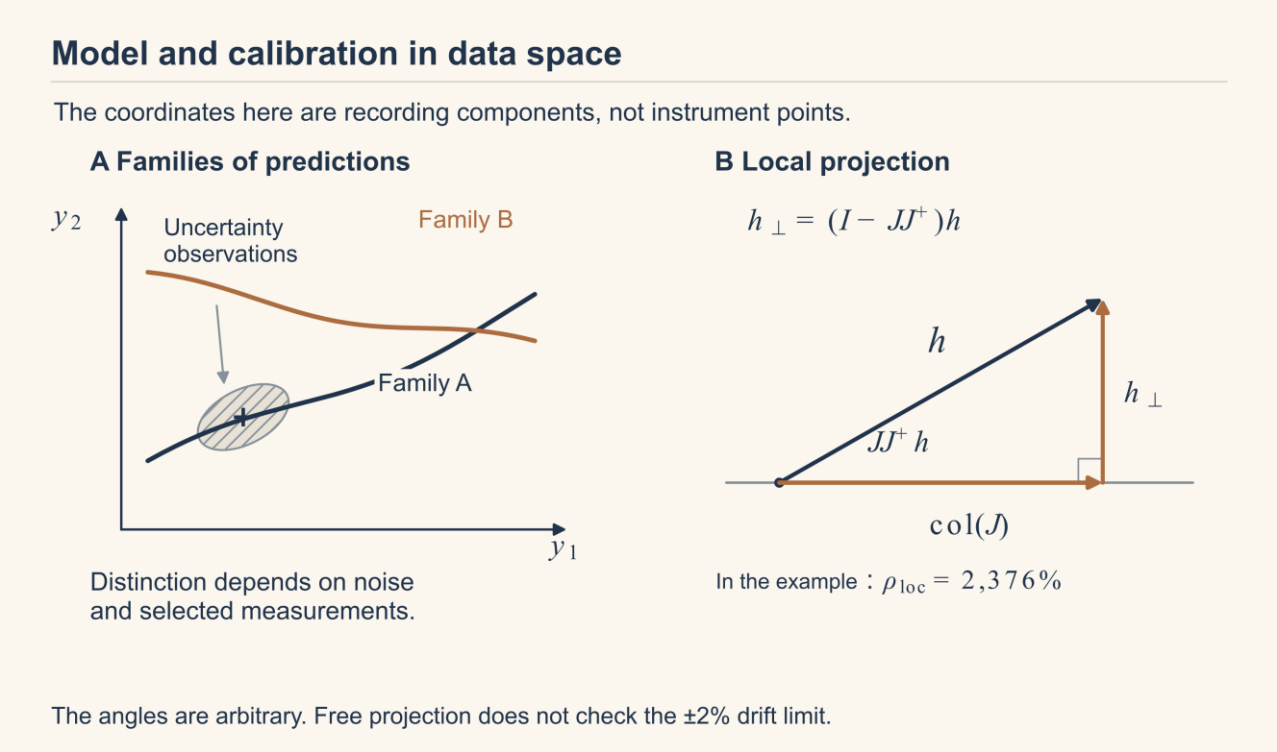


Figure 23. Data space and local calibration ambiguity. On the left are families of predictions and observational uncertainty; it is a diagram, not the physical geometry of an object. On the right, the signal direction h is divided into a calibration projection and a remainder. In the network example, the remainder is 2.376% of the original norm. The angles of the figure are arbitrary: a small free projection in itself does not establish compatibility with the finite drift constraint ±2%.

A useful measurement plan seeks to increase the difference after allowing for allowable calibration. To do this, you can change the source locations, the reading method, or the known operator of the second probe. An increase in the raw signal alone does not guarantee improvement: the calibration change signal may also increase at the same time. In the next chapter, limits will appear that apply to the entire finite range of weights.

Which measurements add distinguishability?

The first way to add information is to change the location of the effect. A source located near the intended end of a hidden link excites the system differently than a distant source. The second way is to change the time scale. A slow response manages to bypass long paths, while a fast response more strongly senses nearby sections and internal delays. The third way is to make a known local change and check how the entire response is rebuilt. In the latter case, the researcher receives information not only about the state of the system, but also about its response to controlled intervention.

For an invertible matrix A, a small known perturbation δA leads to first order δG = −GδAG. This formula relates the sensitivity of the observed response to the location of the intervention. If a change in one node makes a significant difference between two competing configurations, this is where it is advantageous to place a switching element or an additional sensor. Such planning is

much more meaningful than a mechanical increase in the number of measurements. One hundred repetitions of an insensitive channel may provide less useful information than one new independently calibrated channel.

Finally, one should distinguish between the restoration of a graph and the restoration of its physical embedding. The same graph can be implemented by wires on a table, optical paths, or interactions of internal states. The connection matrix itself does not indicate through what space these interactions are laid. Therefore, the book uses network tomography as a school of testable hypotheses. It teaches you to find hidden connections, appreciate ambiguity, and design discriminating experiments. The transition from this result to statements about vacuum requires a separate physical basis, which will be considered after the computational experiment.

Place of this task among existing methods

The joint restoration of several graphs is already an independent direction. Yuan et al. study the estimation of multiple Laplacians with common, distinct, and sparse structure through structured regularization. Navarro et al consider partial observations of stationary graph signals with hidden nodes and similar connectivity across multiple networks. These works provide useful points of comparison; their guarantees relate to their own observation operators and prerequisites. [39] [40]

Problem formulation	Data and object	What to compare
Yuan et al.	Several sets of graph signals; joint estimation of Laplacians	A method for specifying a common and different structure; assessment prerequisites
Navarro et al.	Partial nodal observations; influence of hidden nodes	Relationship between observed statistics and graph and recovery conditions
Example in this book	Managed port responses of a known network; finite drift limits	Which pairs are excluded when changing ports and which remain compatible

The subject of the calculation is narrower than the general problem of the emerging space. The nodes, basic topology, and registration operators are known. Limited changes in weights and possible additional relationships are unknown. The contribution of the completed example is the testable construction of comparison of such explanations: exact response, bounded envelope, dangerous counterexample, and dimension separating the chosen alternatives. The independent scientific novelty of the entire structure will require a separate comparison with the wider literature; well-known identities and the very idea of several probes retain their origins.

Chapter 7
The hypothesis of shared sparse connectivity

From an unusual signal to a testable structure

After discussing the ambiguity, a working hypothesis can be formulated. Let several independently calibrated methods of studying one system indicate a small number of the same additional compounds. Their strength may vary as different processes interact with the object differently. The common arrangement of connections is assumed, and not the coincidence of all signals. Such a hypothesis is specific enough to be incorrect: the restored connections may not match, the prediction on new ports may fail, and the deviation may be entirely due to normal calibration error.

At the first stage we are talking about a finite network with known nodes. The index α denotes the research channel for which its own base operator $L_0α$ is defined. These can be different experimental realizations of the general topology or different physical processes, if the correspondence of the nodes is independently justified for them. Using the same point index in two models is not enough: you need to establish that the sensors are actually accessing the same element of the system. Without such a comparison, the matching structure of the matrices will be a notational convention rather than an observable fact.

$$L_\alpha = L_{0\alpha} + \sum_{e=1}^{m} g_{\alpha e}\, b_e b_e^{\top}, \qquad b_e = e_{a_e} - e_{b_e}, \qquad g_{\alpha e} \geq 0 \qquad (7.1)$$

Sparsity here means that m is small compared to the number of possible pairs. It is not derived from general principles of physics and is introduced as a testable constraint of the model. If the data requires hundreds of independently adjustable relationships, the original hypothesis loses explanatory parsimony. If an individual channel is allowed to arbitrarily not see any inconvenient relationship, verifiability is also weakened. Therefore, before analysis, it is necessary to indicate which interactions should be present in the participating channels and what limits of sensitivity allow the absence of a response to be considered meaningful.

Common vocabulary and common active structure

The matrix of possible edges does not yet determine which edges are physically present. Let B contain two columns, and the first probe has weights (g, 0), the second - (0, g). The candidates' vocabulary turns out to be common; There are no active shared connections. Therefore, the hypothesis of a single device must explicitly identify the set E* of non-zero connections, the limiting number of its elements and the sensitive channels involved.

$$E_\alpha^{\mathrm{act}} = \{e : g_{\alpha e} > 0\}, \qquad E_\alpha^{\mathrm{act}} = E_* \qquad (7.2)$$

Equality only applies to those channels that are pre-set to have non-zero interactions with the links being tested. If the physical theory allows for the absence of interaction in a particular channel, this exception is fixed before analysis. It cannot be inserted every time the next probe is inconveniently at odds with the others. Detectability also requires a range of forces accessible to a given precision; the boundary g = 0 remains the limit of the null hypothesis.

The numerical two-probe example of the chapter 8 selects an even narrower version: m = 1, the same disordered pair, g ranging from 0 to 3 s^{-1} and known positive coefficients ηα, so that gα = ηαg. In the first probe $\eta_1 = 1$, in the second $\eta_2 = 1.6$. This is a given connection between two analogue models, and not a universal relationship between the interactions of different natural fields. The outer boundaries will include g = 0; when zero remains valid, the existence of an active relationship has not been established.

Nodes were mapped prior to analysis. For each probe, the nominal weights, port selection operator, source and response normalization are known. The model without addition, the common pair model, and the model that allows different pairs in two channels are considered separately. Everywhere the same limit of relative change in ordinary weights remains. Thanks to this, the generality of the structure is checked against the background of the same calibration uncertainty.

The difference between a shared candidate dictionary and a truly shared active link can be seen in Figure 24.

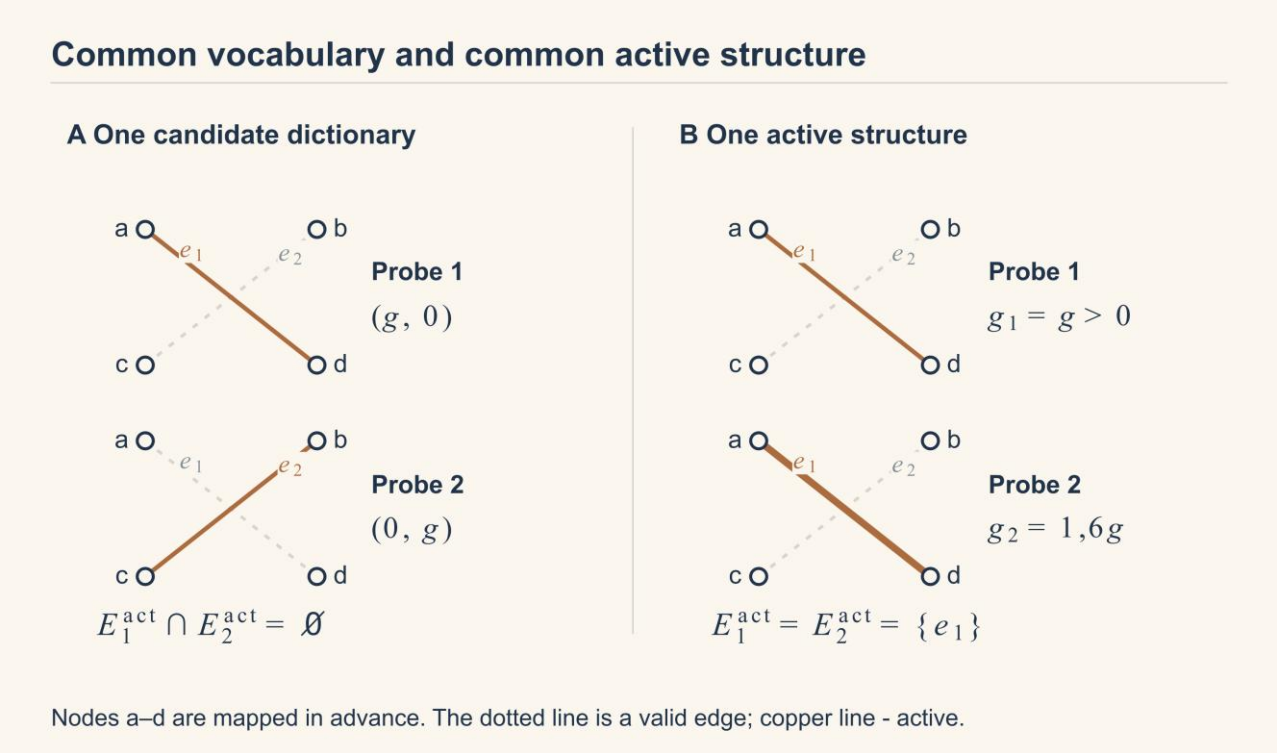


Figure 24. A common vocabulary and a common active structure are different conditions. In the left pair of circuits, both probes admit the same edges e_1 and e_2, but activate different dictionary entries; the intersection of active sets is empty. On the right, the same connection is active between pre-mapped nodes. Coefficients g and 1.6g repeat the given sensitivity ratio of the two-probe model, without expressing the universal law of interaction of natural fields.

What do positive weights guarantee?

The matrix L is constructed from positive edge weights. For an arbitrary real vector x, its quadratic form is the sum of the squares of the differences between neighboring nodes. This implies the non-negativity of the eigenvalues and the stability of the damped modes of the equation $\dot{x} = -Lx$. The uniform state remains the null mode, since each connection responds only to the difference in values at the ends. These properties ensure the mathematical consistency of the selected analogue. They do not prove that the same dynamics describe fundamental space.

$$x^{\mathsf{T}} L x = \sum_{e} w_e \left(x_{a_e} - x_{b_e} \right)^2 \geq 0, \qquad L\mathbf{1} = 0 \qquad (7.3)$$

For real s greater than zero, the operator A = L + sI is strictly positive and invertible. If L has the dimension of inverse time, s is measured in the same units, and $G = A^{-1}$ has the dimension of time. The added coupling factor g is also measured in reciprocal seconds. Vector b is dimensionless. Therefore, the product $g\, b^{T} G_0 b$ is dimensionless, as required for the sum with unity in the following formulas. This verification of units is especially useful when transferring a mathematical model to an electrical circuit or mechanical bench.

Negative increment of an existing connection requires separate consideration. It may be physically admissible if the resulting weight remains non-negative, but no longer belongs to the addition class $g \geq 0$ being tested here. Similarly, directed interactions, active amplifiers, and asymmetric operators change the properties of the model. They cannot be included with one verbal clarification after an unsuccessful fit. Class expansion is possible, but it must be accompanied by new stability conditions, new response formulas, and a re-evaluation of distinguishability.

The exact response of one added link

For one connection, the derivation can be carried out without resorting to cumbersome matrix algebra. Let us denote the previous solution $x_0 = G_0 f$, where f is the given external influence. After adding the connection, the equation becomes $(A_0 + g b b^{T})x = f$. Multiplying by G_0 gives $x = x_0 - g G_0 b (b^{T} x)$. The entire unknown correction now depends on a single scalar $\beta = b^{T} x$, that is, on the difference in state at the ends of the added connection.

$$\beta = \frac{b^{\mathsf{T}} x_0}{1 + g\tau}, \qquad \tau = b^{\mathsf{T}} G_0 b > 0 \qquad (7.4)$$

Substituting β back and taking into account the arbitrariness of the influence f, we obtain a change in the entire transfer matrix. This is a special case of the standard Sherman-Morrison identity. It is important to preserve its historical origin: the subject of the proposed research is the formulation of measurements and verification of connectivity models, and not the assignment of a well-known algebraic formula. Here the formula is re-derived for a specific class of networks so that the reader can check each transition and the conditions for its applicability. [19]

$$\Delta G = -\frac{g}{1 + g\tau}\, u u^{\mathsf{T}}, \qquad u = G_0 b \qquad (7.5)$$

The response is factorized into the product of one spatial profile and itself. Therefore, its rank does not exceed one. For positive s, the correction is negative semidefinite: any quadratic combination of measured quantities gives a non-positive result. However, individual off-diagonal elements can have both signs, since the u components also have different signs. A statement about the sign of a matrix cannot be replaced by a statement about the sign of each of its elements.

If only some ports are available, the selection statement P replaces profile u with Pu. The rank one structure is maintained, but the amplitude may become very small or disappear altogether. The absence of a signal then indicates the lack of sensitivity of the selected ports to this connection. It is not equivalent to the absence of the connection itself. This is why the sensor layout is part of the hypothesis being tested: the same object can be visible in one port configuration and almost invisible in another.

The transition from the added edge to the available port matrix is shown in Figure 25.

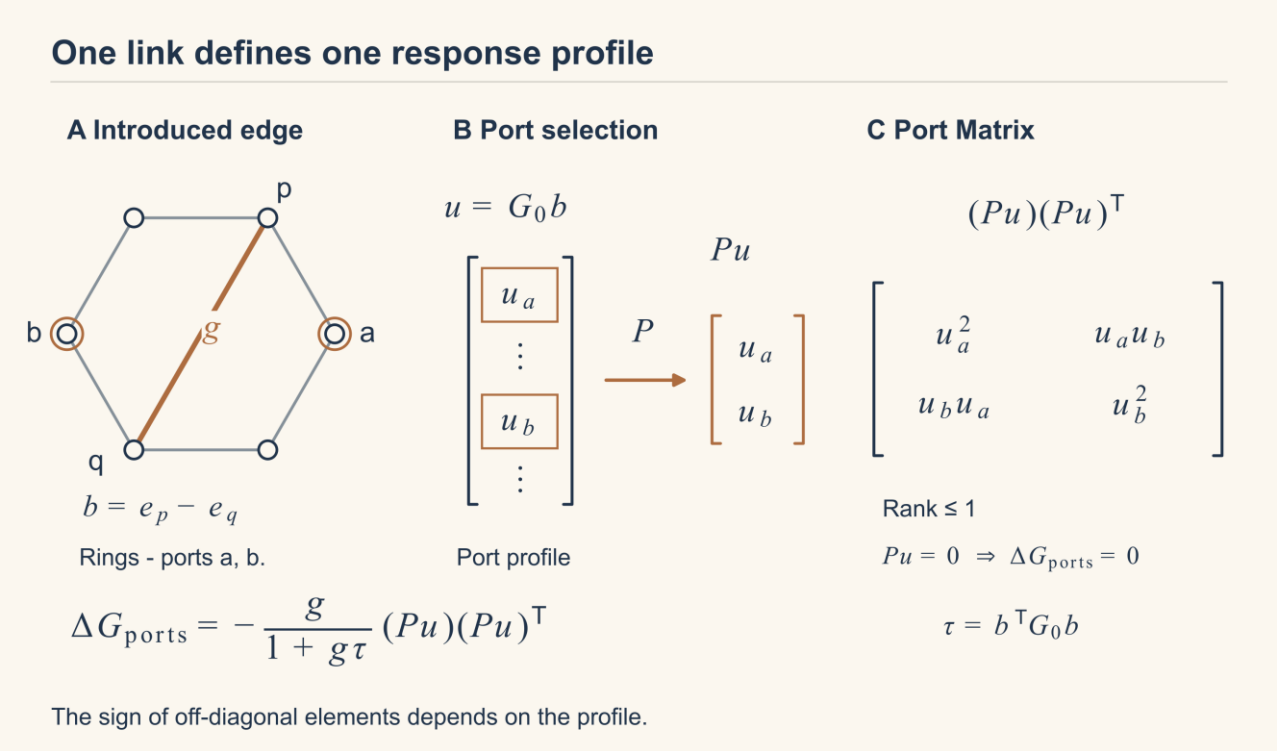


Figure 25. Factorization of the response of one additional connection. The edge between p and q defines the vector b, and the inverse nominal operator transforms it into the profile u. Selecting two illustrative ports preserves only the u_a and u_β components. Their outer product forms an observable correction with a common negative factor. The rank does not exceed one, but individual off-diagonal elements can have any sign. When Pu = 0, the selected ports do not sense the added link.

Why a strong connection is not always measured better

The formula reveals another limitation. As g increases, the amplitude of the factor $g/(1 + g\tau)$ becomes saturated. Two very strong bonds of different weights can pull their ends together almost equally and produce similar responses. The device reliably detects a change, but is poor at estimating its exact strength. This is an example of how detectability and accuracy of parameter

determination diverge even in a perfectly known model. Increasing the sensitivity of the sensor helps only as long as the uncertainty is not determined by the weakest dependence of the signal on g.

$$\frac{\partial \Delta G}{\partial g} = -\frac{uu^{\top}}{(1+g\tau)^2}, \qquad \lim_{g\to\infty} \Delta G = -\frac{uu^{\top}}{\tau} \qquad (7.6)$$

This implies a practical choice of measurement scales. For each pair of ports, it is useful to estimate not only the signal magnitude, but also the derivative with respect to the unknown parameter. The channel with the largest deviation does not necessarily give the smallest error g. Joint analysis of several s can improve the situation, since the profile of u and the value of τ change with scale. But it does not create information for free: the range s is limited by recording time, noise and the accuracy of the model of the real device.

Multiple connections and a shared connectivity pattern

For several additions, we collect the vectors b into the columns of the matrix B and introduce a diagonal matrix Γ of positive weights. It is convenient to put $U = B\Gamma^{1/2}$. Solving the system $A_0x + UU^Tx = f$ comes down to finding a small vector $z = U^Tx$. Multiplying the expression $x = G_0f - G_0Uz$ by U^T gives a linear system for z of dimension m. After solving it, the form of the standard Woodbury identity is obtained.

$$\Delta G = -G_0U\left(I + U^{\top}G_0U\right)^{-1}U^{\top}G_0 \qquad (7.7)$$

For s > 0 the internal matrix is strictly positive. Therefore, the correction is again negative semidefinite, and its rank does not exceed the number of linearly independent columns B. It can be less than the number of added edges: for example, the edge vectors of a cycle are linearly dependent. Measuring only a subset of nodes can further reduce the observed rank. Thus, the number of salient singular values provides limited information about the complexity of the disturbance, but is not a universal counter for hidden connections.

In the multi-channel version, the shared active set of edges is given by the definition above. The B matrices themselves can be written in an extended dictionary, but zero column weights should not create spurious agreement. The test compares the shared-structure model with the separate structure model and with instrumental causes. The number of matched indices is only useful in conjunction with known node mapping and quantitative measurement predictions.

Calibration goes into the hypothesis

Ordinary edges also change. To first order, their contribution is $-G_0\delta LG_0$, where δL is the sum of many small local increments. On limited ports, this contribution may be equivalent to one new link. Therefore, in the following procedure, the standard is replaced by a family of valid calibrations. Let us assume that the relative deviation of each ordinary weight in absolute value does not exceed ε = 0.02. For computational experiment, this is the exact condition of the generator; in the instrument it must be based on an independent calibration.

It is convenient to construct the disagreement function using the vector of residuals r and the covariance matrix of errors C. Then the different accuracies of the channels and the correlations between them are taken into account. But the minimum value of a function after searching through many pairs should not be automatically interpreted as ordinary statistics with one selectable parameter. The algorithm selects both the continuous strength of the connection and the discrete location of its ends. The chance of a random hit should take into account the entire search, not just the last optimization step.

$$\chi^2 = r^{\mathsf{T}} C^{-1} r \qquad (7.8)$$

The two models being compared now differ only in the added connection. In Hcal, normal weights are freely varied within a given range. In Hcal+edge the same limits apply and additional positive coupling is allowed. The threshold obtained for a perfectly stationary reference does not carry over to this comparison. For a limited class, you can build another test that relies on the order of positive matrices and does not require finding the global minimum over all 144 weights.

The envelope of all admissible calibrations

Each ordinary weight is written as $w_e = w_{0e}(1 + \delta_e)$, where $|\delta_e| \le \varepsilon$. For any vector x, the sum $w_{0e}\delta_e(x_a - x_\beta)^2$ is limited in absolute value by $\varepsilon x^{\mathsf{T}} L_0 x$. Therefore, the order of quadratic forms is satisfied immediately for all admissible weights. The sign “precedes” in the formula means exactly this order, and not an element-by-element comparison of matrices.

$$(1 - \varepsilon) L_{0\alpha} \preccurlyeq L_\alpha(\delta_\alpha) \preccurlyeq (1 + \varepsilon) L_{0\alpha} \qquad (7.9)$$

For $s > 0$, all matrices after adding sI are strictly positive. Inversion reverses the order. This can be verified by passing to $B^{-1/2} A B^{-1/2}$: if A is not less than B, the normalized matrix is not less than the identity matrix, and its inverse is not greater than the identity matrix. Returning to the original variables gives the desired inequality. The same positive edge contribution can be added to both boundaries before inversion.

$$A_{\pm,\alpha} = sI + (1 \pm \varepsilon) L_{0\alpha} + \eta_\alpha g b b^{\mathsf{T}} \qquad (7.10)$$

$$A_{+,\alpha}^{-1} \preccurlyeq G_\alpha(s) \preccurlyeq A_{-,\alpha}^{-1} \qquad (7.11)$$

The outer shell of the response is obtained for any distribution of admissible weights, including a specially selected correlated drift. Independence of edge changes is not required. Moreover, different δα vectors may be allowed for different probes. If they are actually common, the class becomes narrower and the shell remains valid. When $\varepsilon < 1$ the positivity of ordinary conductances is not lost.

The limit applies only to the listed variables. Unknown capacitances, ground leaks, directional connections, hidden active elements and inaccurate normalization require separate inclusion in the model. It would be incorrect to attribute protection from any instrument defect to this formula. Its advantage lies in the precise coverage of the finite, clearly named calibration range.

From a matrix bound to a measurable interval

Let us choose a pre-normalized vector a, supported on the available ports, and consider the scalar z = a^{T}Ga. For example, a can highlight one diagonal response or the difference of two ports divided by √2. The matrix order implies an interval for z. A scalar is convenient in that its uncertainty is directly calculated from the covariance of the written matrix elements.

$$a^{\top} A_{+}^{-1} a \le z \le a^{\top} A_{-}^{-1} a \qquad (7.12)$$

For the proposed pair, both boundaries depend on g according to the already derived formula for one connection. Let R denote one of the two inverse nominal matrices with g = 0. Then z_0 = a^{T}Ra, v = a^{T}Rb and d = b^{T}Rb. All these numbers are calculated before adjusting the edge strength.

$$z_R(g) = z_0 - \frac{\eta g v^2}{1 + \eta g d} \qquad (7.13)$$

The curve does not increase. The intersection of its value with a given level z* is found analytically when the denominator is positive. In other cases, the conditions are checked at the ends of the range g; an infinite or negative formal solution is no substitute for this test.

$$g_* = \frac{z_0 - z_*}{\eta\,[v^2 - d(z_0 - z_*)]} \qquad (7.14)$$

Each contrast gives the required interval of strength. Intersection by contrasts, scales, and probes either preserves the g range for a pair or eliminates it entirely. For 64 nodes, the code checks all 2016 unordered pairs without pre-selection. When g = 0 they all denote the same case of no addition; thousands of preserved indexes in this mode do not mean thousands of discovered relationships.

The outer shell allows for values that may require different weights for different contrasts. Therefore, the surviving pair does not yet prove the existence of one compatible vector of components. After pruning, an exact constrained fit of the full response is performed. Finding a valid point serves as evidence of compatibility, but stopping the local optimizer does not prove the absence of such a point. It is this distinction that will allow strict exclusions and useful numerical searches to be used separately.

The logic of combining scalar constraints and its limits is illustrated by figure 26.

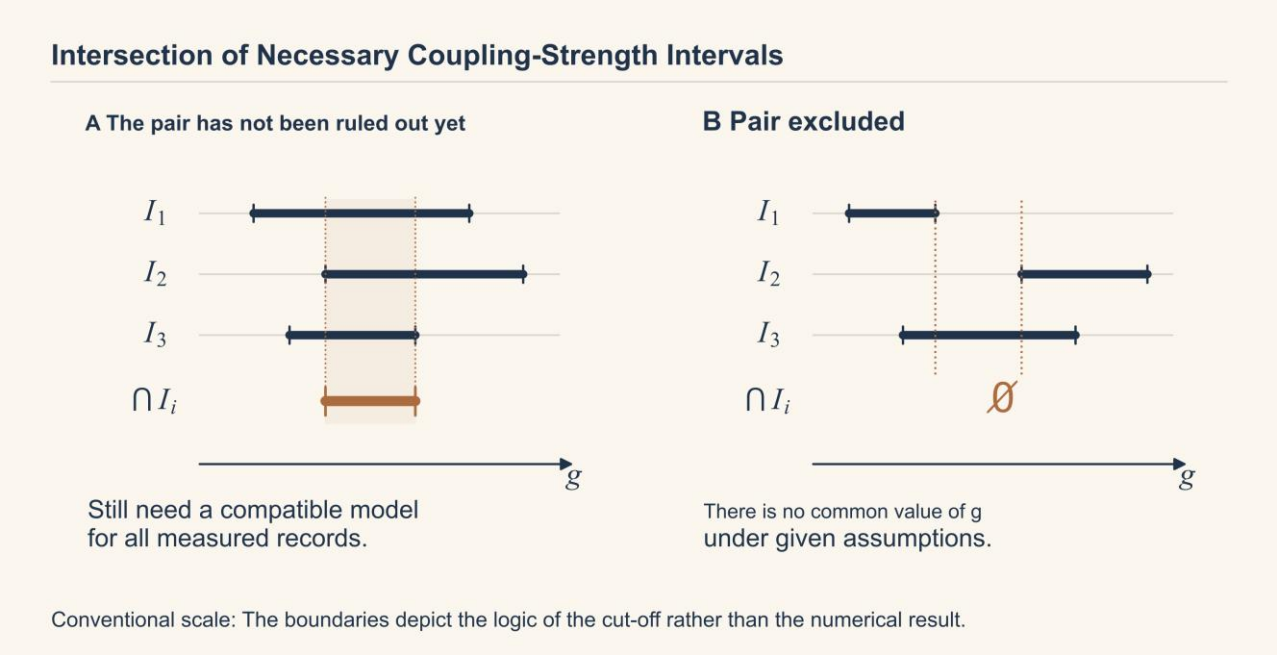


Figure 26. Necessary intervals for the strength of one putative connection. Each contrast limits g, after which the intervals intersect. A non-empty intersection preserves the candidate, but does not yet present a single vector of ordinary weights consistent with all observations. An empty intercept eliminates the pair under the initial assumptions and the chosen simultaneous error bound. The ends of the intervals here are conditional: the figure explains the logic of the outer shell and does not depict the results of a numerical search.

When the second probe repeats the first

A common edge becomes a meaningful constraint if the channels see valid alternatives differently. The simplest control is obtained by scaling the entire operator. If $L_2 = cL_1$ and the Laplace parameters are also multiplied by c, the second response repeats the first with a known factor.

$$L_2 = cL_1, \quad s_2 = cs_1, \quad G_2(cs) = \frac{1}{c}G_1(s) \qquad (7.15)$$

The independent noise of such repetition can reduce statistical uncertainty. But with zero noise, the set of structural explanations remains the same: any admissible model of the first channel corresponds to a scaled model of the second. This is a strict control that an additional data table by itself does not necessarily mean additional geometric information.

The next chapter compares the two options. One probe scales the first. The other changes the nominal translation in directions and addresses the opposite face of the cube. Then another port configuration is introduced, chosen to separate the detected alternatives. Such transitions allow you to indicate which information changed the output and which result remains conditional.

Chapter 8
A computational experiment and its robustness

Why run a small experiment?

The first test of a research idea should be simple enough that it can be replicated in its entirety. An overly complex simulation hides errors behind the number of parameters and makes it difficult to understand what exactly was recovered. Therefore, a finite cubic graph has been chosen for this book. Its structure is known, an additional link is introduced explicitly, and the algorithm receives only limited external data. The experiment allows you to check formulas, build a search procedure and see its limitations before manufacturing the device.

All numbers in this chapter are obtained by calculating given networks. The first stage tests recovery against an exact reference; the second shows how this restoration is destroyed when it fails. Calibration then becomes a full-fledged family of explanations. The reader needs the entire sequence: a successful answer, a dangerous counterexample, and a change in measurement that resolves the chosen ambiguity.

The original example, extended test series, and limited calibration protocol are stored in separate sets. They cannot be mixed: different ports, calibration boundaries and inference rules define different experiments. All recordings are synthetic; the manufacture of the stand is considered separately in the measurement workshop. The correspondence of the sets to the programs is given in the accompanying instructions.

Known lattice and unknown connection

In the system there are 64 nodes located at the integer points of the cube $4 \times 4 \times 4$. Each node is connected only to its nearest neighbors along three coordinates. In total, we get 144 ordinary edges, each with an intensity of 1 s^{-1}. The eight corners of the cube are used as ports. Their indices in the accepted numbering order are 0, 3, 12, 15, 48, 51, 60 and 63. Internal nodes are not directly measured, but their existence and initial connections are known to the algorithm.

Additionally, nodes 5 and 58 are connected with coordinates (0, 1, 1) and (3, 2, 2). The intensity of the new connection is 0.3 s^{-1}. In the previous lattice, at least five nearest edges must be passed between these points. Therefore, relative to a given graph, a connection is a short detour of previous paths. This definition refers to network geometry. In a real electrical implementation, a simple wire can connect these points without creating a new spatial dimension.

At each scale, the change in the port transfer matrix after adding a link is measured. Four positive real parameters of the Laplace transform are used: 0.1; 0.3; 1.0 and 3.0 s^{-1}. The first three are used for fitting, the last one is left to test the prediction. These numbers are not frequencies in hertz. They specify exponential weighting of the time response; a direct transition to a sinusoidal device requires replacing the real parameter with the corresponding complex expression.

Independent Gaussian noise is added to each of the 64 elements of the port matrix at each scale. In the first run, its standard deviation is 10^{-5} s. Although the true matrix is reciprocal, the noise for the i → j and j → i directions is chosen independently: independently acquired records are assumed. Therefore, a noisy matrix does not have to be exactly symmetrical. This is a special registration model, not a violation of physical network reciprocity. There is no error in the basic calibration during the first run.

In Figure 27, three different objects are visible: the known cubic frame, the selected ports, and the inserted connection. The position of the ports should be read as part of the experimental conditions. This will change in subsequent sections; this will be a new measurement protocol with the same 64 nodes.

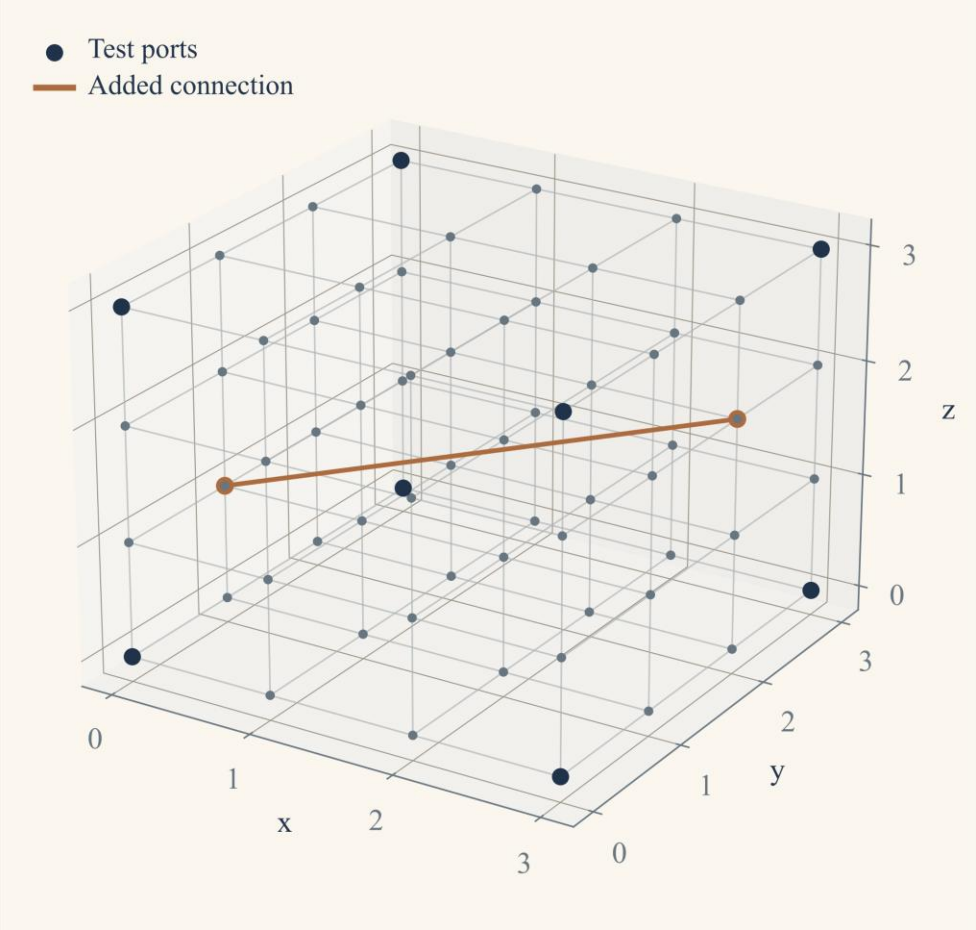


Figure 27. Initial experiment on the cube 4 × 4 × 4. Eight corner ports observe the add action between nodes 5 and 58. The numbering is based on the coordinates x, y, z, with z changing faster than the others.

How the algorithm finds the answer

The algorithm considers all 2016 unordered pairs of 64 nodes. The candidates also include existing local edges: adding a positive weight to them means the usual strengthening of the connection. For each pair, g is selected in the range from 0 to 3 s^{-1}. The prediction is calculated using the exact formula of the previous chapter, and then compared with three noisy matrices.

Therefore, 192 directed records are used. The algorithm is given the explanation class in advance: exactly one positive connection on a known set of nodes has been changed.

The initial state of the random number generator and the computing environment are recorded in the accompanying kit. The closeness of the repeated result to the last digits depends on the accuracy of the numerical procedures. Therefore, the stable numbers, the selected pair, and the behavior of the errors should be compared; machine rounding matching is not in itself a physical result.

Within the program, the direct matrix inversion is compared with the analytical correction. The relative discrepancy at the four scales lies approximately between 2.4×10^{-14} and 4.4×10^{-14}. The ratio of the second singular value of the total error-free correction to the first is also near machine accuracy. This checks the implementation of identity and rank one. Such accuracy does not apply to reconstruction from noisy data, and certainly does not characterize the possible accuracy of the future physical device.

The rank check is illustrated by the figure 28. Shown here are the first eight of the 64 singular values of the complete response change matrix. This is a different matrix than the measured port block 8×8. Almost zero subsequent numbers confirm the algebraic factorization of the error-free full response; noisy port search solves a separate inverse problem.

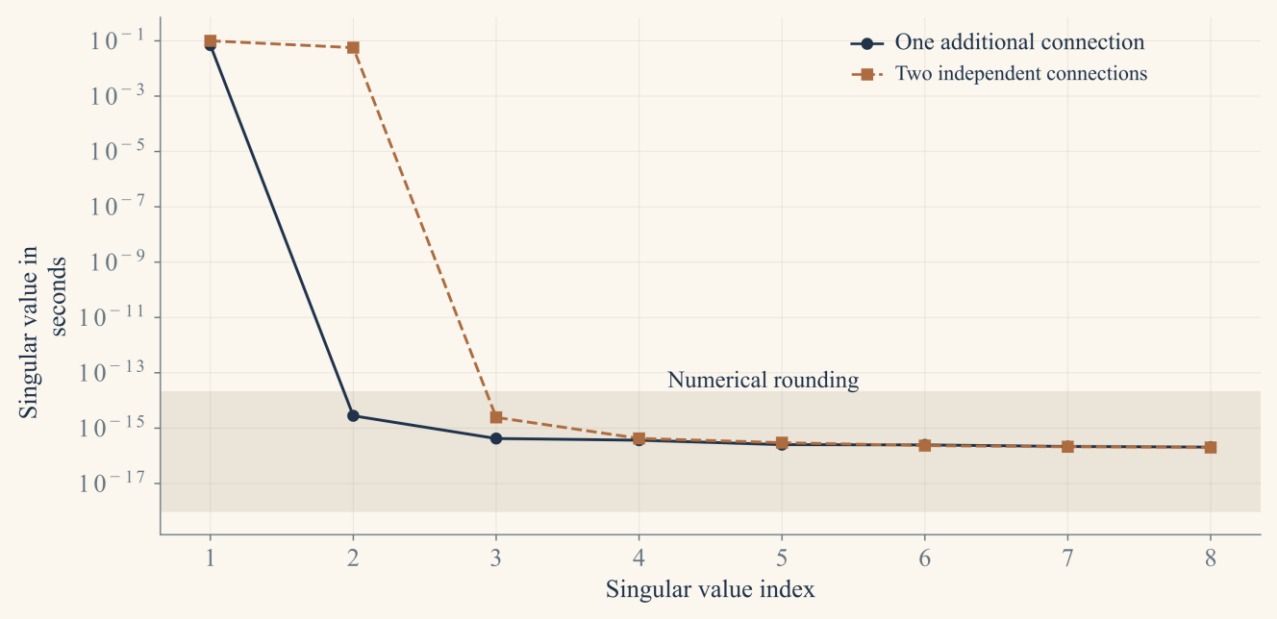


Figure 28. The first eight singular values of the total response of dimension 64×64. Rank one refers to the exact addition of one connection given a known standard. The number of values shown does not indicate the number of ports.

What the first run showed

The best candidate turned out to be the pair 5 and 58. The reconstructed intensity is equal to 0.2994421092 s^{-1}; the relative error is approximately 0.186 percent. The sum of the normalized squared residuals on the training data is equal to 163.636 for 192 records. This is consistent with a good fit to the chosen noise formulation, but the ratio of these numbers itself cannot be converted

into a universal probability of the correctness of the found pair: the choice took place among many candidates.

Magnitude	First run result
Introduced pair	5 and 58
Reconditioned pair	5 and 58
Introduced intensity	0.3000000000 s^{-1}
Restored intensity	0.2994421092 s^{-1}
Relative intensity error	0.18596 %
Pure held-out response prediction error	0.17179 %
Held-out χ^2 per entry	1.30606

The next two candidates, the pairs 5 and 42 and 21 and 58, produced training χ^2 values around 70 584 and 70 763. In this particular low-noise example, the difference between the best and the closest competitors reviewed is large. On a held-out scale of 3 s^{-1}, the relative error in predicting the error-free response was about 0.172 percent. This quantity is calculated relative to a known synthetic truth. In the present experiment there is no such truth, and only the remnants of relatively new noisy measurements are directly available.

The first run therefore shows the possibility of recovery in a carefully limited task. It does not evaluate the success rate for other node pairs, noise levels, or reference errors. It is especially beneficial that forward evaluation and reverse lookup use the same operator class. Held-out scaling tests the prediction within that class, but does not make the simulation an independent test of the physical model. The next stage specifically weakens some of the favorable conditions.

The matrix in Figure 29 shows the spatial pattern of the response. The sign of a particular off-diagonal cell is determined by the product of the profile components u. Therefore, a positive cell does not contradict the negative semi-definiteness of the entire correction. Reconstruction uses the entire consistent matrix rather than one particularly prominent element.

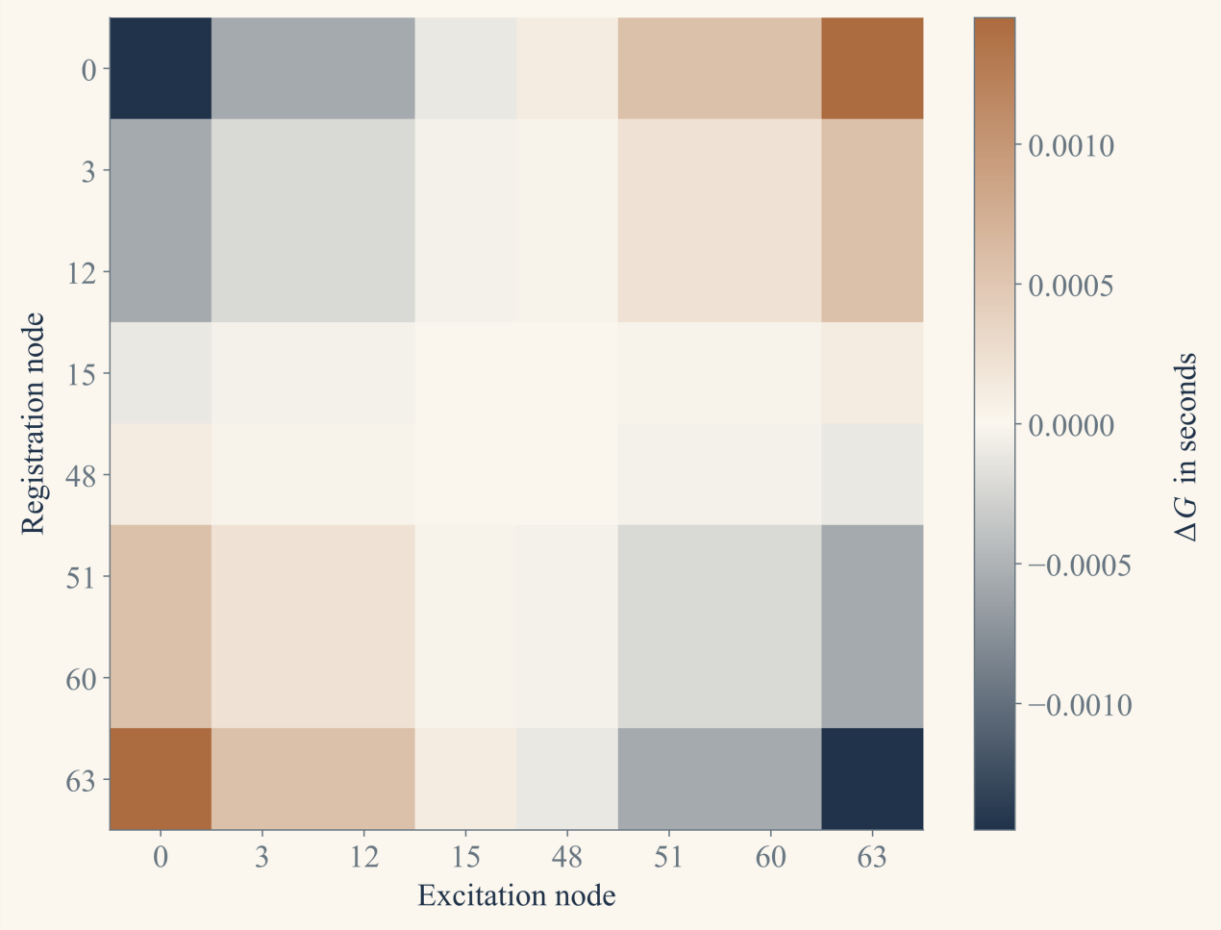


Figure 29. Port response change in the first experiment. The spatial pattern carries information about the supposed ends of the connection, which is lost by one total amplitude.

A series of checks instead of one example

The extended program runs six scenarios of twenty realizations each. In the first three, only the standard deviation of the registration noise changes: 10^{-5}, 10^{-4} and 10^{-3} s. In the next two, an error of ordinary edges unknown to the algorithm is added. Their weights are multiplied by independent positive lognormal factors with a mean equal to one. The standard deviation of the logarithm is 0.005 or 0.02, which for such small values corresponds to approximately 0.5 and 2 percent of the relative spread. The last scenario reinforces the local edge 5-6 instead of the long-distance link.

In the advanced search, all 2016 pairs are initially evaluated on a grid of 161 intensity values, including zero; then the twelve best are refined. A separate test for the three published sets restores the original order of data generation and compares the accelerated search with the refinement of each pair over the entire interval from 0 to 3 s^{-1}, including both ends. The procedure for starting the scan is given in the accompanying instructions.

Scenario	Noise σ in seconds	Faithful pairs	Median error g	Median χ^2 per entry
Accurate standard	10^{-5}	20 out of 20	0.131 %	0.973

Scenario	Noise σ in seconds	Faithful pairs	Median error g	Median χ^2 per entry
Accurate standard	10^{-4}	20 out of 20	1.306 %	0.973
Accurate standard	10^{-3}	12 out of 20	15.913 %	0.965
The spread of the standard is about 0.5%	10^{-4}	18 out of 20	10.134 %	7.290
The spread of the standard is about 2%	10^{-4}	1 out of 20	73.378 %	75.956
Local edge control	10^{-4}	19 out of 20	3.221 %	0.982

The median error in g in the table is calculated across all twenty runs of each scenario, including runs with the wrong pair. If the inferred endpoints are wrong, the estimated weight refers to a different connection; comparison with the true 0.3 s^{-1} then serves as an overall diagnostic of the algorithm, rather than the precision of estimating the same physical quantity. The proportion of correctly identified pairs also describes only a small fixed ensemble. Even 20 successes out of 20 do not establish perfect reliability: the 95 percent Wilson interval for that count runs approximately from 0.839 to 1.

Within each scenario, different random initial states are used from 12000 to 12019. This set is repeated between scenarios to make the comparison of conditions more transparent. Therefore, all 120 runs cannot be considered independent tests of the same general probability of success. In addition, the main series tests one long-distance pair, and the control tests one local pair. The resulting shares cannot be transferred to an arbitrary location of the hidden connection without a new ensemble of geometry and weights.

In all three tests, the same pair 5-58 was selected, and the difference in the found intensities is less than 10^{-7} s^{-1}. For the two records, the previously saved small discrepancies also coincided; for the first, the last signs depend on the complete numerical minimization procedure. The new file retains both values and does not pass off the reconstruction of the missing old mode as a bitwise playback. This test applies to three data sets and does not prove global optimality for any signal.

In Figure 30, you need to distinguish between the correctness of the selected pair and the amount of the remainder. With noise 10^{-3} s, the incorrect pair is still capable of describing the data with a remainder of about one. When there is a standard error, the remainder often becomes large. These different mechanisms require different control experiments.

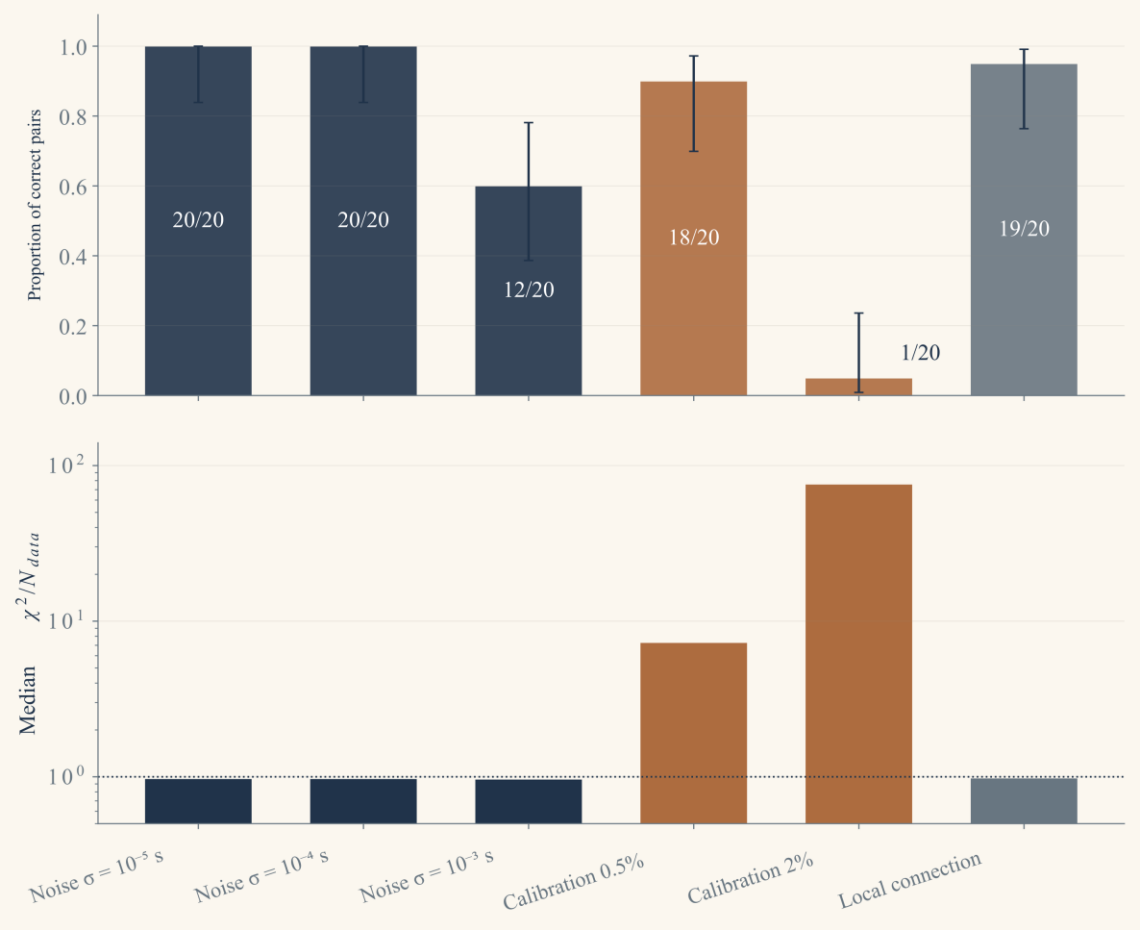


Figure 30. Extended series of tests. Recovery and residual indices refer to the individual ensembles indicated; the total number of runs is not one sample of the reliability of the method.

Why reference-model error matters more than an attractive minimum

In fine calibration, an increase in noise primarily impairs the discernibility of candidates. In the noisiest scenario, correct ends are found in twelve out of twenty cases. In this case, the median of the training χ² per record remains around one. The reason is simple: the wrong configuration sometimes reproduces a weak signal well enough against a background of large noise. An acceptable remainder is a necessary check of the model, but does not in itself establish the truth of the reconstructed internal picture.

Unaccounted variation in the reference network has a different effect. At an error of roughly half a percent, the correct pair is still found in eighteen realizations, but the median intensity error rises to ten percent and the normalized residual becomes appreciably greater than one. At two percent, the correct pair is retained in only one realization out of twenty. The algorithm continues to choose a supposedly best answer confidently, although its assumption that the original lattice is known exactly has already failed. Here, "best" is limited to an incorrect candidate set.

You need to understand exactly how this error is introduced. The actual base graph for the simulation differs from the nominal one, but it is the nominal response that is subtracted from the signal. This models an unrecognized calibration discrepancy. In a physical experiment, if the actual

baseline response under the same conditions is measured before each switch, part of the permanent deviation can be eliminated. Therefore, the percentages given are not universal component acceptance limits. They show the cost of a particular omission in the measurement model and motivate an additional calibration procedure.

The held-out check also requires careful reading. With a spread of about 0.5 percent, the median relative error in predicting net held-out change is about 99 percent, while the normalized error relative to noisy data is about 1.49 per record. These numbers do not contradict each other: a weak clean signal can be poorly reconstructed, remaining comparable to noise. It would not be sufficient to indicate only the relative error or only the normalized residual; together they show sensitivity and quality of description.

Detection threshold and local control

Additionally, one hundred zero realizations were performed without an introduced connection and with an exact standard for each of the three noise levels. In each, the entire algorithm for selecting a pair works. An improvement in χ^2 compared to the null model is recorded. The empirical 95-th percentiles are equal to 12.3293978, respectively; 12.3296483 and 12.3320514. Since the search is repeated in its entirety, the procedure takes into account the effect of candidate selection. But one hundred realizations per level provides only a demonstration threshold for this setting; An independent verification of the stated false positive rate is still needed.

In all twenty realizations of each non-zero scenario, the improvement exceeds the corresponding threshold, including the series where the correct pair is found only once. This clearly separates difference detection from cause identification. In the erroneous reference scenarios, a true complementary relationship is present, so they do not by themselves show a false interpretation of drift alone. To test this possibility, a separate control was performed, described below. Local control also reminds us that exceeding a threshold does not establish the long-range nature of the interaction.

Local control is just as meaningful. The usual gain of the edge 5-6 is determined in nineteen out of twenty realizations and gives the same structure of the analytical correction. Therefore, rank one and significant improvement in fit are not a unique signature of long-distance communication. The difference is determined by the reconstructed arrangement of the ends relative to an independently known lattice. It is the inclusion of local candidates that prevents the algorithm from calling any change non-local just because it is offered exclusively exotic options.

When a normal drift gets the wrong name

In the additional control, no new connection is introduced. Only the weights of the 144 ordinary edges change, while the algorithm continues to explain the deviation as one positive addition. Twenty realizations were run for each spread of approximately 0.5 and 2 percent, with noise of 10^{-4} s and generator initial states from 44000 to 44019. In all forty cases, the improvement exceeds the threshold calibrated on the nominal network without drift. The procedure again returns a selected pair and a positive intensity, even though the actual cause is a distributed change in known components.

Control without a new connection	Above nominal threshold	Median of the found g	Median χ^2 per entry
The spread of ordinary edges is about 0.5%	20 out of 20	0.006220 s^{-1}	5.563
The spread of ordinary edges is about 2%	20 out of 20	0.024068 s^{-1}	76.440

Here we cannot talk about false detection of any change: the system really differs from the standard. A narrower interpretation that attributes the difference to a single added connection is erroneous. Large residuals further show the incompleteness of this explanation. If one looks only at the improvement relative to zero and ignores the absolute quality of the model, normal drift easily gets a convincing but misleading name. Therefore, the criterion for future research should simultaneously require detectable difference, acceptable complete description, and superiority over realistic calibration alternatives.

The final extended check contains 460 of synthetic realizations: 120 with added or boosted coupling, 300 of nominal nulls, and 40 with only calibration error. This sum characterizes the volume of calculations performed, but does not form a single sample of equally distributed independent experiments. Different series answer different questions, and the random initial states within the compared scenarios are repeated. Statistical conclusions should be formulated separately for each formulation and its limitations should be respected.

Drift that leaves a good residual

A large remainder allows us to notice the incompleteness of the single-link model. A more difficult case arises when normal drift is described well by it. To construct it, we selected the weak nominal response of the 5-58 pair at $g = 0.03\ s^{-1}$. The constrained linear problem selects changes in 144 ordinary weights within ±2 percent that approximate this response on the three original scales. Then the exact nonlinear response of the resulting network is calculated, in which there is no additional edge at all.

Only after fixing the weights is added independent Gaussian noise with standard deviation 10^{-4} s and seed = 271828. The initial algorithm selects the pair 5-58, evaluates $g = 0.02836284\ s^{-1}$, and improves χ^2 by 85.69 at the nominal sample threshold 12.33. The training remainder is equal to 0.8884 per record, the held-out remainder is 0.7829. Enumeration of all 2016 pairs confirms this choice. This means that the error of cause persists even when considering the pairs in full.

Figure 31 compares weak addition and matched drift. Their matrices are close, although the internal reasons are different. The construction specifically uses correlated changes in weights. This is evidence of the existence of a dangerous case; it does not estimate the frequency of such a configuration in the original independent lognormal ensemble.

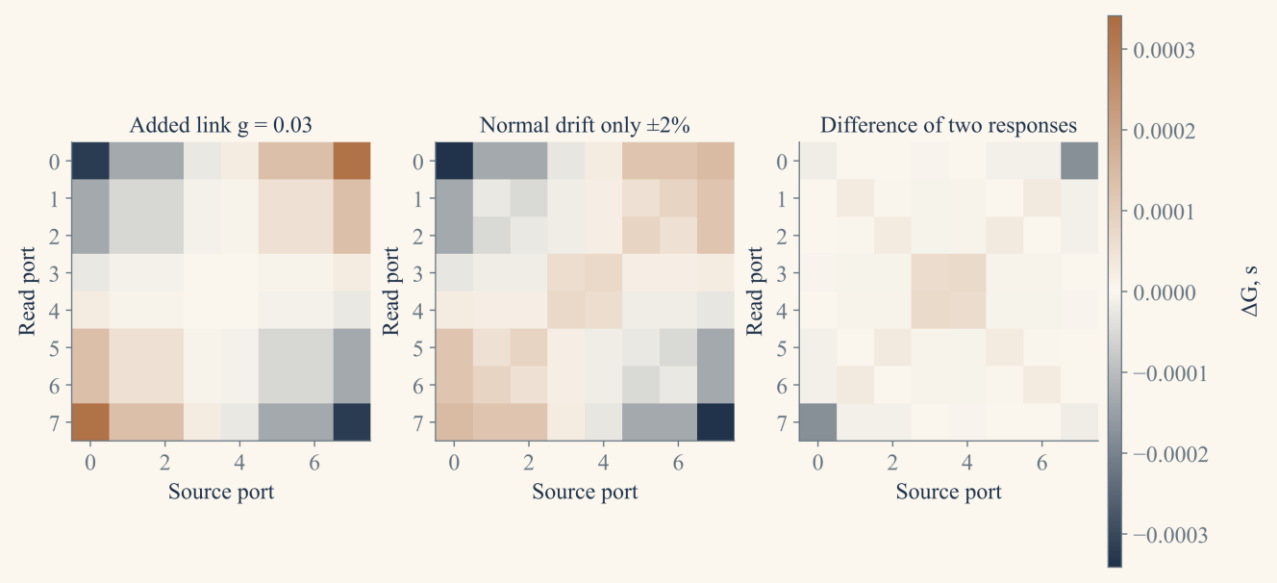


Figure 31. Weak coupling and limited drift at the original corner ports at s = 0.1 s^{-1}. All panels have the same color scale. The right one shows the small difference between the two exact responses before adding registration noise.

Model for the same data	χ^2 per entry	What can be concluded
Nominal network plus one link	0.8884	A good description does not determine the cause
Limited calibration only	0.6105	A valid point was found without additional communication
Same calibration plus communication	0.6085	Adding almost does not change the remainder

The constrained fit started the search with the nominal weights and found the calibration point with $\chi^2 = 117.21$ on the 192 entry. The number is less than the 99 percent radius of the Gaussian ball, equal to 240.50 for 192 components with known independent dispersions. All found weights satisfy the original boundaries. This is sufficient evidence that the data is capable of normal calibration.

The optimizer in this problem reached the calculation limit 160 and did not report final convergence. This is not an obstacle for the presented conclusion: the already found point has been verified by direct calculation and satisfies the restrictions. There is no statement that a global minimum has been achieved. A small additional decrease in the residual in the model with a connection is also not interpreted as its detection. The correct procedure answer here is calibration ambiguity.

A check that barely sees the signal

The initial held-out value s = 3 s^{-1} looked like a natural continuation of the first three scales. But for corner ports, it is in this mode that the additional connection is especially weakly visible. For g = 0.3 s^{-1} and noise 10^{-4} s, the ratio of the norm of the signal matrix to the standard deviation of one element is 75.33; 37.86; 6.75 and 0.388 for successive values of s = 0.1; 0.3; 1 and 3 s^{-1}.

$$\rho = \frac{\| \Delta G \|_F}{\sigma}, \qquad \mathbb{E}\left[\frac{\chi^2_{\mathrm{null}}}{64}\right] = 1 + \frac{\rho^2}{64} \tag{8.1}$$

In the latter mode, even a zero prediction of the additional signal gives an expected χ^2 per record of about 1.00235. Therefore, the successful remainder here almost does not check the restored structure. In the more accurate first experiment with noise 10^{-5} s, the situation is better: the signal-to-noise ratio increases tenfold. The remark relates to a specific mode, and not to the principle of held-out prediction itself.

For a new protocol, the parameters are selected according to the calculated sensitivity before a new series of recordings. Figure 32 compares the old corner ports to the right side of the second probe. In the new mode at s = 0.3 s^{-1} the nominal signal norm is equal to 224.88 standard deviations at $\sigma = 10^{-4}$ s. In the subsequent noisier test $\sigma = 10^{-3}$ s this value decreases tenfold and is still noticeable.

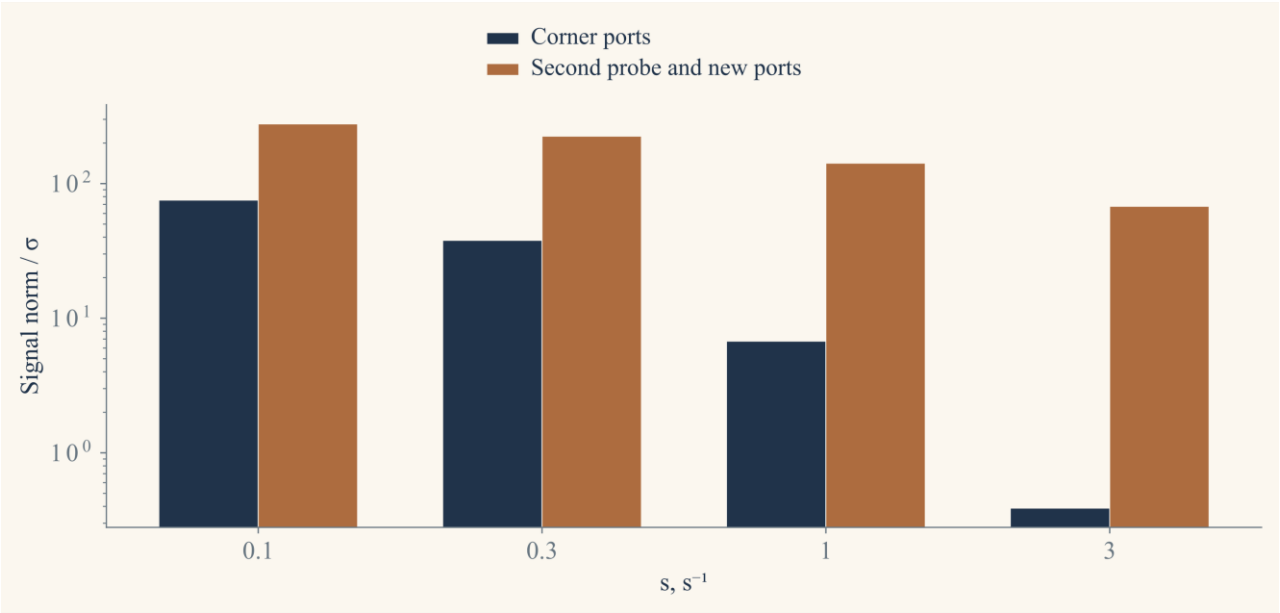


Figure 32. Nominal sensitivity at g = 0.3 s^{-1} and the same $\sigma = 10^{-4}$ s. The second configuration simultaneously changes the operator and ports; the graph shows the final gain of the selected scheme, without separating the contributions of these two changes.

One separate record of the second probe at s = 0.3 s^{-1} was obtained with seed = 930001. For this test, a limited fit of the first probe is performed with a predefined test pair 5-58. The first probe itself leaves 52 pairs in the outer region, so the conditional prediction of the selected pair is checked here, and its unambiguous recovery by one channel has not been established. This prediction gives $\chi^2/64 = 1.081$; nominal model without the added edge - 7.819. Here, held-out data are indeed capable of rejecting the null nominal response. At the same time, the transfer error of the drift estimate remains an independent issue: a zero calibration model with allowed changes in weights is checked using full shells, and not just by comparison with a stationary standard.

Two probes see different ends of the same connection

Now a new experiment is being introduced. The first probe observes nodes 0, 3, 5, 6, 9, 10, 12, 15 on the left side of the cube and has nominal weights 1 s^{-1} in all directions. The second one observes the right side through nodes 48, 51, 53, 54, 57, 58, 60, 63. Its nominal weights in the x, y, z directions are respectively 2; 0.7; 1.4 s^{-1}. The strength of the common pair in the second probe is equal to 1.6g by condition.

The three previous Laplace parameters are used, but these are different spatial data. In a generator, conventional weights have an overall relative drift of ±1 percent; the analysis resolves the entire range of ±2 percent. The true pair is equal to 5-58, g = 0.3 s^{-1}. The independent registration noise has $\sigma = 10^{-3}$ s. Each port block is preset with eight diagonal and 28 difference normalized contrasts, for a total of 108 per probe.

Set of observations	Not excluded pairs
Left side only	52
Right side only	48
The left face and its scaled double	51
Two different probes and opposite faces	1

Both probes individually rule out pure calibration, but leave dozens of possible second ends. In the joint outer region, only the pair 5-58 is stored with an interval g from 0.202 to 0.429 s^{-1}. An exact limited fit of one general vector of relative weights is also found: g = 0.30533 s^{-1}, $\chi^2/384 = 0.7669$. Therefore, in this example, the common pair constraint survived both different observing systems.

In Figure 33, the scaled double leaves 51 as a pair against 52 in the first probe. The small change is due to independent noise; in all corresponding error-free data the number is the same and equal to 44. The scaling identity is satisfied with a relative error of about 7.4×10^{-16}. A different probe with new ports reduces the outer area much more. The example shows the meaning of the new measurement information; it does not establish which part of it is associated only with anisotropy, and which part is associated only with port movement.

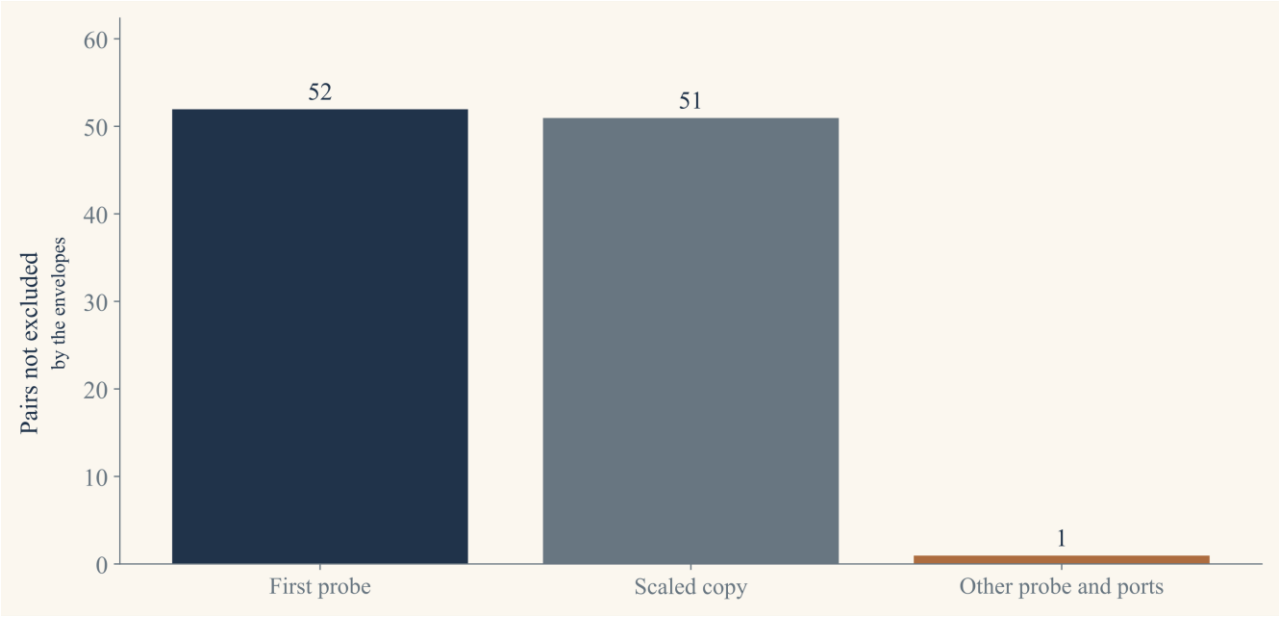


Figure 33. Number of pairs retained after conservative testing in one noisy example. The remaining pair requires further testing of the existence of a joint model and control of separate structures.

The shell of a separate diagonal contrast of the second probe is shown in figure 34. The blue band covers all valid weights for the selected pair, the orange band specifies the simultaneous observation interval. The intersections of different such strips give restrictions on g. Zero weight in the strong case is already outside the acceptable range.

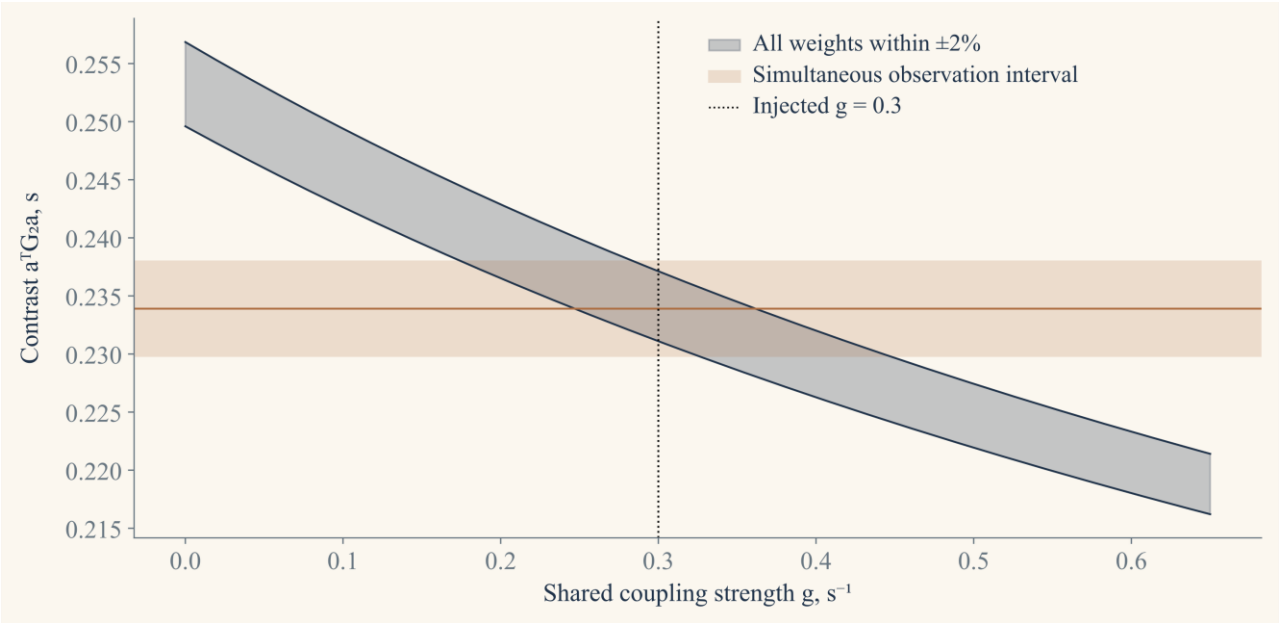


Figure 34. Contrast G_2,58,58 at s = 0.3 s^{-1}. The limits take into account any drift of the conventional scales within ±2 percent. The orange bar uses a correction for the entire predefined set of 216 scalar observations.

Dangerous agreement between two different structures

One remaining common pair still does not equal proof of a shared structure. In the following control, the first probe contains the edge 5-58, and the second probe contains the edge 6-57. The coupling strengths are related by the same known coefficient 1.6; normal drift and registration noise are preserved. From observations of the left side, the end 5 is easily distinguished, from observations of the right - the end 57. The joint search combines these local observations into the pair 5-57.

This hybrid passes more than the scalar envelopes. The full shared model with admissible drift gives $\chi^2/384 = 0.8341$ at $g = 0.2933\ s^{-1}$. The model with two actual, separate pairs is also compatible: $\chi^2/384 = 0.8096$. These records therefore do not establish that the observed agreement corresponds to one physical link. The two plausible explanations require a measurement that distinguishes them.

After studying this design example, a control circuit is designed: the ports 0, 5, 6, 15, 48, 57, 58, 63, are available in both probes. and the measurement is carried out at $s = 0.3\ s^{-1}$. These ports see both competing ends and selected neighboring areas. The circuit is fixed to a new series of noise realizations. This procedure is a test of the designed protocol; it is not presented as a pre-registered blind confirmation of the original hypothesis.

The valid edges, the false common candidate, and the new port selection are compared in Figure 35.

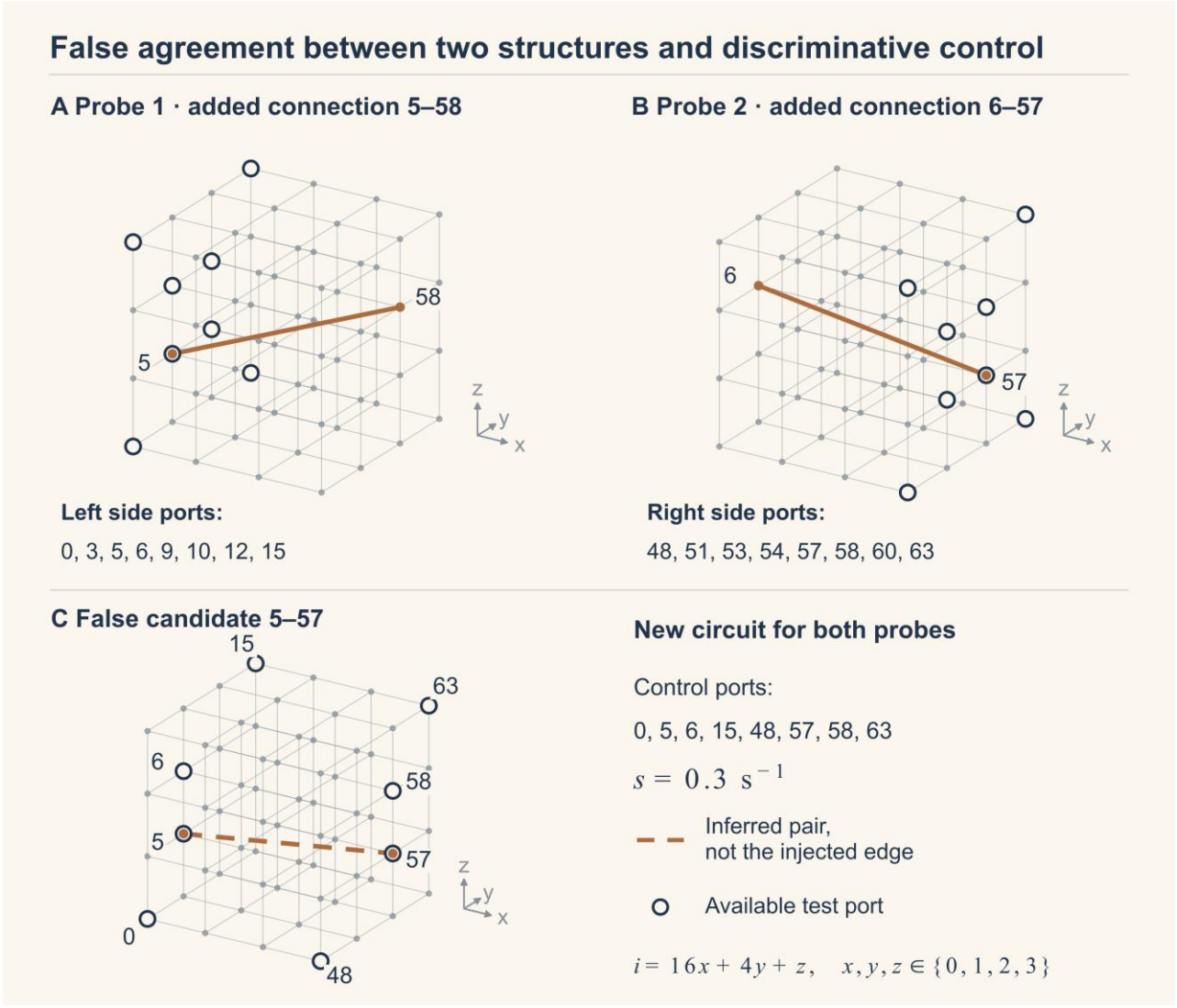


Figure 35. A constructive example of false agreement on a shared structure on the exact frame 4 × 4 × 4. The first probe contains the edge 5-58, and the second probe contains the edge 6-57. Observations of opposite faces suggest a false common pair 5-57, shown in dotted lines. The bottom diagram marks the test ports available in both probes at s = 0.3 s^{-1}. They distinguish named alternatives in the described experiment. The coordinates and numbering of nodes are the same in all three projections.

Scenario	Before control circuit	After control circuit
Common true pair 5-58	One common pair 5-58	Saved 5-58
Separate pairs 5-58 and 6-57	One false common pair 5-57	All common pairs are excluded

For a real common pair, the resulting outer interval g is from 0.2348 to 0.3638 s^{-1}. Fitting all 512 directed entries gives g = 0.30021 s^{-1} and $\chi^2/512 = 0.8075$. In separate control, the elimination of a common edge is obtained by the envelopes for all 2016 pairs at once, rather than from an optimizer

failure. The split model has a feasible point with $\chi^2/512 = 0.8222$. In this limited example, the new experiment did exactly the job it was designed to do.

The result does not imply universal uniqueness for all possible additional connections, capacitances and hidden nodes. It shows a narrower completed transition: a specific ambiguity is detected, a measurement mode is selected, its prediction is derived, and the discrimination of the named alternatives is tested. For other ambiguity classes, the circuit must be designed anew.

Common electronic signal and independent control

The agreement of the two channels can also occur after the physical object, inside the electronics. For verification, the same matrix template was added to both records, specifically matching the response of the edge in the first probe. In nodal models there is no additional connection. This choice creates difficult artificial control of the overall recording path; it does not describe the frequency of occurrence of this particular pattern in a real instrument.

Before additional checks, the outer joint region again leaves one false pair, now 5-53. In a separate reference record, physical propagation is disabled and the suspected electronic leakage path is preserved. This notation gives $\chi^2 = 1919.59$ per 192 element at the 99 percentage bound 240.50 for pure known Gaussian noise. This means that the general signal is available in a channel that should not contain the network dynamics being tested.

The separation of the physical path and the persistent registration path is shown in the functional diagram 36.

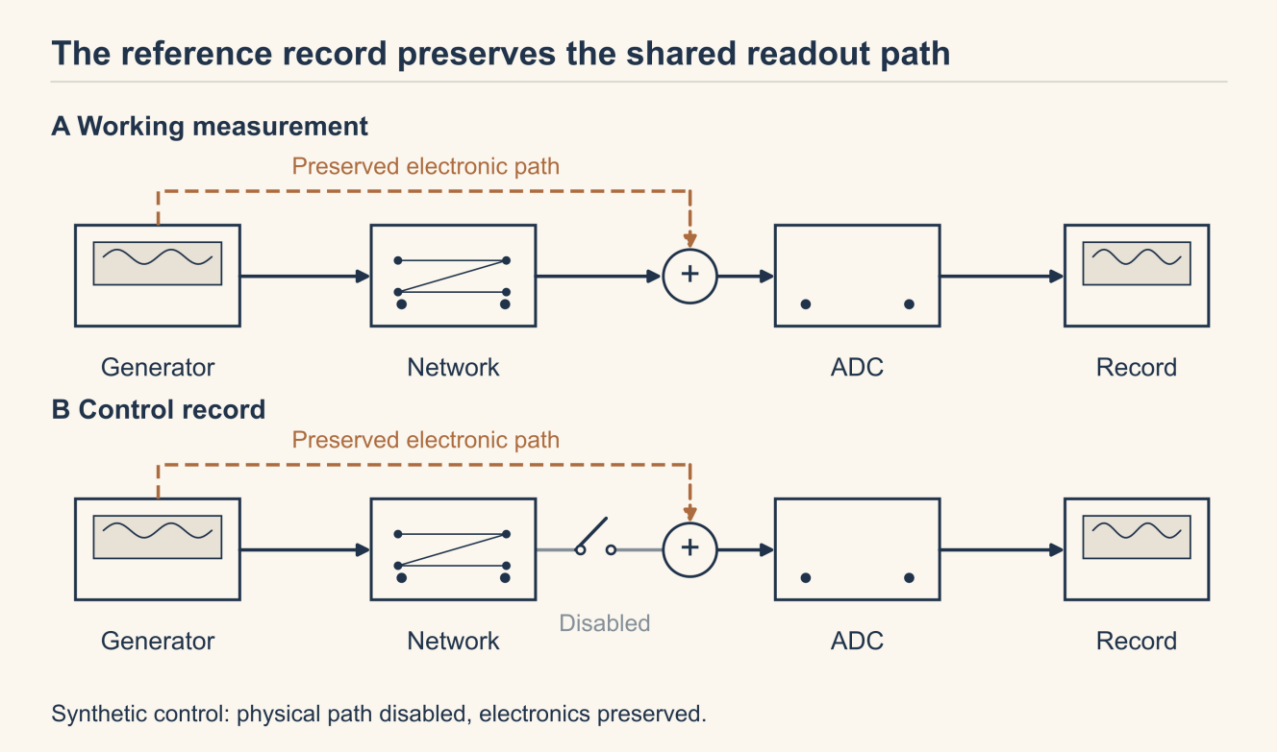


Figure 36. The functional meaning of the reference record in synthetic control. The operational measurement contains the network response and the addition of the common electronic path. In the control condition, the physical path is disabled and the putative electronic path is preserved. The signal remaining in such a recording allows one to test the usual cause of false agreement on a shared structure. The image does not indicate the assembled circuit diagram; the specific test bench must separately confirm that the switching actually preserves the leakage path under study.

Once the reference record is subtracted, a clean calibration is no longer ruled out. The cost of such subtraction is additional noise. Given the same accuracy of two independently acquired records, the standard deviation of the difference is $\sqrt{2}\sigma$. If the same reference entry is subtracted from both probes, their residuals are correlated. The scalar test used remains valid with correct marginal variances because its simultaneous bound does not require independence of contrasts. To fully fit these subtracted data, a joint covariance would be needed.

Control ports also rule out all common single-link explanations for this pattern. The reference record adds another piece of knowledge: it points to the specific section of the measurement circuit where the signal is stored. Such an intervention is much stronger than statistical disagreement alone because it helps to identify the usual cause of the deviation.

New series after protocol selection

After fixing the control circuit, four series of 24 realizations were completed. Each independently generates a general relative drift of conventional weights, uniform within ±2 percent, and fresh Gaussian noise. The initial states start from 3600000, 3601000, 3602000 and 3603000, respectively.

In all cases, the forces, pairs, port map and exclusion criteria are specified by the program. This series is separate from the previous 460 calculations.

Scenario	No pure calibration	After control there is no common pair
Limited drift only	0 out of 24	0 out of 24
Shared pair	24 out of 24	0 out of 24
Different pairs	24 out of 24	24 out of 24
Common electronic crosstalk	24 out of 24	24 out of 24

In 24 realizations of this shared pair, its index is preserved in the outer region. With only acceptable drift, pure calibration was not excluded. Separate connections and copied electronic crosstalk after the control circuit did not have a single valid pair in common. Figure 37 shows these counters together: excluding calibration and eliminating the common edge are different solutions.

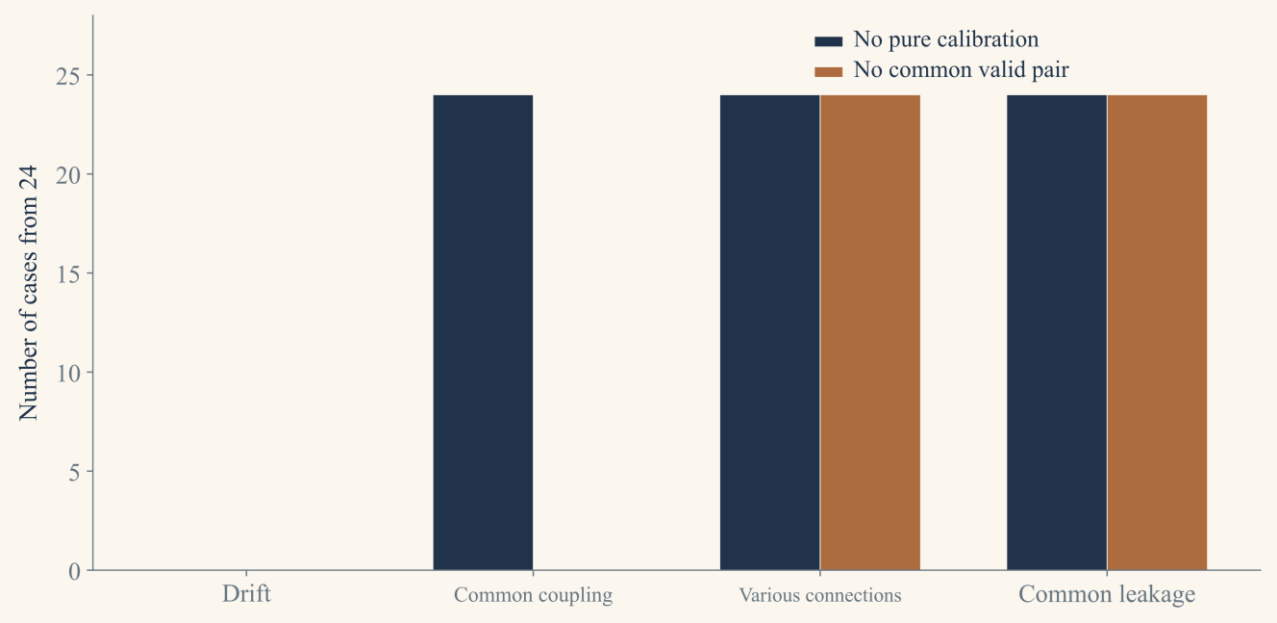


Figure 37. Results 96 of new synthetic realizations after fixing the control mode. The counters describe the four specified classes and these 24 records of each class; they are not universal instrument error probabilities.

A zero rate of false exclusion in the 24 experiments does not prove zero risk. The formal bound for shells is derived in Chapter 14 from assumptions about noise and calibration, rather than being estimated by these small counters. The series checks the code and the selected script. Random selection of all possible pairs, unknown nodes, delays, leaks, and error in the calibration limits themselves remain other challenges.

The relationship between the forward and inverse models is still close: both use a given class of linear network. This relief must be taken into account. In the inverse problem literature, discretization errors and overfitting of models are considered as a source of optimistic reconstructions. Therefore, a physics workshop must add real recordings, parasitic elements, and independent calibration measurements. [21]

Chapter 9
From a network analogue to a causal physical model

Limit of applicability of the equation

A computational network is useful precisely because its design can be controlled. However, this convenient model has its limits. The equation $\dot{x} = -Lx$ describes the equalization of magnitude between nodes, rather than the complete electromagnetic process within the wires. It does not record distributed fields, propagation along lines and movement of energy between individual points of the conductor. As long as the times of interest are much larger than these internal times, a shorthand description may be good. When examining the extreme speed of a signal, missed details become central.

The matrix e^{-tL} on a connected finite graph usually has non-zero elements between remote nodes for any $t > 0$. To see the reason, it is enough to expand the exponential in a series. For a pair separated by r edges of the shortest path, the first non-zero contribution occurs with some power t of order r. It is extremely small for a short time, but does not have to be strictly zero. Therefore, an ideal diffusion model does not contain an exact light cone. Discovering this feature in the formula means finding the limit of approximation, and not discovering the possibility of superluminal transmission.

In the electrical bench, causality provides a more complete description of conductors and fields. The lumped RC model is used after eliminating fast processes. A long wire, which is depicted as a single line in the graph, physically has a length and propagation time. For slow decay studies this may not be significant; for searching for an unusually early arrival of an impulse - decisive. Therefore, a connectivity tomography instrument and a causal structure instrument must have different error models and different calibration requirements.

The difference between the diffusion tail and the causal front is illustrated by figure 38.

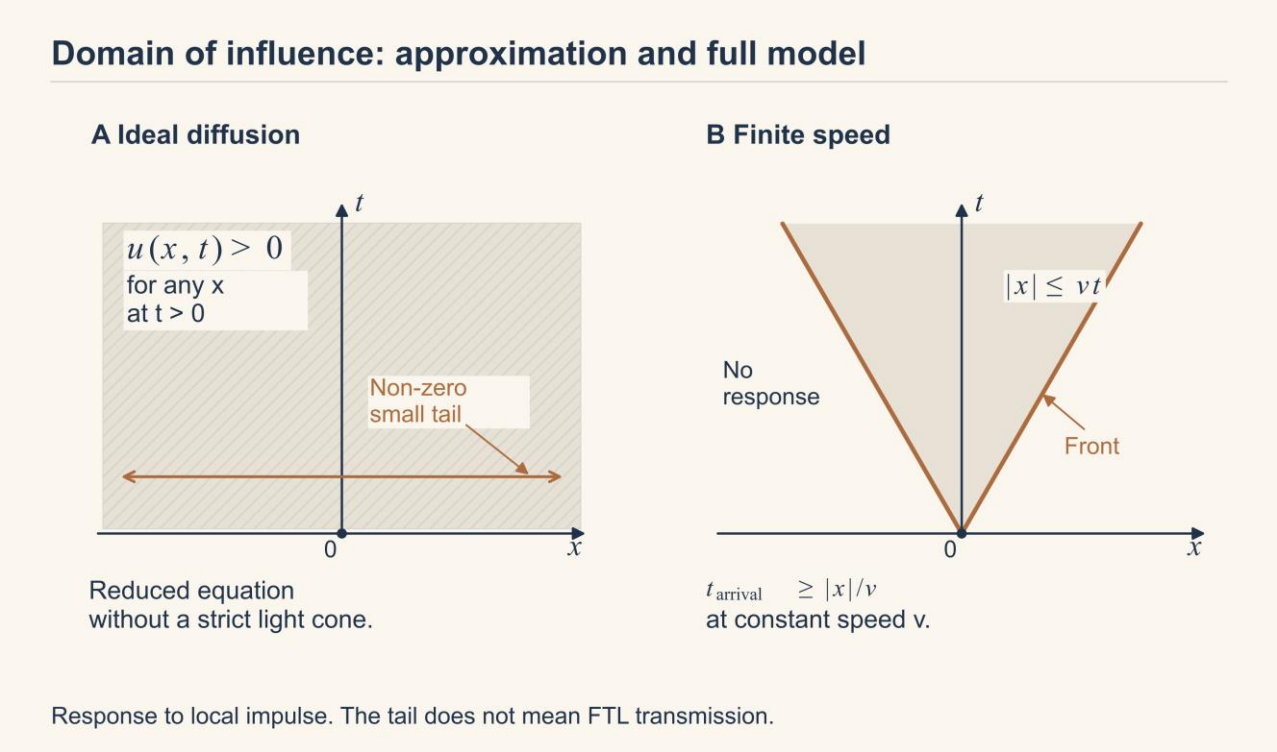


Figure 38. Regions of support for local impulse response in the ideal diffusion description and in the full finite velocity model. On the left, a small mathematical tail appears for any positive time; on the right, the influence is limited to the causal front. The figure is schematic, the axes are not to a numerical scale, and a constant velocity v is chosen to illustrate the boundary. The diffusion tail indicates the limit of the reduced equation and is not evidence of physical superluminal transmission.

Delay must be derived from the apparatus

A natural attempt to improve the model is to add delays. In the frequency or Laplace description, the pure delay is given by the factor exp(−sτ). But arbitrarily replacing the positive weight g with g exp(−sτ) does not guarantee that the resulting equation describes a passive physical connection. Not only useful signals are delayed: feedback, stored energy and stability conditions change. A real transmission line relates input and output quantities by a consistent set of equations, rather than by one decorated coefficient.

This can be seen in the scalar example. Without delay, the equation $\dot{x} = -\gamma x$ for $\gamma > 0$ describes the attenuation. If we replace x(t) on the right side with x(t − τ), the characteristic equation becomes $s + \gamma \exp(-s\tau) = 0$. Substituting the purely imaginary root $s = i\omega$ shows the first stability boundary at $\gamma\tau = \pi/2$. Thus, a sufficiently large delay turns the initially damped rule into an oscillatory instability. The presence of a positive γ no longer provides the same conclusion.

$$\dot{x}(t) = -\gamma x(t-\tau), \qquad s + \gamma e^{-s\tau} = 0, \qquad \gamma\tau = \frac{\pi}{2} \qquad (9.1)$$

This example does not prohibit delayed models. It shows that they need to be checked again. For a laboratory analogue, a physically understandable element is preferred: a transmission line, a

known resonator, or a measured internal circuit. Then the delay, dispersion and loss are determined jointly. Measurements at multiple frequencies make it possible to determine when simple constant coupling is no longer a suitable approximation. It is at this boundary that hidden degrees of freedom can become visible, but their detection first requires conventional engineering explanation.

The memory of an ordinary hidden mediator

It is possible to explicitly construct an element that creates memory after eliminating the internal variable. Let two accessible voltage nodes V_1 and V_2 be connected through a hidden node h by two identical conductances k. A capacitance C_h is installed in the hidden node relative to the common reference conductor. With zero initial charge, the latent voltage equation has the form

$$C_h \dot{V}_h + 2kV_h = k(V_1 + V_2) \qquad (9.2)$$

In the Laplace transform, hence $V_h = k(V_1 + V_2)/(sC_h + 2k)$. Substitution into the current $I_1 = k(V_1 - V_h)$ shows that the coefficient of mutual influence of the ends depends on s. An off-diagonal element −keff(s) appears in the conductance matrix, and the diagonal elements also change. To leave only a new line between the ends and forget these changes would mean losing part of the dynamics of the mediator.

$$k_{\text{eff}}(s) = \frac{k^2}{sC_h + 2k}, \qquad k_{\text{eff}}(0) = \frac{k}{2} \qquad (9.3)$$

In statics, the familiar sum of two identical resistances is obtained. In the time domain, the mutual contribution contains a decaying memory. Its characteristic time $C_h/(2k)$ is determined by capacitance and conductances, and not by the geometric length between the ends.

$$K_{12}(t) = \frac{k^2}{C_h} \exp\left(-\frac{2k}{C_h} t\right) \Theta(t) \qquad (9.4)$$

This kernel describes the magnitude of the positive coefficient of mutual influence; the sign in the current equation is determined by the selected direction of the current. The dimension keff is siemens, the dimension $K_{12}(t)$ is siemens per second. The presence of Θ(t) makes memory delayed in time. It does not create a precise spatial cone of light within the lumped model.

The example links Kron reduction to a measurable trait. Two statically equivalent devices differ in the transient process if the recording band includes the time $C_h/(2k)$. If this scale is outside the band, the memory is hidden in the effective constants. Therefore, the detected frequency dependent channel should first be compared with conventional energy storage and transmission lines. It is a concrete physical bridge from network contraction to observable dynamics.

The diagram of the hidden capacitance and the memory kernel that appears after its exclusion are shown in Figure 39.

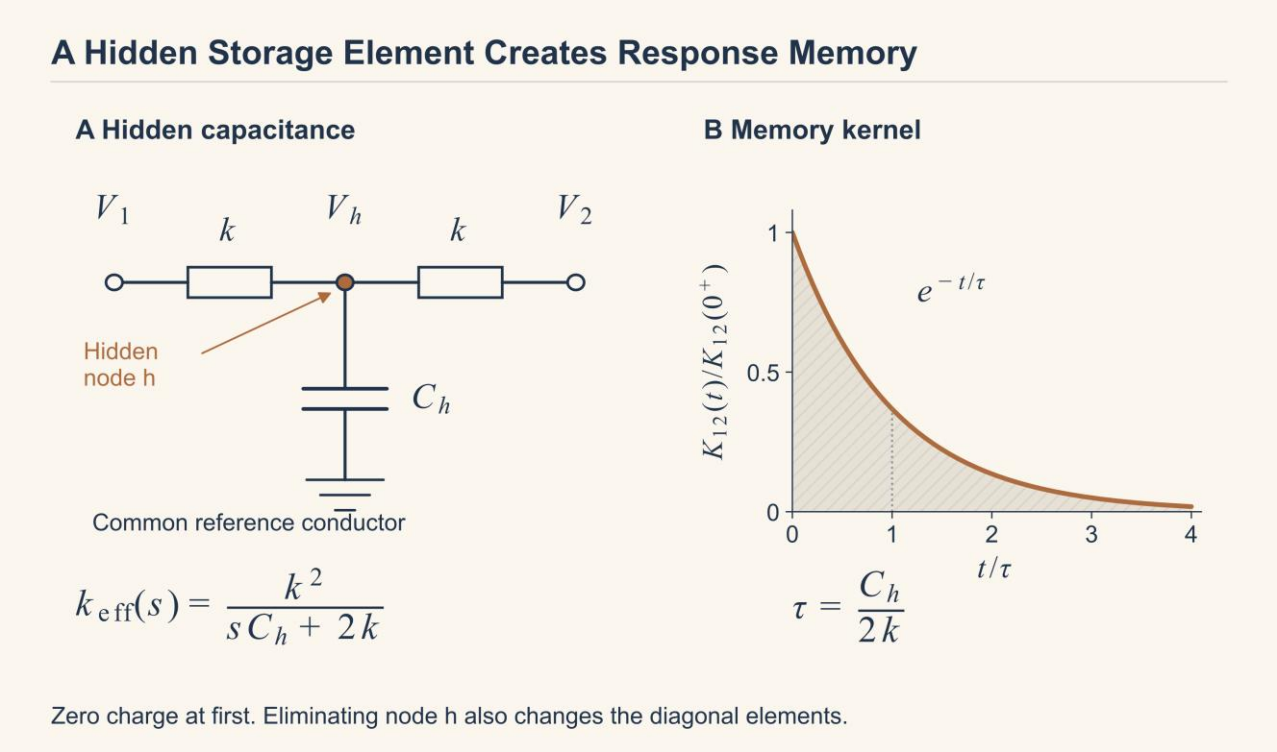


Figure 39. A common hidden intermediary with memory. Two identical conductances k connect the accessible nodes through node h with capacitance C_h relative to a common conductor. With zero initial charge, the elimination of V_h creates a frequency-dependent cross-coefficient and changes the diagonal elements. The exact normalized exponential kernel for $t \geq 0$ with time $\tau = C_h/(2k)$ is shown on the right, rather than the experimental curve. The time delay does not define the spatial light cone.

Passivity as a testable constraint

For an RC network, the energy check is particularly transparent. Let C be the positive diagonal capacitance matrix, K the symmetric admittance matrix, and V the voltage vector. The electrical energy in the capacitors is equal to half the quadratic form $V^{\mathsf{T}}CV$. The equation $C\dot{V} + KV = I$ allows you to calculate its derivative. The result is the difference between the supplied power and the power dissipated by the resistors. From the positivity of the weights, it follows that the network does not release more energy than it received and stored previously.

$$E = \frac{1}{2} V^{\mathsf{T}} C V, \qquad \frac{dE}{dt} = V^{\mathsf{T}} I - V^{\mathsf{T}} K V \leq V^{\mathsf{T}} I \qquad (9.5)$$

This inequality is a special case of the general theory of dissipative systems, where stored energy and external flow are compared. Willems formulated the corresponding approach through the functions of storage and supply. For our stand, it is useful to be able to check passivity both before assembly and according to the device data. An unexpected increase in energy in a model may indicate a sign error, incorrect variable exclusion, or a missed power source. [22]

Passivity does not equal complete physical correctness. A passive electrical circuit remains a material object with a distinct state of rest; it cannot be declared a vacuum model just because it is stable. However, the energy check cuts off some of the erroneous constructions even before discussing the fundamental interpretation. It also helps to distinguish real amplification due to external energy from changes in geometric sensitivity. In a research instrument, these reasons can create a similar increase in amplitude, although their physical meaning is different.

Causal response and observable value

A more general linear model describes the signal as the convolution of a source with a retarded kernel. The time of recording must follow the time of exposure within the accepted causal structure. In a locally flat space with the usual limiting speed c, the impact kernel between the separation points r vanishes before r/c. In curved geometry, the condition is formulated in terms of the corresponding light cone. If a different causal pathway is hypothesized, its geometry must be determined and reconciled with clock and distance measurements.

$$y_i(t) = \sum_j \int_{-\infty}^{t} H_{ij}(t - t') f_j(t')\, dt' \qquad (9.6)$$

What is important is the dependence of the controlled response on the source. A correlation between two sensors recorded without such intervention does not prove the transfer of information between them. It can be created by a common source, a common environment, or a prepared shared state. Claiming a new channel requires showing that a change in a known effect predictably changes the distal outcome, and establishing a time limit for that change. Mixing correlation search and signal velocity measurement would mean answering different questions with the same statistics.

Even given a field, the new theory must produce a specific observable quantity. The metric component at the selected coordinates is not a ready-made photodetector reading. It is necessary to calculate the path of light, the movement of reflectors, the clock rate and the phase comparison procedure. Some disturbances affect both branches of the differential device equally and cancel each other. Therefore, the assumed property of space may be real in the model, but invisible in this particular configuration. The sensitivity is set by the calculation of the measurement procedure, and not by the name of the field.

Positivity of correlations and covariance of the law

If the hypothesis describes a random common signal, it must specify the acceptable covariance of all channels. For any linear combination of records, the spectral power is non-negative. This implies the positive semi-definiteness of the spectral matrix S(f). In particular, the square of the modulus of the mutual spectrum of two channels is limited by the product of their own spectra. An arbitrary beautiful pattern of angular correlations can violate this condition and generally not correspond to any random process. This check is carried out before comparison with the data.

$$z^{\dagger} S(f) z \geq 0, \qquad \left|S_{ij}(f)\right|^2 \leq S_{ii}(f) S_{jj}(f) \qquad (9.7)$$

The term "covariance" in space theory refers to another issue: how the law is written when coordinates change. A coordinately consistent record is necessary for geometric interpretation, but in itself does not prove the absence of a distinguished reference system. The grid is capable of setting specific directions and times; hiding them behind tensor notation is not enough. If Lorentz symmetry is expected to be restored on large scales, the residual deviations must be calculated, the region of approximation indicated, and compared with the corresponding experimental constraints.

Causality, analytical properties of amplitudes, and admissible coefficients of the effective theory are also related. The work of Adams et al shows, using certain classes of effective field models, that the apparent acceptability of a low-energy Lagrangian does not guarantee a consistent high-energy continuation. This is not a universal ban on unusual geometry. This is the basis for checking the signs, the stability of the background and the premises of the theorems used when trying to turn a network rule into a physical law. [23]

What is required to move to vacuum

A complete interpretation must first name its degrees of freedom. Are nodes events, regions of space, states of a field, or just elements of a computational grid? Then the law of their evolution and interaction with matter is required. For a quantum model, the state space, probabilistic interpretation and dynamics are additionally specified, preserving the necessary properties of the state. For an effective open system, dissipation is acceptable, but the source of losses and the limit of applicability of the abbreviated description must be clear.

The tested regimes must then be recovered. If a model introduces additional coupling between distant regions, it must show why ordinary optical, mechanical, and gravitational measurements usually miss it. The explanation may involve a weak interaction, a limited sensitivity band, or a particular coupling to matter. These must be quantitative properties rather than explanations revised after every negative experiment. The model must imply a parameter range in which it can be falsified.

Analog experiments remain useful at all these stages. Electrical networks have already been used to reproduce the properties of hyperbolic geometry and test propagation in the corresponding effective metric. Such a device demonstrates a controlled implementation of a mathematical operator, rather than turning the laboratory space into a fundamentally hyperbolic one. By the same logic, the graph stand under consideration can test methods for restoring hidden connectivity without automatically claiming to measure the structure of the vacuum. [24]

The transition from graph to physics requires sequential correspondences: a model variable is a physical quantity, a coefficient is a measured interaction, a mathematical perturbation is a reproducible procedure, a predicted response is an instrument reading. Until any correspondence is established, the result refers to the mathematical or analog level. It is already possible to make meaningful theorems and instrumental solutions. The fundamental interpretation requires separate verification.

Subsequent chapters consider other realizations of the same research order. For a compact direction, it is necessary to calculate the excitation and registration of modes of the selected field.

For a random potential, the joint response of clocks and accelerations. For an interferometer - light path and phase. These branches have their own physical prerequisites; the general method of comparing predictions does not infer one from the other.

Chapter 10
Hidden Geometry Spectroscopy

What can you learn from the law of force?

After the network experiment, a new question arises: what measurement could link the unusual response to a physical additional direction? One specific implementation has been chosen for this chapter: a scalar field propagates along the usual three coordinates and along a circle. The force between bodies and the dynamic response of the same field are considered. This is an independent physical model; the edge established in the network analogue is not transferred to it as an already discovered property of the space.

Let us imagine an experimenter who does not know the number of spatial directions. The experimenter has access to small masses, a distance meter and a gravity sensor. The experimenter moves the source and records how the force weakens. In ordinary three-dimensional space, the Newtonian force of point masses decreases inversely to the square of the distance. If the flow of a certain field diverges uniformly across a space of a different dimension, the area of the surface surrounding the source changes differently. It seems enough to measure the exponent and get the number of dimensions. However, such reasoning hides the conditions: the field must obey the chosen equation, the source must be practically point-like, and the propagation of the interaction must not change for any other reason. The experiment jointly tests geometry and the physical law that transforms geometry into force.

$$F(r) \propto r^{-(d-1)}, \qquad d_F(r) = 1 - \frac{d\ln|F(r)|}{d\ln r} \qquad (10.1)$$

The value d_F denotes the operational dimension restored by force. This is a convenient language for describing measurement, but not an independent definition of the structure of the world. With a power law, it coincides with d if the above assumptions are met. When moving between modes, it becomes a function of distance. A non-integer result in itself, for example 3.2, does not yet mean a fractional number of physical directions. It can be generated by several simultaneously acting interactions, the finite size of the source, the heterogeneity of the material and the distance error. The research challenge is to determine which of these explanations are discernible given the available data, not to choose the most unusual name for the resulting curve.

A physically meaningful hypothesis of an additional dimension should connect several consequences. The same latent direction device determines the permissible spatial modes, their energies and their contribution to the static interaction. If each measured effect is allowed to have its own free scale, the hypothesis will no longer be testable. Therefore, what follows is a compactness spectroscopy program: recovering a consistent family of scales from different observations. The very idea of compact extra dimensions and their manifestations in gravity has long existed. In the Arkani-Hamed, Dimopoulos and Dvali model, gravitational and standard fields are given different

access to complementary directions; It is this difference that shows why the gravitational prediction cannot be automatically transferred to light or matter. [26]

One new intermediary can change the apparent dimension

Let's start with a counterexample that is more useful than the premature promise of discovery. Let space remain three-dimensional, but in addition to Newtonian attraction, interaction with a finite range arises. Its standard parameterization is called the Yukawa correction. The dimensionless coefficient α specifies the relative force, and λ, measured in meters, determines the range. In this chapter, the sign α is allowed in both forms; expressions for the logarithmic derivative are used only where the total force does not vanish. The formula is a testable effective description, and the origin of the new interaction requires a separate theory. Even such a simple example shows how risky it is to identify an unusual exponent with a changed dimension.

$$V(r) = -\frac{GmM}{r}\left(1 + \alpha e^{-r/\lambda}\right), \qquad x = \frac{r}{\lambda} \qquad (10.2)$$

For B(x) > 0 the interaction remains attractive; It is convenient to work with a positive radial force modulus. Differentiation of the potential gives two contributions: the derivative of the factor 1/r and the derivative of the exponential. The second part is fundamental: if you simply multiply the Newtonian force by the potential correction, the prediction will be incorrect. Let us denote the square bracket in force by B(x). Then the logarithmic derivative contains the usual term −2 and the addition xB′/B. The derivative of B′ is equal to $-\alpha x e^{-x}$. After substitution, we obtain an expression for d_F, in which, for positive α, an addition to three occurs. All factors in this addition are dimensionless, so the formula passes a simple but mandatory unit check.

$$|F(r)| = \frac{GmM}{r^2}|B(x)|, \qquad B(x) = 1 + \alpha(1+x)e^{-x}, \qquad B'(x) = -\alpha x e^{-x} \qquad (10.3)$$

$$d_F(r) = 3 + \frac{\alpha x^2 e^{-x}}{1 + \alpha(1+x)e^{-x}} \qquad (10.4)$$

For small x, the correction is almost constant and mainly changes the effective interaction force. For large x it disappears exponentially. Between these limits there appears an area that can be mistakenly called increased spatial dimension. This conclusion is obtained by ordinary differentiation, and not by experimental discovery. It sets a useful requirement for the future device: it is necessary to measure a sufficiently wide range of distances and check the shape of the transition. On a narrow interval, different functions easily look the same. Even an error-free registration of d_F greater than three will initially only allow us to state that the original force model is insufficient. The next question will concern the physical origin of the detected amendment.

In sections with B < 0, the same logarithmic derivative is calculated via ln|B|. At point B = 0 the d_F indicator is not defined. In these cases, the sign of the force must be shown separately: one graph of its magnitude hides the transition between attraction and repulsion.

A compact direction and a tower of modes

Now consider an explicitly specified model. In addition to the three extended coordinates, there is a periodic coordinate y with period 2πR. A massless scalar field propagates along it; the sources are located at the same y value. Periodicity allows wave numbers n/R, where n is an integer. An observer who has access only to ordinary space describes non-zero modes as massive excitations. This is a training scalar model on the space $R^3 \times S^1$. It allows one to derive the connection between the spectrum and the static potential, but does not replace the tensor theory of gravity: spins, additional fields, a mechanism for fixing the radius and real connections with matter are not yet specified here.

$$q_n = \frac{n}{R}, \qquad m_n = \frac{|n|\hbar}{cR}, \qquad E_n = m_n c^2 = \frac{|n|\hbar c}{R}, \qquad \lambda_n = \frac{R}{|n|} \tag{10.5}$$

If we normalize the zero mode so that the long-range interaction has the usual form, the pair of modes with numbers n and −n gives equal contributions. The sum of the exponents turns into a hyperbolic cotangent. At distances significantly greater than R, the potential 1/r remains. At distances significantly less than R, the field has time to propagate along the additional direction, and the potential becomes proportional to $1/r^2$. Its strength decreases as $1/r^3$. This behavior is derived from the adopted geometry and field propagation rules. The coefficient 2 in front of the sum refers specifically to the selected scalar model; it cannot be transferred without verification to a realistic gravitational hypothesis.

$$V_{\mathrm{sc}}(r) = -\frac{GmM}{r}\left[1 + 2\sum_{n=1}^{\infty} e^{-nr/R}\right] = -\frac{GmM}{r}\coth\left(\frac{r}{2R}\right) \tag{10.6}$$

$$V_{\mathrm{sc}}(r) \simeq -\frac{GmM}{r} \quad (r \gg R), \qquad V_{\mathrm{sc}}(r) \simeq -\frac{2GmMR}{r^2} \quad (r \ll R) \tag{10.7}$$

To illustrate the units, let's take R equal to 10 micrometers. The energy of the first mode is then approximately 0.0197 electronvolts, and the frequency E_1/h is 4.77 terahertz. This is an arithmetic consequence of the chosen radius, not a prediction of detection, and not a statement that a given option is allowed by the combined existing observations. Frequency alone does not determine the possibility of excitation. We need a coupling operator, its coefficient, selection rules, source intensity and reading method. An electromagnetic generator at a specified frequency may not interact with the desired mode at all. The practical meaning of the example is different: one radius simultaneously specifies the range of static force and the energy scale that a complete theory must take into account.

Two different ways to obtain scale structure are compared in Figure 40. On the left, one ordinary mediator creates a deviation of the strength indicator from three. The associated compact mode ranges are shown on the right. The right sequence sets a more stringent hypothesis, but it can only be tested if the measurement is sensitive to at least several of its terms.

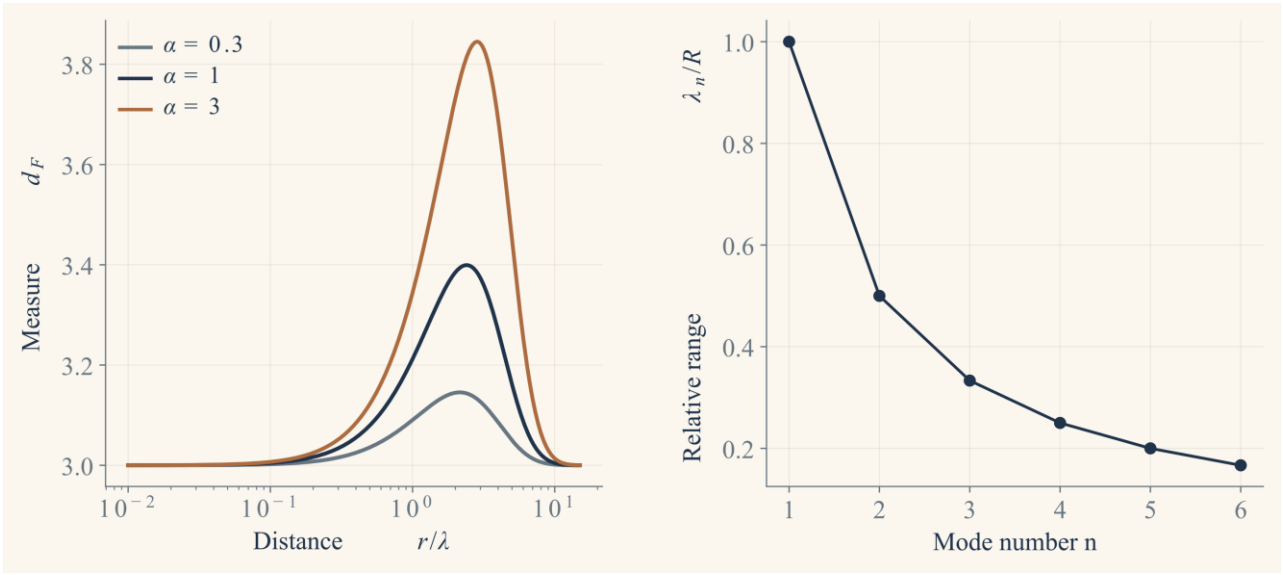


Figure 40. Operational force index for one Yukawa correction and compact mode range. The curves on the left are calculated for positive α; on the right λ_n/R = 1/n. These are consequences of the chosen models, not observations of additional dimensions.

Source, detector and retarded response

In order for the mode spectrum to turn into a device forecast, we set the source. A small body of mass m is located at y = 0 and is displaced along the line towards the detector by ε cos(ωt). Its scalar charge is proportional to its mass. A test body of mass M is also located at y = 0 and interacts with the potential through the energy MΦ_s. The movement of the source is supported by an external drive; ε is significantly less than the distance r, and the speed εω is significantly less than c. Linear scalar dynamics with a fixed radius R are adopted. It completely defines this example, keeping separate the question of the possibility of its implementation in nature.

In Figure 41, the source motion, retarded response, and power channel reading are separated as different parts of a single measurement operator.

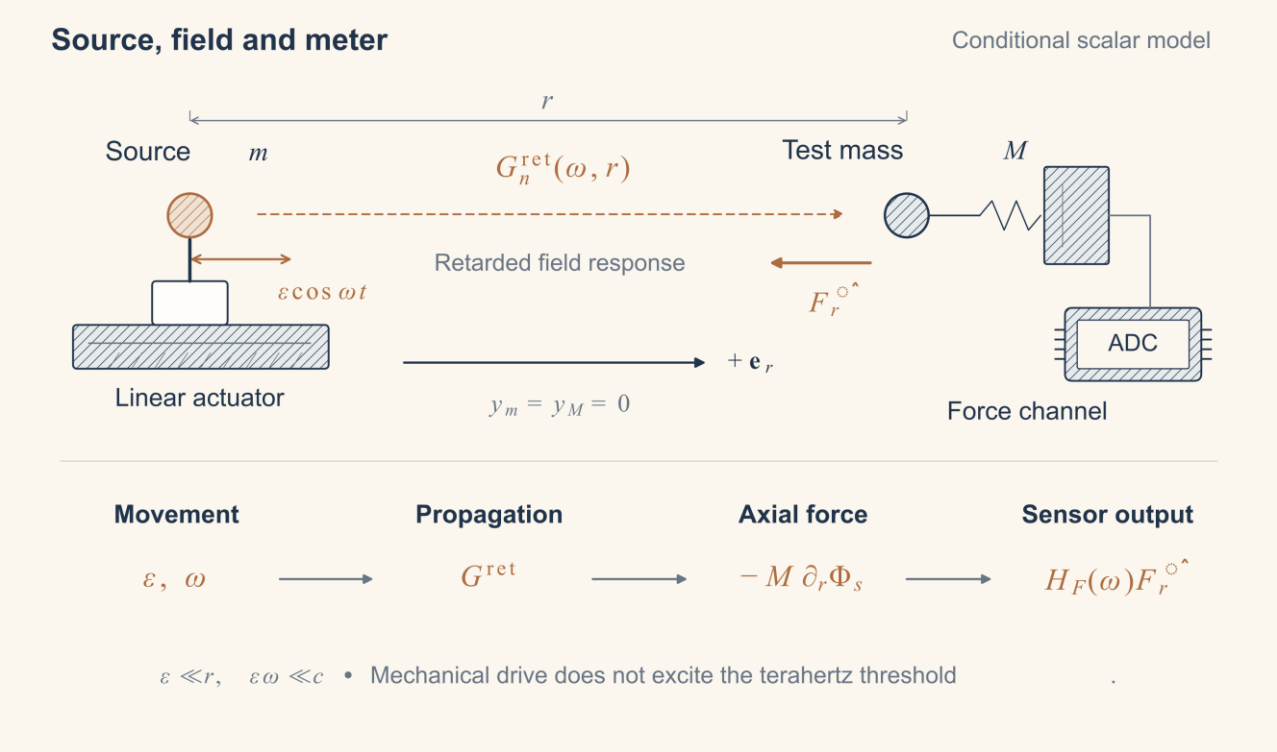


Figure 41. The source m and the test mass M are located at the same compact coordinate y = 0. The actuator displaces the source along the positive radial direction; the force arrow fixes the sign of the attractive quasi-static response. Between the motion and the digital output are the Green's function, the spatial derivative of the potential, and the response of the force sensor. The design of the measuring principle in a given scalar model is depicted. Mechanical excitation at 100 Hz does not become a terahertz source due to the presence of a compact threshold in the field equation.

$$\left(\nabla_{\mathbf{x}}^2 + \partial_y^2 - c^{-2}\,\partial_t^2\right)\Phi_s = 4\pi G_4 \rho_4, \qquad G_4 = 2\pi R G_s, \qquad (10.8)$$

$$\rho_4 = m\,\delta^{(3)}(\mathbf{x} - \epsilon\cos(\omega t)\mathbf{e}_r)\delta_{2\pi R}(y) \qquad (10.9)$$

Here Φ_s has units of m²/s², the four-dimensional spatial density ρ_4 is kg/m⁴, and G_4 is m⁴/(kg s²). The periodic delta function integrates into a unit around the circle. The coefficient G_s determines the far scalar force after selecting the zero mode. All complex amplitudes are then multiplied by exp(−iωt). The outgoing radial wave therefore contains exp(ik_nr), and the branch of the root is chosen with a non-negative imaginary part.

$$k_n(\omega) = \sqrt{\frac{(\omega + i0)^2}{c^2} - \frac{n^2}{R^2}}, \qquad G_n^{\mathrm{ret}}(\omega, r) = \frac{e^{ik_n r}}{4\pi r} \qquad (10.10)$$

For ω < nc/R, the number k_n is imaginary: the contribution decreases exponentially and does not transfer the free propagating mode over a large distance. Above the threshold, k_n becomes real. The usual radial momentum remains continuous, so the threshold does not have to be a narrow spectral line. Resonance would require additional confinement, reflection, or specific source dynamics. The static limit of the same function gives exp(−nr/R)/r and returns the potential already

obtained. This check connects two parts of the model with one operator. The connection between the compact spectrum and Yukawa corrections has been studied in the primary literature; the coefficients depend on the geometry and degeneracy of the modes. [45]

A small movement of the source differentiates the Green's function according to the position of the source. The measured force requires another derivative with respect to the detector position. For a coaxial point experiment, the amplitude of the radial force has the form

$$\widehat{F}_r(\omega) = -\frac{G_s m M \epsilon}{r^3}\mathcal{D}(\omega, r), \qquad \mathcal{D} = \sum_{n=0}^{\infty} w_n\, e^{ik_n r}\left[2 - 2ik_n r - (k_n r)^2\right], \qquad (10.11)$$

$$w_0 = 1, \qquad w_n = 2\ (n \geq 1) \qquad (10.12)$$

The sign corresponds to the radial axis from the source to the detector. When ω = 0 the first bracket is equal to two for the zero mode, and for the massive mode it becomes 2 + 2nr/R + (nr/R)². Thus, the dynamic reading is defined along with its amplitude and phase. Point approximation conditions require body sizes much smaller than r; Below, the finite bodies will be calculated using a separate integral.

For R = 10 μm the first threshold is 4.7713 THz, while a drive at 100 Hz gives ωR/c = 2.10 × 10^{-11}. The available mechanical movement explores almost static force. The mere presence of a calculated terahertz scale does not make a mechanical source a terahertz exciter. The left panel of figure 44 shows the dimensionless dynamic reference at r = 3R; the high-frequency region serves as a prediction of the specified field equation, and not as a specification of the proposed mechanical experiment.

From point masses to measured torques

A real mass has a shape, thickness and density distribution. When the gap is comparable to its dimensions, the force between the centers does not describe the sensor reading. It is necessary to sum the interactions of all pairs of elements of a substance. For a rotating source, first calculate the total potential energy at angle θ, and then its derivative with respect to this angle. The integral includes the measured surfaces, density inhomogeneities, holes and screen. This operation occupies a central place in the instrument model: a weak effect that disappears after the geometry is refined does not indicate a changed space. The geometry of the device itself must be known better than the geometry it is intended to discover.

$$U(\theta) = -G\int d^3x\, d^3y\, \frac{\rho_1(\mathbf{x})\rho_2(\mathbf{y})}{s(\mathbf{x},\mathbf{y},\theta)}\left[1 + \sum_n \alpha_n\, e^{-s(\mathbf{x},\mathbf{y},\theta)/\lambda_n}\right], \qquad \tau_z = -\frac{\partial U}{\partial \theta} \qquad (10.13)$$

Here s is the actual distance between the elements of the bodies after the source has been rotated. Densities have units of kilogram per cubic meter, energy integral is joule, and moment is newton meter. A useful source design contains several spatial periods. As they rotate, they create different

harmonics, each of which weighs the distances within the integral differently. Changing the gap adds independent information. This approach helps to separate the shape of the interaction from the overall gain of the sensor. But multiple harmonics should not be considered a priori as independent experiments: the same surface or position errors can simultaneously bias all channels, and their total covariance must be included in the analysis.

Li et al tested the interaction at gaps ranging from 52 μm to 3 mm. In their analysis of 2020, the range of the Yukawa correction of the gravitational force in magnitude, |α| = 1, limited to a value less than 38.6 μm with a confidence level of 95%. This is a specific cross-section point of the region (α, λ), and not a universal limit on the radius of any additional direction. In the work of Tan et al., suppressing the motion of the shielding membrane reduced the effect of the residual surface potential. Both examples show that the interpretation of force depends on the interaction model and the measured properties of the setup. [27] [28]

Fully specified calculation of two finite disks

Let us consider two homogeneous coaxial disks with a radius a = 5 mm and a thickness t = 100 μm each. The density of both bodies is set equal to 19 300 kg/m³. The average gap z_0 is 50 μm, and the drive reduces it by ε cos(ωt), where ε = 0.1 μm and the frequency is 100 Hz. The sensor measures the first harmonic of the axial force. The values determine the design model: the properties of the drive, screen and force sensor must still be checked on a separate model.

For comparison with the usual long-range force, it is convenient to introduce β. If the far scalar component is G_s and the measured total coefficient is G_N, let β = G_s/G_N. For the sum of two attracting contributions, $0 \le \beta \le 1$; the value β = 1 returns a pure scalar reference. The zero mode is already included in G_N. The additional Yukawa terms then have α_n = 2β and λ_n = R/n. The numbers below use G_N = 6.67430 × 10⁻¹¹ m³/(kg s²).

$$V(r) = -\frac{G_N m M}{r}\left[1 + 2\beta \sum_{n=1}^{\infty} e^{-nr/R}\right] \qquad (10.14)$$

The integral over two cylindrical bodies can be reduced to two variables without replacing the finite disks with infinite plates. With a transverse displacement u, the overlap area of their projections is equal to A_ov(u). The sum of the depths of two elements w has a triangular weight b(w). These geometric weights take into account all pairs of elements of a substance.

$$A_{\mathrm{ov}}(u) = 2a^2 \arccos\frac{u}{2a} - \frac{u}{2}\sqrt{4a^2 - u^2}, \qquad 0 \le u \le 2a, \qquad (10.15)$$

$$b(w) = \min(w, 2t - w), \quad s = \sqrt{u^2 + (z_0 + w)^2}, \quad 0 \le w \le 2t \qquad (10.16)$$

The geometric values of the integral and the direction of gap modulation are collected in Figure 42.

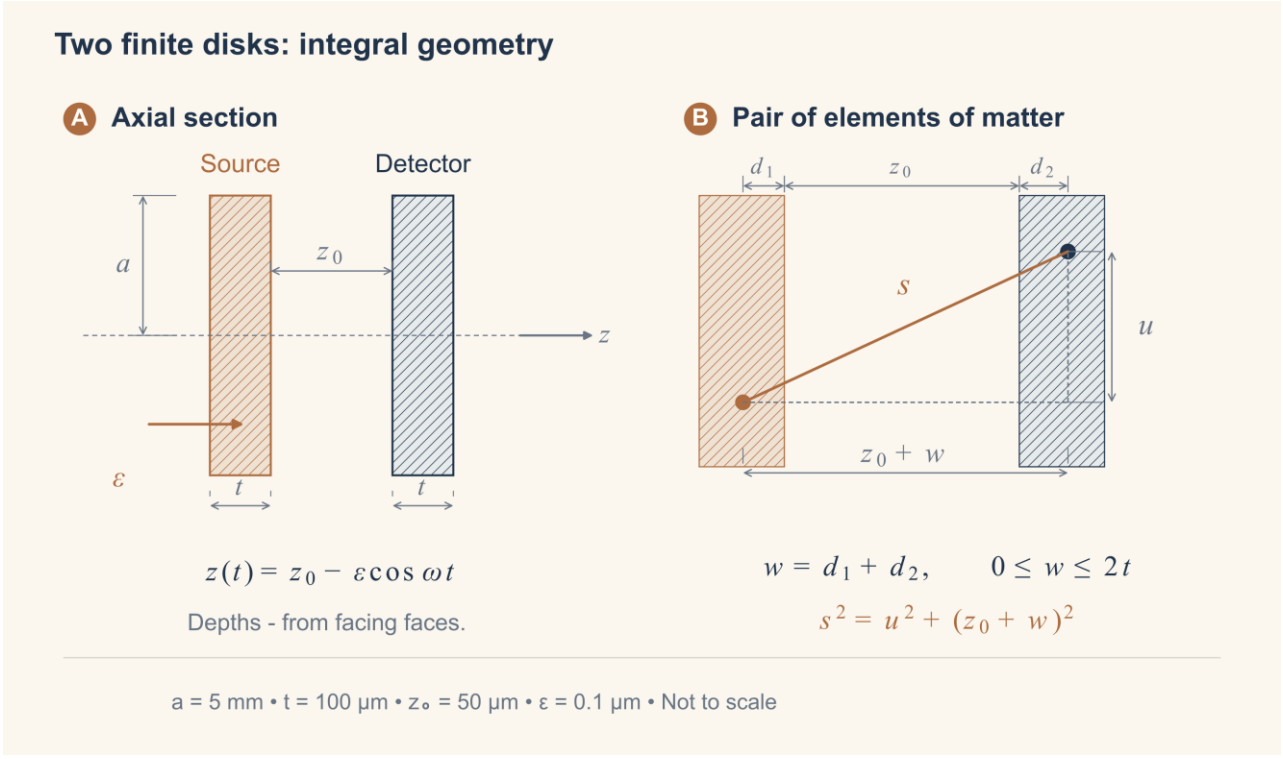


Figure 42. Two homogeneous coaxial disks have the same radius a and thickness t. Moving the source reduces the average gap z_0 by ε cos(ωt). In an enlarged pair of elements, d_1 and d_2 are counted inside the bodies from the facing faces; their sum w specifies the axial distance $z_0 + w$, and u specifies the transverse distance. Therefore, the distance of the pair is $s = \sqrt{[u^2 + (z_0 + w)^2]}$. Thickness, clearance and movement are not shown to scale; no additional screen is included in the calculated geometry.

$$F_Y(z_0;\lambda,\alpha) = 2\pi G_N \rho^2 \alpha \int_0^{2a} u\, A_{\mathrm{ov}}(u)\, du \int_0^{2t} b\,(w)\, \frac{z_0 + w}{s^3} \left(1 + \frac{s}{\lambda}\right) e^{-s/\lambda}\, dw \qquad (10.17)$$

$$F_{1,Y} = -\epsilon \frac{\partial F_Y}{\partial z_0}, \qquad F_{1,\mathrm{tower}} = \sum_{n\geq 1} F_{1,Y}\,(z_0; R/n, 2\beta) \qquad (10.18)$$

The force F_Y in the entry (10.17) is positive for attraction. As the gap decreases, it increases; therefore the amplitude of the first harmonic is positive. In the program, the derivative of the kernel is calculated analytically, after which the quadrature is performed. The Newtonian contribution is obtained by replacing the exponential factor by one and is also integrated over the finite bodies. It does not disappear upon modulation: the edge fields of the finite disk create a nonzero derivative of the force.

Value at R = 10 μm and β = 1	Calculation result
Constant Newtonian force	1.12028×10^{-13} N

Value at R = 10 μm and β = 1	Calculation result
Newtonian first harmonic	5.66708×10^{-18} N
Additional harmonics of the entire tower	1.65240×10^{-19} N
Additional harmonic of the first pair of modes	1.64682×10^{-19} N
The share of the following modes in the additional harmonic	0.3377%

Increasing the order of quadrature changed the additional harmonic by less than 10^{-13} relative to its magnitude, and the Newtonian harmonic by approximately 1.2×10^{-11}. This is a test of the numerical integration of the selected ideal geometry. It does not evaluate errors in actual dimensions, density and position. Linearization in ε gives a separate correction of order $(\varepsilon/\lambda)^2$ for a separate mode; at $\varepsilon/R = 0.01$ the leading mode is deeply in the linear regime. Higher modes, for which the ratio is larger, are here exponentially suppressed by the gap.

The resulting Newtonian harmonic background is approximately 34 times greater than the additional signal. Its calibration is included in the task along with the sensitivity of the sensor. If, after all corrections, the standard harmonic error 3×10^{-20} N is required, the geometric and Newtonian budget must also fit within this number. The mere promise of such low readout noise does not ensure the resulting accuracy.

Sensitivity map and competing intermediary

Let the standard error of the already estimated force harmonic, including the named residual parameters, be equal to $\sigma_F = 3 \times 10^{-20}$ N. For a fixed R, the nominal two-sided scale $1.96\sigma_F$ gives $\beta_{min} = 1.96\sigma_F/F_1(\beta = 1)$. This is the characteristic of one pre-selected test in the Gaussian approximation. Many-R searches and background shape uncertainty will require the general statistical procedure of Chapter 14.

$$\beta_{\min}(R) = \frac{1.96\,\sigma_F}{F_{1,\text{tower}}(R, \beta = 1)} \qquad (10.19)$$

When R = 10 μm, $\beta_{min} = 0.35584$ is obtained. This is the scale of crossing a given threshold, and not a guarantee of high power: a signal with mathematical expectation $1.96\sigma_F$ crosses the upper threshold in approximately half of the realizations. For a power of about 80% with the same two-sided nominal rule, approximately $2.80\sigma_F$ is required, which here corresponds to β about 0.509. Figure 43 shows this conventional sensitivity area. It describes the consequences of a given error, not the experimental limit reached. It also does not highlight the region supposedly resolved by all existing observations: to do this, it is necessary to separately transfer real restrictions to the mode tower and its connections with matter. Literary limit at $|\alpha| = 1$ refers to one Yukawa amendment; it is impossible to turn it into an exact boundary for the entire tower without re-analysis.

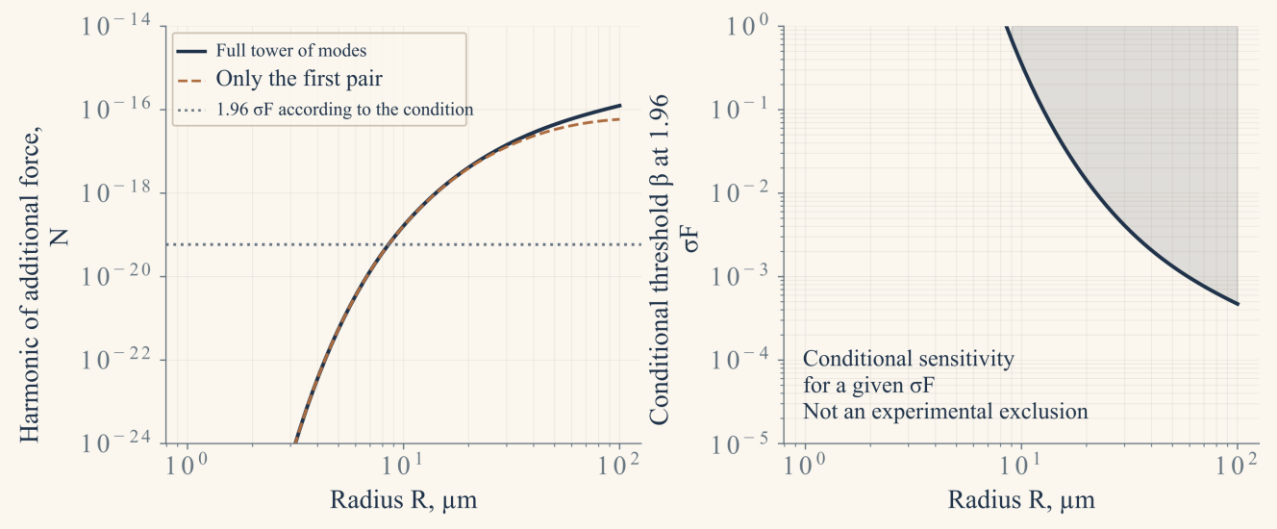


Figure 43. Finite disks and a given noise budget. On the left, the additional force harmonic is calculated for β = 1, on the right - β_min for σ_F = 3 × 10⁻²⁰ N. Shading indicates only conditional distinguishability in this calculation; experimental excluded areas are not plotted here.

The next test asks whether the tower is distinguishable from one ordinary intermediary. In the artificial standard, R = 20 μm and β = 0.1 are specified. Free α and λ of a single mediator are selected according to exact harmonics at gaps 60 and 100 μm. α = 0.2144505 and λ = 19.77856 μm were obtained. Both training points coincide with the tower in the accuracy of the numerical search. This is expected: two parameters are adjusted to two numbers.

New gap	Difference between tower and fitted mediator	Difference / σ_F
20 μm	3.56857 × 10⁻¹⁹ N	11.90
30 μm	9.68061 × 10⁻²⁰ N	3.23
40 μm	2.47110 × 10⁻²⁰ N	0.82

Data at 40 microns in the adopted budget almost do not share these explanations. At 20 μm their predictions differ noticeably. The right panel of Figure 44 shows this difference and marks the adjustment points. The values in the last column express the distance between two fixed forecasts in units of assigned error. They are not ready-made discovery values: parameter uncertainty, general clearance errors, and re-fitting to real noisy data will increase the overlap area.

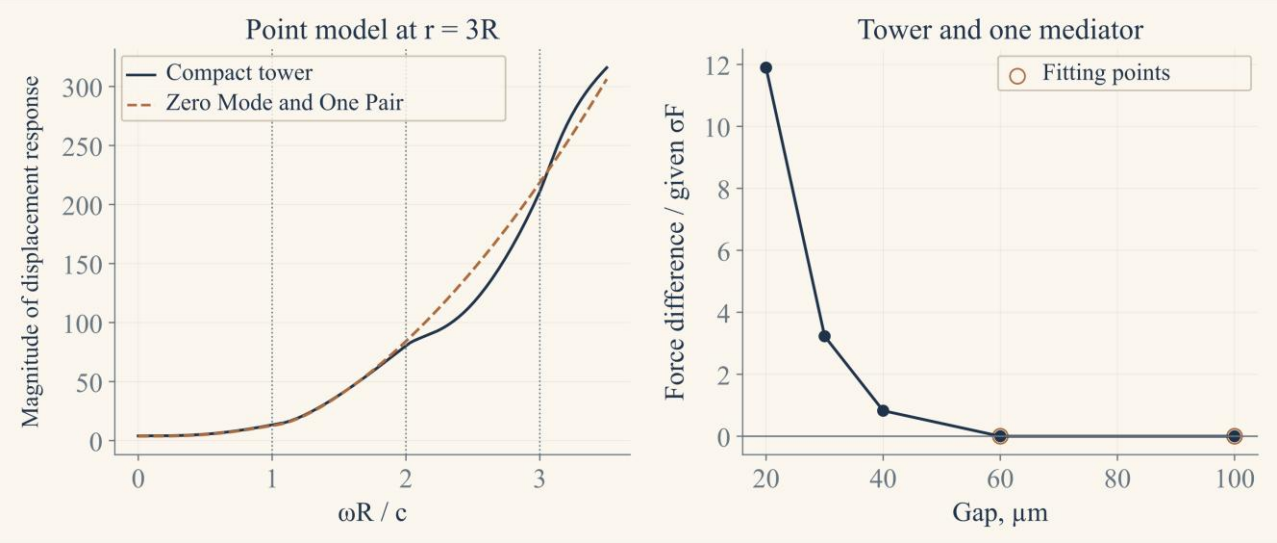


Figure 44. Two checks of the compact model. On the left is the point dynamic response to source displacement at r = 3R; the verticals mark the thresholds ωR/c = 1, 2, 3. On the right is the difference in end-disk harmonics between the tower and a single mediator matched at two training points. The numbers were obtained by calculation.

All results in this section are reproduced by the physics_revision.py program. It performs the finite body integral, fits the usual mediator, and constructs both panels. This example clarifies the meaning of the spectroscopy of geometry: there are few related scales in the equation; what is needed are regimes in which their contribution exceeds the uncertainty of the competing explanation.

What conclusion does this experiment allow?

In the chosen scalar model, a single radius determines the static ranges, propagation thresholds, and dynamic response. The integral for the finite discs converts them to a force harmonic, and a comparison with a single mediator indicates the discriminating gap.

Physical search requires measuring geometry, background and full error budget, then performing recorded gap changes. A deviation would establish additional interaction in this band. A geometric interpretation would require agreement between other predictions of the same operator and testing of a wider class of proxies.

Next, the consistency of clock frequencies and spatial field gradient is considered. It will require separate monitoring of instrument movement and general interference.

Chapter 11
Clocks and gravimeters as a joint probe of space

One cause and two ways to observe

Two identical instruments can confirm the repeatability of the reading. Two different types of instruments further test the relationship between observed quantities. In a weak quasi-static field, the comparison of clocks is related to the potential difference, and the acceleration of the test body is related to its spatial gradient. Therefore, clocks and gravimeters can be combined to test one cause. This chapter takes the selected statistical model to a joint spectrum, specific geometry, noise budget, and clock-permuted synthetic experiment.

In a weak field, we denote the additional potential by $\delta\Phi$ and introduce the dimensionless quantity $q = \delta\Phi/c^2$. For a fixed clock with slow changes and after taking into account known effects, the relative frequency correction between points a and b is approximately equal to the difference q. The sign chosen depends on which frequency ratio is named y_ab; Below we use exactly the definition written in the formula. The gravimetric channel is associated with a negative spatial potential gradient. The actual sensor on the support measures motion relative to its mechanical system, so its response to this quantity needs to be calibrated. The field equation in itself is not yet an equation for the instrument reading. The notation q in this chapter refers only to the dimensionless potential and is not used for the matrix scalar of the network problem.

$$q(\mathbf{x},t) = \frac{\delta\Phi(\mathbf{x},t)}{c^2}, \qquad y_{ab}(t) \simeq q(\mathbf{x}_a,t) - q(\mathbf{x}_b,t), \qquad \delta\mathbf{a}(\mathbf{x},t) = -c^2\nabla q(\mathbf{x},t) \qquad (11.1)$$

The ability to measure very small gravitational differences using clocks has been confirmed by individual experiments, but this is not evidence of the proposed additional field. Bothwell and co-authors observed a gravitational frequency gradient within a millimeter-sized atomic sample. Zheng and co-authors performed a blind redshift test on an array of five atomic ensembles with a total height difference of one centimeter. For this chapter, these works provide evidence for the measurement principle and culture of monitoring systematic effects. Their results cannot be translated into ready-made sensitivities of an arbitrary network: other distances, transmission lines, polling intervals and environments will require their own evaluation. [29] [30]

Accelerated clocks in flat spacetime

Before attributing a joint signal to curvature, it is useful to examine a case where it definitely does not exist. Let the system of observers be uniformly accelerated along x. In Rindler coordinates, the interval has the form

$$ds^2 = -N(x)^2c^2dt^2 + dx^2 + dy^2 + dz^2, \qquad N(x) = 1 + \frac{a_0 x}{c^2} > 0 \qquad (11.2)$$

For clocks stationary in these coordinates, proper time is $d\tau = N(x)dt$. Comparing them reveals a position-dependent frequency shift. At $a_0 = 9.81$ m/s² and a short baseline of one meter, the first-order shift is 1.0915×10^{-16}. An accelerometer attached to the support also gives a nonzero reading: the observer's proper acceleration is $a_0/N(x)$. Nevertheless, spacetime is flat, as the transformation to inertial coordinates shows directly.

$$cT = \left(x + \frac{c^2}{a_0}\right)\sinh\frac{a_0 t}{c}, \qquad X = \left(x + \frac{c^2}{a_0}\right)\cosh\frac{a_0 t}{c} - \frac{c^2}{a_0} \qquad (11.3)$$

The substitution (11.3) turns the metric into $-c^2dT^2 + dX^2 + dy^2 + dz^2$, so the entire Riemann tensor is zero. Even the spatial gradient of the readings of accelerated supports should not be directly identified with tidal curvature. For $\alpha(x) = a_0/N(x)$ the exact relation holds

$$\partial_x \alpha + \frac{\alpha^2}{c^2} = 0 \qquad (11.4)$$

The second term takes into account the kinematics of the selected accelerated system. The relative acceleration of free test bodies in the local inertial frame has a different meaning: after taking into account the initial velocities and the movement of the measuring base, it is related to the tidal components of curvature. In general, a measurement protocol is required that includes observers, signal exchange, and support movement. It is precisely such operational issues that are considered in the works on the clock compass and the relativistic geoid. [41] [42]

The Rindler control specifies a specific requirement for the extended procedure: it must return zero curvature after accounting for system acceleration. Now let's check the same design against a background with a predetermined non-zero tidal component.

Non-zero curvature: clock and tidal gradiometer

Now let's set a background with a non-zero tidal action and draw both measuring channels through it. Let us preserve the static metric with Euclidean spatial sections by adding a quadratic term to the function N. The parameter a_0 has units of acceleration, κ - the reciprocal second squared. The region $N > 0$ is considered, where both additional terms are small. This is a given local geometric example; the source of its stresses is not derived from Einstein's equations, and it is not declared a model of the earth's field.

$$ds^2 = -N(x)^2c^2dt^2 + dx^2 + dy^2 + dz^2, \qquad N(x) = 1 + \frac{a_0 x}{c^2} + \frac{\kappa x^2}{2c^2} \qquad (11.5)$$

In order for the sign of curvature to be verifiable, we fix the agreement for the Riemann tensor with the following formula. The coordinate x^0 is equal to ct. The primes further denote derivatives with respect to x, which here simultaneously measures its own spatial length on a static section.

$$R^{\rho}_{\sigma\mu\nu} = \partial_\mu \Gamma^{\rho}_{\nu\sigma} - \partial_\nu \Gamma^{\rho}_{\mu\sigma} + \Gamma^{\rho}_{\mu\lambda}\Gamma^{\lambda}_{\nu\sigma} - \Gamma^{\rho}_{\nu\lambda}\Gamma^{\lambda}_{\mu\sigma} \qquad (11.6)$$

In the time and x sector, the nonzero connection coefficients are $\Gamma^0_{0x} = \Gamma^0_{x0} = N'/N$ and $\Gamma^x_{00} = NN'$. Substituting them gives $R^x_{0x0} = NN''$. Going to the orthonormal reference of the stationary

observer divides the two time components by N. If $\alpha = c^2 N'/N$ is the measured proper acceleration of the support along the positive x-axis, the result is conveniently expressed in tidal gradient units:

$$\mathcal{K}(x) = c^2 R_{\hat{0}\hat{x}\hat{0}\hat{x}} = c^2 \frac{N''}{N} = \partial_x \alpha + \frac{\alpha^2}{c^2}, \qquad \mathcal{K}(0) = \kappa \tag{11.7}$$

We will place the static clock at x = 0 and x = ±h. Two extreme sources with the same natural frequency ν_0 send light to a central observer, who compares the received frequencies with his clock. For each ray, the frequency is proportional to $-u \cdot k$; preserving the covariant time component of the wave vector in the static metric specifies the exact relationship. Therefore, the recorded shifts y± are equal to N(±h) − 1. Their sum removes the linear acceleration term:

$$\frac{\nu_R}{\nu_E} = \frac{\left(u^\mu k_\mu\right)_R}{\left(u^\mu k_\mu\right)_E} = \frac{N_E}{N_R}, \qquad C_2 = y_+ + y_- = \frac{\kappa h^2}{c^2} \tag{11.8}$$

The second channel is the difference between the readings of two static accelerometers at the ends of the same base, supplemented by the reading of the central support. Their axes are aligned along x. The finite difference estimates the derivative, and the separately measured squared acceleration removes the kinematic contribution. The resulting value has an independent physical interpretation: free nearby bodies in a non-rotating local inertial frame experience relative tidal acceleration. For positive κ it is compressive. The relationship to measurement frames and the movement of supports is part of the clock compass protocol. [41]

$$\widehat{\kappa}_g = \frac{\alpha(h) - \alpha(-h)}{2h} + \frac{\alpha(0)^2}{c^2}, \qquad \delta a_{\parallel} = -\mathcal{K}\, \xi_{\parallel} \tag{11.9}$$

Figure 45 compares the same clock and accelerometric protocol under accelerated flat background and under positive tidal curvature.

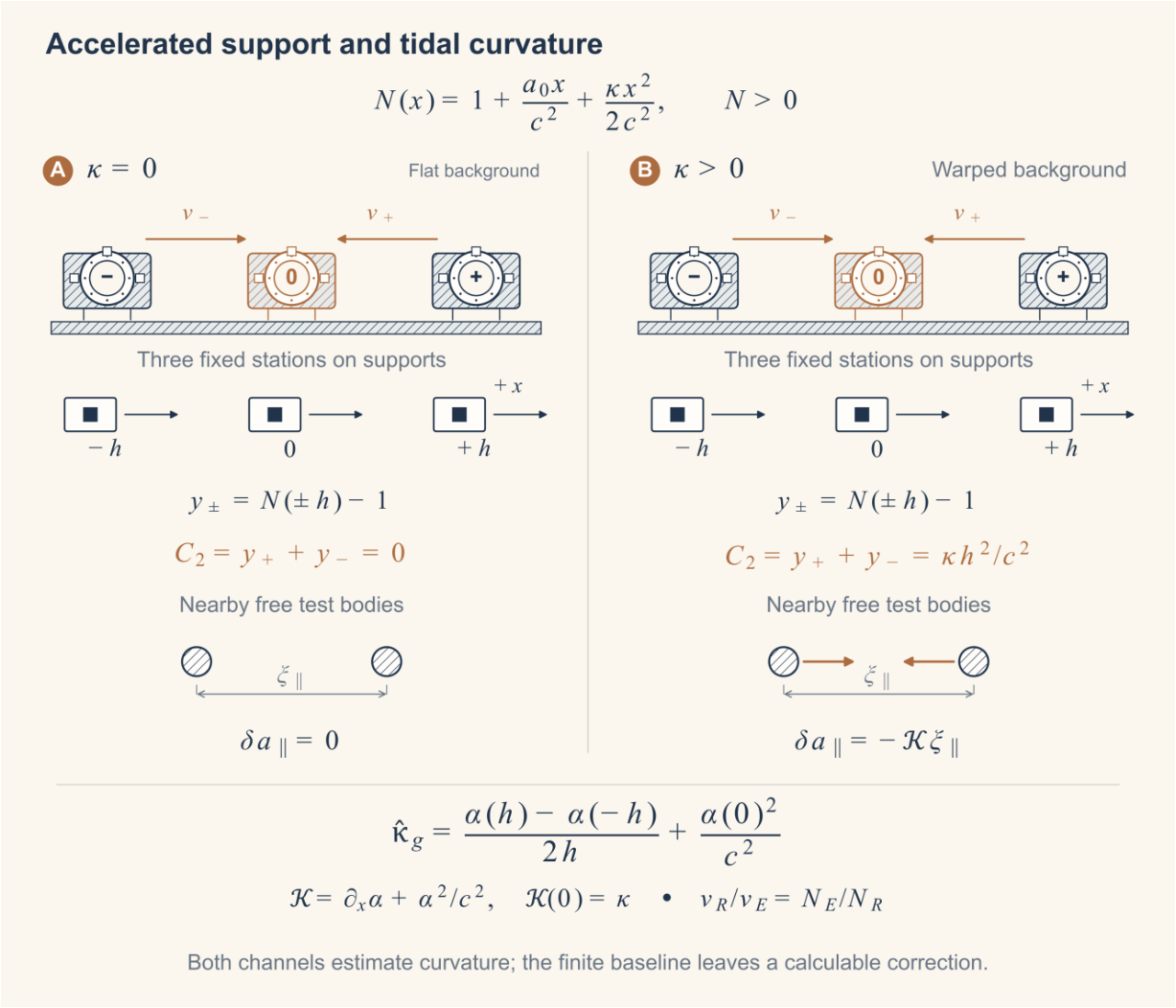


Figure 45. The outer atomic clocks transmit light to one central clock; all three stations are supported on supports, and the axes of the accelerometers are directed along +x. Frequency shifts are defined as N(±h) − 1. Their sum removes the linear acceleration term. The acceleration gradient requires a separate central correction $\alpha(0)^2/c^2$. The lower pairs indicate free test bodies, not clock supports: positive κ gives compression. This is a given local metric; it does not depict the inferred field of the Earth. The finite baseline leaves a calculated correction to the gradient estimate.

Let us choose $a_0 = 9.81$ m/s², $\kappa = 3 \times 10^{-6}$ s^{-2} and h = 100 m. Then $C_2 = 3.33795 \times 10^{-19}$, and the central component of curvature is equal to 3.33795×10^{-23} m^{-2}. The difference in acceleration of the supports is $5.999999998 \times 10^{-4}$ m/s². The kinematic correction is equal to 1.07077×10^{-15} s^{-2}; after adding it, the estimate κ differs from the given value by -5.01×10^{-25} s^{-2} due to the finite base. The corresponding free relative acceleration based on 200 m in the local approximation is -6×10^{-4} m/s².

Let us assign full standard errors after averaging: to each of the three independent clock channels 10^{-20}, to each accelerometer 2×10^{-5} m/s². These are calculation conditions, not stated installation characteristics. The common central clock is included in both frequency differences: their

covariance is σ^2, so the error C_2 is $\sqrt{6}\,\sigma$ rather than 2σ. Frequency transmission is assumed to be calibrated; an unknown additional correlation would require a budget recalculation.

The geometry has two different errors: the standard error of the common half-base is 1 mm, the position of the middle of the outer devices relative to the central one is 10 μm. The latter is especially significant: the displacement of the middle b adds a linear term $2a_0b/c^2$ to C_2. The independent measurement of centering cannot be replaced by the promise of symmetry. Taking these errors into account, the first linear uncertainty transfer gives $\sigma(\kappa) = 2.2102 \times 10^{-7}$ s^{-2} for the clock and 1.4142×10^{-7} s^{-2} for the gradiometer. The ratios of the specified signal to these errors are 13.6 and 21.2; this is a notional budget for a fixed configuration.

For the control Rindler at $\kappa = 0$ the same clock contrast is exactly zero, as is the local curvature. The finite difference of accelerations leaves only the calculated remainder -1.28×10^{-43} s^{-2}. This means that the protocol distinguishes between an accelerated flat system and a given curved background. The calculation is performed with increased arithmetic precision: the usual subtraction of three numbers around one here loses the clock contrast. This computational precaution does not dictate the accuracy of the clock. Next, we return to the random potential: its joint signal in itself does not replace the tidal control performed here.

Checkable random field pattern

To begin with, it is enough to construct a limited phenomenological hypothesis. Let q have zero mean, equal variance at each point, and spatial correlation decreasing at scale ℓ. Over time, the correlation decays with the characteristic time τ_c. The simplest convenient option combines a Gaussian dependence on distance with an exponential dependence on time shift. Parameter A describes the root-mean-square amplitude q, ℓ is measured in meters, τ_c - in seconds. This choice does not follow from the proven theory of quantum gravity. It specifies a specific test object for which it is possible to derive observed relationships in advance and determine which sensor configurations are the most informative.

$$C_q(r, \Delta t) = \langle q(\mathbf{x}, t) q(\mathbf{x} + \mathbf{r}, t + \Delta t) \rangle = A^2 \exp\left(-\frac{r^2}{2\ell^2}\right) \exp\left(-\frac{|\Delta t|}{\tau_c}\right) \qquad (11.10)$$

The correlation function cannot be chosen only by its beautiful appearance. For any set of points, the matrix of its values must give a non-negative dispersion of any linear combination of signals. Here this condition is satisfied: the spatial Gaussian kernel and the temporal exponential kernel are positive definite, and their product retains the desired property. But probabilistic admissibility does not yet mean physical completeness. It is necessary to explain what dynamics generate the field, how it is connected with matter, and what transformations it is subject to when changing the reference system. A given covariance describes the statistics in the selected observation system and does not by itself determine either the causal response or the transmission rate of the effect.

The limit of long correlation length is especially important. If all the clocks are in a region significantly smaller than ℓ, the field shifts their frequencies almost equally, and the difference measurement suppresses the effect. The network does not become more sensitive to a completely general shift just because its clock is very accurate. In the opposite limit, when the distance is much

larger than ℓ, the clocks see almost independent values and the variance of the difference saturates. Hidden between these limits is information about spatial scale. Therefore, different bases are needed, and not a single distance. For the same time band, a variance formula showing both modes immediately follows from the selected kernel.

$$\mathrm{Var}(y_{ab}) = 2A^2\left[1 - \exp\left(-\frac{d_{ab}^2}{2\ell^2}\right)\right] \qquad (11.11)$$

$$\sqrt{\mathrm{Var}(y_{ab})} \simeq A\frac{d_{ab}}{\ell} \quad (d_{ab} \ll \ell), \qquad \sqrt{\mathrm{Var}(y_{ab})} \to \sqrt{2}A \quad (d_{ab} \gg \ell) \qquad (11.12)$$

In Figure 46, the suppression of the difference with a small base is visible on the left, and the time strip of the model is visible on the right. The designation ℓ_c on the horizontal axis of the figure means the same value of ℓ that is used in the text; there is no separate second spatial scale here.

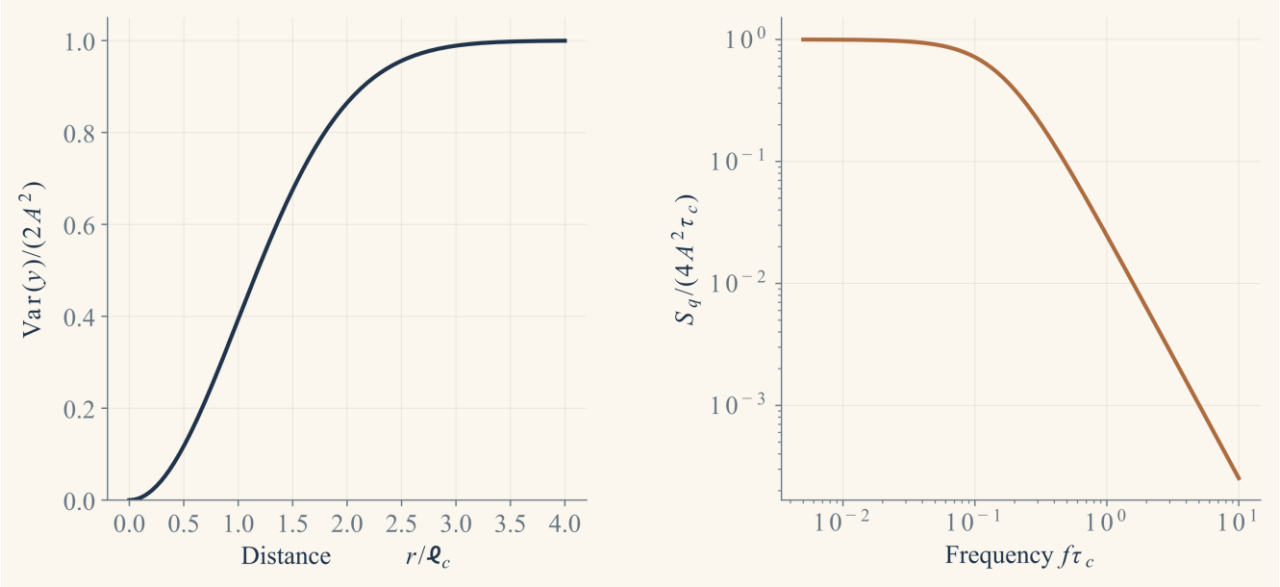


Figure 46. Spatial and temporal parts of the selected covariance. On the left is the variance of the two-clock difference normalized to 2A²; on the right is the normalized Lorentzian spectrum of one q. In the figure, ℓ_c denotes the ℓ used in the text.

One physical interpretation and its limits

The coordinated clock and gravimetric signal may have a common origin. A moving mass creates a potential −GM/|x − x_s(t)|; its difference and gradient will fall into both channels with the same quasi-static coefficients. Therefore, the first physical result of such a network will be an estimate of the general field, and the origin of this field will have to be established separately. Service measurements of pressure, movement of supports and distribution of nearby masses become part of scientific experiment.

For a spatial Gaussian template, a quasi-static Newtonian interpretation can be explicitly constructed. In the chosen system, we set a small density fluctuation around a positive background distribution so that the Poisson equation is satisfied. Then

$$\delta\rho(\mathbf{x},t)=\frac{c^2}{4\pi G}\nabla^2 q(\mathbf{x},t),\qquad P_{\delta\rho}(\mathbf{k},f)=\frac{c^4k^4}{(4\pi G)^2}P_q(\mathbf{k},f)\qquad(11.13)$$

The spectrum remains positive. In three spatial dimensions, the Gaussian kernel gives the root mean square density $c^2\sqrt{15}\,A/(4\pi G\ell^2)$. For the numerical example below it is 4.15 kg/m³. The value characterizes the required statistics of the distributed material background in this interpretation, and not the measured density and not proof of its existence. Locally negative δρ means a decrease relative to the background density. Using the Gaussian law remains an approximation of small fluctuations; its infinite tails cannot be taken as a literal model of negative total mass.

Such a field is not a strictly harmonic potential in a region without sources: $\nabla^2 q$ is usually nonzero. The assumption of an ambient vacuum cannot therefore be simultaneously combined with this material explanation without changing the model. For a real background, the laws of motion of matter, conservation of mass, and measurement of its spectrum will also be required. The relation (11.13) completes the static connection between the source and the potential, but does not replace the hydrodynamics or elasticity of the source.

Exponential time covariance corresponds to a process with a kink at zero time shift. It is suitable for a spectral pattern in a limited band, but a full smooth metric at all frequencies would require additional ultraviolet description. Here the operating signals are filtered; When constructing a physical source, the high-frequency spectrum should be smoothly cut off above the experimental band. The conditions $2\pi f\ell/c \ll 1$ allow the use of a quasi-static approximation. The spatial correlation of noise in itself does not determine the transmission rate of the controlled effect.

In stochastic semiclassical gravity, the random part of the metric response is associated with energy-momentum fluctuations and the Einstein-Langevin equation. This is an example of a deeper dynamical formulation, rather than a deduced origin of the Gaussian kernel chosen here. [43] For this chapter it is enough to fix the reference system, band and status of the potential as a tested effective model.

Spectrum of frequency differences and gradient

In the frequency domain, the chosen time law gives a Lorentzian spectrum. Below, one-sided spectral density is used: the integral over non-negative frequencies is equal to the total dispersion. Therefore, the coefficient 4 in the numerator is due to the normalization convention and not to additional physics. For dimensionless q, the unit of spectral density is the inverse hertz. By denoting the spatial kernel between points i and j by K_ij, one can obtain the mutual spectrum of any two clock comparisons. Its four terms correspond to four pairs of points. The clocks present in both comparisons simultaneously produce common instrumental errors; these errors must be considered separately from the hypothetical field.

$$S_q(r,f)=\frac{4A^2\tau_c}{1+(2\pi f\tau_c)^2}\exp\left(-\frac{r^2}{2\ell^2}\right),\qquad K_{ij}=e^{-d_{ij}^2/(2\ell^2)},\qquad f\geq 0\qquad(11.14)$$

$$S_{y_{ab}y_{cd}}(f) = \frac{4A^2\tau_c}{1+(2\pi f\tau_c)^2}(K_{ac} - K_{ad} - K_{bc} + K_{bd}) \qquad (11.15)$$

The gravimetric prediction is obtained by spatial differentiation of the same kernel. Let r = x − x′. Since the accelerations each contain one derivative, their covariance contains a mixed second derivative with respect to the coordinates of the two points. At zero separation, the root mean square value of one component is c^2A/ℓ. On a non-zero basis, covariance depends not only on the distance, but also on the orientation of the component being measured. Longitudinal and transverse channels therefore carry different information. This difference arises from the gradient nature of the field; it should not be added to the fit as an independent arbitrary angular function. Otherwise, the general physical meaning of the two measurements will be lost.

$$\langle \delta a_i(\mathbf{x},t)\delta a_j(\mathbf{x}',t)\rangle = c^4A^2\left(\frac{\delta_{ij}}{\ell^2} - \frac{r_i r_j}{\ell^4}\right)e^{-r^2/(2\ell^2)}, \qquad a_{i,\mathrm{rms}} = \frac{c^2A}{\ell} \qquad (11.16)$$

With a small base, the potential difference is approximately equal to the derivative times the distance. This gives us a practical test: the clock signal along the base must correspond to the acceleration projection with a known coefficient d/c^2 and a chosen sign. This relationship is more useful than the coincidence of two spectral peaks because it captures the relative amplitude. However, it is only valid when d is much smaller than ℓ, the same time filtering and the correct response model of both devices. If one channel was averaged for a minute and the other recorded rapid fluctuations, their total RMS values cannot be directly compared. A simple dimensional check will not correct the misalignment of the measurement bands.

$$y_{ab} \simeq -\frac{\delta a_{\parallel} d_{ab}}{c^2} \qquad (d_{ab} \ll \ell) \qquad (11.17)$$

The cross spectrum of two different instruments

Let us introduce $S_0(f) = 4A^2\tau_c/[1 + (2\pi f\tau_c)^2]$ and $K(x,z) = \exp[-|x - z|^2/(2\ell^2)]$. Spectral amplitudes are multiplied by $\exp(-i2\pi ft)$, and the mutual spectrum is determined by the order $S_{uv} = \langle \tilde{u}\tilde{v}^*\rangle$. The mixed channel is obtained by one derivative of the same kernel. Since $\partial K(x,z)/\partial z_i = (x_i - z_i)K/\ell^2$, the sign of the acceleration is explicitly preserved:

$$S_{y_{ab},a_i(\mathbf{z})}(f) = -\frac{c^2S_0(f)}{\ell^2}[(x_a - z)_i K(\mathbf{x}_a,\mathbf{z}) - (x_b - z)_i K(\mathbf{x}_b,\mathbf{z})] \qquad (11.18)$$

Unit (11.18) - $(m/s^2)/Hz$: the first channel is dimensionless, the second is acceleration. The acceleration autospectrum has a unit of $(m/s^2)^2/Hz$. These different dimensions should be preserved when constructing the joint matrix; For numerical inversion, it is convenient to normalize it to the characteristic noise of each channel.

Let us place clock a at x = +d/2, clock b at x = −d/2, and the gravimeter at x = 0. Its positive direction coincides with positive x. Then the negative sign of the cross spectrum means that the

positive potential difference directs the acceleration in the opposite direction. The three signal elements of the matrix take a simple form:

$$S_{yy} = 2S_0\left(1 - e^{-d^2/(2\ell^2)}\right), \qquad S_{aa} = \frac{c^4 S_0}{\ell^2}, \qquad S_{ya} = -\frac{c^2 S_0 d}{\ell^2} e^{-d^2/(8\ell^2)} \tag{11.19}$$

$$\gamma^2 = \frac{|S_{ya}|^2}{S_{yy} S_{aa}} = \frac{x}{\sinh x}, \qquad x = \frac{d^2}{4\ell^2} \tag{11.20}$$

This is a consequence of the chosen covariance. As $d/\ell \to 0$, the coherence tends to unity, but the dispersion of the clock difference simultaneously tends to zero. When $d/\ell \gg 1$ the clock sees almost independent potentials, and the middle gravimeter is weakly coupled to both. Between these limits, you need to choose a base taking into account noise, and not based on one maximum value of γ^2. At $d = \ell$ the ideal coherence is equal to 0.98966.

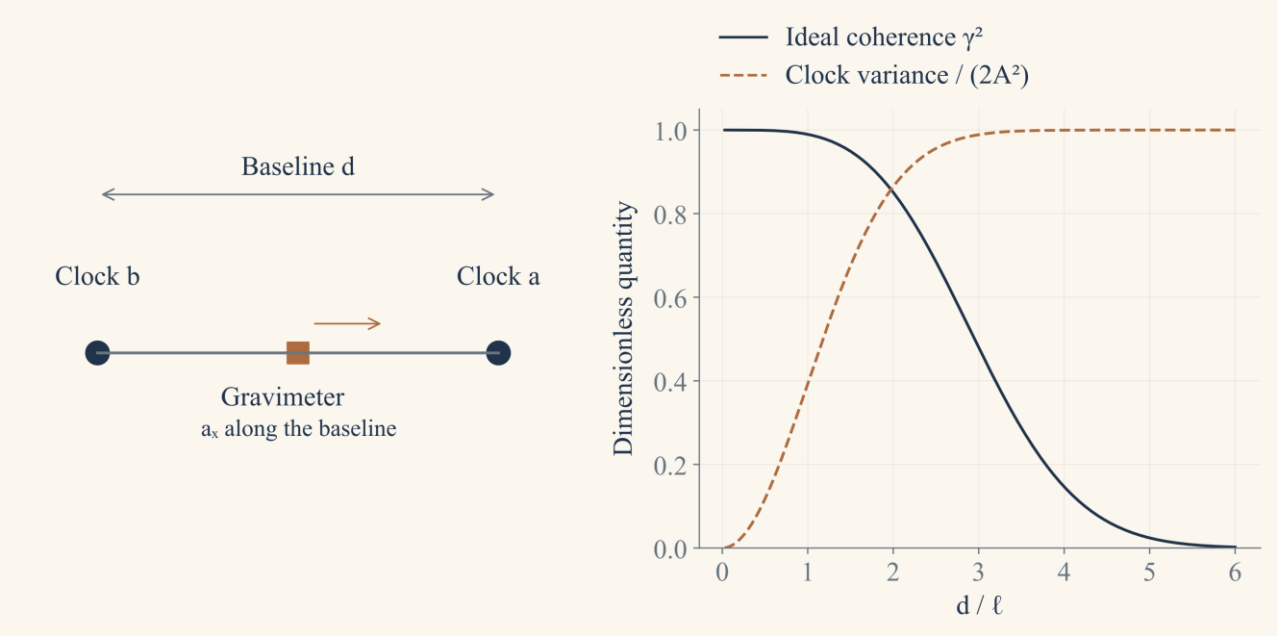


Figure 47. Two clocks and a central gravimeter. The positive direction of acceleration is from b to a. The ideal signal coherence and relative dispersion of the clock channel are shown on the right. High coherence with a small base is accompanied by a small amplitude of the measured difference.

Figure 47 explains why a series of baselines is useful. In the long-wavelength spatial regime, the signal ratio mainly fixes the gradient, and information about the correlation length itself is weak. Measuring near $d \simeq \ell$ and over a larger base changes the shape of the spectral matrix and helps separate A and ℓ. This is a parameter estimation problem that cannot be solved by simply increasing the time on a near-zero baseline.

A shared measurement band

The theoretical spectrum becomes observable only after passing through the interrogation time window, transmission line, and processing algorithm. The clock can measure the average phase or frequency in individual cycles. The gravimeter has its own sensitivity to frequency, mechanical resonance or a sequence of atomic pulses. Before joint analysis, each channel is associated with a complex transfer function H(f), including amplitude and phase. The transition to the common band is performed taking into account these functions. Frequencies at which the response is poorly known or almost zero cannot be reconstructed by uncontrolled division: such an operation amplifies noise and creates the appearance of structure where the data contains no information.

$$S_{ab}^{\mathrm{obs}}(f) = H_a(f) H_b^*(f) S_{ab}^{\mathrm{field}}(f) + S_{ab}^{\mathrm{noise}}(f) \qquad (11.21)$$

The quasi-static formula for the frequency difference requires, in particular, that the characteristic time of the field change be significantly longer than the time of light propagation over the base: the product 2πfd/c should be small in the band used. For faster changes, the contribution of the signal path, the movement of the line ends, and the selection of events being compared must be calculated in full. This is not a correction that can automatically be reduced to additional noise. It changes the physical prognosis itself. Even in slow mode, platform movement, height changes, thermal line extension, and residual frequency transmission error are capable of simulating part of the signal. Therefore, time, geometry and calibration must be recorded along with the basic data.

For an ideal rectangular frequency window between f_min and f_max, the variance fraction of the selected Lorentzian process is expressed in terms of the difference in arctangents. This formula is convenient for a preliminary budget: it immediately shows what part of the expected field the device generally observes. If τ_c is very large compared to the duration of the experiment, the process appears to be an almost constant drift. If it is too small compared to the polling interval, most of the power remains out of band and may cause aliasing if not filtered sufficiently. This means that the absence of a visible signal makes sense only in conjunction with the specified range of τ_c and with the data selection model.

$$B(f_{\min}, f_{\max}) = \frac{2}{\pi}\left[\arctan(2\pi f_{\max}\tau_c) - \arctan(2\pi f_{\min}\tau_c)\right], \qquad \mathrm{Var}_{\mathrm{band}}(q) = A^2 B \qquad (11.22)$$

A synthetic experiment with common noise and exchanged clocks

Let's consider one completely defined case with known ℓ = 1000 m and τ_c = 10 s. The base is equal to 1000 m, the frequency of the spectral cell is f_0 = 0.01 Hz, the introduced amplitude is A = 10^{-20}. The output noise of the clock is given by n_y = $10^{-18}/\sqrt{\mathrm{Hz}}$, and the noise of the gravimeter is given by n_a = 10^{-7} m/s²/√Hz. These values are the input conditions for the calculation. They do not report the constructed network with such precision.

The introduced A corresponds to the total root-mean-square acceleration of one component 8.99 × 10^{-7} m/s². It is chosen for computational experiment, and not as an established feasible region of the new cosmological field. The compatibility of such a field with all existing measurements is not

stated here. The Newtonian interpretation above shows how strong a material background would accompany this pattern.

The clock frequency is averaged one second with a timestamp in the middle of the window; H_y = sinc(πfT_y), where sinc(z) = sin(z)/z. For the gravimeter, a calibrated single-pole function H_a = 1/(1 − if/f_c) with f_c = 0.1 Hz and the accepted sign of the Fourier amplitudes is selected. The output noise includes a positive overall correlation ρ_n = 0.3. At each frequency the observed matrix is equal to

$$\mathbf{S}^{\mathrm{obs}} = \mathbf{H}\mathbf{S}^{\mathrm{field}}\mathbf{H}^{\dagger} + \mathbf{N}, \qquad \mathbf{H} = \mathrm{diag}\left(H_y, H_a\right), \qquad (11.23)$$

$$\mathbf{N} = \begin{pmatrix} n_y^2 & \rho_n n_y n_a \\ \rho_n n_y n_a & n_a^2 \end{pmatrix}, \qquad |\rho_n| \le 1 \qquad (11.24)$$

The interference matrix (11.24) is non-negative definite. Filtering also preserves the positivity of the signal matrix, so complex Gaussian observations can be generated through the Cholesky decomposition of the normalized sum. The program uses seeds 20261113 and 4096 of independent spectral realizations for each configuration. The resulting values are synthetic data with known covariance.

In the second configuration, the clocks are swapped, but the gravimeter and electronic channels are retained. The identities a and b are instrument-specific: the permutation changes the sign of the field S_ya, while the selected total electronic noise remains the same. This interference behavior is a verifiable assumption of the protocol. If the rearrangement changes the electronics themselves or their relationship to vibration, a separate model for that change will be required.

The identity of the clocks, the fixed direction of the gravimeter and the preservation of the electronic channels when rearranged are shown in figure 48.

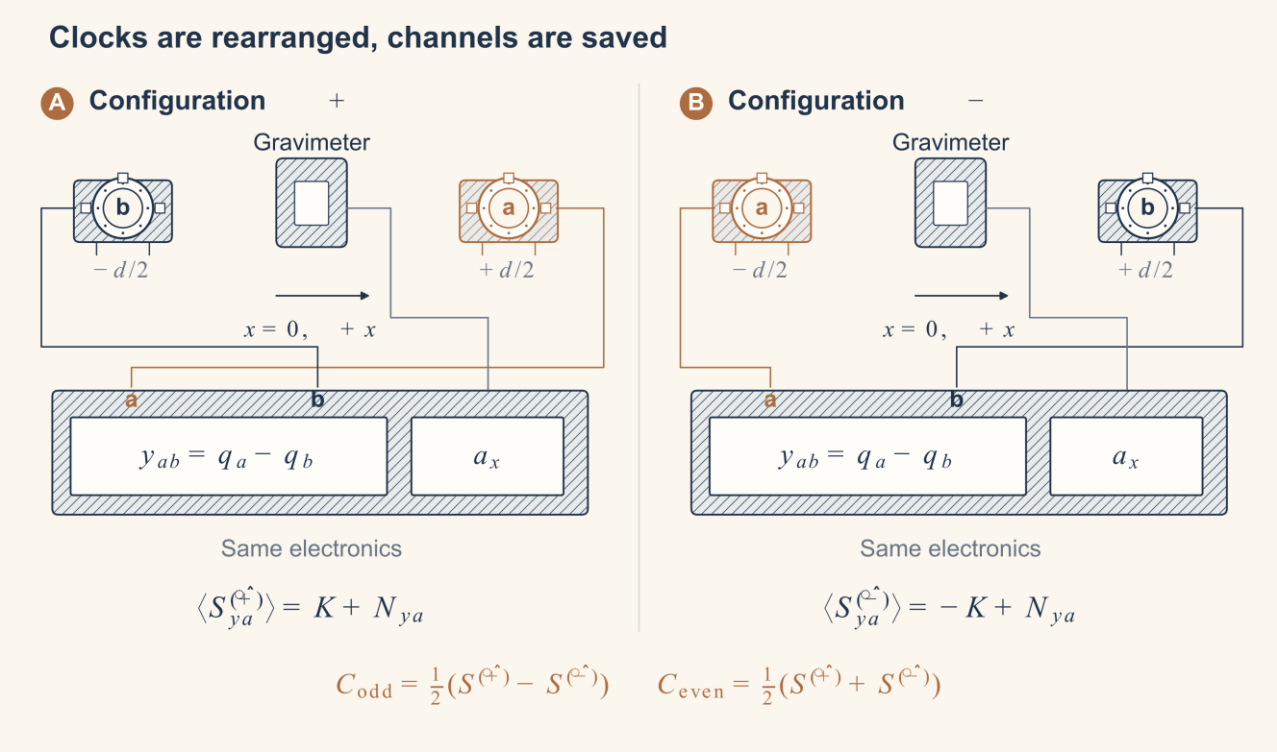


Figure 48. In the first configuration, clock a is at +d/2, clock b is at −d/2; in the second, only their physical positions change. Electronic comparison preserves the definition y_ab = q_a − q_b, the gravimeter remains in the center and does not change the positive axis. Here K denotes the filtered field cross spectrum. The selected total electronic interference N_ya is considered even with respect to the interference. This is a testable assumption of a particular experiment: the usual spatial gravitational contribution also changes sign and is not automatically excluded.

$$C_{\text{odd}} = \frac{\hat{S}_{ya}^{(+)} - \hat{S}_{ya}^{(-)}}{2}, \qquad C_{\text{even}} = \frac{\hat{S}_{ya}^{(+)} + \hat{S}_{ya}^{(-)}}{2} \qquad (11.25)$$

On average, the odd part contains H_yH_a* S_ya fields, and the even part contains N_ya total noise. Let us put K = H_yH_a* S_ya(A = 1). The estimate of the square amplitude before the non-negativity constraint is Re(K* C_odd)/|K|². A negative value on noise data should be retained when checking the estimate bias, and the boundary $A^2 \geq 0$ should be separately considered when reporting the physical limit.

Magnitude	The result of this calculation
Ideal signal γ^2	0.98966
Observed γ^2 in the first configuration	0.001678
Injected A^2	$1{,}0000 \times 10^{-40}$
Recovered A^2	$1{,}2252 \times 10^{-40}$
Standard error A^2 given covariance	$1{,}6575 \times 10^{-41}$

Magnitude	The result of this calculation
Recovered A	$1{,}1069 \times 10^{-20}$
A^2 score in a separate experiment with only a common noise	0.157 standard error from zero

The drop in observed coherence by almost 590 times shows the role of clock noise. Nevertheless, the accumulation of a given number of independent realizations makes it possible to isolate an odd cross spectrum. The nominal interval $A^2 \pm 2\sigma$ is $[8.94 \times 10^{-41}; 1.56 \times 10^{-40}]$ and contains the entered value. It is calculated with fixed ℓ, τ_c, transfer functions and covariance; adjusting these parameters together will widen the uncertainty.

In the control run, the field is turned off, but the overall interference is retained. The even part gives 3.102×10^{-26} (m/s²)/Hz with the expected 3.000×10^{-26}, and the odd estimate A^2 deviates from zero only by 0.157 standard error. One such run tests the logic of a given intervention. The frequency of false decisions must be determined in a separate series with new noises and with those classes of common causes that are actually present in the installation.

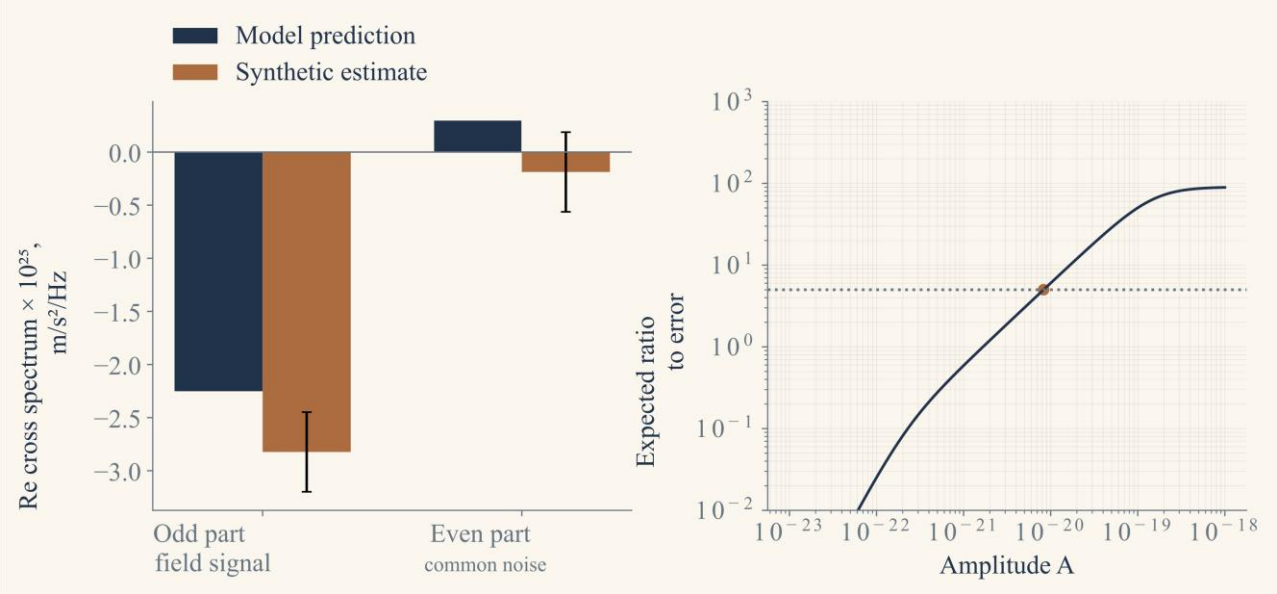


Figure 49. Synthetic joint experiment. On the left are the expected and obtained real parts of the cross spectrum; the error bars show one standard error given the model. On the right is the expected ratio of an odd field signal to its error when A changes and other parameters remain unchanged.

From the right panel of figure 49, an expected signal to error ratio of five is achieved when $A \approx 8.28 \times 10^{-21}$. This is a conditional threshold of sensitivity to a fixed pattern, not a universal significance of the discovery. When $A = 10^{-20}$ the expected ratio is 6.03. If the effective width of an independent spectral cell is equal to 0.001 Hz, a simple estimate $T \approx 2M/\Delta f$ gives about 94.8 days for both configurations even before taking into account interruptions. This period immediately places demands on the stability of interference and calibration.

The permutation distinguishes between a field and a specific unchanging electronic connection. The usual spatial gravitational field will change sign along with the hypothetical one. Therefore, experiment establishes the general gradient signal and verifies its statistical form; it does not

automatically determine its quantum origin. This requires external source information and additional configurations.

How to separate a field from a common cause in hardware

Two instruments on the same table have many common reasons for correlation. They are combined by reference, power, temperature, reference oscillator and software processing. Even independent meters can respond to one common gravitational disturbance: the movement of mass, a change in pressure, or the redistribution of water. Therefore, the physical network must include service channels and controlled configuration changes. It is useful to move clocks between points, change the length of the base while maintaining some of the electronics, compare different types of clock transitions, and make blind additions of a known signal. Each intervention is selected because the intended field and the specific interference make different predictions for it.

Checking that is done by definition should be avoided. If three relative frequencies are calculated from the same local frequencies, the sum y_ab + y_bc + y_ca is equal to zero algebraically. Successful closure of such a triangle does not confirm the new geometry. It can check the consistency of independent transmission channels, if they are truly independent, but the meaning of the result is then instrumental. Likewise, a high correlation between all pairs is not independent evidence of a universal field: the general error of the standard can create a matrix with the same low rank. Geometric inference requires a response to spatial rearrangements that cannot be reproduced by unchanged general electronics.

The result of a complete physical search must contain the region of valid A, ℓ and τ_c along with the background parameters. The completed example shows the processing of one section of this problem with known ℓ and τ_c. Several bases and frequency bands are needed to restore other parameters; tidal control is needed to infer curvature. If different channels require incompatible parameters, the selected kernel is rejected. If they agree, the next object of study becomes the source of the common field. In the interferometric chapter, the same principle will be applied to a completed light path.

Chapter 12
What can an interferometer hear?

Light measures the completed path

An interferometer compares the phases of light waves that have traveled different paths and then meet again at the detector. It is often depicted as a ruler of extreme precision. For the study of space, such a representation is useful only as a first approximation. The reading depends on the movement of the mirrors, the propagation of light, the phase reference and the reading method. If the theory changes the metric, all of these elements can change in concert. You cannot first declare that space has expanded by a certain amount, and then, without calculation, attribute the same amount to the output of the device. It is necessary to determine which events are compared and which physical phase is returned to the measurement location.

In normal operation, a small change in the difference in arm lengths is associated with a phase shift. For a simple round trip, the coefficient contains 4π/λ_laser, where λ_laser is the laser wavelength. However, this formula applies to specific geometries and low frequencies of mechanical change. In the presence of resonators, light passes through the arm many times, and with fast disturbances, different sections of the path experience different field values. The transfer function acquires frequency zeros and phase delays. Increasing the optical power improves part of the noise budget, but does not restore the physical signal at a frequency to which the selected configuration is insensitive.

$$\delta\varphi \simeq \frac{4\pi}{\lambda_{\mathrm{laser}}}\,\delta L_{\mathrm{diff}} \qquad \text{for a simple two-pass low-frequency regime} \qquad (12.1)$$

Therefore, when designing a geometric probe, the disturbance model is first specified, then the full response is calculated, and only after that the arm length, frequency band and recording method are selected. In some cases, a wide bandwidth is optimal to distinguish the shape of the spectrum. In others, a narrow region of the maximum expected signal is more important. The work of Sharmila, Vermeulen and Datta, published in Nature Communications in 2026, systematically relates several classes of correlations of putative fluctuations to frequency and scale signatures of interferometer output. It confirms the productivity of such a sequence, but does not report the discovery of the quantum structure of space. [33]

Coordinates should not become a signal

The metric of a weakly perturbed space can be written as the sum of the background metric and the small field h_μν. However, the components of h themselves depend on the choice of coordinates. With a small transformation of coordinates, they change to derivatives of the transformation function. If the calculated signal changes only because the researcher has renamed the coordinates, that signal does not match the instrument reading. The calculation must consistently transform light trajectories, mirror world lines, and phase comparison events. The invariant result is a physically

defined phase or proper time, and not an arbitrarily chosen component of the disturbance. This requirement is especially important for hypotheses in which the unusual behavior of space is represented by a single scalar function.

$$g_{\mu\nu} = \eta_{\mu\nu} + h_{\mu\nu}, \qquad h_{\mu\nu} \to h_{\mu\nu} - \partial_\mu \xi_\nu - \partial_\nu \xi_\mu \qquad (12.2)$$

A simple example shows how easy it is to get a false forecast. In the long-wavelength approximation, a standard equal-arm interferometer is sensitive to a certain tensor combination of spatial perturbation. If the unit directions of the arms are denoted by u and v, its geometric tensor is equal to half the difference between u_i u_j and v_i v_j. The trace of this tensor is zero. Consequently, the net equal isotropic deformation of spatial lengths is reduced in such a differential combination. This is not a universal prohibition on recording any scalar field: other components of the metric, the movement of mirrors, unequal arms and the finite wavelength require separate calculations. But the automatic identification of scalar noise with the arm difference already turns out to be incorrect.

$$D^{ij} = \frac{1}{2}\left(u^i u^j - v^i v^j\right), \qquad D^{ij}\delta_{ij} = 0, \qquad h_{ij} \propto \delta_{ij} \Rightarrow D^{ij} h_{ij} = 0 \qquad (12.3)$$

For the general linear model, it is convenient to represent the output of each sensor as a convolution of the field with the response kernel. This core includes spatial path, delays, polarization sensitivity, and conversion to selected reading units. The cross-spectral density of the sensors is then obtained by applying two such kernels to the field correlation. The schematic notation below highlights the structure of the calculation; it does not replace the specific expression for the chosen theory. Until this expression appears, one cannot claim that the device has achieved sensitivity to amplitude h, since even the relationship between h and the measured voltage may still remain uncertain.

$$s_A(f) = \int d^3k \, R_A^{\mu\nu}(\mathbf{k}, f) h_{\mu\nu}(\mathbf{k}, f) + n_A(f) \qquad (12.4)$$

Complete test case with a transverse wave

For the complete calculation, a well-known physical model was chosen: a weak plane transverse traceless gravitational wave in a linear approximation. It provides a strict standard for converting a metric disturbance into phase. Any new hypothesis that reduces in a given strip to the same tensor sector uses the resulting response function; a hypothesis with a different field structure will need its own calculation. The test case itself is not claimed to be a new mechanism of quantum geometry.

$$ds^2 = -c^2 dt^2 + \left[\delta_{ij} + e_{ij} h\left(t - \frac{\mathbf{n}\cdot\mathbf{x}}{c}\right)\right] dx^i dx^j, \qquad (12.5)$$

Vector n specifies the direction of propagation, e_ij is the selected polarization tensor, h is the dimensionless small amplitude. A simple equal-arm interferometer has arms of length L along the unit vectors u and v. The beam splitter is located at the origin, the distant mirrors are at points Lu and Lv. In a transverse traceless system, freely falling mirrors with zero initial coordinate velocity preserve these coordinates in the first order. The time on the beam splitter coincides with its own time.

The last condition completes the model of movement of the ends. Adding another manually assigned “stretch” to the mirrors fixed here would mean counting the same effect twice. If the mirrors are rigidly held or enter the region of mechanical resonances of the gimbal, their world lines will change and a measured mechanical function must be included in response. Next, we consider the free mass in the operating band above significant mechanical resonances and the optical design without Fabry-Perot cavities.

Let t be the time the light returns to the beam splitter, T = L/c and μ = n·u. From the condition ds² = 0 it follows that the small additional travel time is equal to half the integral h_ij u_i u_j along the unperturbed ray, divided by c. For the round trip path, the field argument values are different:

$$I_-(t) = \int_0^L h\left(t - 2T + \frac{(1-\mu)l}{c}\right) dl, \qquad (12.6)$$

$$I_+(t) = \int_0^L h\left(t - T(1+\mu) + \frac{(1+\mu)l}{c}\right) dl, \qquad (12.7)$$

$$\delta T_u(t) = \frac{u^i e_{ij} u^j}{2c}\left[I_-(t) + I_+(t)\right] \qquad (12.8)$$

In the first integral, the photon moves from the beam splitter, and in the second, from the distant mirror. The correction to the trajectory itself inside the already small h does not need to be taken into account in this order: it gives the following order. The two beams are compared after returning to the same event at the beam splitter, so the result refers to the completed measurement. The exact response through the light path time and its difference from the long-wavelength approximation is discussed in detail in the primary work of Rakhmanov, Romano and Whelan. [44]

The closed light path of a simple interferometer and the three events of a single round trip are shown in Figure 50.

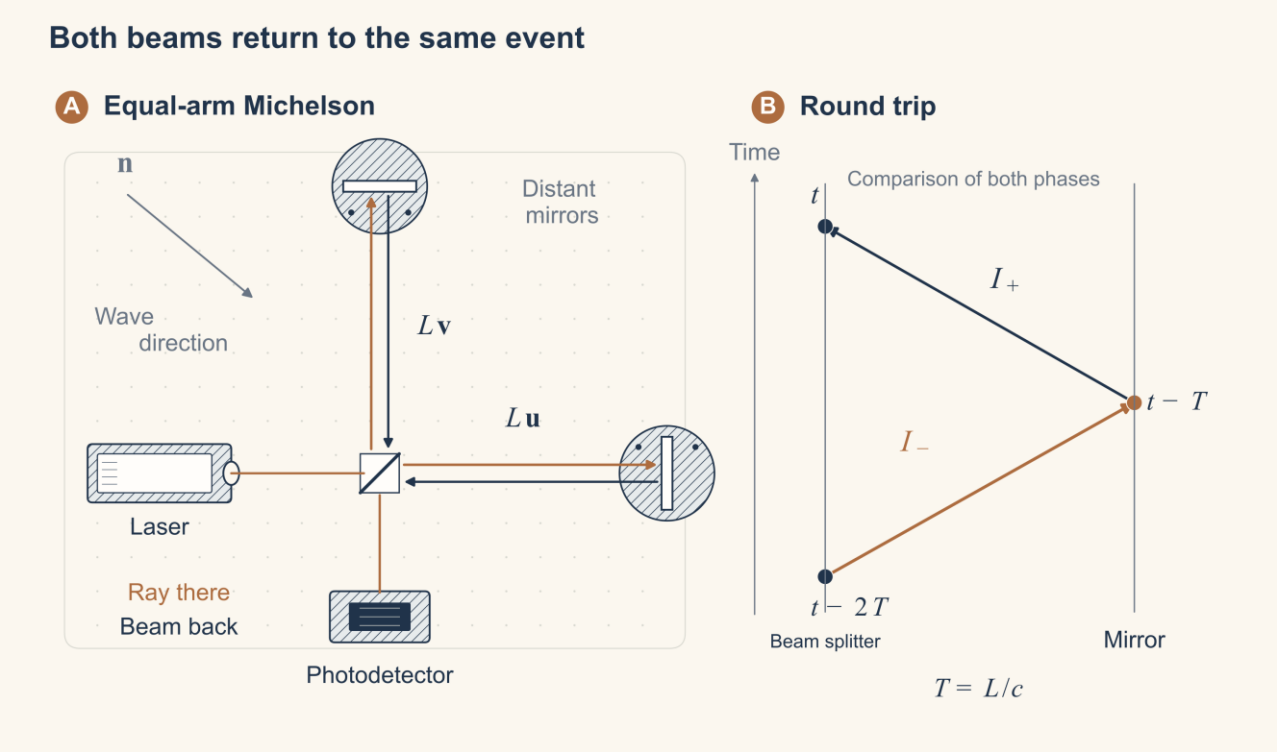


Figure 50. In a simple equal-armed Michelson, each ray travels a distance L to the far mirror and L back. The copper and blue sections separate the forward and reverse strokes; in the drawing they are slightly spaced for readability. The right figure captures the departure, reflection, and return of the overall phase comparison event. The conditions for the movement of the mirrors correspond to the free masses in the selected TT model. There are no Fabry-Perot cavities. For an oblique wave, the different field arguments along I_- and I_+ are preserved in integrals rather than being replaced by a single time.

Frequency and direction enter into the measured response

Let's substitute h(t) = h_ω exp(−iωt). Each integral (12.6) and (12.7) is an integral of an exponential over a finite segment. Let us introduce Ω = ωL/c and sinc(z) = sin(z)/z with a continuous value sinc(0) = 1. Then

$$\delta T_u = T\left(u^i e_{ij} u^j\right) \mathcal{T}(\Omega, \mu) h_\omega e^{-i\omega t}, \qquad \mathcal{T} = \frac{t_- + t_+}{2}, \tag{12.9}$$

$$t_- = e^{i\Omega(3+\mu)/2} \operatorname{sinc} \frac{\Omega(1-\mu)}{2}, \qquad t_+ = e^{i\Omega(1+\mu)/2} \operatorname{sinc} \frac{\Omega(1+\mu)}{2} \tag{12.10}$$

Positive phase factors reflect that the field along the path was observed before the light returned; the sign corresponds to the accepted exp(−iωt). As Ω → 0 both factors tend to unity. Let us define the positive phase lag as ω_laser(δT_u − δT_v). The arm difference gives

$$\widehat{\delta\varphi} = \frac{4\pi L}{\lambda_{\text{laser}}} \mathcal{F}(\omega, \mathbf{n}, e) h_\omega, \tag{12.11}$$

$$\mathcal{F} = \frac{1}{2}\left[\left(u^i e_{ij} u^j\right)\mathcal{T}(\Omega, \mathbf{n}\cdot\mathbf{u}) - \left(v^i e_{ij} v^j\right)\mathcal{T}(\Omega, \mathbf{n}\cdot\mathbf{v})\right] \qquad (12.12)$$

This takes into account the light path, tensor sensitivity and the selected movement of the mirrors. The function F is dimensionless. With normal incidence on the plane of orthogonal arms and polarization e_xx = 1, e_yy = −1, it reduces to a particularly simple form:

$$\mathcal{F}_\perp = e^{i\Omega}\mathrm{sinc}(\Omega), \qquad f_{\mathrm{null},1} = \frac{c}{2L} \qquad (12.13)$$

The first zero occurs when different sections of the complete light path cancel each other out. For L = 40 m this is 3.7474 MHz. At this frequency, the chosen normal plane wave does not create a first-order differential phase, although the field itself is non-zero. The tilt changes the phase along the arms, so the zeros and amplitudes of other directions are different. In the program, the normal limit is checked against a general formula; on the calculation grid the discrepancy does not exceed 4.1×10^{-16} in dimensionless amplitude.

The mechanism of the first zero of the transfer function can be seen as the compensation of the full path contributions in Figure 51.

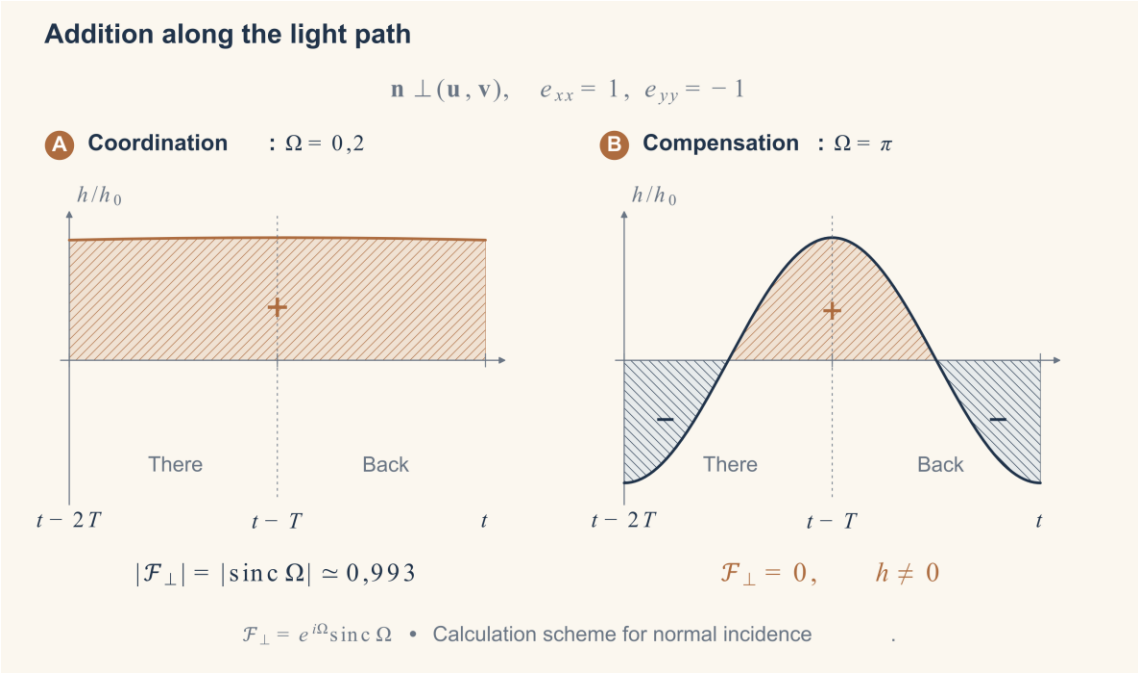


Figure 51. The actual quadrature of the harmonic TT wave is shown at normal incidence and polarization e_xx = 1, e_yy = −1. The phase zero is chosen in the middle of the full path: the integrand is proportional to cos[Ω(t′ − t + T)/T]. At Ω = 0.2 the contributions are almost consistent; at Ω = π, positive and negative areas cancel each other out. The odd quadrature also integrates into zero. Therefore F⊥ = 0 for a non-zero field. This is an exact calculation diagram, not a detector recording; for other directions the zeros change.

If the amplitude h is a stationary random process of one given direction and polarization, its spectrum is converted to S_φ by multiplying by |4πLF/λ_laser|². For the distribution of directions and polarizations, the corresponding integral will be required, and for a pair of installations, the spatial phase between them will also be required. Thus, the calculated answer refers to the precisely

named sector of the model; it does not serve as a universal converter of any scalar or "holographic" fluctuation into length noise.

Conditional numerical budget of a simple interferometer

Let's take L = 40 m, laser wavelength 1064 nm, optical power at the input of the reading photodetectors 10 mW and quantum efficiency η = 0.8. For an idealized balanced readout in quadrature, we set the one-sided phase power spectral density of Poisson noise S_φ,shot = 2/Ṅ, where Ṅ = ηP/(hν) is the effective flux of detected photons. Power here refers to the readout and not automatically to the power in the long arms or inside the resonator.

$$\dot{N} = \frac{\eta P \lambda_{\mathrm{laser}}}{hc}, \qquad \sqrt{S_{\varphi,\mathrm{shot}}} = \sqrt{\frac{2}{\dot{N}}} \qquad (12.14)$$

Additionally, we assign independent technical and electronic phase noise 10^{-8} and 3×10^{-9} rad/√Hz. These are conditional constant levels in the band under consideration. Addition in quadrature gives the total phase noise. In a real instrument, the noise may be colored and correlated, and its measured transfer functions will replace these simple constants.

The square root of the power spectral density is called the amplitude spectral density (ASD). For phase noise, its unit is radian per square root of hertz. In the table below, all noise components are reduced to one such value.

Component	Accepted or calculated value
Effective photon flux	4.2850×10^{16} s^{-1}
Poisson phase ASD	6.8318×10^{-9} rad/√Hz
Technical phase ASD	1.0000×10^{-8} rad/√Hz
Electronic phase ASD	3.0000×10^{-9} rad/√Hz
Total phase ASD	1.2477×10^{-8} rad/√Hz
Phase coefficient at F = 1	4.7242×10^{8} rad per unit h

$$\sqrt{S_h^{\mathrm{equiv}}(f)} = \frac{\sqrt{S_{\varphi,\mathrm{total}}(f)}}{|4\pi L \mathcal{F}(f)/\lambda_{\mathrm{laser}}|} \qquad (12.15)$$

At the low frequency limit of normal incidence, the equivalent strain noise is 2.6411×10^{-17}/√Hz. At 1 MHz it is equal to 2.9778×10^{-17}/√Hz, at 3 MHz it is 1.1328×10^{-16}/√Hz, and at 10 MHz - 2.5653×10^{-16}/√Hz. This is not a measured result from an apparatus. The difference in numbers occurs with constant phase noise only due to the calculated frequency dependence of the response.

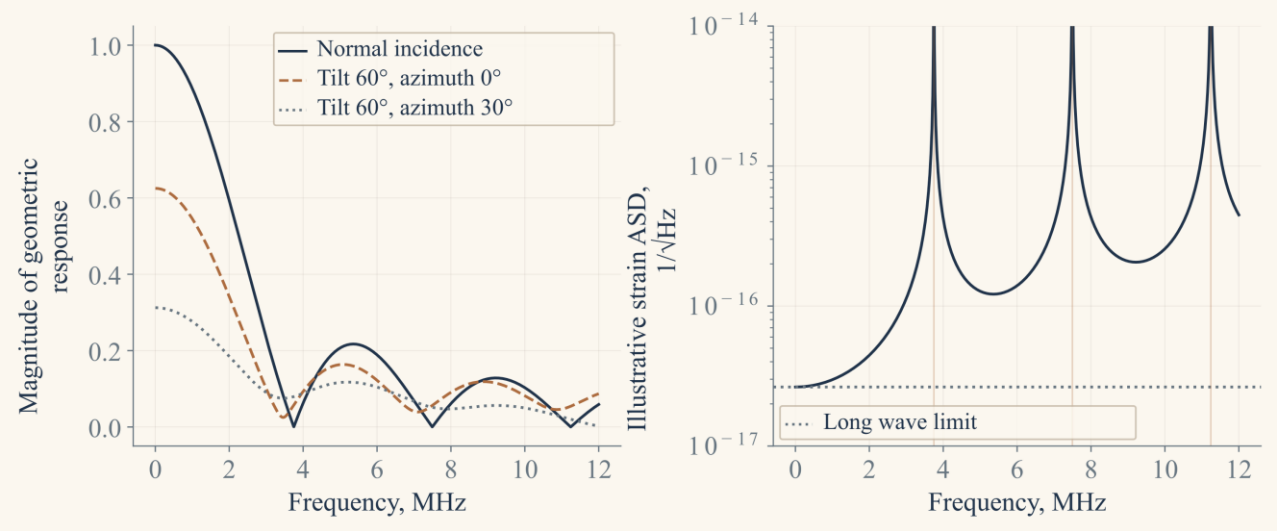


Figure 52. Response of a simple 40-meter interferometer to a selected TT polarization. On the left is normal and two oblique directions; on the right is the equivalent strain noise for normal incidence at a given phase budget. The verticals mark geometric zeros. Near zeros, the phase transition in h becomes unstable.

Figure 52 shows why optimization must take into account the form of the hypothesis. Increasing the power reduces the Poisson contribution, but does not remove the geometric zero. Changing the length or direction adds information that is not present in insensitive mode. For a conditional stochastic TT field, the table allows you to specify the spectrum in the band and calculate the expected data; For a new fluctuation mechanism, you first need to check whether its field really belongs to this sector.

A simple budget does not include cavities, radiation pressure, squeezed light and technical losses of a complex optical path. They should be added when choosing the appropriate implementation, preserving the calculated meaning of the phase. Here the task is completed at the selected level: the field, the light path, the freely moving mirrors, the response function and all the numbers of the assigned noise example are connected by one chain.

The correlation must be mathematically valid

A network of interferometers is useful in that a hypothetical field can produce consistent signals, while some of the instruments' own noise is independent. But an arbitrary table of desired correlations does not necessarily describe a possible random process. At each frequency, the spectral matrix must be Hermitian and non-negative definite. For a pair of channels, this follows a familiar restriction: the square of the modulus of the mutual spectrum does not exceed the product of its own spectra. If the model violates this condition, no increase in measurement time will make it physically meaningful. The positivity check must be performed for the entire network matrix, since the validity of individual pairs does not guarantee the validity of the overall population.

$$\mathbf{S}(f) = \mathbf{S}^{\dagger}(f), \qquad \mathbf{z}^{\dagger}\mathbf{S}(f)\mathbf{z} \geq 0, \qquad |S_{AB}(f)|^2 \leq S_{AA}(f)S_{BB}(f) \qquad (12.16)$$

To test algorithms, you can use a known valid pattern of output correlations. Let $S_0(f)$ be the non-negative spectral density of some scalar process, and the spatial kernel equal to the exponential

minus the square of the distance. Multiplying the kernel by the complex response coefficients R_i and their conjugates retains positivity. This template is useful for blind digital inputs, estimating the separation of independent and total noise, and planning bases. It describes the possible statistics of signals, but does not yet prove that these signals are capable of generating physically consistent fluctuations of the metric. The transition from the template to the gravitational interpretation requires a previous calculation of the light paths.

$$S_{ij}^{\text{template}}(f) = R_i(f)R_j^*(f)S_0(f)\exp\left(-\frac{d_{ij}^2}{2\ell_c^2}\right), \qquad S_0(f) \geq 0 \qquad (12.17)$$

For the same reason, you cannot assign an additional arbitrary coefficient for each angle and distance and then call a successful fit a discovery of geometry. Rotating the device should change its response according to the general field model. The separation of instruments should change the correlation consistent with the same spatial structure. If rotation simultaneously changes wiring, fiber tension, and cooling conditions, the observed difference is not a pure geometric test. The design of a series of experiments should provide several different interventions: some predominantly change the intended physical response, others - specific instrumental communication pathways. Only a comparison of such series makes it possible to distinguish the causes of the common signal.

What Holometer showed

The Fermilab Holometer was specifically designed to capture rapid, correlated changes in differential position. The description of the 2017 installation shows two adjacent independent interferometers with arms of about 40 meters and correlation reading up to tens of megahertz. The 2021 work used a configuration where one arm of each 39 meter interferometer was bent for sensitivity to specific rotational perturbations. The findings constrained a specific model of spatially consistent rotational fluctuations. These experiments show that an unusual hypothesis can be turned into a testable spectral prediction. They do not mean that any possible quantum properties of space are excluded. [31] [32]

Particular care should be taken when comparing the strain spectral density with the Planck time. Deformation is dimensionless, so its spectral density has the dimension of time; the comparison of units here is correct. But the sensitivity of spectral density is not equal to the instantaneous distance measurement error expressed in meters. To go to dispersion, you need to integrate the spectrum in the specified band and take into account the spatial response. To move to the parameters of the quantum model, additional assumptions about normalization and correlations are required. The phrase about Planck sensitivity without these clarifications easily creates the erroneous impression that the apparatus directly distinguishes individual segments of the Planck length.

The practical lesson is also the limitations of every negative outcome. A configuration that is sensitive to one perturbation symmetry may have little or no response to another. If a theory changes form after each exception, it is necessary to record openly which previous version is rejected and which new assumption is added. For a future program, it is more useful to compose in advance a set of truly different models and calculate the response of each to several configurations. Then the new experiment reduces the explanatory space in a certain way. Without such an account, even high

accuracy risks remaining a number that is difficult to translate into knowledge about the structure of space.

QUEST and GQuEST as different measurement strategies

In the first published QUEST series, two benchtop interferometers were used to search for correlated length fluctuations. Patra et al reported limits in the region 13 to 80 megahertz; the accumulation lasted 10^4 seconds, and the reduced strain sensitivity at 40 megahertz was 3×10^{-20} per square root of hertz. The same work indicates the design sensitivity of a separate interferometer 2×10^{-19} meters per square root of hertz over a wider band. These are different quantities with different units and status: the project, the measured result and the result of correlation averaging cannot be replaced with each other. [34]

A separate direction of development for QUEST is related to squeezed light. Bergamin et al., in 2025, examined a source designed for such an application and recorded up to 6.8 decibels of squeezing; no less than 3 decibels remained in the studied band 100 megahertz. These values characterize the specific optical source and measurement procedure. Once incorporated into a large device, some of the benefit may be lost due to optical loss, phase noise, and mode mismatch. Therefore, the source characteristics cannot be automatically recorded in the specification of the finished interferometer. This is an example of step-by-step confirmation: first a component, then a subsystem, then a complete scientific channel. [35]

GQuEST uses a different readout idea: isolating and counting photons associated with a suspected disturbance, instead of the usual detection of a small phase against a background of a strong optical field. The paper 2025 by Vermeulen et al. presents the project being implemented and evaluates its benefit for selected geontropic fluctuation models. This is a study of the project and expected information, not a message about the detection of quantum gravity. The method requires its own assessment of background photons, detection efficiency, filtering and losses. Claiming to overcome the limitations of a particular interferometric sensing method does not mean the elimination of all quantum and technical measurement limitations. [36]

These directions show why you cannot choose a device based on one record number. The correlation scheme, squeezed light and photon counting solve different problems and have different weaknesses. For your own hypothesis, you should calculate the expected output statistics and compare the methods with the same physical signal, time and realistic losses. If one approach produces a narrower band, its gain in amplitude may be accompanied by a loss of information about the shape of the correlation. If the other retains a broad spectrum, it is the waveform that can help distinguish the hypothesis from the background. The criterion becomes the ability to distinguish between explanations, rather than a single sensitivity figure.

The difference between the three operations on the measuring signal is shown in Figure 53.

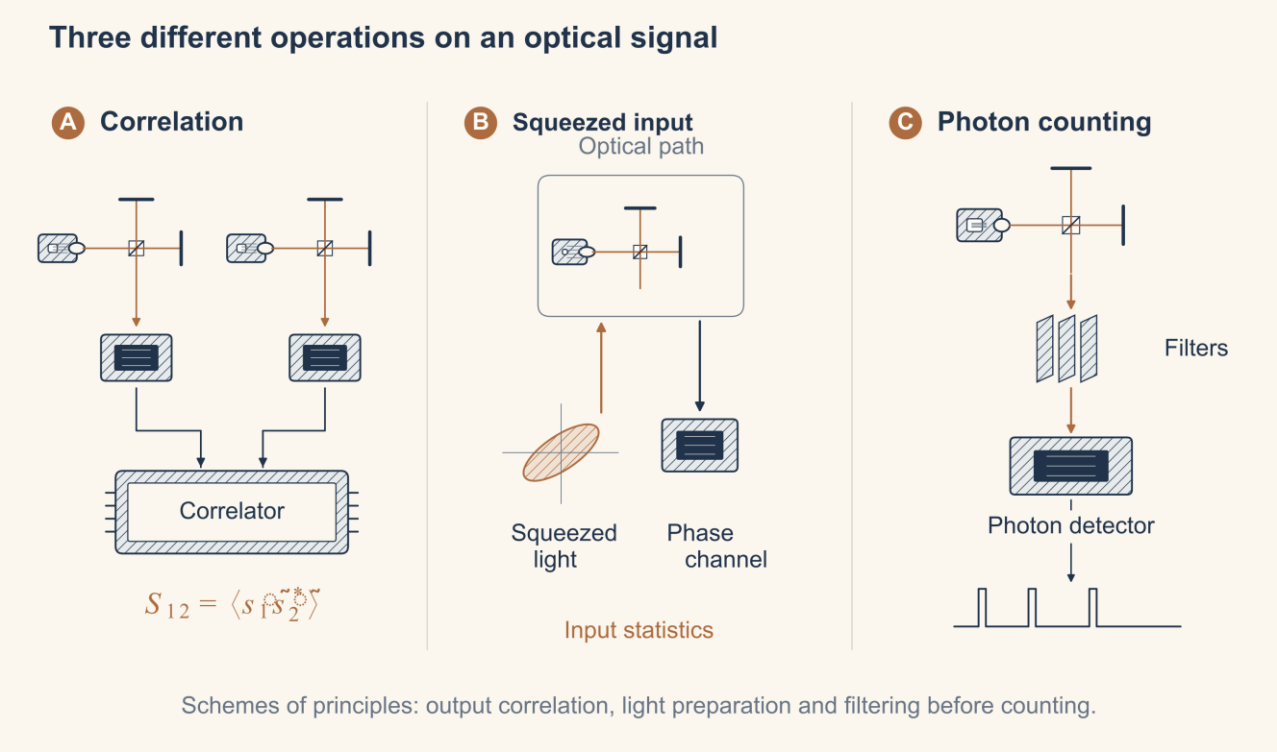


Figure 53. On the left, two independent interferometric outputs feed into cross-spectrum estimation. At the center, the prepared squeezed light changes the quantum statistics of a single optical input; The symbolic arrows indicate operations rather than a complete map of ports. On the right, optical filtering precedes the detection of individual photons. The principles of the three strategies are shown, not the exact wiring diagrams of Holometer, QUEST or GQuEST. The gain of each approach requires its own estimate of loss, band, background, and output statistics.

Why averaging does not replace control

With independent noise, the average mutual spectrum of two channels tends to zero, and the random error in its estimation decreases with the number of independent samples. In the approximation of a weak signal and Gaussian independent noise, the variance of the real part of the estimate is of the order of the product of the autospectra divided by twice the number of averages. This raises an important distinction: the spectral power threshold improves approximately as the inverse square root of time, while the amplitude spectral density threshold of a stochastic signal improves as the inverse of the fourth root of time. This is not a law for all measurement methods, but a consequence of the specified correlation procedure. Optimal correlation methods and the role of total noise are developed in detail in the work of Allen and Romano. [37]

$$\mathrm{Var}\left[\mathrm{Re}\hat{S}_{12}\right] \simeq \frac{S_{11}S_{22}}{2M}, \qquad M \sim T\Delta f \quad \text{for independent effective averages} \qquad (12.18)$$

The general interference does not disappear with such accumulation. On the contrary, its assessment is becoming more accurate, and statistical confidence in the presence of a correlation is growing. Therefore, every promise to improve sensitivity over time must be accompanied by a question about the margin of systematic error. Independent reference oscillators, channel swapping,

electrical interference control, optical path-occluded measurements, and deliberate targeting of suspected noise sources are useful. However, no control is universal: blocking the light changes the detector's mode, and rearranging the electronics can leave an overall mechanical connection. Conviction arises from a coherent set of tests selected for specific alternative explanations.

A scientific result requires a map of the output as a function of frequency, length, and configuration. The completed TT example shows how to obtain such a map from the physical field and how to detect blind installation modes even before assembly. Correlation searches test broader statistical models but use the same sequence: computed response, measured noise, and preselected differences between explanations. The next chapter translates this approach into engineering dossiers and a full workshop on an accessible RC network.

Chapter 13
Three instruments and the path from signal to inference

The measured quantity defines the project

The geometric hypothesis has to be translated into the language of output signals: voltage, angle, frequency ratio. Each such translation has its own exact price. An initial state preparation error in an electrical network can look like a different propagation. Moving the source of mass slightly changes the calculated force. A common generator can link clock readings that were thought to be independent. Therefore, instrument design begins with determining what data it produces and how much of the output is based on individually measured parameters.

This chapter examines three levels of research. The electrical grid makes it possible to experience restoration of connectivity in a system whose design can be intentionally changed. A mechanical sensor checks the law of interaction of material bodies. A network of clocks and gravimeters compares the potential and gradient channels in a common band. What they have in common is a procedure: specify a model, calculate an indication, obtain a calibration, and test a competing explanation. Moving to the next level requires its own data.

Project	Direct data	Verifiable result
RC network	Node voltages after known preparation	Distinction between additional and ordinary connections in an artificial system
Mechanical sensor	Angle or offset and phase of harmonic response	Limitation of the chosen force law with a known geometry
Clock and gravimeter	Frequency ratios and acceleration in the common band	Compatibility of two channels with a given common field

The electrical level below has been brought to an executable workshop: the original recordings and the program for processing them are attached. All these recordings are synthetic. For the other two directions, estimated budgets and transfer conditions to a real installation are given. This allows us to separate the numerical experiments that have already been performed from the hardware characteristics that have yet to be measured.

Electrical connectivity spectrometer

Each node of the electrical prototype contains a capacitor connected to a common reference conductor. There are resistors between the nodes. The voltages are equalized at rates determined by the conductances of the connections and the capacitances of the nodes. After turning off external sources, the circuit implements linear propagation, convenient for testing the inverse problem. The

network approach has predecessors: Nokkala, Piilo and Bianconi investigated the determination of spectral dimensionality through low-frequency modes of a network of quantum oscillators. The RC model uses classical dynamics and solves its own measurement problem. [38]

$$C_i \frac{dV_i}{dt} = \sum_j g_{ij}\left(V_j - V_i\right) - g_{i0}V_i + I_i(t), \qquad \mathbf{C}\dot{\mathbf{V}} = -\mathbf{K}\mathbf{V} + \mathbf{I} \tag{13.1}$$

Conductance g has units of siemens, capacitance C has units of farads, and the ratio g/C has units of reciprocal seconds. With equal capacitances C_0 and no leakage, the operator $L=K/C_0$ is symmetrical. Preparing the voltage at node j only and then observing node i gives the matrix exponential element. The full set of preparations reveals the propagation matrix; several available ports provide only its observable block.

$$\mathbf{V}(t) = e^{-t\mathbf{L}}\mathbf{V}(0), \qquad \mathbf{G}(s) = (s\mathbf{I} + \mathbf{L})^{-1} = \int_0^\infty e^{-st}\, e^{-t\mathbf{L}}\, dt \tag{13.2}$$

The simplest complete example consists of four nodes connected in a chain. Each has a capacitor 100 nF, and between neighbors there is a resistor 100 kOhm. The nominal time of one link is 10 ms, the connection intensity is 100 s^{-1}. For the control experiment, an additional resistor 500 kOhm is installed between the ends of the circuit, that is, a connection with an intensity of 20 s^{-1}. These values determine the design layout; The accuracy of finished components and meters does not follow from them.

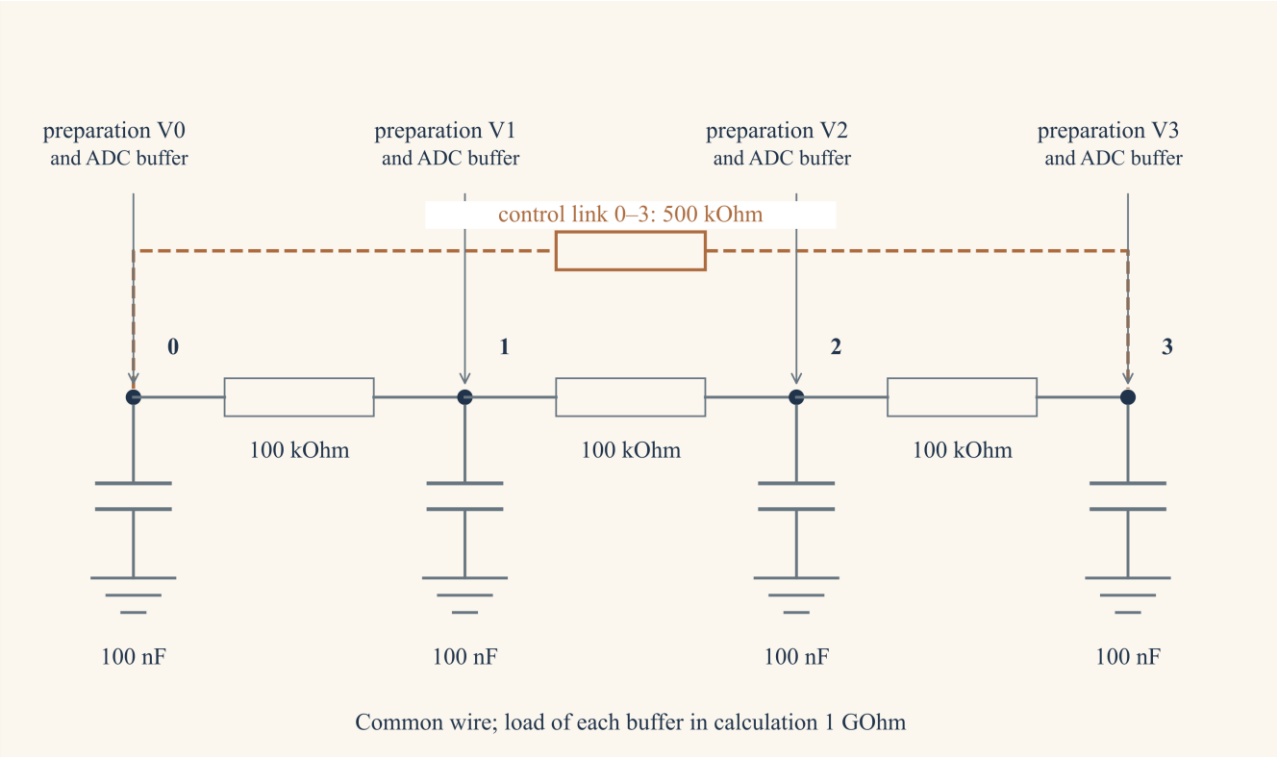


Figure 54. Four-node RC layout. Conventional connections have a nominal value of 100 kOhm, each node - 100 nF relative to the common wire. Orange shows the additional connection 0-3 via 500 kOhm. Arrows indicate preparation and high-resistance readout channels; intersections without nodes do not form electrical connections. In the numerical example, the load of each input is equal to 1 GOhm.

Figure 54 shows the reason for choosing a small layout: all nodes are known, four independent states can be prepared and the entire response can be measured. In the large network from chapter 8 there is no such access. The small experiment first checks the normalization and statistics of measurements; After this, the number of ports can be reduced and observed which differences are no longer available.

The connection with the current method is also clear. At zero initial state, the transfer matrix from current to voltage is equal to $H V I(s)=(sC+K)^{-1}$. For identical capacitances $G(s)=C_0 H V I(s)$. The first matrix is measured in ohms, the second - in seconds. Therefore, the numerical noise in G cannot be directly declared as a requirement for the accuracy of the voltmeter. It is necessary to take into account the excitation, capacitance, recording time and method of estimating the integral.

An end-to-end experiment with blinded labels

The “From Voltage to Connectivity Reconstruction” workshop uses four initial preparations around 1 V. The preparations are slightly mixed: a small voltage is also present in neighboring nodes. Their actual matrix is included in the calibration in advance. The readout has a known identical leakage corresponding to the input impedance 1 GΩ. An independent Gaussian noise with a standard deviation of 0.2 mV is added to each sample. This noise describes the adopted digital example, not the promised performance of a particular analog-to-digital converter (ADC).

For each preparation, a recording with a duration of 0.25 s was obtained with a step of 50 μs. The processing restores the normalized response at s=20, 60 and 200 s^{-1}, taking into account the mixing of initial states, load and the common finite interval. Since the three integrals are calculated from the same records, their errors are correlated. For example, the correlation for the first two values of s is 0.866. The full covariance is passed into the fit rather than three independent estimates.

Before analysis, one contrast between the ends of the chain is selected. It gives the scalar reading $z=a^{T} G(20) a$, where $a=(1,0,0,-1)/\sqrt{2}$. For any combination of ordinary conductances within ±2%, a strict shell of its possible values is known. In this layout it extends from 11.10052 to 11.43981 ms. To this is added the calculated noise margin, finite tail and numerical integration. The rule does not require trying out all possible drift patterns.

Record	Contrast at s=20 s^{-1}, ms	Rule Result	Markup after analysis
A	7.75782	Limited local model rejected	Drift and communication 0-3
B	11.26718	Valid local model compatible	Reference circuit
C	11.23150	Valid local model compatible	Drift of ordinary connections

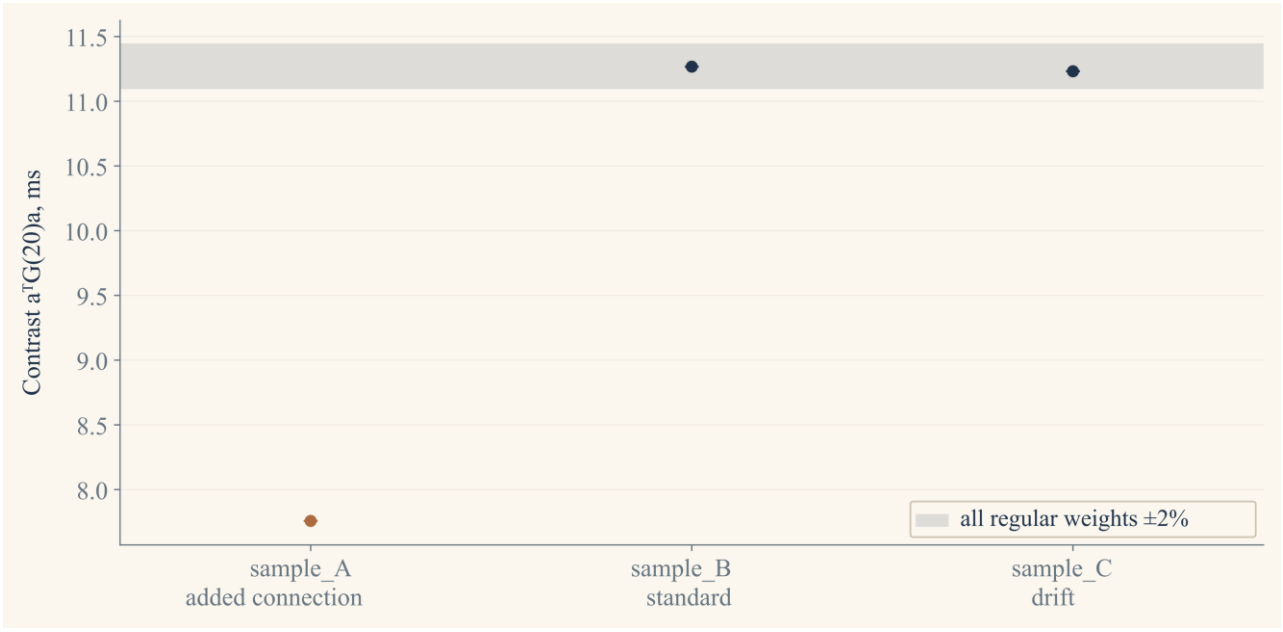


Figure 55. Synthetic verification of three records. The band contains possible contrasts of all common conductances within ±2%. The bars include five standard errors, a tail bound, and quadratures; at this scale they are small. The markings under the letters are revealed after the analysis is completed. The analysis program does not read the file containing the true parameters.

In Figure 55, the additional coupling is chosen to be strong enough so that its effect confidently goes beyond the permissible calibration interval. Fitting the extended model determined the pair 0-3 and the intensity 19.9974 s^{-1} with the introduced 20 s^{-1}. The ratio of χ^2 to 48 scalar observations is equal to 0.871. In the other two cases, an additional edge is not required to explain the data. This is not equivalent to proving the absence of any connection, no matter how weak.

Discriminability here is significantly better than in the difficult example of a large network. All four nodes are observable, the initial states are known, and the added conductance is 20% of the usual one. The workshop shows the operation of the entire measuring chain in the selected mode. It does not measure universal reconstruction accuracy and does not invalidate the calibration counterexample of chapter 8. The next step is to deliberately reduce access to nodes or weaken the connection and trace the applicability boundary of the same rule.

The components and meter enter the operator

In the assembled circuit, the equality of capacitances will have to be checked. For unequal C_i, the $C^{-1}K$ matrix is usually asymmetric in voltage coordinates. The symmetric operator appears after the replacement $u=C^{1/2}V$. Dot products and probe normalizations must correspond to this replacement. The full trace under the similarity transformation is preserved: the normalized diagonal voltage responses still give the trace of the exponential, but the operator and the stationary mode projector must be calculated with the actual capacitances. If we continue to fit the equal capacitance model, component differences will be mistakenly attributed to connections.

$$\mathbf{L}_{\mathrm{sym}} = \mathbf{C}^{-1/2}\mathbf{K}\mathbf{C}^{-1/2}, \qquad \mathbf{u} = \mathbf{C}^{1/2}\mathbf{V} \tag{13.3}$$

The input impedance and the capacitors' own leakage add coupling to the common wire. For equal leakage, L becomes L+γI. Then the return signal receives a multiplier exp(−γt), and the estimate of the spectral dimension increases by 2γt. In the design model, γ=0.01 s^{-1} is known in advance and is removed during processing. An unequal unknown leak cannot be corrected by such a scalar correction: it must enter the matrix of the measuring operator.

$$\widetilde{P}(t) = e^{-\gamma t} P(t), \qquad \tilde{d}_s(t) = d_s(t) + 2\gamma t \qquad (13.4)$$

Preparation also requires calibration. Low-impedance sources hold four set voltages and then open simultaneously. The resistance of the switches, unequal opening times and the release of charge change the initial vector. In the workshop, instead of an ideal unit vector, a measurement preparation matrix W is used. If it is invertible and well-conditioned, the propagation is restored by multiplying the recorded voltages by W^{-1}. Here the condition number is 1.0049, so the operation adds almost no noise. With almost identical preparations, the inversion would become unreliable.

In Figure 56, the physical network is included in the complete preparation and high-impedance digital registration path.

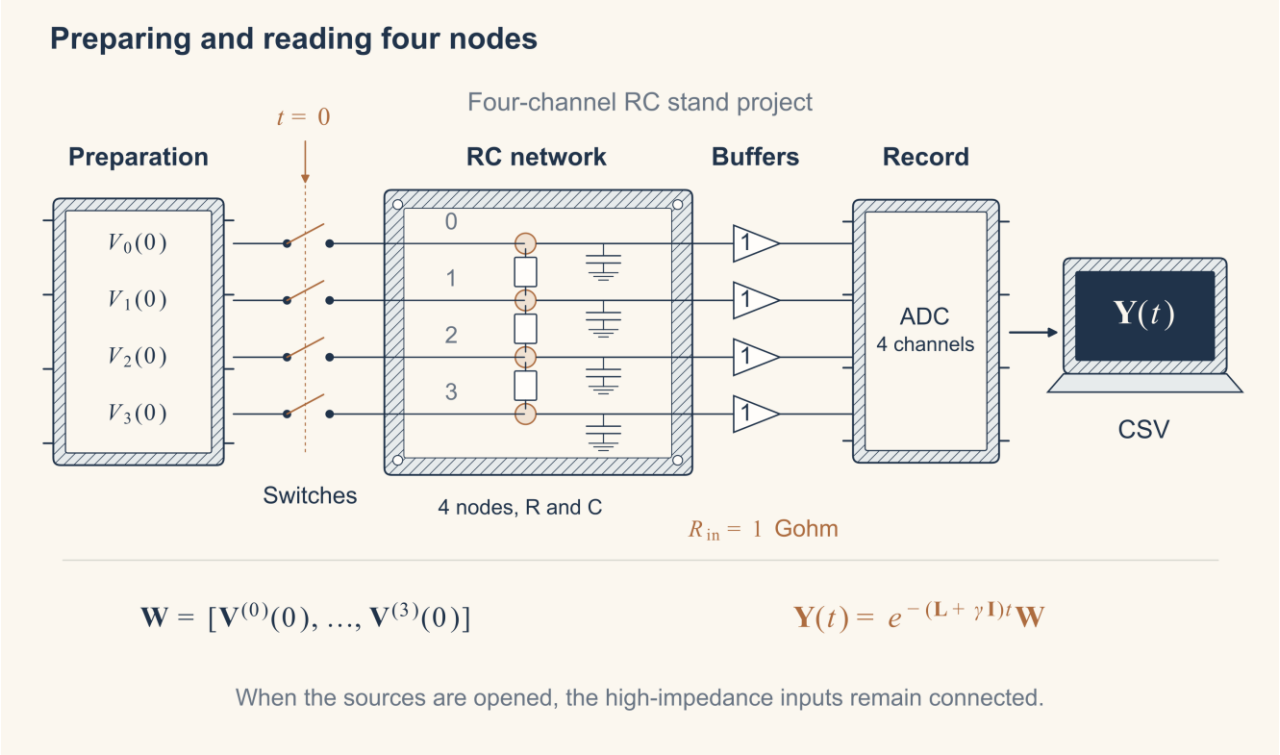


Figure 56. Four sources hold the full initial vector, then four switches are opened by a single event. Monitoring continues through separate high-impedance buffers and ADCs. The value R_in = 1 GΩ refers to the input load of the design example; it does not mean there is no leakage. Matrix W contains the actual prepared states, and Y(t) contains the recorded voltages. The board is shown as a modern stand design; The exact topology and capacitors are disclosed separately in the circuit diagram. Connecting the low impedance input directly to the nodes would change the operator.

Thermal noise in resistors is due to dissipation. For a single resistance in the classical mode, the one-sided voltage power spectral density is equal to 4kBTR. In a network, intrinsic current noise passes through a common operator and creates correlations between nodes. NIST noise thermometry

measurements show how significant frequency response matching, crosstalk, and readout noise separation are. [46] [47]

The layout budget must separately consider the uncertainty of W, capacitance, leakage, gain, and time scale. The random part can be carried through covariance. Systematic uncertainty should be included in the admissible class of models or assessed on an interval basis. In the attached data, these calibration values are specified precisely, and ±2% refer only to ordinary conductances. To apply the same wrapper to a physical circuit, the remaining errors must be independently constrained and added to the margin.

Mechanical specifications and an illustrative torque budget

A controlled mass source creates a varying torque, and a sensing element, such as a torsional oscillator, turns it into an angle. For small vibrations, the moment of inertia I, stiffness κ and viscous damping coefficient b are used. The amplitude and phase of the mechanical susceptibility determine the translation of the optical reading into the moment. They are tested over an operating range with known exposure.

Figure 57 relates the layout of a torsional sensor to the sequence of converting torque into a measured signal.

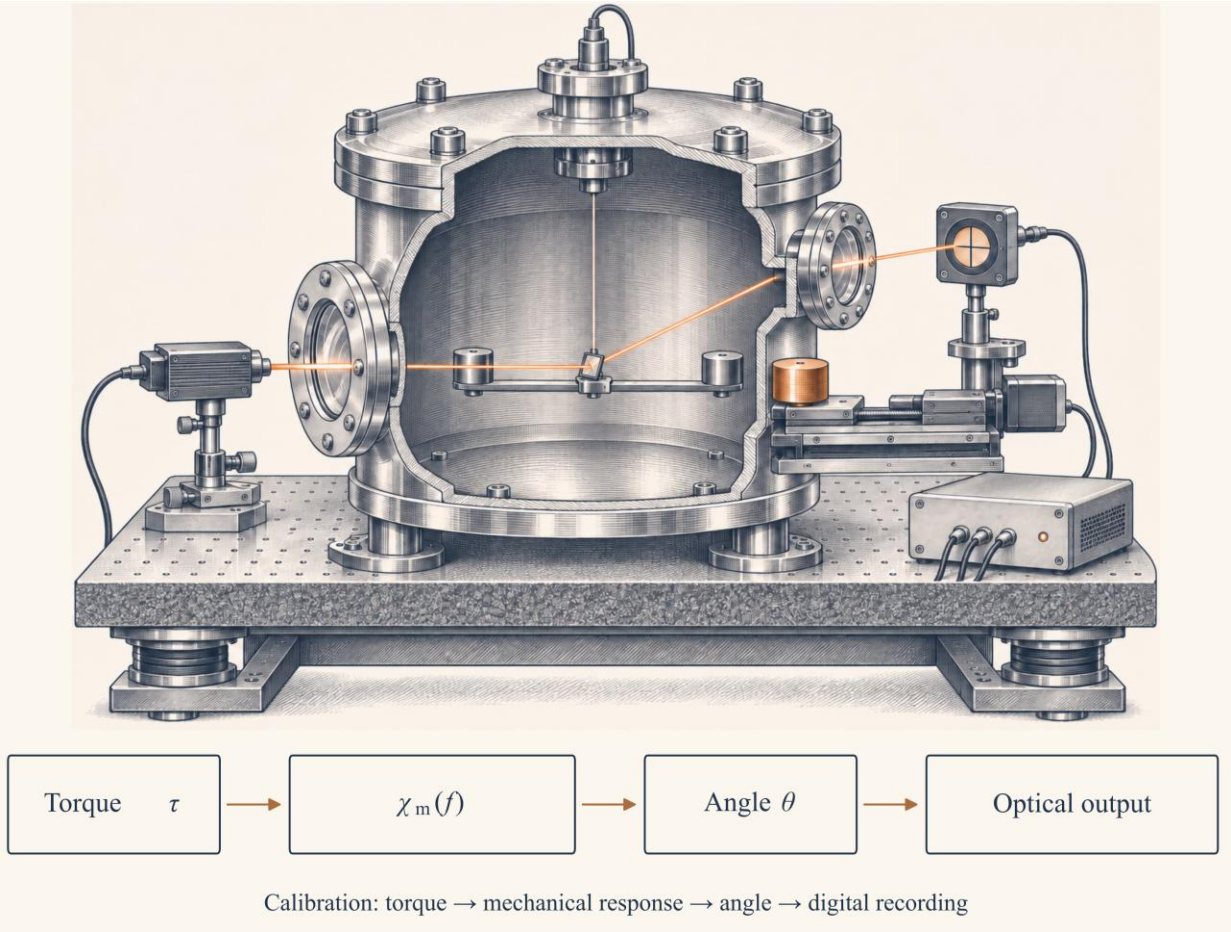


Figure 57. Concept of a modern torsional sensor. The sensing beam is suspended by a thin thread in a vacuum housing; the controlled mass creates the torque, and the laser readout registers the angle. The lower chain separates torque, mechanical susceptibility, angle and recorder output. This is an illustration of a possible layout: the dimensions, shielding and sensitivity of the constructed device are not stated here. The conditional low-frequency budget in the text does not carry over to the two-disc experiment of the chapter 10.

$$I\ddot{\theta} + b\dot{\theta} + \kappa\theta = \tau(t), \qquad \chi_{\theta\tau}(\omega) = \frac{1}{\kappa - I\omega^2 + ib\omega} \qquad (13.5)$$

Below, a low-frequency standard is selected for calculation, and not a specification of existing equipment. Let $I=10^{-6}$ kg m², natural frequency $f_0=0.01$ Hz, quality factor $Q=1000$, temperature 300 K. The source is modulated at $f=0.005$ Hz, and the optical reading noise is assumed to be 10^{-8} rad/√Hz. For viscous damping $\kappa=I(2\pi f_0)^2$ and $b=I2\pi f_0/Q$. These assumptions complete the calculation of the simple model.

$$S_\tau^{\text{th}} = 4k_B T b, \qquad S_\tau^{\text{ro}}(f) = \frac{S_\theta^{\text{ro}}(f)}{|\chi_{\theta\tau}(2\pi f)|^2} \qquad (13.6)$$

Magnitude	Calculated value
Torsional stiffness κ	3.948×10^{-9} Nm/rad

Magnitude	Calculated value
Coefficient b	6.283×10^{-11} N m s/rad
Susceptibility module at 0.005 Hz	3.377×10^{8} rad/(Nm)
Thermal torque ASD	1.020×10^{-15} Nm/√Hz
ASD reading in torque units	2.961×10^{-17} Nm/√Hz
Amplitude error for 10^{5} s with known phase	3.228×10^{-18} Nm

The last line is obtained to estimate the amplitude $2T^{-1}\int\tau(t)\cos(2\pi ft)dt$ for many periods and stationary white torque noise. For the accepted one-sided density, its dispersion is approximately equal to $S\tau(f)/T$. If both quadratures are unknown, the modulus distribution and detection rule change. For arm 1 cm, the indicated torque error corresponds to a force harmonic error of about 3.23×10^{-16} N.

This calculation helps estimate the distance between a simple mechanical layout and a specific search requirement. The illustrative force example of the chapter 10 specifies its geometry, modulation frequency and required error. The low-frequency torsional standard does not automatically obtain these characteristics: the transfer requires recalculating the susceptibility, the force-torque relationship, and the total error. A higher source frequency can dramatically weaken its angular response.

Viscous damping is chosen here as an explicitly defined model. For internal structural friction, the frequency law of thermal noise is different; the relevant distinction is discussed in detail by Saulson. Therefore, the measured quality factor at one frequency does not yet determine the entire spectrum. [48]

The main part of the real budget may be systematic. The clearance error δd changes the predicted torque by $(\partial\tau/\partial d)\delta d$; for a short-range correction, this change can simulate the desired effect. Screen motion, surface potentials, vibrations, density and source dimensions are tested separately. They are not included in the calculation of the table. The first hardware test should reproduce a known effect and a small change introduced in several geometries. After this, the measured spectrum and permissible errors are used in the integral over bodies from chapter 10.

Clock network with a common gravimetric channel

In chapter 11, the geometry of two clocks and a gravimeter in the middle of the base was chosen. The joint spectrum relates the potential difference to the directional derivative of the same field. To check the spatial law, several bases or a change in geometry are needed. If all distances are much smaller than the correlation length, the A/ℓ combination predominates and individual parameters are poorly determined. The spatial scale is selected based on the change in predictions, and not just on the convenience of placing instruments.

The numerical example of the chapter 11 uses the base 1000 m, the correlation length 1000 m, the correlation time 10 s and the dimensionless field amplitude $A=10^{-20}$. For instrument noise, the

conditional output ASD $10^{-18}/\sqrt{\text{Hz}}$ in the clock channel and 10^{-7} m/s²/√Hz in the acceleration channel are set. The common noise component and a test by changing the sign of the spatial response are also included. These numbers define the synthetic experiment, and the individual laboratory must provide its own spectra and sensitivity functions.

Before combining records, the overall time scale, delays, frequency filters, and orientation of the gravimeter's sensitive axis are recorded. Clock comparisons and accelerations are translated into one frequency band. The log includes the location of atomic samples, movement of supports, temperature, magnetic field, pressure and movements of nearby significant masses. Channel matching is carried out based on independently measured response; a freely adjustable phase correction can hide the hardware cause of the correlation.

The number of channels does not in itself ensure independence. A single transmission line, a common optical oscillator, or a common clock system can link different frequency comparisons. Therefore, the network specification contains both local spectra and cross-interference elements. A separate control that retains the hardware connection but changes the sign or suppresses the spatial field response is useful. It is this role that the geometric permutation, discussed in chapter 11, plays.

$$\delta y \simeq \frac{g\,\delta h}{c^2}, \qquad \delta h = 1\ \text{mm} \ \Rightarrow\ \delta y \simeq 1.09 \times 10^{-19} \qquad (13.7)$$

The estimate (13.7) at g≈9.81 m/s² shows why height measurement becomes part of the frequency experiment. Thermal expansion of the support or displacement of the sample by a millimeter creates a frequency effect noticeable for the selected scale. This is a consequence of the low-field formula, and not a characteristic of the new sensor. Calibration with a moving mass also requires preliminary calculation: the value of ΔΦ/c² may be too small for the clock channel, although the acceleration is already visible with the gravimeter.

Engineering inference should be limited to the observable value. The matching of the potential and gradient channels verifies the adopted general field model. Curvature inference additionally requires kinematic and tidal controls, described in chapter 11. These measurements are included in the plant configuration prior to searching for unusual residue.

What does measurement readiness mean?

Each project must have an executable version of a model of a known system. This includes not only the object being examined, but also preparation, readout, bandwidth, geometry and calibration. After adding a hypothetical effect, it is checked which features remain distinguishable with acceptable changes in other parameters. The set of such features determines the useful range of the device.

The RC workshop completes this chain on a small synthetic system: from volts in CSV to a normalized response and an informed decision about the selected local class. The transfer to the laboratory model begins with the measurement of those parameters that are currently specified precisely in the calibration file. The mechanical and clock dossiers use the same logic, but require different techniques and independent confirmation of the noise budget.

Acceptance includes both detection of the introduced effect and work in its absence or indistinguishability. The saved original recordings allow you to repeat the analysis with a different interference model and check which step changed the output. The next chapter formalizes this procedure: how to select test cases, compare explanations, and report the result when the data do not specify a single answer.

Chapter 14
How to distinguish a discovery from a convincing mistake

The statement must precede the result

The statement being verified captures the object, the model class, the data, and the decision rule. After viewing the result, you can formulate a new hypothesis and design the next experiment. It is important to maintain consistency: the research that prompted the question and the records that tested it serve different roles. In the above example, this is exactly how the transition from a hybrid pair to control ports works.

In the proposed program, the main object of testing is the distinguishability of geometry and dynamics. Operational dimension may change due to connectivity, transport method, frequency dispersion, leakage or miscalibration. Therefore, the null model should not be cartoonishly simple. Along with it, several meaningful alternatives are specified: conventional geometry with inhomogeneous parameters, a new field without an additional dimension, and an instrumental general process. If an unusual hypothesis is compared only with an admittedly incomplete description, winning that comparison reveals little about the world. The scientific goal is to win against the strongest reasonable explanations, not against a specially weakened opponent.

Before starting the expensive phase, it is useful to create a prediction table for several interventions. For example, changing distance, changing material, rotating the sensor and rearranging the electronics affect the model differently. If two hypotheses make the same predictions for all available interventions, increasing the precision of the same measurement may not resolve the dispute. A new monitored channel will be required. Such a conclusion can be obtained even before the construction of the device and thereby avoid long-term accumulation of data that fundamentally does not answer the question posed. The preliminary calculation of distinguishability becomes an independent research result, since it determines the necessary conditions for a future discovery.

Blind testing as part of the design

Blinded analysis limits inadvertent adjustment of processing to an expected answer. The data may contain an offset unknown to analysts, a hidden permutation of labels, or an injected signal. Selection, calibration, and uncertainty-estimation rules are fixed before unblinding. The blinding method must still permit real faults to be detected. For example, an absolute scale can be hidden while diagnostic relationships between channels are preserved. Zheng and colleagues already used a blinded procedure in a laboratory test of gravitational redshift. Here, the principle is proposed for testing operational dimension; a test not yet performed is not presented as a completed experiment. [30]

For an electrical prototype, it is convenient to prepare several hidden networks. The operator measures them using one protocol, the analyst receives time series without connection diagrams, and the person responsible for the labels preserves the true structure until the end of the calculation. In some sets, ordinary resistance inhomogeneities and leaks are introduced that can simulate unusual connectivity. Others add a true additional current path. The proportion of correct recoveries, the false discovery rate, and the ability to recognize uncertainty must be assessed simultaneously. An algorithm that always confidently names one structure may look successful on a convenient set, but fail on specially selected degenerate examples.

Hardware addition and digital addition solve different problems. The digital signal checks the mathematical processing after the application location. Movement of the calibration mirror checks the optics and readout, but does not necessarily reproduce the intended metric along the light path. Changing mass tests the mechanical and gravitational model, but may simultaneously create vibration. Therefore, each application is accompanied by an indication of which part of the measuring circuit it was tested. It is useful to have several independent entry methods and control records without entry. Successful completion of such a program confirms the suitability of the device for a certain class of signals, leaving open the question of their nature.

The order of access to the structure, records and key in the proposed blind trial is shown in Figure 58.

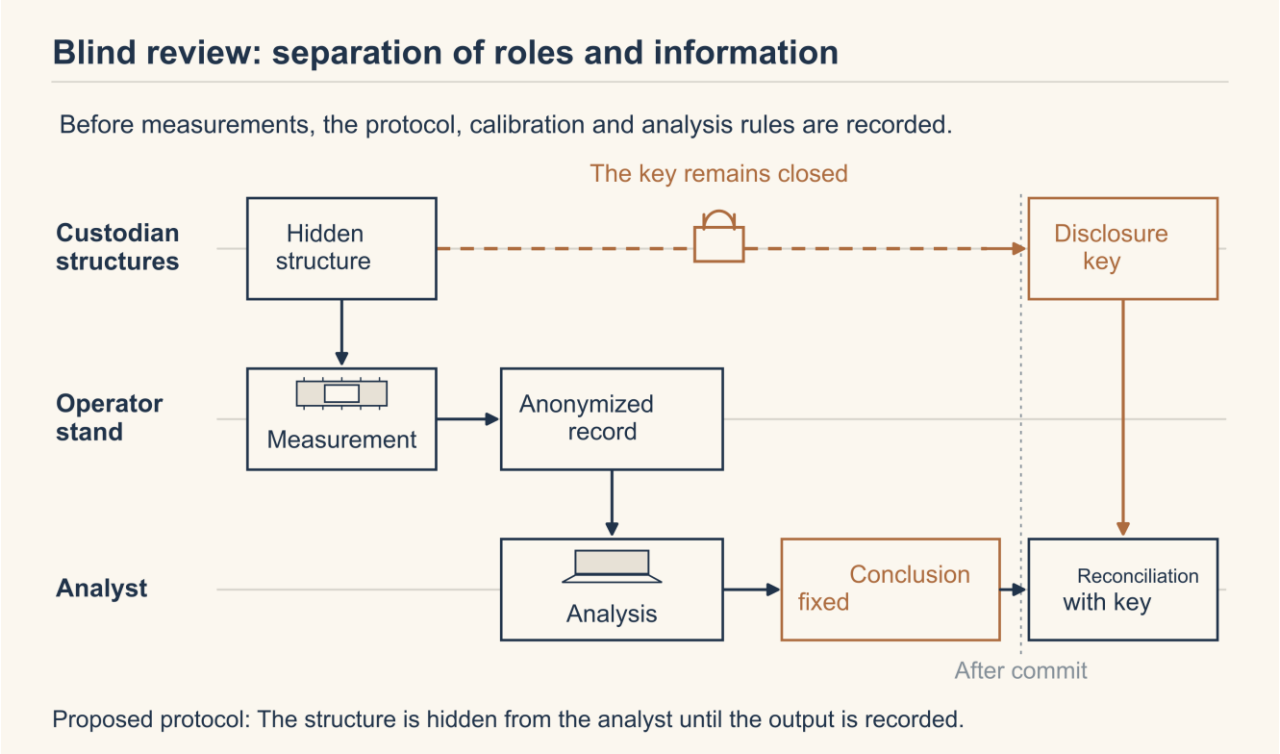


Figure 58. Proposed division of roles in a blind trial. The custodian saves the true structure and key of the tags, the operator performs measurements according to a pre-fixed protocol, and the analyst receives anonymized records. The output is committed until the key is revealed; only then is a comparison with the known structure performed. The diagram shows the order of access to information, not the experiment that took place. It must be combined with accessible fault diagnostics and an explicit indication of the area being tested by each input signal.

Probabilistic inference and interference parameters

The statistical model must describe not only the average expected value, but also the error correlations. For a real data vector, the Gaussian approximation uses a quadratic form with an inverse covariance matrix. If the covariance itself depends on the parameters of the hypothesis, it is necessary to preserve the term with its determinant. Removing this term may encourage a model that simply increases the declared noise. The formula below gives the conditional likelihood under the physics parameters θ and the calibration parameters η. If there is significant non-Gaussianity, a small number of averagings, or other counter statistics, the distribution should be changed; the familiarity of the Gaussian form is not a justification for its use.

$$-2\ln\mathcal{L} = (\mathbf{d}-\boldsymbol{\mu})^{T}\mathbf{C}^{-1}(\mathbf{d}-\boldsymbol{\mu}) + \ln\det\mathbf{C} + N\ln(2\pi), \qquad \boldsymbol{\mu} = \boldsymbol{\mu}(\theta,\eta), \quad \mathbf{C} = \mathbf{C}(\theta,\eta) \tag{14.1}$$

Calibration parameters cannot simply be substituted into convenient exact numbers if their error is comparable to the intended effect. They are constrained to independent measurements and then either profiled or integrated with explicitly specified uncertainty distributions. Different statistical approaches answer different questions, and the results should be labeled accordingly. The confidence region is not the probability of a theory being true, and the Bayesian evidence ratio depends on given model families and parameter distributions. Instead of a single impressive metric, it is useful to publish residuals, robustness to alternative noise models, and predictions for held-out data. This makes the conclusion testable beyond the chosen method of statistical representation.

The reason for the indistinguishability can be seen already in the linear approximation. A small change in the expected signal consists of the contributions of geometric and calibration parameters. If the direction of change assigned to the geometry matches the combination of the directions of the calibration errors, the data cannot separate these causes without external information. The sensitivity matrices in the formula contain derivatives of the signal with respect to the corresponding parameters. Their close linear dependence does not mean the weakness of the computational algorithm, but a lack of information in the experiment. Increasing the number of decimal places in the optimizer does not correct this problem. A different configuration, an independent calibration, or a new observable is needed.

$$\delta\boldsymbol{\mu} = \mathbf{J}_{\mathrm{geom}}\delta\boldsymbol{\theta} + \mathbf{J}_{\mathrm{cal}}\delta\boldsymbol{\eta} \tag{14.2}$$

By searching through a large number of correlation lengths, frequency intervals, or possible hidden connections, the likelihood of finding an interesting combination by chance increases. Therefore, the detection threshold is calibrated for the entire search procedure, including the selection of the best result. A suitable way is to run multiple simulations of the null model with the same search and the same stopping rules. However, such a calibration is only valid to the extent that the null simulation reproduces the essential properties of real noise. An unaccounted general disturbance can make a formally rare event common. That is why the correlation search should combine statistical averaging with checking the physical sources of the common signal, and not consider these tasks separately.

Simultaneous intervals for a bounded network

In the protocol of Chapter 8, each scalar observation has the form $z_j = a_j^{T}\, G_{obs}\, a_j$. If the independently acquired directed matrix elements have equal variance σ^2 and a_j has unit norm, the variance of z_j is also σ^2. The contrasts themselves are dependent: two vectors may use the same elements. For a general covariance, c_j denotes the coefficient vector of the linear combination of recorded data.

$$\sigma_j^2 = c_j^{\mathsf{T}} C c_j, \qquad c_j = \operatorname{vec}\left(a_j a_j^{\mathsf{T}}\right) \qquad (14.3)$$

Let M contrasts be selected before the test series. For Gaussian marginal errors with known variances, we assign to each a two-sided interval with a miss probability of no more than β/M. Combining miss events then has a probability of at most β regardless of the correlation of the contrasts. For β = 0.01 the following multiplier is used:

$$k = \Phi^{-1}\left(1 - \frac{\beta}{2M}\right), \qquad I_j = \left[z_j - k\sigma_j,\; z_j + k\sigma_j\right] \qquad (14.4)$$

For two initial probes M = 216 and k = 4.07358. After adding two control records for 36 contrasts M = 288; the multiplier is recalculated for the entire final set. If the true weights lie in the declared box and the marginal noise model is correct, its response with a probability not lower than 1 − β falls into all intervals. At this event, the outer matrix shells retain their true parameters.

Enumerating 2016 pairs does not require another factor 2016 in this design. First, one simultaneous region is constructed for all preselected observations, then it is inverted onto the parameter space. Whatever a true pair from a given class is, it is not cut off at the general coverage event. This is a different way to control error than finding the maximum improvement in χ^2 and empirically calibrating its threshold.

Level 1 percentage refers to the erroneous exclusion of a true parameter by this shell rule under its premises. It is not the probability of truth of the remaining pair and does not cover missing physical causes. If variances are estimated from a small number of records, have non-Gaussian tails, or change after choosing an interesting channel, the formula must be replaced or supplemented. For a general time record, the correct covariance of the transformed data is first calculated.

Evidence of compatibility and proof of exclusion

These two actions have different computational costs. To show the compatibility of the model, it is enough to present one valid set of parameters whose direct response lies in the selected error region. To exclude, you need to make sure that there are no such sets. The local optimizer is able to help the first action, but stopping it at a large remainder does not prove the second.

In the book, the limited search for the exact response uses the analytical Jacobian and weight limits ±2 percent. For two probes, the evidence search additionally considers the overall relative drift. This is a narrower subclass than the individual drifts allowed in shells; the found point also belongs to the wide class. Failure in a narrow subclass would not exclude a broad one. All remainder values are calculated by repeated direct substitution of parameters.

$$\chi^2(\theta) = \big(d - \mu(\theta)\big)^{\mathsf{T}} C^{-1} \big(d - \mu(\theta)\big) \le q_{0.99,N} \qquad (14.5)$$

In this diagnostic test, $q_{0.99,n}$ is a quantile of χ^2 for N known independent normalized errors. The number N is not reduced by the number of parameters found: the existence of a point in the data ball is checked, rather than the standard asymptotic residual statistic after estimation. The small minimum at 144 calibration variables is not evidence that such a flexible model is preferable; it shows that it cannot be rejected by the data in the selected area.

The complete remainder ball and the family of scalar intervals are different diagnostic constructs. In a program, rigorous exclusions are made only by shells; the absence of evidence found transfers the result to indeterminate status. Therefore, a separate 99 percent error ball is not issued as a new overall level of the entire procedure. If a future protocol rejects models using multiple rules at once, its cumulative error will need to be controlled separately.

Observed situation	Valid output
Restricted gauge without edge found	Conventional calibration is compatible; add is not installed
Calibration is excluded by shells; there is a certificate for a common pair	A common pair is compatible within a given class; separate and hardware reasons are checked
All common pairs are excluded; separate model has certificate	This version of the shared single-link model is rejected
Shells allow pairs, but no evidence found	Calculation or model uncertainty; no exception statement
The overall signal is stored in independent hardware control	There is reason to investigate the corresponding section of the registration path

Lessons from the book's numerical experiment

The first series established the performance of single-link reconstruction in a known low-noise network and its vulnerability to reference error. The limited counterexample of chapter 8 showed a more dangerous situation: even a good remainder does not separate a new connection from a small tailored drift. Including calibration in the class of explanations allowed us to present a common cause for these data.

The two probes then narrowed down the set of possible pairs. But controlling for separate structures created a false consensus that passed and limited fitting. Additional ports were selected after studying this case and then fixed until the new series. They made it possible to exclude all common pairs for a given counterexample. Here the specific research chain is completed, including the failure of the intermediate criterion.

The given 96 new realizations check the selected protocol under the declared ranges and noise. They do not estimate the probability of an arbitrary natural anomaly. In particular, the result for the pair 5-58 and several specially defined alternatives does not automatically carry over to the entire set of pairs. To scale the method, separate geometry ensembles, additional physical errors, and independent hardware recordings are required.

Stages of physical proof

To maintain clarity, it is useful to distinguish between several levels of outcome. First, the mathematical consistency of the model and the correctness of the response calculation are checked. The method is then tested on an artificial system with known properties. The next level is a reproducible deviation in a physical experiment. After this, a specific common cause is established and only then is the geometric interpretation discussed. Finally, quantum origins would require features that cannot be explained by a suitable classical random model within the accepted assumptions. These levels do not have to take the same amount of time, but jumping between them makes the conclusion stronger than the available data and destroys the possibility of fair testing.

Level	What has been established	What cannot be confirmed yet
Calculation	Model and response are consistent with specified assumptions	That the model is realized by nature
Controlled analogue	The method recognizes the properties of an artificial network	That the dimension of free space has been changed
Reproducible remainder	The original data model is insufficient	That the reason is necessarily geometric
General physical mechanism	Multiple observations explained by one proven cause	That the mechanism has only one interpretation
Geometric hypothesis	Its distinctive predictions stand up to independent scrutiny.	That quantum nature is automatically proven
Quantum interpretation	Features that distinguish given quantum and classical explanations have been verified	That all conceivable alternatives are excluded

Independent replication must change at least some of the possible error paths. Repeating on the same device is useful for stability, but retains its systematic features. Repeating another group on a copy of the diagram reduces some risks and leaves others. The experiment with a different physical principle of reading is especially convincing if both installations check a quantitatively related quantity. However, the discrepancy between the results should not be immediately explained by a new dependence of the effect on each difference in conditions. First you need to determine whether the same modes are being compared and whether the parameters are transferred correctly. The new condition is theoretically valid, but must create a new testable prediction.

Zero registration can also be a strong result if it is shown in advance what parameter range the experiment is capable of testing. The publication should include limitations under different noise assumptions, an open calculation of the response, and a description of excluded data intervals. If a device does not reach the required level due to identified systematics, this should be called an engineering limitation rather than a limit of nature. Such a report preserves the possibility of improvement: the next group understands what exactly needs to be changed. If sensitivity is achieved and there is no model signal, the theory receives a real limitation. It is these differences that make the research program cumulative rather than a succession of disparate statements.

Transition from a completed calculation to the next experiment

The computational stage now has a completed limited result: model classes are specified, a conservative shell is derived, compatible parameters are found, difficult negative cases are constructed, and the discriminative mode is tested. The next meaningful step is to transfer precisely these conditions to the electrical workshop. We need to measure the weight limits, capacitances, read load, time window, and covariance, and then determine which assumptions of the numerical example hold up in the real world.

After checking the electrical prototype, you can choose a more complex installation for a specific physical hypothesis. Such a transition requires a calculated signal in the geometry of the selected instrument, a comparison with the measured background, and an intervention that distinguishes the underlying explanations. The success of the network protocol provides a proven method for working with limited classes, but does not automatically specify the interaction of the vacuum with clocks, masses or light. These connections are derived in the physics chapters for individual conditional models.

The third result is an independent test of a consistent family of predictions. For compact geometries, these may be associated ranges and spectral scales in a fully specified matter coupling model. For a weak random potential - the joint spatial and temporal structure of clocks and gravimeters. For the interferometric hypothesis, the dependence on light path, orientation and frequency, calculated before observation. At any stage, the program can refute its own original idea. At the same time, proven methods, limitations and instrumental knowledge will remain. It is precisely this design of work that creates a chance for a qualitative leap: an unusual hypothesis has the opportunity to turn out to be correct, and the experiment retains the right to show that space is structured differently.

Chapter 15
What has been established and how to continue testing

Results that can be repeated

The book began with the question of reconstructing the structure of space based on available observations. This question received several different answers in the completed examples. One averaged measurement sometimes loses discriminative information completely. With richer data, the structure can be restored, but a standard error can change the meaning of the result. The additional probe helps only to the extent that it accesses the lost information.

The first exact example is given by two three-node networks of chapter 2. Their spectra coincide, so the entire heat trace also coincides. Local excitation distinguishes networks already at one pre-named node. This result does not depend on numerical optimization: it is verified by diagonalizing two small matrices and calculating their exponents.

A larger experiment has revealed a more practical ambiguity. The correlated drift of 144 ordinary weights within ±2% simulates a weak additional connection. A single-link model with respect to an unchanged standard selects the pair 5-58, gives an improvement in χ^2 around 85.69 and favorable remainders. After including the permissible drift, an explanation was found without additional connection with $\chi^2/192 \approx 0.6105$. This is evidence that the data is compatible with the calibration; the basis for a positive conclusion about the new connection disappears.

The limitation ±2% has an independent meaning here. It specifies the class of source models to be checked. For a real instrument, such an interval should be based on calibration measurements. Narrowing the interval makes elimination easier, but is scientifically valid only when the accuracy of the components is actually better known.

The matrix shells of chapter 7 produce a different kind of result than a local fit. If the measuring contrast goes beyond the simultaneous limit, it excludes the entire limited calibration class under the accepted statistical assumptions. Getting inside the shell preserves the possibility of the model, but does not prove the existence of a common set of weights. For compatibility, an acceptable point of precise direct calculation is additionally presented. The failure of the local optimizer remains a computational fact and does not replace the exclusion bound.

What did the second probe add?

The new two-probe example uses different known underlying operators and accesses opposite edges of the network. Individual data sets leave 52 and 48 as valid pairs; joint necessary conditions leave one pair 5-58. A limited fit of the general case gives $g \approx 0.3053\ s^{-1}$ with the introduced value $0.3\ s^{-1}$ and $\chi^2/384 \approx 0.7669$. This is the result for a given class from a single non-negative relationship, a known node registration, and a defined signal strength relationship between probes.

A scaled copy of the first channel provides significantly less new structural information. In the noisy control experiment, the 51 pair remains. Without noise, the original channel and its scaled take retain the same 44 pairs. Independent repetition is beneficial for accuracy, but changing time and amplitude units does not create missing spatial information.

The most difficult control occurred with different true pairs for two probes: 5-58 and 6-57. Joint analysis of the source ports leaves a false hybrid pair 5-57. Even an accurate fit of the general model is subject to noise. Therefore, the one remaining pair in the final data set does not yet confirm the physical assumption of the overall structure.

After studying this design example, an additional port pattern is selected and fixed to a new series of noises. It includes nodes 0, 5, 6, 15, 48, 57, 58 and 63 with s = 0.3 s^{-1} for both probes. This control preserves the true shared-link case and eliminates the shared single-link class in the hybrid example. The origin of the design is significant: it is a test of a designed protocol on new data, rather than a blind test of a design chosen before encountering a difficult example.

New series class	Number of realizations	Result after additional control
Limited drift without additional communication	24	The calibration model is not excluded in 24 cases
One true common connection	24	True pair saved in 24 cases
Different true pairs of two probes	24	The shared single-link class is excluded in 24 cases
Specified common electronic parasitic channel	24	The shared single-link class is excluded in 24 cases

These 96 realizations refer to four given designs and new noise generator values. They do not determine error rates for arbitrary networks, unknown types of interference, or other calibration uncertainties. Their purpose is to test the reproducibility of a particular sequence of decisions, including the rejection of false agreement.

From a time series to structure

The RC workshop completes a separate path from the measuring signal to the model. Four nodes and three hidden cases generate twelve time-series files. The processing takes into account the initial state, voltage normalization, input load, finite window, and joint covariance of the Laplace-transform estimates. The analysis works with observation files; The generator key is used separately to test the solution.

For the selected contrast and local conductance range ±2%, the calibration envelope is approximately 11.1005-11.4398 ms. The reference case and the drift case fall into this region. The added connection 0-3 gives about 7.7578 ms and excludes the local class. Its intensity was restored as 19.9974 s^{-1} with true 20 s^{-1}. Here the difference is deliberately large enough that the entire processing can be verified on a simple circuit.

The workshop remains a synthetic stand. Its finished result is consistency of equations, units, files and algorithm. The next physics experiment is to find out how well the adopted load, noise and calibration models describe the assembled circuit. If there is a discrepancy, you should first expand the measurement model and repeat the test cases.

Physical models have measurable consequences

The compact branch now relates the mode spectrum to the static and dynamic response of the selected scalar probe. In the static example, the finite dimensions of the source and detector are taken into account, and then the force harmonic is calculated when the gap is modulated. Dynamic calculation shows propagation thresholds. It allows you to check which features really follow from compactness, and which require an additional resonator or a coupling law with the device.

In the clock example, all blocks of the joint signal spectrum are displayed, including the mixed channel with the gravimeter. The introduced signal and the specified even electronic noise are separated by a physical rearrangement of the position of the clock sensors while maintaining the reading channels. This control is based on the properties of the selected interference. A spatial environmental cause with the same symmetry will require its own measurement.

Rindler's example limits the geometric interpretation: the gradient of the clock and the readings of the accelerated instrument are possible with a zero curvature tensor. Therefore, the matched clock and acceleration signal first tests the overall observation model. To infer curvature, one must take into account the motion of the reference frame and tidal information.

The interferometric branch is brought to an exact response function in the selected sector of the transverse traceless plane wave and the conditional free mirror mode. The low-frequency approximation is compared with a finite time of flight. Sensitivity dips at certain frequencies show why the field spectrum cannot be directly called the spectrum of the measured phase. The numerical budget sets the requirements for the selected scheme; it does not replace the measured noise of an actual installed installation.

In all three cases, more than the name of the device is obtained: there is a calculated path from the model parameters to the reading. Checking the physical admissibility of the parameters, independent calibration and search for signals from nature form the next experimental task.

The scope of the book's original result

The presentation uses well-known matrix identities, linear response theory, spectral methods and physical models indicated in the bibliography. Joint network reconstruction and geometric interpretations of correlations also have prior literature. The combination of several probes itself does not establish scientific priority.

The specific content of the executed program consists in a consistent formulation of a limited experiment: the calibration class is specified explicitly, the ambiguity is presented by the data, the exclusion shells are separated from the fit, the false two-probe agreement is checked by a separate

impact, and the measurement procedure is brought to time-series records. These elements can be reproduced and compared with other algorithms on the same input data.

Publication as an independent study will require a more focused question. For example, how much does a particular port choice reduce the worst-case calibration ambiguity for a fixed number of measurements? Or what additional contrasts are guaranteed to separate two predefined connectivity classes? Such questions can be answered with a theorem, a counterexample, or a reproducible numerical comparison. Their formulation specifies the subject of novelty being tested.

The next physical experiment

The first practical step is to assemble a small RC network and reproduce the procedure in Appendix E. Before revealing the control changes, the original capacitances, conductances, load and noise should be measured, then the error model and decision rule should be recorded. After this, the reference, permissible drift and additional communication are checked. The calculated accuracy must be compared with the actual spread of duplicate entries.

The transition to a larger network is justified after checking the entire chain on a small one. The number of ports, their location and driving modes are then selected based on their ability to distinguish between competing models. Noise reduction is useful as long as the desired difference is measured; if two classes provide the same available data, the experiment itself needs to be changed.

For the compact, clock and interferometric branches, the next step is determined by the corresponding budget. It is necessary to measure the transfer functions and interference that were specified in the calculation. It is then useful to introduce a known reference signal and test for recovery of its amplitude, spatial pattern, and time dependence. The success of such input verifies the acquisition path and analysis, keeping the origin of a possible natural signal separate.

Open questions in the physics of space

Beyond the completed examples, there remains an unknown reference topology, unlimited hidden nodes, several weak links, unknown laws of connection between probes and a common object, and incomplete calibration. Under these conditions, it will be necessary to redefine the class of alternatives. The given formulas help set the problem, but do not provide an automatic solution for any device.

Even deeper lies the transition from the effective operator to fundamental geometry. It requires dynamics, coordination of different fields, causality and observable consequences that can withstand comparison with already known physical mechanisms. A detected connection in an electrical analogue establishes a property of the analogue. A statement about the structure of space requires a corresponding physical experiment.

Advancement begins where the question becomes precise enough to be tested against data. One measurement circuit loses the distinction between the two networks; the other returns it. One model erroneously attributes drift to a new connection; advanced monitoring detects this error. This

transition from assumption to discriminating experiment constitutes the working basis for further exploration of space.

Appendix A
Mathematical Conventions

Symbols and units

The same designation sometimes has different meanings in different areas of physics. In this book, the network operator is denoted by the letter L, and the physical length of the interferometer arm is denoted by the symbol $\mathscr{L}$ or by an explicitly named length. The parameter s refers to the Laplace transform; frequency f is measured in hertz, angular frequency ω is equal to 2πf. The diffusion parameter σ in a continuum heat kernel can have the dimension of the square of the length, while the time t in the electrical analogue is measured in seconds. It is impossible to identify them without a normalization coefficient.

Designation	Meaning	Units in the model used
L	Laplacian of a normalized diffusion network	s^{-1}
g	Coupling rate	s^{-1}
G(s)	Normalized response matrix	s
s	Laplace transform parameter	s^{-1}
K	Electrical conductance matrix	siemens
C	Node capacitance or capacitance matrix in an electrical model	farad
R	Compact direction radius	m
q_n	Inverse spatial mode scale	m^{-1}
q	Potential fluctuation $\delta\Phi/c^2$ in the clock model	1
A	RMS field amplitude q in the clock model	1
ℓ and τc	Length and correlation time of the clock pattern	m and s
S(f)	Power Spectral Density	square of signal units per Hz
$\tau = b^T G_0 b$	Coupling-change scalar in Chapter 7; depends on the pair and s	s
C in statistical test	Covariance matrix of measurement errors	square of measured signal units
$A_0 = L_0 + sI$	Network equation matrix in chapter 7	s^{-1}

Designation	Meaning	Units in the model used
σ registration noise	Standard deviation of matrix response errors	s
δ_e and ε	Relative change in weight and the limit of its modulus	1
η_a	Known factor of the connection between the general parameter g and probe a	1
$a^{T}G(s)a$	Measuring contrast at normalized a	s
α statistical family	Acceptable probability of going beyond at least one joint boundary for a given noise model	1
α of the Yukawa contribution and β of the mode tower	Relative amplitudes of interactions; are determined separately from statistical α	1
$K(t) = \exp(-Lt)$	Impulse response of a normalized network; different from the electric matrix K	1
HVI(s)	Transfer from current to voltage	ohm
Hφ(f)	Transfer from selected field amplitude to phase	rad per unit field

The graph scalar $\tau = b^{T}G_{0}b$ has units of time. Clock $q = \delta\Phi/c^{2}$ is dimensionless. Different values of the letter K are also indicated locally: the electrical matrix of conductances is measured in siemens, and the impulse response K(t) of the normalized network is dimensionless. When moving between chapters, determining the magnitude is more important than matching the letter.

A square matrix acts on a vector of measured quantities. For a voltage network, such a vector contains the voltages of all nodes. The response matrix relates the vector of excitations to the vector of responses for a fixed value of the parameter s. Its diagonal element describes the response at the same node where the impact is applied; off-diagonal - the answer is at another node. The transpose is indicated by the superscript T, and the Hermitian conjugate of a complex matrix is indicated by an asterisk, together with the transpose or † sign according to the context. In real symmetric network models these differences are simplified.

The Frobenius norm of a matrix is equal to the square root of the sum of the squares of the moduli of its elements. Relative error refers to an explicitly specified entity: coupling intensity, response change, or overall response. In the main 64-node experiment, the change in ΔG relative to the standard is analyzed. In the RC workshop, the accuracy of the full G is separately shown, and the connection decision is made by discriminative contrast and model comparison. A small error in the full response may mask a large relative error in the weak additive component.

$$\| M \|_F = \left(\sum_{i,j} |M_{ij}|^2 \right)^{1/2}, \qquad \varepsilon_M = \frac{\| M_{\text{pred}} - M_{\text{true}} \|_F}{\| M_{\text{true}} \|_F} \qquad \text{(A.1)}$$

About probabilities and spectra

A positive Laplacian of a network with non-negative weights of neighboring links generates probability-preserving diffusion. For a finite connected network, the normalized heat trace tends to unity at zero time and to the inverse number of nodes at large times. This means that the spectral dimension calculated from the logarithmic derivative tends to zero at both ends of the range. A possible dimension plateau should be sought between these modes, checking whether it remains the same as the network increases and the resolution changes.

Quantum unitary propagation and ordinary diffusion use different evolution operators. The probability of survival of a quantum state cannot be substituted without inference for the heat trace. Similarly, power spectral density and its square root have different units. For dimensionless strain, the first is measured in Hz^{-1}, and the second in $\text{Hz}^{-1/2}$. Comparing instrument sensitivities also requires the same conventions regarding one-sided or two-sided spectrum, acquisition time, and frequency bandwidth.

$$P(t) = \frac{1}{N} \operatorname{Tr} e^{-tL}, \qquad P(0) = 1, \qquad \lim_{t \to \infty} P(t) = \frac{1}{N} \qquad \text{(A.2)}$$

Matrix order and compatibility region

The notation $A \preccurlyeq B$ means that $v^T(B - A)v \geq 0$ for every real vector v. This is the Löwner order on symmetric matrices. For positive-definite matrices, inversion reverses the order. In the network experiment, positive s ensures invertibility even when the Laplacian has a zero mode.

$$0 \prec A \preccurlyeq B \quad \Rightarrow \quad B^{-1} \preccurlyeq A^{-1} \qquad \text{(A.3)}$$

The set of individually acceptable contrasts defines the outer region of possible data. Not every point in this region is generated by one shared conductance vector. Therefore, the remaining candidate receives the status of not being excluded by the shell. The specific feasible set of parameters calculated through the exact forward model provides additional numerical evidence of compatibility.

The χ^2/N values in the tables mean the sum of the normalized squares of the residuals per number of records. Here N is not replaced by the number of degrees of freedom after selecting the parameters and choosing the structure. These values are convenient for comparing the scale of the remainder, but in themselves they do not constitute a ready probability of discovery.

Appendix B
Repetition of computational experiments

Kit contents

The initial data and programs for computational experiments are given in the accompanying kit. Programs use relative paths, so the directory structure should be preserved. Numerical graphs are reproduced using the same formulas and data; illustrations of apparatus are marked as conceptual.

Program	What is reproduced	Main result
revision2/code/foundations.py	Three nodes, an isospectral pair and a sphere	results/foundations.json
revision2/code/math_revision.py	Limited calibration, two probes, difficult controls and 96 new realizations	results/math_revision.json
revision2/code/physics_revision.py	Compact response, mixed clock spectrum and interferometer	results/physics_revision.json
revision2/code/rc_practicum.py	Generation and processing of time-series records of a small RC stand	data/rc and results/rc_analysis.json

The names of the results in the third column are counted from the revision2 directory. The programs create data from mathematical models; Having a CSV file does not turn a synthetic entry into a lab entry. Launch commands and requirements for the software environment are given in the accompanying instructions for the calculations.

The programs repeat computational experiments and save the results in the appropriate files. A separate program book/study_v02.py reproduces a series of 460 realizations; it takes longer to start.

Repetition accuracy and search verification

The initial states of the generators, noise parameters and the order of data acquisition are recorded in programs. In a different environment, the last digits of linear algebra and optimization may differ. Therefore, the check must compare the selected pair, the physical units, the constraint boundaries, and the specified numerical precision, while retaining the original result for comparison.

A separate search check reproduces the original three data sets based on the stored seeds and generation order. All 2016 pairs are tested with limited scalar minimization on [0; 3] and both ends of the interval. The selected pairs match the quick search; the difference in coupling-strength estimates is less than 10^{-7} s^{-1}. Two records coincided with the previous numerical differences up to the given figures; in the first, the last figures changed. Both results are saved with indication of the conditions for the numerical calculation.

The verification concerns the named data. It does not prove the global optimality of the search for any possible noise implementation. The new exclusionary inferences use matrix bounds, and local fitting separately provides feasible numerical examples.

Reanalysis of time-series files

The generate mode creates records and a separate ground-truth key. The analyse mode processes existing files and shared calibration information without reading that key. The full all mode regenerates the synthetic CSV files, performs the analysis, then reveals the labels and creates the figures. For your own records, use analyse with a separately specified data directory; all is intended to reproduce the demonstration. The format and instrumental covariance of your own records must be specified according to Appendix E.

In a physical experiment, a single seed does not ensure reproducibility. Wiring diagrams, firmware versions, drive modes, initial calibrations, timestamps, and unmodified records will be required. Appendix E describes a sufficient set for the first small stand. The synthetic kit files serve as a sample of processing and format.

Appendix C
A map of testable claims

Result and conditions for its application

The table links the main results with their status and data that could change the conclusion. It is intended to be read repeatedly. Detailed prerequisites, standards and experimental schemes are found in the corresponding chapters.

Statement	Status and background	Check or restriction
The spectral index does not uniquely determine the structure	Exact three-node example of chapter 2	Identical spectra and different K_{11} are calculated directly
Drift is capable of simulating a weak new connection	Constructed example at ±2% and given noise	All weights and acceptable Hcal fit presented
Calibration class can be eliminated without global adjustment	Matrix shells and simultaneous intervals for given boundaries and error distributions	Changing the calibration interval or covariance requires recalculation
The second probe is capable of reducing many pairs	Two well-known operators, node registration and given amplitude coupling	Scaled take and different true pairs are checked separately
False agreement is detected by additional control	Scheme fixed after development; four conditional classes according to 24 implementation	Other pairs and interference require new testing, universal frequency not rated
RC network response is extracted from time-series files	Synthetic stand with a given load and covariance	Physical assembly should check the reading and drift pattern
The compact model predicts a ladder of static and dynamic contributions	Selected scalar operator and relation to sources	Conventional proxy and experimental limits are compared in the same parameters
The mixed clock signal has a calculated geometry	Specified spatial kernel, band and filters	Coincidence with field and environmental interference may require an additional channel
Clock gradient does not define curvature	Rindler's exact example	The curvature tensor is zero for a non-zero clock gradient
The interferometer has frequency dips	Selected TT plane wave and free mirror mode	Different optics or mechanics require a different transfer function

Geometric interpretation of a signal requires a specific physical model and testing of available alternatives.

Appendix D
Dictionary of basic concepts

Rereading Concepts

Internal geometry. Description of distances, angles and curvature by means of the space under study itself. It does not require the assumption of an external space within which a given geometry is supposedly located.

Geodesic. A locally selected line of geometry defined by a metric and corresponding equation of motion. On a sphere, geodesics are the arcs of great circles; a geodesic does not have to be the globally shortest path between any two of its points.

Curvature. Characteristics of geometry deviation from a locally flat structure in finite regions. It can be studied through the transfer of directions, the behavior of geodesics and the measurement of distances, without considering the bending of the surface from the outside.

Topology. Properties of connectivity and global structure of space that are preserved under continuous deformations of a suitable type. Topology differs from specific distances and angles.

Compact direction. Spatial direction described by a compact manifold. In the simplest model under consideration, it closes into a circle of finite radius. The small radius can make its additional modes inaccessible to low-energy observation.

Synthetic dimension. An organized set of internal states or controlled parameters in which interactions reproduce the mathematical structure of an additional direction. Its implementation in the device does not in itself increase the number of coordinates of the surrounding space.

Spectral dimension. A scaling indicator for a heat trace or other strictly defined spectral object. Its value depends on the geometry, the propagation operator, and the selected scale range.

Laplacian of the network. A matrix composed of the intensities of connections between nodes. For a symmetric network with positive weights, it describes diffusive exchange, has a non-negative spectrum and maintains a homogeneous mode.

Resolvent. Inverse matrix or operator of the form $(L+sI)^{-1}$. It relates the structure of the dynamic operator to the measured transformed response.

Rank. The number of linearly independent directions in the matrix image. In the model under consideration, a limited number of independent additions sets the upper bound on the rank of response change. The converse conclusion is generally incorrect: the small observed rank does not establish the number of hidden disturbances and is not equal to the number of spatial measurements.

Kron reduction. Exclusion of internal nodes of a linear network using the Schur complement. On the outside, the reduced network may have connections that do not correspond to the immediate connections of the original system.

Isospectrality. Coincidence of the spectra of two operators or geometric objects. Different shapes can be isospectral, so the set of resonances does not always uniquely define the geometry.

Identifiability. The ability to uniquely determine a property or parameter within a specified class of models using available data. It depends on the measurement setup and prerequisites, and not just on the accuracy of the numerical algorithm.

Calibration. Determination of the relationship between recorded quantities and the physical impact, including the uncertainties of this relationship. An unknown calibration error may simulate a change in the system under test.

Null model. Description against which the need for an additional effect is checked. It must include relevant known signals and noise, not just the idealized absence of any movement.

Spectral density. The distribution of power or covariance of a signal over frequency under a selected conversion convention. It cannot be compared with amplitude without taking into account units and frequency band.

Retarded response. The change in the observed value after an applied impact, taking into account the causal order. It differs from the correlation of two quantities in the prepared state.

Passivity. The property of a system that does not output more energy than it received or had in reserve, given specified inputs and outputs. In an analog device, it helps eliminate self-excitation as a source of a false signal.

Falsifiability. The presence of observation results that are inconsistent with the statement under predetermined conditions. The ability to explain any outcome by adding free parameters weakens testability.

Scope of applicability. The set of scales, states and regimes in which the description used is justified. A successful model within this domain does not automatically gain the right to describe all of nature.

Measuring contrast. A predefined combination of readings selected to test a particular model difference. In a matrix experiment, $a^{T}Ga$ corresponds to excitation and readout along one normalized spatial profile.

Löwner order. A comparison of symmetric matrices through the signs of all their quadratic forms. It allows bounds on an entire class of operators and their inverses without enumerating every admissible weight.

External compatibility area. A set of necessary conditions containing all data of a given class with accepted errors. Getting into this area does not guarantee the existence of one model that simultaneously reproduces all its coordinates.

Numerical evidence of compatibility. Specific parameters within acceptable limits, for which an accurate direct calculation is consistent with the data according to the established rule. The absence of such a result from the local optimizer is not evidence of the absence of a solution.

Coherence. A normalized quantity constructed from the mixed spectrum of two signals and their autospectra. Characterizes consistency in the selected frequency band. A high value does not identify a physical cause and is not a substitute for estimating signal amplitude.

Joint covariance. Error matrix of several estimates taking into account their mutual dependence. This is especially significant when different transformations are calculated from the same time record.

Held-out measurement. Data that was not used to determine the parameters being tested. Its significance depends on sensitivity to the difference between competing predictions, not just on the independence of noise.

Blind control. Organization of experiment in which the change being tested is hidden from the decision-making procedure until the result is recorded. Synthetic separation of generator and analysis tests the processing logic; hardware blinding additionally requires independent assignment of changes.

Appendix E
Practical work: from voltages to link reconstruction

Task and measurement files

The task of the workshop is to check, using time records of a four-node electrical circuit, whether ordinary connections with acceptable drift are sufficient. Three sets of voltages are given with letter labels. The analysis uses the same pre-written rules. Once completed, a separate file reveals the configuration that generated each entry. This is a software separation of data and markup; all signals were generated; the physical setup was not used in this experiment.

The conductances of ordinary edges 0-1, 1-2 and 2-3 are expressed as w_e/R_0, where R_0=100 kOhm and $0.98 \le w_e \le 1.02$. Equal capacitances C_0=100 nF give the nominal intensity $\kappa = 1/(R_0 C_0) = 100$ s^{-1}. An additional connection is understood as one of the edges 0-2, 0-3 or 1-3. Its intensity is allowed within the range from 0 to 60 s^{-1}. In the control configuration, the connection 0-3 with intensity 20 s^{-1} was introduced.

File or directory	Contents
revision2/data/rc/calibration.json	Nominals, initial voltage matrix, load, pitch, window, noise and solution rule
sample_A_source_0.csv and similar	Time and four voltages for one initial preparation
revision2/data/rc/truth_key.json	True parameters and seeds; analysis does not read this file
revision2/results/rc_analysis.json	G estimates, total covariance, fits, and unlabeled solution
revision2/results/rc_validation.json	Comparison with true response after markup expansion

In total, 12 CSV is presented: three sets of four preparations. The header of each file is the same: time_s,v0_V,v1_V,v2_V,v3_V. It contains 5001 line of readings from 0 to 0.25 s with step 0.00005 s. The source number means the prepared state, the v number means the observed node. This separation prevents confusion between row and column of the response matrix.

The W matrix in calibration is measured in volts. Its jth column is equal to the actual initial vector for preparation j. Diagonal elements are close to 1 V; neighboring elements are equal to 0.0015 V. The rest are equal to zero. A small amount of mixing is intentionally included in the task so that processing does not depend on the assumption of an ideal unit excitation.

Preparation and physical scheme

For hardware implementation, four capacitors are used relative to the common wire and three replaceable resistors, as in figure 54. Each node has a separate voltage channel. Simultaneous

counting is desirable; if a multiplexer is used, its delays are included in the time grid of each channel and are taken into account before integration. Input resistances and parasitic capacitances are measured along with the connected cables.

Before recording, low-impedance sources hold the specified voltages of the four nodes. All sources are then disconnected by a common trigger event, and the high-impedance meters continue monitoring. The initial voltages should be determined by recalibrating in the same switching mode. The ideal state e_j is not required: four clearly distinguishable columns of W are sufficient. What is important is the reproducibility of these columns and an independent estimate of their error.

Direct connection of only one node to the source while leaving the network free does not create the required initial state: the voltage has time to transfer to its neighbors. Therefore, either synchronous retention of all nodes or measurement of the actual resulting full vector is chosen. The opening of the switches must be faster than the significant network dynamics, and the transient surge is recorded or included in W. If the recording starts later, a new origin and the corresponding W are determined consistently.

Recovery between experiments is performed by actively resetting all nodes to a common wire. Passive waiting is not enough here: an ideal ungrounded network retains the total charge, and the load 1 GOhm gives a leakage time of about 100 s. Before the next preparation, the residual voltages are checked. After each series, they return to the original configuration to separate connection changes from slow drift.

The switching sequence and continuity of high-resistance monitoring are shown in Figure 59.

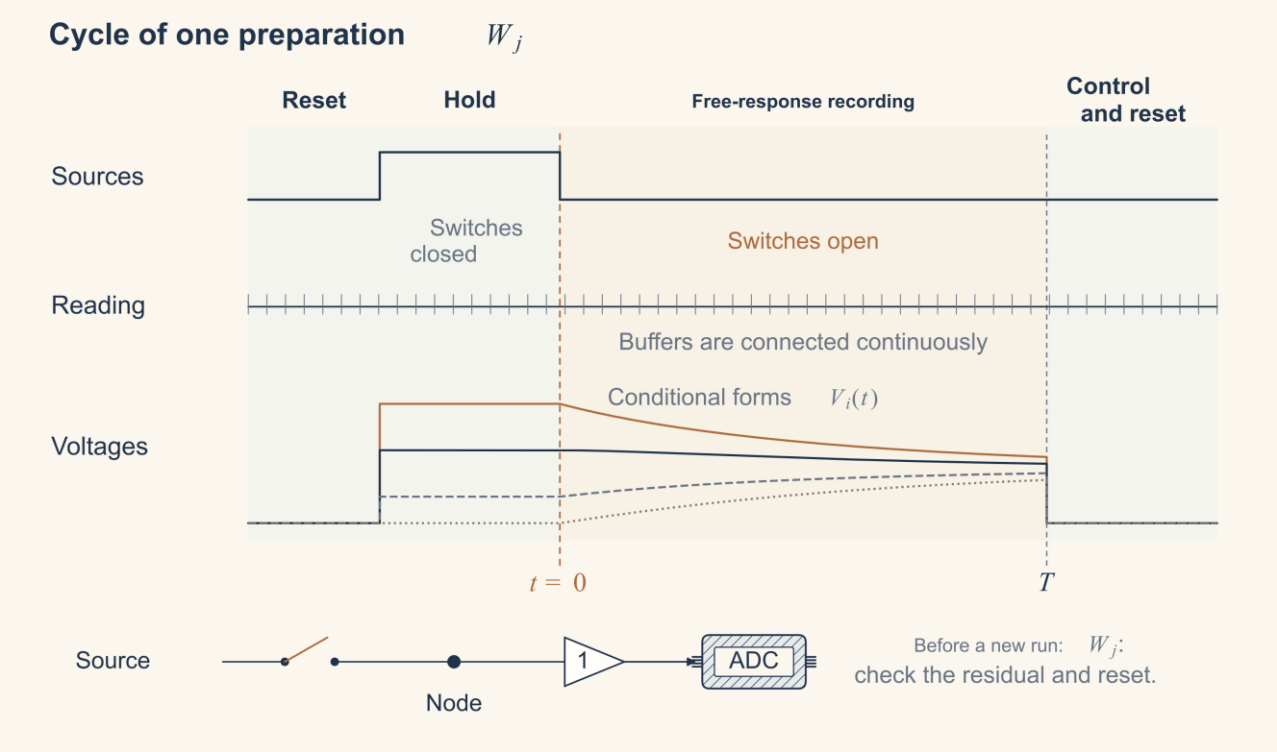


Figure 59. The cycle includes an active reset, simultaneous holding of four initial voltages, general disconnection of sources at t = 0 and recording of free dynamics. Buffers and ADC remain connected. Then the residual voltages are checked and all components are reset before the next preparation. The V_i(t) forms are conditional: they are calculated for an illustrative starting vector of the nominal circuit and do not replace the attached CSVs. The duration of preparation and reset is not specified numerically. Natural waiting does not replace the active removal of total charge.

Parameter	**In this calculation**	**What is required during physical transfer**
R_0 and C_0	100 kOhm and 100 nF	Measured values and their uncertainties
Input load	1 GOhm in each node	Testing Resistance, Bias, and Input Capacitance
Preparation matrix W	Specified exactly, cond(W)=1.0049	Re-evaluation after switching
Step and window	50 μs and 0.25 s	Timeline and Delay Calibration
Random counting error	0.2 mV, independent Gaussian noise	Spectrum and interchannel covariance measurements

If the actual capacitances differ markedly, the operator $C^{-1}K$ and its symmetric form from (13.3) should be used. Changing the number C_0 in the program alone is not enough. For this workshop, the equality of capacitances is a verifiable prerequisite: the calculation file specifies it exactly, and the hardware protocol must either confirm it with the required error, or expand the model.

From a voltage matrix to a normalized response

Let us denote by Y(t) the matrix of recorded voltages: its columns correspond to four preparations. With a known identical load γ and without a random error, $Y(t)=\exp[-(L+\gamma I)t]W$. Multiplying on the right by W^{-1} removes the mixing of preparations; the multiplier $\exp(\gamma t)$ returns the unloaded network dynamics. In the numerical example, $\gamma=1/(RinC_0)=0.01\ s^{-1}$.

$$\widehat{\mathbf{E}}(t) = e^{\gamma t}\mathbf{Y}(t)\mathbf{W}^{-1}, \qquad \mathbb{E}\widehat{\mathbf{E}}(t) = e^{-t\mathbf{L}} \qquad \text{(E.1)}$$

The normalized response E is dimensionless. Its integral with weight exp(−st) has units of time. The parameter s here is real and positive; it specifies the damping of the integral weight and is not the sinusoidal excitation frequency in hertz. For current measurement at zero initial conditions, the same relationship has the form:

$$\mathbf{H}_{VI}(s) = (s\mathbf{C}+\mathbf{K})^{-1}, \qquad \mathbf{G}(s) = C_0\mathbf{H}_{VI}(s), \qquad [H_{VI}] = \Omega,\ [G] = \mathrm{s} \qquad \text{(E.2)}$$

In this formula, K refers to the selected unloaded network. If the current response is measured with the same input load γ, then $H_{VI,meas}(s)=G(s+\gamma)/C_0$. To restore the original G, a shift of the argument is required: $G(s)=C_0H_{VI,meas}(s-\gamma)$, for $s>\gamma$ used here. In the initial state method, the same shift is implemented by the weight $\exp[-(s-\gamma)t]$.

If the teaching-network operator uses a unit intensity for an ordinary edge, while the physical apparatus has intensity κ, then $L_{phys}=\kappa L_{unit}$. The quantity s and the entire response matrix must be scaled consistently. For example, $s_{unit}=0.2$ corresponds to $20\ s^{-1}$ when $\kappa=100\ s^{-1}$; the physical G is a hundred times smaller than the value computed in the original network's time units.

$$\mathbf{L}_{\mathrm{phys}} = \kappa\mathbf{L}_{\mathrm{unit}}, \qquad s_{\mathrm{phys}} = \kappa s_{\mathrm{unit}}, \qquad \mathbf{G}_{\mathrm{phys}}(\kappa s) = \kappa^{-1}\mathbf{G}_{\mathrm{unit}}(s) \qquad \text{(E.3)}$$

Normalization to the reference also requires discipline. Here, G is estimated from the absolute voltages, and the nominal matrix G_0 is calculated from the calibration model. Therefore, $\Delta G=G-G_0$ has the same random error covariance as G. If G_0 is obtained by a separate noisy record, its covariance is added; With common calibration parameters, cross terms appear. The uncertainty of the standard cannot be removed by simple subtraction.

The complete processing sequence and the control key disclosure branch separated from it are shown in Figure 60.

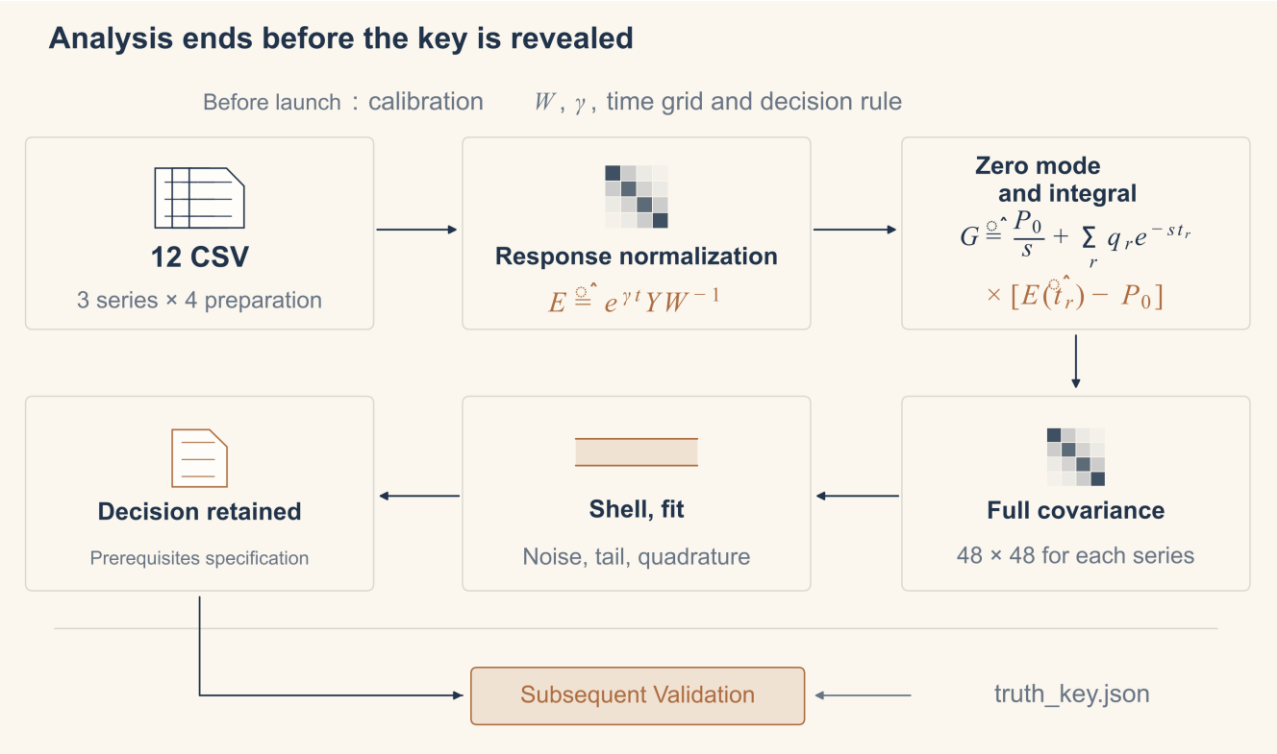


Figure 60. The calibration and decision rule are specified before analyzing the twelve CSVs. The normalized response is restored from the voltages, the known zero mode is subtracted before numerical integration, and it is returned analytically as P_0/s. Total covariance relates matrix elements and three s values from the same entries. The calibration shell is then checked, tail and quadrature are taken into account, diagnostic fits are made, and the solution is saved. The truth_key.json file is only used for subsequent validation; there is no way back to analysis.

Why a finite window is sufficient

The integral to finite T is different from the resolvent. For a well-known linear operator, the offset has the exact form:

$$\mathbf{G}_T(s) = \int_0^T e^{-st}\, e^{-t\mathbf{L}}\, dt = \mathbf{G}(s)\left[\mathbf{I} - e^{-(s\mathbf{I}+\mathbf{L})T}\right] \qquad \text{(E.4)}$$

A connected ungrounded graph has a known zero mode: the same voltage at all nodes. Its projector $P_0=11^T/4$ does not decay. Therefore, the full voltage should not simply be cut off at the end of a short window. In this experiment, the common component is subtracted before integration and added back analytically as P_0/s. Only damped inhomogeneous modes remain to be integrated.

$$\widehat{\mathbf{G}}(s) = \frac{\mathbf{P}_0}{s} + \sum_{r=0}^{M} q_r\, e^{-st_r}\left[\widehat{\mathbf{E}}(t_r) - \mathbf{P}_0\right] \qquad \text{(E.5)}$$

The weights q_r are the weights of the composite Simpson formula: h/3 at the ends, 4h/3 at the odd internal nodes and 2h/3 at the even ones. The number of intervals is 5000. The first non-zero eigenvalue of the nominal circuit is equal to 58.5786 s^{-1}, the largest is 341.4214 s^{-1}. If the usual

weights are limited from below by the number 0.98, the damping of non-uniform modes is guaranteed to be no slower than 57.4071 s^{-1}.

For the chosen contrast with unit norm and zero sum components, the absolute tail under the hypothesis of ordinary connections is limited by $\exp[-(s+0.98\lambda_2)T]/(s+0.98\lambda_2)$. When $s=20\ s^{-1}$ it does not exceed 5.10×10^{-11} s. The conservative error limit of the Simpson formula is 1.60×10^{-10} s. Both values are much smaller than the standard random contrast error 2.36×10^{-7} s.

$$\varepsilon_{\mathrm{tail}} \le \frac{e^{-(s+0.98\lambda_2)T}}{s+0.98\lambda_2}, \qquad \varepsilon_{\mathrm{quad}} \le \frac{Th^4}{180}(s+1.02\lambda_{\max})^4 \qquad \text{(E.6)}$$

The quadrature bound refers to the null hypothesis with limited ordinary conductances: its scalar integrand is a positive mixture of damped exponentials. Tail and quadrature errors are added to the tolerance when testing this hypothesis. For a specific connection entered, the program additionally compares the processing of the clean record with the exact inverse matrix. The rate of deterministic error there is about 6.9×10^{-12} s.

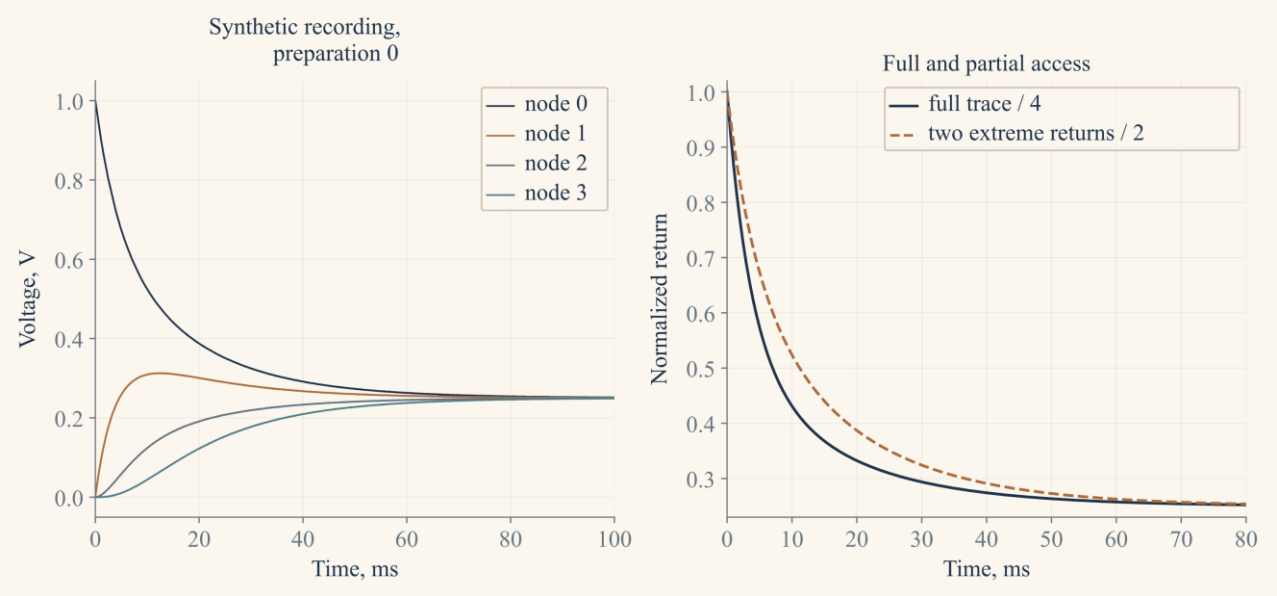


Figure 61. On the left are the synthetic voltages of four nodes after preparing 0 in the reference circuit. On the right is the full normalized heat trace and the average of the two extreme returns for a pure unloaded operator. Partial observation provides a different function, although both use the same network.

In the left panel of Figure 61, the voltages approach a common component of about a quarter volt. Restoring G preserves its analytical contribution. The right panel shows why the two available returns cannot be called a complete heat trace. In the reference circuit, the maximum absolute difference between these functions is about 0.102; it is caused by incomplete access, not noise.

Covariance from one time record

Let each initial voltage error be independent in time, channel and preparation and have a variance σV^2. After inverting W, the errors of different reconstructed columns are related, and after

integration, different s are also related. To preserve both dependencies, it is convenient to denote $M=W^{-1}$ and $a_r(s)=q_r\exp[-(s-\gamma)t_r]$. Then the covariance of individual elements has the form:

$$\mathrm{Cov}\left[\hat{G}_{ij}(s),\hat{G}_{kl}(s')\right]=\delta_{ik}\sigma_V^2\left(\mathbf{M}^{\mathsf{T}}\mathbf{M}\right)_{jl}\sum_r a_r(s)a_r(s') \qquad \text{(E.7)}$$

The observation vector contains 48 elements: three values s along 16 directed matrix elements. The program plots the covariance of size 48×48 in the order “s, observed node, preparation.” It is positive definite for a given set of weights and invertible W. To calculate χ^2, the Cholesky decomposition is used so that the remainder is compared to the noise in consistent units.

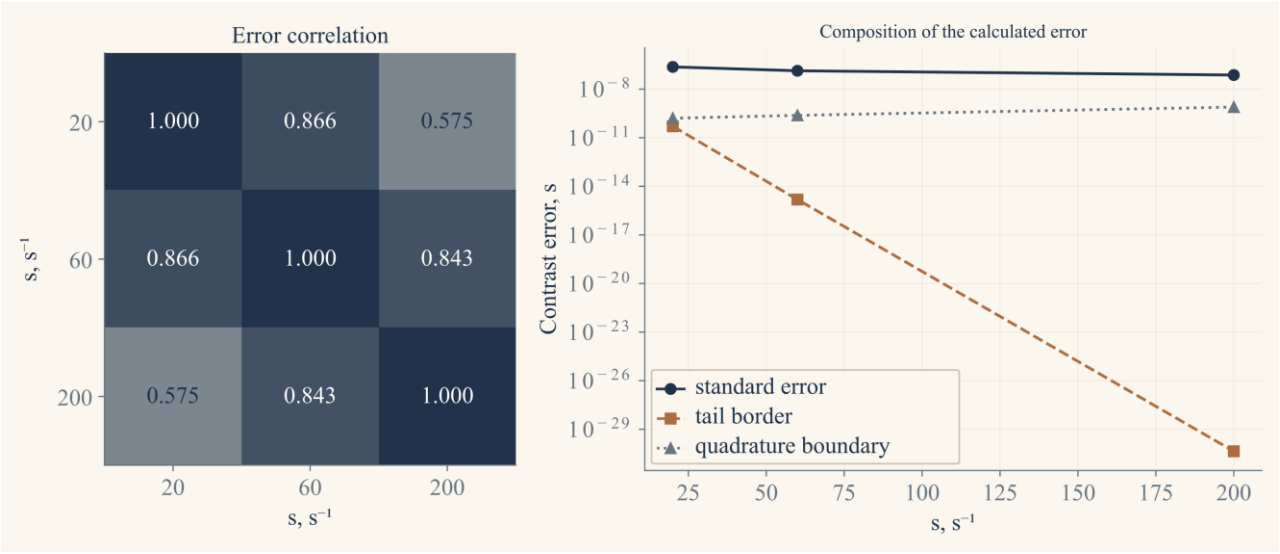


Figure 62. On the left - correlations of random errors of Laplace integrals from one record for s=20,60,200 s^{-1}. On the right is the standard error of the selected contrast, conservative tail and quadrature bounds. The latter were calculated under the hypothesis of ordinary conductances within ±2%.

The correlation in Figure 62 remains high even for spaced values of s. If you remove off-diagonal elements, the previous entries will be mistakenly considered more independent. Dividing the integrals of one oscillogram into “training” and “testing” does not in itself create independent noise. For such a check, a separate record or a conditional distribution taking into account full covariance is needed.

For real colored noise, the formula (E.7) is replaced by transferring the measured covariance of the original samples through the same linear operator. If W, γ, or gains are also estimated in error, they add individual terms or become parameters of the admissible model. The attached program records them accurately in order to separately check the calculation and use of correlations for one time series.

Predefined calibration shell

The null hypothesis Hcal allows any combination of the three conventional weights within 0.98-1.02. It does not require the independence of their drift. Since each edge adds a positive semidefinite matrix, the order of the operators follows from the boundaries of the weights. Inverting positive definite matrices changes the direction of the inequality:

$$0.98\mathbf{L}_0 \preccurlyeq \mathbf{L} \preccurlyeq 1.02\mathbf{L}_0 \quad \Rightarrow \quad (s\mathbf{I} + 1.02\mathbf{L}_0)^{-1} \preccurlyeq \mathbf{G}(s) \preccurlyeq (s\mathbf{I} + 0.98\mathbf{L}_0)^{-1} \qquad \text{(E.8)}$$

For a pre-selected a=(1,0,0,−1)/√2, the matrix inequality gives the interval for z=a^{T}Ga. When s=20 s^{-1} the boundaries are equal to 0.01110051757 and 0.01143981347 s. They cover the entire admissible class of ordinary conductances, including the consistent drift of all three edges. This is the difference between such a check and the failure of a single numerical optimizer.

The error z is calculated from the same total covariance. In this set σz=2.3572 × 10^{-7} s. 5σz and two deterministic boundaries (E.6) are added to the interval on each side; the total margin is equal to 1.1788 × 10^{-6} s. For one preselected Gaussian contrast, a margin of five standard deviations has a known tail value. Here it serves as a specific rule of teaching experiment rather than as a statement of the level of significance of a broad search across multiple geometries.

Exceeding the extended interval rejects Hcal under the given assumptions. It does not prove the uniqueness of the extra edge among all possible physical causes: unknown capacitance, nonlinearity, incorrect time scale, or unaccounted load are other alternatives. Therefore, the solution is accompanied by a specification of the included parameters. Being inside the interval only means that the shell did not reject the class. For the compatibility of all observations, it is additionally required to find one common feasible vector of weights. In records B and C such a vector is found; An absolute absence of new connections does not follow from this.

Fitting and opening control configurations

Additionally, a nonlinear adjustment of Hcal is performed for all 48 values and three adjustments of Hcal+edge for candidates 0-2, 0-3, 1-3. The normal weights in both classes have the same boundaries. The intensity of the additional edge is non-negative. The objective function is the squared norm of the remainder, whitened by the total covariance. A successful fit demonstrates the compatibility of the found parameters; global exclusion of the local class relies on the envelope, not the solver status.

$$\chi^2(\theta) = (\widehat{\mathbf{g}} - \mathbf{g}(\theta))^{\mathsf{T}} \mathbf{C}_G^{-1} \big(\widehat{\mathbf{g}} - \mathbf{g}(\theta)\big) \qquad \text{(E.9)}$$

For the found vector of parameters, it is checked whether it falls into the joint 99-percentage noise ellipsoid of dimension 48. The fitted parameters are not subtracted from the number of measurements: the region of the feasible mean vector is constructed here, rather than a test of improvement of the extended model. The radius is equal to the root of the corresponding quantile χ^2 with 48 degrees of freedom plus a conservative bound for the whitened shift of the integral. For a local class it turns out to be about 8.64, for an allowed additional edge - 8.72. The presence of such a point is calculated evidence of compatibility. If the solver did not find it, this in itself does not prove that it does not exist.

For record A, the local model achieves $\chi^2/48 \approx 5.87 \times 10^6$, and the model with the relationship 0-3 gives 0.871. Common weights in the extended fit are approximately 1.010048; 0.990024; 1.005033. The additional intensity estimate is 19.9974 s^{-1}. After opening the markings, it turns out that the

weights 1.01 have been entered; 0.99; 1.005 and intensity 20 s^{-1}. The example is deliberately chosen to be easily distinguishable.

Record B is obtained from the nominal weights 1;1;1. Its local fit gives $\chi^2/48=1.028$. Records C contain the weights 1.015;0.985;1.01 without a new edge; value $\chi^2/48=1.149$. In both cases, a small additional positive edge sometimes slightly reduces the remainder, but the rule does not declare it necessary. This shows why it would be a wrong procedure to always select the extended model only by the smaller χ^2.

Check after disclosure	A	B	C
Relative error of the entire G according to the Frobenius norm	0.00186%	0.00222%	0.00197%
Maximum absolute error of element G	4.61×10^{-7} s	4.35×10^{-7} s	4.41×10^{-7} s
$\chi^2/48$ of the best model with an additional edge	0.871	1.027	1.149
Global shell Hcal	Violated	Complied with	Complied with

These are three test realizations and not a statistical estimate of the error rate of the entire algorithm. Seeds and full initial parameters are saved to repeat a specific calculation. To estimate the operating range, it is necessary to pre-specify the series in terms of coupling amplitude, capacitance uncertainty, load and noise. The limit of such a range will be a property of the selected layout and measurement procedure.

Full trace and monitored ports

The heat trace of a complete N-node operator is equal to the average of N diagonal returns. To directly measure it, it is necessary to prepare and observe each node or apply a separately validated method for estimating the trace. In a four-node practice, full access exists, so both functions in the right panel of figure 61 are uniquely evaluated.

$$P(t)=\frac{1}{4}\sum_{i=0}^{3}E_{ii}(t),\qquad P_{\{0,3\}}(t)=\frac{1}{2}\left[E_{00}(t)+E_{33}(t)\right] \qquad (E.10)$$

If only the outermost ports are available, the second function is measured. It weighs more strongly the modes visible at the ends of the chain and therefore has a different time dependence. Its logarithmic slope can be described as a measure of the selected observed return, but without further justification it is not equal to the spectral dimension of the full operator.

Even the full trace of four nodes does not provide a wide power-law range. At very short times, discreteness appears; at long times, the zero mode remains and $P \to 1/4$. The main task of a small experiment is to restore the known dynamics and check the measurement transformations. Going to 64 nodes with eight ports preserves the matrix procedure of the observed block, but does not automatically give the entire heat trace.

Calibration order and independent repetitions

First, one RC circuit is tested: time constant, polarity, voltage scale and timing error. Then four nodes are connected without an additional edge. Actual capacitances are measured taking into account inputs, conductance and leakage currents. Several repetitions of the preparation give the average W and its variability. If the calibration error is comparable to the desired effect, it is included in the feasible model before processing the control configurations.

The next pass is performed with the circuit stationary and zero excitation to evaluate the intrinsic offsets, noise bandwidth, and overall channel interference. The standard is then recorded during normal preparation. Changing the polarity and amplitude allows you to check linearity. For each such impact, it is the predicted normalized response that is compared; arbitrary reconfiguration of coefficients after the result deprives the test of independence.

The control link is established by the operator, who stores the markup separately from the analyzer. After the series, it is useful to repeat the original connection. If the standard has changed, the sequence itself shows the drift and makes it possible to limit its magnitude. Testing on a new time series uses a new preparation and a new record; the additional integrals of the previous series remain correlated data.

During hardware acceptance, a small change in one capacitance and an increase in the input load are added to the three executed configurations. These two additional controls are specifically outside the narrow Hcal of this executable example. The correct response of the procedure is to detect the discrepancy and expand the hardware model, rather than automatically assigning any anomaly to a new edge.

Reproduction and reanalysis

The accompanying kit allows you to repeat the entire calculation: create synthetic records, perform analysis without access to the key, then separately open the markup and build drawings. Commands and requirements for the computing environment are given in the instructions for calculations.

When analyzing your own records, calibration information and observed voltages are used; the true markup key is not included in the calculation. Files must adhere to the specified schema and prerequisites. For colored noise or unequal capacitances, the appropriate covariance or dynamics model needs to be modified.

The result obtained completes the specific task: the response in seconds is reconstructed from the voltage readings, its joint error is calculated, the limited local class is verified, and a compatible explanation for the strong control signal is found. The next step is to replace the synthetic calibration with measured parameters. This is when promises about the accuracy of a physical device become verifiable.

References

[1] Albert Einstein. Die Grundlage der allgemeinen Relativitätstheorie. 1916. DOI 10.1002/andp.19163540702. https://doi.org/10.1002/andp.19163540702

[2] Hermann Weyl. Das asymptotische Verteilungsgesetz der Eigenwerte linearer partieller Differentialgleichungen (mit einer Anwendung auf die Theorie der Hohlraumstrahlung). 1912. DOI 10.1007/BF01456804.
https://link.springer.com/article/10.1007/BF01456804

[3] Jan Ambjørn, Jerzy Jurkiewicz, Renate Loll. The Spectral Dimension of the Universe is Scale Dependent. 2005. DOI 10.1103/PhysRevLett.95.171301.
https://arxiv.org/abs/hep-th/0505113

[4] Luca Bombelli, Joohan Lee, David Meyer, Rafael D. Sorkin. Space-time as a causal set. 1987. DOI 10.1103/PhysRevLett.59.521.
https://journals.aps.org/prl/abstract/10.1103/PhysRevLett.59.521

[5] J. Abajian, Steven Carlip. Dimensional reduction in manifoldlike causal sets. 2018. DOI 10.1103/PhysRevD.97.066007.
https://arxiv.org/abs/1710.00938

[6] Petr Hořava. Spectral Dimension of the Universe in Quantum Gravity at a Lifshitz Point. 2009. DOI 10.1103/PhysRevLett.102.161301.
https://arxiv.org/abs/0902.3657

[7] Oliver Lauscher, Martin Reuter. Fractal Spacetime Structure in Asymptotically Safe Gravity. 2005. DOI 10.1088/1126-6708/2005/10/050.
https://arxiv.org/abs/hep-th/0508202

[8] Oskar Klein. Quantentheorie und fünfdimensionale Relativitätstheorie. 1926. DOI 10.1007/BF01397481.
https://link.springer.com/article/10.1007/BF01397481

[9] Michael Lohse, Christian Schweizer, Hannah M. Price, Oded Zilberberg, Immanuel Bloch. Exploring 4D quantum Hall physics with a 2D topological charge pump. 2018. DOI 10.1038/nature25000.
https://arxiv.org/abs/1705.08371

[10] Juan M. Maldacena. The Large N Limit of Superconformal Field Theories and Supergravity. 1998. DOI 10.1023/A:1026654312961.
https://arxiv.org/abs/hep-th/9711200

[11] Shinsei Ryu, Tadashi Takayanagi. Holographic Derivation of Entanglement Entropy from AdS/CFT. 2006. DOI 10.1103/PhysRevLett.96.181602.
https://arxiv.org/abs/hep-th/0603001

[12] Mark Van Raamsdonk. Building up spacetime with quantum entanglement. 2010. DOI 10.1007/s10714-010-1034-0.
https://arxiv.org/abs/1005.3035

[13] Ryogo Kubo. Statistical-Mechanical Theory of Irreversible Processes. I. General Theory and Simple Applications to Magnetic and Conduction Problems. 1957. DOI 10.1143/JPSJ.12.570.
https://www.jstage.jst.go.jp/article/jpsj1946/12/6/12_6_570/_article/-char/en

[14] Elliott H. Lieb, Derek W. Robinson. The finite group velocity of quantum spin systems. 1972. DOI 10.1007/BF01645779.
https://www-thphys.physics.ox.ac.uk/talks/CMTjournalclub/sources/LR.pdf

[15] Ji-Seong Chae. Covariant holographic entanglement entropy inversion to reconstruct bulk geometry. 2026. DOI 10.1007/JHEP09(2026)251.
https://link.springer.com/article/10.1007/JHEP09(2026)251

[16] Carolyn Gordon, David L. Webb, Scott Wolpert. One cannot hear the shape of a drum. 1992. DOI 10.48550/arXiv.math/9207215.
https://arxiv.org/abs/math/9207215

[17] Florian Dörfler, Francesco Bullo. Kron Reduction of Graphs With Applications to Electrical Networks. 2013. DOI 10.1109/TCSI.2012.2215780.
https://arxiv.org/abs/1102.2950

[18] John Sylvester, Gunther Uhlmann. A global uniqueness theorem for an inverse boundary value problem. 1987. DOI 10.2307/1971291.
https://annals.math.princeton.edu/1987/125-1/p04

[19] Jack Sherman, Winifred J. Morrison. Adjustment of an Inverse Matrix Corresponding to a Change in One Element of a Given Matrix. 1950. DOI 10.1214/aoms/1177729893.
https://www.jstor.org/stable/2236561

[20] Sina Y. Caliskan, Paulo Tabuada. Kron Reduction of Generalized Electrical Networks. 2012. DOI 10.48550/arXiv.1207.0563.
https://arxiv.org/abs/1207.0563

[21] Jari Kaipio, Erkki Somersalo. Statistical inverse problems: Discretization, model reduction and inverse crimes. 2007. DOI 10.1016/j.cam.2005.09.027.
https://www.sciencedirect.com/science/article/pii/S0377042705007296

[22] Jan C. Willems. Dissipative dynamical systems part I: General theory. 1972. DOI 10.1007/BF00276493.
https://link.springer.com/article/10.1007/BF00276493

[23] Allan Adams, Nima Arkani-Hamed, Sergei Dubovsky, Alberto Nicolis, Riccardo Rattazzi. Causality, Analyticity and an IR Obstruction to UV Completion. 2006. DOI 10.1088/1126-6708/2006/10/014.
https://arxiv.org/abs/hep-th/0602178

[24] Patrick M. Lenggenhager et al. Simulating hyperbolic space on a circuit board. 2022. DOI 10.1038/s41467-022-32042-4.
https://arxiv.org/abs/2109.01148

[25] Gianluca Calcagni, Astrid Eichhorn, Frank Saueressig. Probing the quantum nature of spacetime by diffusion. 2013. DOI 10.1103/PhysRevD.87.124028.
https://arxiv.org/abs/1304.7247

[26] Nima Arkani-Hamed; Savas Dimopoulos; Gia Dvali. The Hierarchy Problem and New Dimensions at a Millimeter. 1998. DOI 10.1016/S0370-2693(98)00466-3.
https://arxiv.org/abs/hep-ph/9803315

[27] J. G. Lee; E. G. Adelberger; T. S. Cook; S. M. Fleischer; B. R. Heckel. New Test of the Gravitational $1/r^2$ Law at Separations down to 52 μm. 2020. DOI 10.1103/PhysRevLett.124.101101.
https://journals.aps.org/prl/abstract/10.1103/PhysRevLett.124.101101

[28] Wen-Hai Tan; An-Bin Du; Wen-Can Dong; Shan-Qing Yang; Cheng-Gang Shao; Sheng-Guo Guan; Qing-Lan Wang; Bi-Fu Zhan; Peng-Shun Luo; Liang-Cheng Tu; Jun Luo. Improvement for Testing the Gravitational Inverse-Square Law at the Submillimeter Range. 2020. DOI 10.1103/PhysRevLett.124.051301. https://journals.aps.org/prl/abstract/10.1103/PhysRevLett.124.051301

[29] Tobias Bothwell; Colin J. Kennedy; Alexander Aeppli; Dhruv Kedar; John M. Robinson; Eric Oelker; Alexander Staron; Jun Ye. Resolving the gravitational redshift across a millimetre-scale atomic sample. 2022. DOI 10.1038/s41586-021-04349-7. https://www.nature.com/articles/s41586-021-04349-7

[30] Xin Zheng; Jonathan Dolde; Matthew C. Cambria; Hong Ming Lim; Shimon Kolkowitz. A lab-based test of the gravitational redshift with a miniature clock network. 2023. DOI 10.1038/s41467-023-40629-8. https://www.nature.com/articles/s41467-023-40629-8

[31] Aaron Chou; Henry Glass; H. Richard Gustafson; Craig Hogan; Brittany L. Kamai; Ohkyung Kwon; Robert Lanza; Lee McCuller; Stephan S. Meyer; Jonathan Richardson; Chris Stoughton; Ray Tomlin; Rainer Weiss. The Holometer: An Instrument to Probe Planckian Quantum Geometry. 2017. DOI 10.1088/1361-6382/aa5e5c. https://arxiv.org/abs/1611.08265

[32] Jonathan W. Richardson; Ohkyung Kwon; H. Richard Gustafson; Craig Hogan; Brittany L. Kamai; Lee P. McCuller; Stephan S. Meyer; Chris Stoughton; Raymond E. Tomlin; Rainer Weiss. Interferometric Constraints on Spacelike Coherent Rotational Fluctuations. 2021. DOI 10.1103/PhysRevLett.126.241301. https://journals.aps.org/prl/abstract/10.1103/PhysRevLett.126.241301

[33] B. Sharmila; Sander M. Vermeulen; Animesh Datta. Signatures of correlation of spacetime fluctuations in laser interferometers. 2026. DOI 10.1038/s41467-025-67313-3. https://www.nature.com/articles/s41467-025-67313-3

[34] Abhinav Patra; Lorenzo Aiello; Aldo Ejlli; William L. Griffiths; Alasdair L. James; Nikitha Kuntimaddi; Ohkyung Kwon; Eyal Schwartz; Henning Vahlbruch; Sander M. Vermeulen; Keiko Kokeyama; Katherine L. Dooley; Hartmut Grote. Broadband Limits on Stochastic Length Fluctuations from a Pair of Table-Top Interferometers. 2025. DOI 10.1103/61j9-cjkk. https://arxiv.org/abs/2410.09175

[35] Fabio Bergamin; Nikitha Kuntimaddi; Abhinav Patra; Stephanie Montoya; Moritz Mehmet; Katherine Dooley; Hartmut Grote; Henning Vahlbruch. A broadband squeezed light source for table-top interferometry. 2025. DOI 10.1088/1367-2630/ae2987. https://arxiv.org/abs/2508.08857

[36] Sander M. Vermeulen; Torrey Cullen; Daniel Grass; Ian A. O. MacMillan; Alexander J. Ramirez; Jeffrey Wack; Boris Korzh; Vincent S. H. Lee; Kathryn M. Zurek; Chris Stoughton; Lee McCuller. Photon-Counting Interferometry to Detect Geontropic Space-Time Fluctuations with GQuEST. 2025. DOI 10.1103/PhysRevX.15.011034. https://journals.aps.org/prx/abstract/10.1103/PhysRevX.15.011034

[37] Bruce Allen; Joseph D. Romano. Detecting a stochastic background of gravitational radiation: Signal processing strategies and sensitivities. 1999. DOI 10.1103/PhysRevD.59.102001. https://arxiv.org/abs/gr-qc/9710117

[38] Johannes Nokkala; Jyrki Piilo; Ginestra Bianconi. Probing the spectral dimension of quantum network geometries. 2020. DOI 10.48550/arXiv.2005.09665. https://arxiv.org/abs/2005.09665

[39] Yanli Yuan; De Wen Soh; Xiao Yang; Kun Guo; Tony Q. S. Quek. Joint Network Topology Inference via Structured Fusion Regularization. 2021. DOI 10.48550/arXiv.2103.03471. https://arxiv.org/abs/2103.03471

[40] Madeline Navarro; Samuel Rey; Andrei Buciulea; Antonio G. Marques; Santiago Segarra. Joint Network Topology Inference in the Presence of Hidden Nodes. 2024. DOI 10.1109/TSP.2024.3392348. https://arxiv.org/abs/2306.17364

[41] D. Puetzfeld, Y. N. Obukhov, C. Lämmerzahl. Gravitational clock compass in General Relativity. 2018. DOI 10.1103/PhysRevD.98.024032. https://arxiv.org/abs/1805.10673

[42] D. Philipp, E. Hackmann, C. Lämmerzahl, J. Müller. The Relativistic Geoid: Gravity Potential and Relativistic Effects. 2020. DOI 10.1103/PhysRevD.101.064032. https://arxiv.org/abs/1912.10159

[43] R. Martín, E. Verdaguer. Stochastic semiclassical gravity. 1999. DOI 10.1103/PhysRevD.60.084008. https://arxiv.org/abs/gr-qc/9904021

[44] M. Rakhmanov, J. D. Romano, J. T. Whelan. High-frequency corrections to the detector response and their effect on searches for gravitational waves. 2008. DOI 10.1088/0264-9381/25/18/184017. https://arxiv.org/abs/0808.3805

[45] A. Kehagias, K. Sfetsos. Deviations from the $1/r^2$ Newton law due to extra dimensions. 2000. DOI 10.1016/S0370-2693(99)01421-5. https://arxiv.org/abs/hep-ph/9905417

[46] Harry Nyquist. Thermal Agitation of Electric Charge in Conductors. 1928. DOI 10.1103/PhysRev.32.110. https://journals.aps.org/pr/abstract/10.1103/PhysRev.32.110

[47] Nathan E. Flowers-Jacobs; Alessio Pollarolo; Kevin J. Coakley; Adam C. Weis; Anna E. Fox; Horst Rogalla; Weston L. Tew; Samuel P. Benz. The NIST Johnson Noise Thermometry System for the Determination of the Boltzmann Constant. 2017. DOI 10.6028/jres.122.046. https://nvlpubs.nist.gov/nistpubs/jres/122/jres.122.046.pdf

[48] Peter R. Saulson. Thermal noise in mechanical experiments. 1990. DOI 10.1103/PhysRevD.42.2437. https://journals.aps.org/prd/abstract/10.1103/PhysRevD.42.2437

Index of illustrations

1. Observer inside the measuring network 8

2. Coordinates, independent directions and length 10

3. Two internal curvature tests 12

4. Local geometry and global closure 13

5. Time, light cone and permissible trajectories 15

6. How the available area grows 17

7. Geodetic disks and sphere scale index 18

8. Return and propagation distance 20

9. From three nodes to the response matrix 23

10. Isospectral networks and discriminative local response 25

11. Three regimes of a finite apparatus 26

12. Two ways to define discrete geometry 30

13. The coordinates are saved, the spectral indicator changes 32

14. Direction closed in a circle 35

15. Periodicity and mode family 36

16. Heat trace of compact direction 38

17. Synthetic axis in a modern resonator 40

18. Common cause and controlled effect 44

19. Boundary area and surface in volume 45

20. Two reconstruction protocols for one system 49

21. Closed network and accessible ports 51

22. Static exclusion of hidden node 54

23. Data space: two models and calibration direction 57

24. Common edge dictionary and truly common connection 60

25. One link, one profile and port observation 62

26. How intervals of individual contrasts limit the strength of the connection 66

27. Original lattice and added edge 5–58 68

28. Singular values of total response change 69

29. Spatial pattern of port response 71

30. Restoration stability in the first series 73

31. Weak coupling and limited drift simulating it 76

32. Sensitivity of the original and new configuration 77

33. How many candidates does each set of observations store 79

34. Limited shell of separate contrast 79

35. False common pair and control ports 81
36. Reference record preserving electronic leakage 83
37. Results 96 of synthetic checks of the fixed protocol 84
38. Diffusion approximation and causal front 86
39. Hidden capacitor and response memory 88
40. Power indicator and range ladder of compact mods 95
41. From source movement to detector reading 96
42. Geometry of two finite disks 99
43. Additional force and conditional sensitivity of finite disks 101
44. Dynamic thresholds and discriminating gap 102
45. Acceleration and tidal curvature: one protocol, two backgrounds 106
46. Scale and time band of clock covariance 108
47. Geometry of two clocks and central gravimeter; coherence 111
48. Physical rearrangement of clocks while maintaining electronics 114
49. Results of synthetic clock permutation 115
50. Completed light path of interferometer 120
51. Why can a non-zero field produce a zero output 121
52. Frequency response and equivalent noise of the interferometer 123
53. Three interferometric readout strategies 126
54. Precise electrical diagram of four-node RC breadboard 129
55. Blind comparison of three RC records with calibration shell 131
56. Modern hardware path of RC experiment 132
57. Modern torsional sensor and torque measuring path 134
58. Blind protocol: who sees the device, record and key 139
59. Prepare, write and reset cycle 161
60. From CSV to hypothesis testing: complete processing chain 163
61. Time-series records and full/partial return 164
62. Covariance of integrals and error components 165

Author and projects

Email: info@brenev.com

Author website: brenev.com

Mira website: mira.technology

Other projects: haraizen.tech

Telegram: https://t.me/Eudgenee